

---

# **Search for Diboson Resonances with CMS and Pixel Barrel Detector Calibration and Upgrade**

---

Dissertation

zur  
Erlangung der naturwissenschaftlichen Doktorwürde  
(Dr. sc. nat.)

vorgelegt der  
Mathematisch-naturwissenschaftlichen Fakultät  
der  
Universität Zürich

von  
Jennifer Ngadiuba  
aus  
Italien

Promotionskomitee  
Prof. Dr. Benjamin Kilminster  
Prof. Dr. Florencia Canelli  
Dr. Andreas Hinzmann  
Dr. Lea Caminada

Zürich 2017



## Abstract

This doctoral thesis presents a search for new massive particles decaying to pairs of W, Z, and Higgs bosons performed with the CMS detector at the Large Hadron Collider (LHC). Such processes are the prominent feature of several extensions of the standard model that aim to clarify open questions in the SM, such as the apparently large difference between the electroweak and the gravitational scales. The semi-leptonic final states are considered, in which one of the bosons decays leptonically and the other hadronically. The first study is focused on a WH resonance decaying into the  $\ell\nu b\bar{b}$  final state and based on data recorded in proton-proton (pp) collisions at a center-of-mass energy  $\sqrt{s} = 8$  TeV during 2012 (LHC Run 1). The second study is focused on a WW or WZ resonance decaying into the  $\ell\nu q\bar{q}$  final state and based on 2015 data corresponding to pp collisions at  $\sqrt{s} = 13$  TeV (LHC Run 2). These final states are particularly challenging because for large resonance masses the bosons are highly energetic and the two quarks from the decay are separated by a small angle in space, resulting in the presence of one single merged jet after hadronization. This jet is identified as coming from a Higgs, W or Z boson applying novel jet substructure techniques and dedicated algorithms for the identification of b jets. The results for these two studies are finally combined with limits derived in companion CMS searches for resonances decaying to a pair of bosons in several different final states, with data collected in both LHC Run 1 and Run 2. This is the first combined search for high mass resonances with both WW/WZ and WH/ZH signatures.

Excellent detector performance is of utmost importance to search for new and rare physical phenomena. The efficient reconstruction of secondary vertices and precise measurements of the track impact parameter rely on this detector. Hence, the inner tracking pixel detector is a key component to tag events involving Higgs bosons decaying into  $b\bar{b}$ . Stable performance and future upgrades are thus necessary to maintain high identification efficiency of b jets for the entire lifespan of the LHC. Various aspects of my contributions to the CMS pixel barrel detector are detailed in the second part of the thesis. In particular, a major effort has been put after LHC Run 1 to replace and test faulty channels, and to perform calibrations aimed at optimizing the detector after it has been heavily irradiated during Run 1. The detector has been re-installed into CMS in December 2014 and the large effort in commissioning and calibration resulted in the successful and stable operation of the CMS pixel detector during data-taking in 2015 and 2016. Despite the excellent performance up to now, the pixel detector has not been designed to cope with the upcoming high luminosities of the LHC in the next years. Hence, a stepwise upgrade is foreseen, which is referred to as the “Phase I Pixel Upgrade”, which will be installed in Spring 2017. A test stand at the University of Zurich has been setup, which includes a slice of the CMS pixel data-acquisition system and all components of the upgraded read-out chain, together with a number of detector modules. The test system has been fundamental to develop new tests and procedures to be used during the upgraded detector assembly, commissioning and calibration.



## Zusammenfassung

Die vorliegende Doktorarbeit stellt eine Suche nach neuartigen schweren Teilchen am CMS Detektor am Large Hadron Collider (LHC) vor. Die Suche befasst sich mit dem Zerfall dieser neuartigen Teilchen in Paare von W, Z oder Higgs Bosonen. Diese Zerfälle sind ein wichtiges Merkmal verschiedener Erweiterungen des Standard Modells, die beabsichtigen offene Fragen des SM, wie zum Beispiel die deutliche Differenz zwischen der elektroschwachen Skala und der Planck-Skala, zu beantworten. Die Suche basiert auf semileptonischen Zerfällen, in denen eines der Bosonen leptonisch und das andere hadronisch zerfällt. Die erste Analyse befasst sich mit WH Resonanzen im Endzustand  $\ell\nu b\bar{b}$  und benutzt die Daten, die im Jahr 2012 bei Proton-Proton Kollisionen mit einer Schwerpunktsenergie von  $\sqrt{s} = 8 \text{ TeV}$  (LHC Run 1) aufgezeichnet wurden. Die zweite Analyse befasst sich mit WW und WZ Resonanzen im Endzustand  $\ell\nu q\bar{q}$  und benutzt die Daten, die im Jahr 2015 bei Proton-Proton Kollisionen mit einer Schwerpunktsenergie von  $\sqrt{s} = 13 \text{ TeV}$  (LHC Run 2) aufgezeichnet wurden. Die Rekonstruktion dieser Zerfälle ist äussert anspruchsvoll. Aufgrund der grossen Masse der Resonanz haben die Bosonen eine sehr hohe Energie, wodurch die Quarks im hadronischen Zerfall in einen kleinen Raumwinkel emittiert werden und sich zu einem einzigen Teilchenjet im Detektor zusammenfügen. Um diesen Teilchenjet als das Zerfallsprodukt von Higgs, W oder Z Bosonen zu identifizieren, werden neuartige Methoden angewandt, um die Unterstruktur der Teilchenjets aufzulösen und spezielle Algorithmen benutzt, um b-Quarks zu identifizieren. Die Resultate der beiden Analysen werden mit den Resultaten weiterer CMS Analysen, die in anderen Zerfallskanälen nach massiven Resonanzen suchen, kombiniert. Die Kombination beinhaltet die Daten von LHC Run 1 und Run 2. Die hier vorgestellte Arbeit ist die erste Suche nach massiven Resonanzen, die sowohl WW/WZ als auch WH/ZH Signaturen behandelt.

Der einwandfreie Betrieb des CMS Detektors ist unerlässlich für die Suche nach neuen und seltenen physikalischen Phänomenen. Insbesondere beruht sie auf der effizienten Rekonstruktion von Sekundärvertices und der präzisen Messung des Stossparameters von rekonstruierten Spuren. Der Pixeldetektor im Innersten des CMS Detektors ist folglich eine Schlüsselkomponente, um Ereignisse mit Higgs Bosonen, die in Paare von b-Quarks zerfallen, zu identifizieren. Um die hohe Rekonstruktionseffizienz von b-Quarks am CMS Detektor während der gesamten Laufzeit des LHCs zu gewährleisten, sind eine zuverlässige Datennahme und später neue und verbesserte Detektoren erforderlich. Meine vielfältigen Beiträge zum CMS Barrel Pixeldetektor werden im zweiten Teil dieser Arbeit besprochen. Dabei ist insbesondere das Testen und die Reparatur des Detektors nach LHC Run 1 zu erwähnen, sowie die optimale neue Kalibration, die den Effekt allfälliger Strahlenschäden mildert. Der Pixeldetektor wurde im Dezember 2014 wieder in CMS installiert und die Anstrengungen, die unternommen wurden, um den Detektor in Betrieb zu nehmen und zu kalibrieren, bilden die Grundlage für die zuverlässige und äusserst erfolgreiche Datennahme während 2015 und 2016. Trotz des bis anhin einwandfreien Betriebs des Pixeldetektors, ist er nicht dafür geschaffen, die bevorstehenden hohen Luminositäten der nächsten Jahre am LHC zu bewältigen. Deshalb sind schrittweise Verbesserungen des Detektors vorgesehen. Der erste verbesserte Detektor, der sogenannte "Phase 1 Pixel Upgrade", wird im Frühling 2017 installiert. An der Universität Zürich wurde ein Testsystem für den Phase 1 Pixeldetektor aufgebaut, das einen Teil des CMS Datennahmesystems, sowie alle Komponenten der Ausleseelektronik des Pixeldetektors und einige Detektormodule umfasst. Die wichtigsten neuen Tests und Prozeduren, die für den Bau, die Inbetriebnahme und die Kalibration des Phase 1 Pixeldetektors benötigt werden, sind an diesem Testsystem entwickelt worden.



# Contents

<b>1</b>	<b>Introduction</b>	<b>1</b>
<b>2</b>	<b>The standard model and beyond</b>	<b>4</b>
2.1	The standard model . . . . .	4
2.1.1	Electroweak theory . . . . .	6
2.1.2	Spontaneous symmetry breaking . . . . .	9
2.1.3	The Higgs mechanism . . . . .	10
2.1.4	The Higgs and Yukawa interactions . . . . .	12
2.1.5	Observation of a particle compatible with the standard model Higgs boson . . . . .	13
2.1.6	Quantum chromodynamics . . . . .	17
2.2	Limitations of the standard model . . . . .	18
2.3	Theories of new physics . . . . .	21
2.3.1	Warped extra dimensions . . . . .	21
2.3.2	Compositeness . . . . .	24
2.3.3	Heavy vector triplet . . . . .	26
<b>3</b>	<b>The CMS experiment at the LHC</b>	<b>29</b>
3.1	The Large Hadron Collider . . . . .	29
3.2	The CMS detector . . . . .	32
3.2.1	Tracking detectors . . . . .	33
3.2.2	Calorimetry . . . . .	36
3.2.3	Muon detectors . . . . .	38
3.2.4	The trigger system . . . . .	40
<b>I</b>	<b>Search for diboson resonances with CMS</b>	<b>44</b>
<b>4</b>	<b>Diboson resonances as signature for new physics</b>	<b>45</b>
<b>5</b>	<b>Data sets and simulated samples</b>	<b>48</b>
5.1	Simulation of proton-proton collisions . . . . .	48
5.1.1	Monte Carlo event generators . . . . .	48
5.1.2	CMS detector simulation . . . . .	53
5.2	Simulated samples . . . . .	53
5.2.1	Simulation of signal processes . . . . .	53
5.2.2	Simulation of background processes . . . . .	56
5.3	Data sets . . . . .	57
<b>6</b>	<b>Object and event reconstruction</b>	<b>60</b>
6.1	Tracks and vertices . . . . .	60
6.1.1	Track reconstruction . . . . .	60
6.1.2	Vertex reconstruction . . . . .	62
6.2	Electrons . . . . .	63
6.2.1	Electron reconstruction . . . . .	63
6.2.2	Electron trigger . . . . .	65

6.2.3	Electron identification . . . . .	68
6.3	Muons . . . . .	72
6.3.1	Muon reconstruction . . . . .	72
6.3.2	Muon trigger . . . . .	75
6.3.3	Muon identification . . . . .	77
6.4	Jets . . . . .	78
6.4.1	Jet clustering algorithms . . . . .	79
6.4.2	Jet reconstruction and calibration . . . . .	81
6.4.3	Identification of b jets . . . . .	88
6.5	Missing transverse energy . . . . .	92
6.6	$W \rightarrow \ell\nu$ reconstruction . . . . .	95
<b>7</b>	<b>Identification of highly boosted <math>W/Z \rightarrow q\bar{q}^{(\prime)}</math> and <math>H \rightarrow b\bar{b}</math></b>	<b>97</b>
7.1	Jet substructure observables . . . . .	97
7.1.1	Pruned jet mass . . . . .	97
7.1.2	N-subjettiness . . . . .	98
7.2	The V tagging algorithm . . . . .	100
7.3	The H tagging algorithm . . . . .	102
<b>8</b>	<b>Analysis strategy</b>	<b>105</b>
8.1	Final event selection and categorization . . . . .	105
8.2	$W+jets$ background estimate with $\alpha$ ratio method . . . . .	109
8.2.1	Description . . . . .	109
8.2.2	Extraction of the $W+jets$ normalization . . . . .	110
8.2.3	Extraction of the $W+jets$ shape . . . . .	110
8.2.4	Validation of the $\alpha$ method . . . . .	114
8.3	Modelling of top quark production . . . . .	116
8.4	Signal modeling . . . . .	117
8.5	Systematic uncertainties . . . . .	121
8.5.1	Systematic uncertainties in the background estimation . . . . .	121
8.5.2	Systematic uncertainties in the signal prediction . . . . .	123
8.6	Testing new resonance hypothesis . . . . .	125
8.6.1	Limit setting procedure . . . . .	126
8.6.2	The asymptotic approximation . . . . .	128
8.6.3	Quantifying an excess of events . . . . .	130
<b>9</b>	<b>Results with 8 TeV data</b>	<b>132</b>
9.1	Final $m_{WH}$ distribution . . . . .	132
9.2	Significance of the data . . . . .	132
9.3	Cross section limits . . . . .	134
<b>10</b>	<b>Results with 13 TeV data</b>	<b>136</b>
10.1	Final $m_{WV}$ distribution . . . . .	136
10.2	Cross section limits . . . . .	137
<b>11</b>	<b>Combination of searches for diboson resonances at <math>\sqrt{s} = 8</math> and 13 TeV</b>	<b>139</b>
11.1	Inputs to the combination . . . . .	140
11.1.1	Reinterpretations . . . . .	140
11.2	Combination procedure . . . . .	142
11.3	Results . . . . .	143

11.3.1	Limits on $W'$ and $Z'$ singlets . . . . .	143
11.3.2	Limits on heavy vector triplet ( $W' + Z'$ ) . . . . .	145
11.3.3	Limits on bulk graviton . . . . .	146
11.3.4	Significance at 2 TeV . . . . .	146
<b>12</b>	<b>Conclusions</b>	<b>148</b>
<b>II</b>	<b>Calibration and upgrade of the CMS pixel barrel detector</b>	<b>149</b>
<b>13</b>	<b>Introduction</b>	<b>150</b>
<b>14</b>	<b>The CMS pixel barrel detector</b>	<b>152</b>
14.1	Design . . . . .	152
14.2	Detector modules . . . . .	153
14.2.1	Sensor . . . . .	153
14.2.2	Readout chip . . . . .	156
14.2.3	Token bit manager . . . . .	158
14.3	Detector readout and control . . . . .	158
14.3.1	Readout of the analog signal . . . . .	159
14.3.2	Detector control and programming . . . . .	160
14.3.3	Supply tubes . . . . .	161
14.4	Pixel online software . . . . .	162
<b>15</b>	<b>Optimization and commissioning for LHC Run 2</b>	<b>164</b>
15.1	Effects of radiation damage in LHC Run 1 . . . . .	164
15.2	Optimization for LHC Run 2 . . . . .	167
15.3	Overview of pixel calibrations . . . . .	169
15.3.1	Adjustment of readout chain settings . . . . .	169
15.3.2	Optimization of the pulse height information . . . . .	177
15.4	Re-commissioning for LHC Run 2 . . . . .	181
15.4.1	Installation into CMS . . . . .	181
15.4.2	Calibrations at -10°C . . . . .	182
15.5	Performance at the start of Run 2 . . . . .	183
<b>16</b>	<b>Phase I upgrade of the CMS pixel barrel detector</b>	<b>187</b>
16.1	Motivations . . . . .	188
16.2	Detector layout . . . . .	190
16.3	Pixel modules . . . . .	191
16.3.1	The digital ROC . . . . .	192
16.3.2	The TBM and readout . . . . .	192
16.4	Supply tubes . . . . .	195
16.5	The test stand . . . . .	196
16.6	Testing and calibration . . . . .	199
16.6.1	Delay adjustments . . . . .	199
16.6.2	POH bias and gain . . . . .	200
16.6.3	Read back test . . . . .	201
16.6.4	ROC analog current and digital voltage . . . . .	202
<b>17</b>	<b>Conclusions</b>	<b>204</b>

<b>III Summary</b>	<b>205</b>
<b>A Studies on track reconstruction problems</b>	<b>206</b>
<b>Bibliography</b>	<b>210</b>

# CHAPTER 1

# Introduction

---

The current understanding of the fundamental constituents of matter and the interactions between them dates back to the middle of the 1970’s and is summarized in a theory called the *standard model* (SM) of particle physics. Although the SM has demonstrated remarkable and continued successes in providing experimental predictions and describing the observations, it does leave some phenomena unexplained. Thus, it is believed to be only an approximation to a more complete theory. The SM does not incorporate the full theory of gravitation as described by general relativity, or account for the accelerating expansion of the Universe (as possibly described by dark energy). The model does not contain any viable dark matter particle that possesses all of the required properties deduced from observational cosmology. Furthermore, it is not yet understood why gravitation is sixteen orders of magnitudes weaker than electroweak interaction.

In order to obtain conditions in which production of elementary particles can be studied, particle accelerators are used. The start-up of the Large Hadron Collider (LHC) at CERN in 2009 marked the beginning of a new era in particle physics. Being the highest energy collider ever built, it allows one to probe particle physics in an energy domain out of reach so far. A first milestone was already recently reached, in 2012, when the last unproven prediction of the SM, namely the existence of the scalar Higgs boson through the interaction of which the elementary particles can acquire mass, was finally confirmed by the LHC experiments, ATLAS and CMS. Despite this last remarkable confirmation of the SM, a major effort is ongoing to verify the existence of new physics exploiting the frontier energies achievable by the LHC. An important example of such quest is provided by the work described in this thesis. In fact, a search is presented for new massive particles decaying to pairs of W, Z, and Higgs bosons performed with the CMS detector. Several theories of new physics predict the existence of heavy particles that preferentially decay to such final states. These models usually aim to clarify open questions in the SM such as the apparently aforementioned large difference between the electroweak and the gravitational scales. Notable examples of such models include theories of extra dimensions and scenarios with composite Higgs bosons.

First, a study has been conducted focused on the search for a WH resonance in the  $\ell\nu b\bar{b}$  final state and based on data recorded in proton-proton (pp) collisions at a center-of-mass energy  $\sqrt{s} = 8 \text{ TeV}$  during 2012 (Run 1). This is one of the first searches for new physics with the Higgs boson in the final state, being made possible only after its discovery and measurement of its mass. A second study has then been performed focused on a WW or WZ resonance in the  $\ell\nu q\bar{q}$  final state and based on 2015 data corresponding to pp collisions at  $\sqrt{s} = 13 \text{ TeV}$  (Run 2). These final states are particularly challenging because for large resonance masses the bosons are highly energetic and the hadronization products from their decay overlap in the detector, preventing their identification as resolved jets. Thus, they are accessible only through novel jet reconstruction techniques, called “V tagging” or “H tagging”, which exploit the substructure of such objects and help to resolve the collimated decay products. Furthermore, additional sensitivity is achieved in the  $\ell\nu b\bar{b}$  search channel combining jet substructure algorithms with the specific characteristics of jets arising from the hadronization of bottom quarks (b jets).

The search in the  $\ell\nu b\bar{b}$  final state performed with data collected during Run 1, reported

a deviation of 2.2 standard deviations with respect to the SM expectations at a reconstructed WH invariant mass of 1.8 TeV, arousing large interest in the physics community. The excitement was further enhanced by the deviation reported in the same mass range by the ATLAS collaboration in a search for heavy diboson resonances in the all-hadronic final state. Therefore, when LHC resumed physics collisions at higher energy in 2015, a major effort has been put to explore the mass region of the excess with the first new data. The results of the second search described in this thesis and based on 2015 data did not confirm the excess. However, in order to fully understand the compatibility of the excess, a statistical combination is performed of these results together with limits derived in similar CMS searches for resonances decaying to a pair of bosons in several different final states, with data collected in both LHC Run 1 and Run 2. This is the first combined search for high mass resonances with both WW/WZ and WH/ZH signatures.

The CMS pixel barrel detector constitutes the central part of the CMS detector with about 48 million readout channels. Thanks to its capability of measuring secondary vertices with high precision, it plays a key role in the identification of events with long-lived objects such as bottom quarks. Its excellent performances are thus fundamental to access physical processes with a low cross section and b quarks in the final states, which is one of the main features of the analysis described in this thesis. The barrel part of the CMS pixel detector was developed, designed and built at PSI in cooperation with ETH Zurich and the University of Zurich. In the framework of this thesis important contributions were made. These include calibrations and testing of the detector after it has been heavily irradiated during the first LHC data-taking period. This work has been carried out during the two years (2013–2014) of shut down of the LHC after Run 1. Furthermore, after the re-installation of the pixel detector into CMS in December 2014, a large effort has been put in commissioning and calibration. The detector was then successfully operated during pp collision data-taking in 2015 and 2016.

My contributions have additionally been focused on the upgrade of the barrel pixel detector, required to fulfill the continuous increment of the LHC luminosity and the consequent increment of the event rate per collision. The project, referred to as “Phase 1 Pixel Upgrade”, was defined in 2012. The new system is currently under assembly and testing and it will be installed into CMS in Spring 2017. During the design and prototyping phase of the upgrade barrel system, the University of Zurich has been responsible for the testing of the complete system. For this purpose, a test stand has been setup, which includes a slice of the full readout chain consisting of a group of pixel detector modules connected through optical links to the front-end boards for readout and control and powered using a set of DC-DC converters. The main goal of the system test was to test all components of the detector system prior to full production, as well as establish test and calibration procedures for the assembly and commissioning. I have contributed to the assembly of the test system and I implemented some of its functionalities. Furthermore, I employed the system to test new calibration procedures aimed at guaranteeing a quick verification of the detector functionality during assembly and commissioning, as well as stable operations at the beginning of the 2017 data-taking period.

This thesis is organized in two parts. The first part is dedicated to the search for diboson resonances introduced above. In particular, in Chapter 2 a review of the standard model of particle physics is given, together with a discussion about its limitations and an introduction on scenarios of new physics predicting the existence of massive resonances decaying to pairs of W, Z, and Higgs bosons. Chapter 3 summarises the experimental setup, focusing on the Large Hadron Collider and the CMS detector, that was used to collect the data analyzed in this work. A brief overview of the signals under study and of the analysis strategy is

given in Chapter 4. The description of proton-proton collisions and their generation using Monte Carlo simulations is the topic of Chapter 5, while Chapter 6 is devoted to a description of the methods used in CMS to reconstruct the event and the physics objects relevant for this analysis. The algorithms used to identify the substructure inside highly energetic jet present in the decay of massive resonances represent a key aspect of this analysis and are reviewed in Chapter 7. Chapter 8 contains the main steps of the analysis, including details on the final event selection, the estimation of the SM background, the modelling of the signal, systematic uncertainties and statistical methods. The final results for the two independent searches are presented in Chapter 9 and Chapter 9 for the 8 TeV and 13 TeV data analyses, respectively. In Chapter 11 the aforementioned statistical combination of all CMS searches for diboson resonances is presented. Finally, Chapter 12 provides a brief summary of this work.

The second part of the thesis concentrates on hardware related work including the various aspects of my contributions to the CMS pixel barrel detector. An overview of the project is first given in Chapter 13, followed by a description of the design and main features of the present detector. Chapter 15 is dedicated to the efforts put during LS1 in optimizing and maintaining the detector, as well as the steps of the re-installation into CMS and commissioning for LHC Run 2. Since most of the work has been focused on calibrating the detector, and overview of the calibration procedure is provided together with the results from commissioning. Furthermore, the performance of the detector at the start up of Run 2 are discussed. The design and main features of the upgraded system and of the test stand at the University of Zurich are described in Chapter 16, where the new calibration procedure developed for the commissioning of the new detector are also detailed. Finally, a summary of this work is provided in Chapter 17.

# The standard model and beyond

---

Elementary particles and their interactions are described by a fundamental theory called standard model (SM) [1]. It describes three of the four fundamental forces of nature, namely the electromagnetic, weak and strong interactions, in the form of quantum field theories (QFT) with local gauge invariance. This theory has been confirmed by a large number of experimental results in the last forty years: from the precision measurements performed at the Large Electron Positron (LEP) and Tevatron [2] to the recent Large Hadron Collider (LHC) era (Chapter 3). The SM constitutes one of the most successful achievements in modern physics. It provides a very elegant theoretical framework, which is able to describe most of the known experimental phenomena in particle physics with high precision.

The basic ingredients of the SM are reviewed in Section 2.1. This is followed by a discussion in Section 2.2 about few of the main open issues of the SM, which motivate theories of new physics. Finally, three of the most popular theories beyond the standard model are introduced in Section 2.3. These models provide the theoretical framework, in which the search for new particles described in this thesis is conducted.

## 2.1 The standard model

The standard model attempts to explain all the phenomena in nature in terms of the properties and interactions of a small number of fundamental particles of three distinct categories (Table 2.1): two spin-1/2 families of fermions called *leptons* and *quarks*, and one family of spin-1 bosons called *gauge bosons*, which act as ‘force carriers’ in the theory. All particles of the SM are assumed to be *elementary*, i.e. they are treated as point particles, without internal structure or excited states.

The class of fermions include six quarks (up, down, charm, strange, top, bottom) and six leptons (electron, electron neutrino, muon, muon neutrino, tau, tau neutrino), which are organized in three groups (generations) of pairs from each category:

$$\begin{pmatrix} \nu_e & u \\ e & d \end{pmatrix} \quad , \quad \begin{pmatrix} \nu_\mu & c \\ \mu & s \end{pmatrix} \quad , \quad \begin{pmatrix} \nu_\tau & t \\ \tau & b \end{pmatrix}.$$

The defining property of the quarks is that they carry color charge, and hence, interact via the *strong interaction*. A phenomenon called color confinement results in quarks being very strongly bound to one another, forming color-neutral composite particles (*hadrons*) containing either a quark and an antiquark (*mesons*) or three quarks (*baryons*). Familiar examples of baryons are the proton and neutron, which also have the smallest mass among this family of particles. As quarks also carry electric charge and weak isospin, they interact with other fermions both via the *electromagnetic and weak interactions*. The three neutrinos do not carry electric charge, so their interaction is only driven by the weak force, which makes them difficult to detect. However, since they carry an electric charge, the electron, muon, and tau all interact electromagnetically. Each member of a generation has greater mass than the corresponding particles of lower generations. As the first generation charged

**Table 2.1:** Particles of the standard model [3].

	Symbol	Name	Mass (MeV)	Charge ( $e$ )	Spin
Up-type quarks	$u$	up	2.2	+2/3	1/2
	$c$	charm	1.27	+2/3	1/2
	$t$	top	173.21	+2/3	1/2
Down-type quarks	$d$	down	4.7	-1/3	1/2
	$s$	strange	96	-1/3	1/2
	$b$	bottom	4.18	-1/3	1/2
Up-type leptons	$\nu_e$	electron neutrino	< 2 eV	0	1/2
	$\nu_\mu$	muon neutrino	< 0.19	0	1/2
	$\nu_\tau$	tau neutrino	< 18.2	0	1/2
Down-type leptons	$e$	electron	0.51	-1	1/2
	$\mu$	muon	105.7	-1	1/2
	$\tau$	tau	1776.9	-1	1/2
Gauge bosons	$\gamma$	photon	0	0	1
	$W^\pm$	W	80.4 GeV	$\pm 1$	1
	Z	Z	91.2 GeV	0	1
	$g$	gluon	0	0	1
Higgs boson	H	Higgs	125.1 GeV	0	0

particles do not decay, all ordinary matter is composed of such particles. In particular, all atoms consist of electrons orbiting around atomic nuclei, ultimately constituted of up and down quarks. Second and third generation charged particles, on the other hand, decay with very short half lives, and are observed only in very high-energy environments. Neutrinos of all generations also do not decay, and pervade the universe, but rarely interact with ordinary matter. Although neutrinos were originally assumed to be massless in the standard model, it is now known from experimental results that they have very small but finite masses. To each of these fermions is associated an anti-particle with same mass and opposite quantum numbers.

In the SM, gauge bosons are defined as force carriers that mediate the strong, weak, and electromagnetic fundamental interactions. The use of the word ‘gauge’ refers to the fact that all three fundamental interactions arise as consequences of requiring invariance under local gauge symmetries. Specifically, the gauge symmetry group of the SM is  $SU(3)_C \times SU(2)_L \times U(1)_Y$ . Among the gauge bosons, the *photons* mediate the electromagnetic force between electrically charged particles. The photon is massless and is well-described by the theory of *quantum electrodynamics* (QED). The  $W^\pm$  and Z gauge bosons mediate the weak interactions between particles of different flavors (all quarks and leptons). They are massive, with the Z being slightly heavier than the W. The weak interactions involving the W exclusively act on left-handed particles and right-handed antiparticles. Furthermore, the W carries an electric charge and couples to the electromagnetic interaction. The electrically neutral Z boson interacts with both left-handed particles and antiparticles. These three gauge bosons along with the photons are grouped together, as collectively mediating the *electroweak interaction*, which is described in Section 2.1.1.

Eight massless *gluons* carrying color charge, mediate the strong interactions between quarks and also interact among themselves. The gluons and their interactions are described by the theory of *quantum chromodynamics* (QCD), which is described in Section 2.1.6.

As discussed in more detail in Section 2.1.2, one additional spin-0 particle, called the *Higgs boson*, is postulated to explain the origin of mass within the theory, since without it all the particles in the model are predicted to have zero mass.

In addition to the strong, weak and electromagnetic interactions between quarks and leptons, there is a fourth force of nature, gravity, which is not accounted for in the standard model. In fact, the gravitational interaction between elementary particles is so small that it can be neglected at the presently accessible energies.

### 2.1.1 Electroweak theory

The theory of electroweak interactions is based on the  $SU(2)_L \times U(1)_Y$  gauge group with the quantum numbers of weak isospin  $I$  and hypercharge  $Y$ . Quarks and leptons are represented by spinor fields  $\psi$ , which are functions of continuous space-time coordinates  $x^\mu$ . From experimental evidences it is known that the weak interaction is of the form of vector minus axial current ( $V - A$ ), or in other words, it couples only to left-handed chirality states. It is therefore convenient to write the field  $\psi$  as the sum of the two chirality components:

$$\psi_L(x) = \frac{1 - \gamma^5}{2} \psi(x) \quad \text{and} \quad \psi_R(x) = \frac{1 + \gamma^5}{2} \psi(x). \quad (2.1)$$

The left-handed fields are grouped into  $SU(2)_L$  doublets consisting of one charged and one neutral lepton, or one up and one down quark, with a weak isospin  $I = 1/2$ :

$$\begin{pmatrix} \nu_\ell \\ \ell \end{pmatrix}_L \quad \text{and} \quad \begin{pmatrix} q_u \\ q_d \end{pmatrix}_L.$$

For up-type quarks and neutrinos the third component of the weak isospin is assigned as  $I_3 = +1/2$ ; for down-type quarks and charged leptons the component is  $I_3 = -1/2$ . The right-handed partners ( $\ell_R$ ,  $q_{uR}$ ,  $q_{dR}$ ) transform as  $SU(2)_L$  singlet with weak isospin  $I_3 = 0$ . The weak hypercharge  $Y$  aforementioned is then defined via electric charge  $Q$  and weak isospin to be  $Y = 2Q - 2I_3$ . Thus, members within a doublet carry the same hypercharge:  $Y = -1$  for leptons and  $Y = 1/3$  for quarks.

In quantum field theories, the equations of motion for the different fields considered are derived from the Lagrangian that contains all the information on the fields and on their interaction. In the SM, the fermionic fields are added by hand to the Lagrangian to account for experimental observations. The situation is however different for the bosonic fields, as their existence is a direct consequence of invariance properties of the Lagrangian. This mechanism can be understood by starting from the Lagrangian for a free spin-1/2 particle with mass  $m$ :

$$\mathcal{L}_0 = i\bar{\psi}\gamma^\mu\partial_\mu\psi - m\bar{\psi}\psi, \quad (2.2)$$

where  $\gamma^\mu$  are the Dirac matrices. It is straightforward to verify that the  $\mathcal{L}_0$  is invariant under global  $U(1)$  transformations

$$\psi(x) \xrightarrow{U(1)} \psi'(x) \equiv e^{iQ\theta}\psi(x), \quad (2.3)$$

where  $Q$  is the electric charge carried by the particle involved and  $\theta$  an arbitrary constant. However, the free Lagrangian is no longer invariant if one allows the phase transformation to depend on the space-time coordinate, i.e. under local phase redefinitions  $\theta = \theta(x)$ , because

$$\partial_\mu\psi(x) \xrightarrow{U(1)} e^{iQ\theta}(\partial_\mu + iQ\partial_\mu\theta)\psi(x), \quad (2.4)$$

and  $\mathcal{L}_0$  picks up an extra term. The *gauge invariance* is the requirement that the  $U(1)$  phase invariance should hold locally. This is only possible if some additional terms are added to the Lagrangian, so to cancel the  $\partial_\mu \theta$  term in Eq. 2.4. This is achieved by introducing a new spin-1 field  $A_\mu(x)$ , called a “gauge” field, that transforms as

$$A_\mu(x) \xrightarrow{U(1)} A'_\mu(x) \equiv A_\mu(x) + \frac{1}{e} \partial_\mu \theta, \quad (2.5)$$

and by defining a covariant derivative

$$\mathcal{D}_\mu \equiv \partial_\mu - ieQ A_\mu, \quad (2.6)$$

which has the required property of transforming like the field itself:

$$\mathcal{D}_\mu \psi(x) \xrightarrow{U(1)} (\mathcal{D}_\mu \psi)'(x) \equiv e^{iQ\theta} \mathcal{D}_\mu \psi(x). \quad (2.7)$$

The resulting Lagrangian

$$\mathcal{L} = i\bar{\psi} \gamma^\mu \mathcal{D}_\mu \psi - m\bar{\psi} \psi = \mathcal{L}_0 + eQ A_\mu \bar{\psi} \gamma^\mu \psi \quad (2.8)$$

is then invariant under local  $U(1)$  transformations. For the new gauge field to be a true propagating field, a gauge-invariant kinetic term has to be added to the Lagrangian

$$\mathcal{L}_A = -\frac{1}{4} F_{\mu\nu} F^{\mu\nu}, \quad (2.9)$$

where  $F_{\mu\nu} \equiv \partial_\mu A_\nu - \partial_\nu A_\mu$ . A possible mass term for the gauge field,  $m^2 A^\mu A_\mu$ , is forbidden because it would violate gauge invariance, so that it is predicted to be massless. The new gauge field can be easily identified with the electromagnetic potential, and the total Lagrangian

$$\mathcal{L} = [i\bar{\psi} \gamma^\mu \partial_\mu \psi - m\bar{\psi} \psi] + \left[ -\frac{1}{4} F_{\mu\nu} F^{\mu\nu} \right] + [eQ A_\mu \bar{\psi} \gamma^\mu \psi] \quad (2.10)$$

gives rise to the well-known Maxwell equations of the electrodynamics

$$\partial_\mu F^{\mu\nu} = J^\nu, \quad J^\nu = -eQ \bar{\psi} \gamma^\nu \psi, \quad (2.11)$$

where  $J^\nu$  is the fermion electromagnetic current. Thus, the final Lagrangian in Eq. 2.10 represents the final expression for the Lagrangian of quantum electrodynamics, describing Dirac fields (fermions) interacting wth Maxwell fields (photons).

To describe weak interactions, a more elaborated structure is needed, with several fermionic flavors and different properties for left- and right-handed fields. Moreover, the left-handed fermions must appear in doublets, and massive gauge bosons  $W^\pm$  and  $Z$  must be present in addition to the photon. The simplest group with doublet representations is  $SU(2)$ , and since the theory must include QED as well, the additional  $U(1)$  group is needed. Hence, the obvious symmetry group to consider is  $SU(2)_L \times U(1)_Y$ , where  $L$  refers to left-handed fields and  $Y$  to the hypercharge.

The free Lagrangian for a generation of quarks (or leptons) is given by

$$\mathcal{L}_0 = \sum_{j=1}^3 i\bar{\psi}_j \gamma^\mu \partial_\mu \psi_j, \quad (2.12)$$

where the following notation has been introduced

$$\psi_1(x) = \begin{pmatrix} u \\ d \end{pmatrix}_L, \quad \psi_2(x) = u_R, \quad \psi_3(x) = d_R. \quad (2.13)$$

The free Lagrangian  $\mathcal{L}_0$  is invariant under global  $G$  transformations in flavor space:

$$\begin{aligned} \psi_1(x) &\xrightarrow{G} \psi'_1(x) \equiv e^{iY_1\beta} U_L \psi_1(x) \\ \psi_2(x) &\xrightarrow{G} \psi'_2(x) \equiv e^{ig'Y_2\beta} \psi_2(x) \\ \psi_3(x) &\xrightarrow{G} \psi'_3(x) \equiv e^{ig'Y_3\beta} \psi_3(x) \end{aligned} \quad (2.14)$$

where the  $SU(2)_L$  transformation

$$U_L \equiv e^{ig\frac{\tau^i}{2}\alpha^i} \quad (i = 1, 2, 3) \quad (2.15)$$

only acts on the doublet field  $\psi_1$ . The parameters  $Y_i$  are three different values (one per each field) of the hypercharge, which represents the generator of the symmetry group  $U(1)_Y$ . The  $\beta$  parameter is the phase of the  $U(1)_Y$  transformation and is one-dimensional. The matrices  $\tau_i$  are the Pauli matrices and represent the three  $SU(2)_L$  transformation generators which are combined in the weak isospin operator  $\mathbf{T} = (\tau_1, \tau_2, \tau_3)$ . These matrices form a Lie group, which is defined by the commutator relation  $[\tau_i, \tau_j] = i\epsilon_{ijk}\tau_k$ . As the  $\tau_i$  do not commute, the  $SU(2)_L$  group is called non-Abelian. Due to the generator structure, the phase  $\alpha = (\alpha_1, \alpha_2, \alpha_3)$  of the  $SU(2)_L$  transformation has to be extended to a three-component vector with the same dependencies as above. The couplings  $g$  and  $g'$  have been introduced for the  $SU(2)_L$  and  $U(1)_Y$ , respectively, quantifying the strength of the interactions.

The free Lagrangian in Eq. 2.12 is then required to be invariant under local  $SU(2)_L \times U(1)_Y$  gauge transformations, i.e. with  $\alpha_i = \alpha_i(x)$  and  $\beta = \beta(x)$ . In order to satisfy this symmetry requirement, the fermion derivatives are exchanged with covariant objects. Since there are now four gauge parameters,  $\alpha_i(x)$  and  $\beta(x)$ , four different gauge fields are needed:

$$\mathcal{D}_\mu \equiv \partial_\mu + ig\mathbf{W}_\mu \cdot \mathbf{T} + ig'\frac{Y}{2}B_\mu. \quad (2.16)$$

Thus, four additional vector fields of spin 1 have been added: the isotriplet  $\mathbf{W}_\mu = (W_{1\mu}, W_{2\mu}, W_{3\mu})$  for the  $SU(2)_L$  and the singlet  $B_\mu$  for the  $U(1)_Y$ . The quanta of these fields are called gauge bosons. In order to build the gauge-invariant kinetic term for the gauge bosons, the corresponding field strengths are introduced:

$$\begin{aligned} B_{\mu\nu} &\equiv \partial_\mu B_\nu - \partial_\nu B_\mu \\ W_{\mu\nu}^i &\equiv \partial_\mu W_\nu^i - \partial_\nu W_\mu^i - g\epsilon_{ijk}W_\mu^jW_\nu^k. \end{aligned} \quad (2.17)$$

The final  $SU(2)_L \times U(1)_Y$  Lagrangian is then given by

$$\mathcal{L}_{SU(2)_L \times U(1)_Y} = \mathcal{L}_f + \mathcal{L}_g, \quad (2.18)$$

where  $\mathcal{L}_f$  is the Lagrangian for the free fermion fields

$$\mathcal{L}_f = i \sum_j \bar{\psi}_L^j \gamma^\mu [\partial_\mu + ig\mathbf{W}_\mu \cdot \mathbf{T} + ig'\frac{Y_L}{2}B_\mu] \psi_L^j + i \sum_j \bar{\psi}_R^j [\partial_\mu - g'Y_R B_\mu] \psi_R^j \quad (2.19)$$

and  $\mathcal{L}_g$  is the Lagrangian for the gauge bosons

$$\mathcal{L}_g = -\frac{1}{4} \mathbf{W}_{\mu\nu} \cdot \mathbf{W}^{\mu\nu} - \frac{1}{4} B_{\mu\nu} \cdot B^{\mu\nu}. \quad (2.20)$$

Since the field strengths  $W_{\mu\nu}^i$  contain a quadratic term, the Lagrangian  $\mathcal{L}_g$  gives rise to cubic and quartic self-interactions among the gauge fields. The strength of these interactions is given by the same  $SU(2)_L$  coupling  $g$  which appears in the fermionic piece of the Lagrangian. The final Lagrangian represents the unified electroweak theory, developed by Glashow [4], Weinberg [5] and Salam [6]. However, this is not the entire theory since the gauge symmetry forbids to write a mass term for the gauge bosons. Fermionic masses are also not possible, because they would connect the left- and right-handed fields, which have different transformation properties, and therefore would produce an explicit breaking of the gauge symmetry. Thus, the  $SU(2)_L \times U(1)_Y$  Lagrangian in Eq. 2.17 only contains massless fields. The mass terms are introduced through a procedure that exploits spontaneous symmetry breaking as described in the following.

### 2.1.2 Spontaneous symmetry breaking

In order to generate masses, the gauge symmetry needs to be broken in such way to maintain the full symmetry of the Lagrangian. The main idea is based on the possibility to obtain non-symmetric results from a Lagrangian that possess the following properties: it is invariant under a group  $G$  of transformations and has a degenerate set of states with minimal energy, which transform under  $G$  as the members of a given multiplet. As it will be demonstrated in the following, by arbitrary selecting one of those states as the ground state of the system, one says that the symmetry becomes spontaneously broken.

In order to explain this mechanism the Lagrangian for a complex scalar field  $\phi(x) = \phi_1(x) + i\phi_2(x)$  is considered

$$\mathcal{L} = \partial_\mu \phi^\dagger \partial^\mu \phi - V(\phi), \quad V(\phi) = \mu^2 \phi^\dagger \phi + h(\phi^\dagger \phi)^2 \quad (2.21)$$

where  $V(\phi)$  is a potential. The Lagrangian  $\mathcal{L}$  is invariant under global phase transformations of the scalar field

$$\phi(x) \xrightarrow{U(1)} \phi'(x) \equiv e^{i\theta} \phi(x). \quad (2.22)$$

In order to allow for a minimum or “ground state” of the potential, the parameter  $h$  has to be  $\geq 0$ . For the quadratic term there are the two following possibilities. If  $\mu^2 \geq 0$ , the potential acquires only the trivial minimum  $\phi_m = 0$ . If  $\mu^2 \leq 0$  the minimum is obtained for all those field configurations satisfying

$$|\phi_m| = \sqrt{\frac{-\mu^2}{2h}} \equiv \frac{v}{\sqrt{2}} \geq 0 \quad \Rightarrow \quad V(\phi_m) = -\frac{h}{4} v^4 \quad (2.23)$$

As the Lagrangian is invariant under  $U(1)$  phase transformations, there is an infinite number of degenerate states of minimum energy given by  $\phi_m(x) = \frac{v}{\sqrt{2}} e^{i\theta}$ . A particular solution can be chosen, e.g.  $\theta = 0$ , corresponding to the minimum of the field given by  $\phi_{1m} = v/\sqrt{2}$  and  $\phi_{2m} = 0$ . Since the Feynman calculus is a perturbation procedure, in which starting from a ground state the fields are treated as fluctuations about that state, two new real fields  $\eta(x)$  and  $\xi(x)$  are introduced representing these fluctuations

$$\eta(x) = \phi_1(x) - \frac{v}{\sqrt{2}} \quad \text{and} \quad \xi(x) = \phi_2(x). \quad (2.24)$$

In terms of these new fields, the potential  $V(\phi)$  takes the form

$$V(\phi) = V(\phi_m) - \mu^2 \eta^2 + h v \eta (\eta^2 + \xi^2) + \frac{h}{4} (\eta^2 + \xi^2)^2 \quad (2.25)$$

and the resulting Lagrangian does not share the same symmetry of the original one. Thus, by choosing a particular solution as the ground state, the symmetry gets spontaneously broken. At the same time, the second term of the potential in Eq. 2.25 is a mass term, so the real field  $\eta$  describes a massive state of mass  $m_\eta = -2\mu^2$ . The second real field  $\xi$  is massless, and its appearance can be understood as follows. The field  $\xi$  describes excitations around a flat direction in the potential, i.e. into states with the same energy as the chosen ground state. Since those excitations do not cost any energy, they correspond to a massless state. The fact that there are massless excitations associated with the spontaneous symmetry breaking mechanism is a general result, known as the *Goldstone theorem*: if a Lagrangian is invariant under a continuous symmetry group  $G$ , but the vacuum is only invariant under a subgroup  $H \subset G$ , then there must exist as many massless spin-0 particles (*Goldstone bosons*) as broken generators (i.e. generators of  $G$  which do not belong to  $H$ ).

### 2.1.3 The Higgs mechanism

The mechanism of spontaneous symmetry breaking described in the previous section does not account for the mass of the gauge fields of the weak interaction, since it introduces an additional massless scalar boson that is not included in the set of the known elementary particles. However, further elements are added to the theory when applying the idea of spontaneous symmetry breaking to the case of local gauge invariance. In order to achieve this, the complex scalar field  $\phi(x)$  introduced in the previous section is replaced with a  $SU(2)_L$  doublet of complex scalar fields with  $U(1)$  hypercharge  $Y = +1/2$ :

$$\phi(x) \equiv \begin{pmatrix} \phi^+(x) \\ \phi^0(x) \end{pmatrix} = \frac{1}{\sqrt{2}} \begin{pmatrix} \phi_1(x) - i\phi_2(x) \\ \phi_3(x) - i\phi_4(x) \end{pmatrix}. \quad (2.26)$$

The gauged scalar Lagrangian of the Goldstone model (Eq. 2.21) is now given by

$$\begin{aligned} \mathcal{L}_\phi &= \mathcal{D}_\mu \phi^\dagger \mathcal{D}^\mu \phi - \mu^2 \phi^\dagger \phi + h (\phi^\dagger \phi)^2, & (h \geq 0, \mu^2 \leq 0), \\ \mathcal{D}^\mu \phi &= [\partial^\mu + ig \mathbf{W}_\mu \cdot \mathbf{T} + ig' \frac{Y}{2} B_\mu], & (Y = Q - \tau_3 = \frac{1}{2}), \end{aligned} \quad (2.27)$$

and it is invariant under local  $SU(2)_L \times U(1)_Y$  transformations. The value of the scalar hypercharge is fixed by the requirement of having the correct couplings between  $\phi(x)$  and  $B_\mu(x)$ , i.e. that the photon does not couple to  $\phi^0$ , and one has the right electric charge for  $\phi^+$ . As observed in the previous section, there is an infinite set of degenerate states with minimum energy satisfying

$$\begin{aligned} \langle 0 | \phi_i | 0 \rangle &= 0 \quad \text{for } i = 1, 2, 4 \\ \langle 0 | \phi_3 | 0 \rangle &= \sqrt{\frac{-\mu^2}{2h}} \equiv \frac{v}{\sqrt{2}}. \end{aligned} \quad (2.28)$$

Since the electric charge is a conserved quantity, only the neutral scalar field can acquire a vacuum expectation value. Once a particular ground state is chosen, the  $SU(2)_L \times U(1)_Y$  symmetry gets spontaneously broken. On the other hand, the vacuum carries no electric charge, so the  $U(1)_Q$  of QED is not broken. Thus, the  $SU(2)_L \times U(1)_Y$  group of the electroweak theory is spontaneously broken to the  $U(1)_Q$  subgroup, i.e.  $SU(2)_L \times U(1)_Y \rightarrow U(1)_Q$ .

The scalar doublet can now be written in its general, gauge-invariant form as a fluctuation over the ground state

$$\phi(x) = e^{i\frac{\tau^i}{2}\theta^i(x)} \frac{1}{\sqrt{2}} \begin{pmatrix} 0 \\ v + H(x) \end{pmatrix} \quad (2.29)$$

with 4 real fields  $\theta^i(x)$  and  $H(x)$ . The crucial point is that the local  $SU(2)_L$  invariance of the Lagrangian allows one to rotate away any dependence on  $\theta^i(x)$ . These three fields would be precisely the massless Goldstone bosons associated with the spontaneous symmetry breaking mechanism. The additional ingredient of gauge symmetry makes these massless excitations unphysical. In fact, it can be demonstrated that by choosing the physical (unitary) gauge  $\theta^i(x) = 0$ , the 3 massless Goldstone bosons arising from the three broken generators can be eliminated from the Lagrangian. At the same time, the kinetic piece of the scalar Lagrangian in Eq. 2.27 takes the form

$$(\mathcal{D}_\mu \phi)^\dagger \mathcal{D}^\mu \phi \xrightarrow{\theta^i=0} \frac{1}{2} \partial_\mu H \partial^\mu H + (v + H)^2 \left\{ \frac{g^2}{4} W_\mu^\dagger W^\mu + \frac{g^2}{8 \cos^2 \theta_W} Z_\mu Z^\mu \right\}. \quad (2.30)$$

The vacuum expectation value of the neutral scalar has generated a quadratic term, i.e. mass terms, for the gauge bosons. Usually, one rewrites the fields in terms of the three massive vector bosons  $W^\pm$  and  $Z$ , and a massless vector boson, the photon  $A$ . One finds that they are mixtures of the original gauge fields  $\mathbf{W}_\mu$  and  $B_\mu$ :

$$W_\mu^\pm = \frac{(W_\mu^1 \mp iW_\mu^2)}{\sqrt{2}}, \quad (2.31)$$

$$\begin{pmatrix} A_\mu \\ Z_\mu \end{pmatrix} = \begin{pmatrix} \cos \theta_W & \sin \theta_W \\ -\sin \theta_W & \cos \theta_W \end{pmatrix} \begin{pmatrix} B_\mu \\ W_\mu^3 \end{pmatrix} \quad (2.32)$$

where the Weinberg angle  $\theta_W$  is defined as the ratio of coupling constants:  $\tan \theta_W \equiv g'/g$ . The masses of the gauge bosons  $W^\pm$  and the  $Z$  are then given by:

$$M_W = \frac{1}{2} v g \quad \text{and} \quad M_Z = \frac{v \sqrt{g^2 + g'^2}}{2} = \frac{M_W}{\cos \theta_W}. \quad (2.33)$$

The Lagrangian  $\mathcal{L}_\phi$  has to be added to the electroweak theory given by the Lagrangian of Eqs. 2.18–2.20, such that

$$\mathcal{L}_{SU(2)_L \times U(1)_Y} = \mathcal{L}_f + \mathcal{L}_g + \mathcal{L}_\phi. \quad (2.34)$$

The total Lagrangian is invariant under gauge transformations, which guarantees the renormalizability of the associated quantum field theory. After spontaneous symmetry breaking, three massless Goldstone bosons are generated, however, they are then eliminated from the Lagrangian by exploiting local gauge symmetry. Going to the unitary gauge, the  $W^\pm$  and the  $Z$  (but not the photon, because  $U(1)_Q$  is an unbroken symmetry) have acquired masses given by Eq. 2.33. In fact, before the spontaneous symmetry breaking mechanism, the massless  $W^\pm$  and  $Z$  bosons lead to  $3 \times 2 = 6$  degrees of freedom (d.o.f.), due to the two possible polarizations of a massless spin-1 field. The four real scalar fields are also present at this stage, corresponding to additional four d.o.f. After spontaneous symmetry breaking, the three Goldstone modes are “eaten” by the weak gauge bosons, which become massive, and therefore acquire one additional longitudinal polarization. This leads to a total of  $3 \times 3 = 9$  d.o.f. in the gauge sector, plus the remaining scalar particle  $H$ , which is called the *Higgs*

*boson*. The total number of d.o.f. is obviously conserved. This theory is generally called the *Higgs mechanism* and it was proposed by three independent groups in 1964: by Brout and Englert [7], by Higgs [8–10], and by Guralnik, Hagen, and Kibble [11].

The W and Z were discovered at CERN by the UA1 [12] and UA2 [13] groups in 1983. Subsequent measurements of their masses and other properties at Tevatron and LEP have been in excellent agreement with the standard model expectations [14, 15]. The current values are  $M_W = 80.385 \pm 0.015$  GeV and  $M_Z = 91.1876 \pm 0.0021$  GeV [3].

#### 2.1.4 The Higgs and Yukawa interactions

The scalar Lagrangian in Eq. 2.27 has introduced a new scalar particle into the model: the Higgs boson H. In terms of the physical fields (unitary gauge),  $\mathcal{L}_\phi$  takes the form

$$\mathcal{L}_\phi = \frac{1}{4}hv^4 + \mathcal{L}_H + \mathcal{L}_{HG^2}, \quad (2.35)$$

where

$$\begin{aligned} \mathcal{L}_H &= \frac{1}{2}\partial_\mu H\partial^\mu H - \frac{1}{2}M_H^2 H^2 - \frac{M_H^2}{2v}H^3 - \frac{M_H^2}{8v^2}H^4, \\ \mathcal{L}_{HG^2} &= M_W^2 W_\mu^\dagger W^\mu \left\{ 1 + \frac{2}{v}H + \frac{H^2}{v^2} \right\} + \frac{1}{2}M_Z^2 Z_\mu Z^\mu \left\{ 1 + \frac{2}{v}H + \frac{H^2}{v^2} \right\}, \end{aligned} \quad (2.36)$$

and the Higgs boson mass is given by

$$M_H = \sqrt{-2\mu^2} = \sqrt{2h}v. \quad (2.37)$$

A fermionic mass term  $-m\bar{\psi}\psi$  is not allowed, because it breaks the gauge symmetry. However, by adding Yukawa interaction terms of the fermion and Higgs field to the Lagrangian, the fermion masses can also be generated by spontaneous symmetry breaking. This procedure is briefly described in the following.

The most general Yukawa Lagrangian can be written in the form

$$\sum_{jk} \left\{ (\bar{u}'_j, \bar{d}'_j)_L \left[ c_{jk}^{(d)} \begin{pmatrix} \phi^+ \\ \phi^0 \end{pmatrix} d'_{kR} + c_{jk}^{(u)} \begin{pmatrix} \phi^{0*} \\ -\phi^- \end{pmatrix} u'_{kR} \right] + (\bar{\nu}'_j, \bar{\ell}'_j)_L c_{jk}^{(\ell)} \begin{pmatrix} \phi^+ \\ \phi^0 \end{pmatrix} \ell'_{kR} \right\} + h.c. \quad (2.38)$$

where the indexes run over the three generations of fermions;  $u'_j$ ,  $d'_j$ ,  $\ell'_j$  and  $\nu'_j$  denote the weak eigenstates for the members of each generation  $j$ , and  $c_{jk}^{(d)}$ ,  $c_{jk}^{(u)}$ , and  $c_{jk}^{(\ell)}$  are the so-called Yukawa couplings. After spontaneous symmetry breaking, the Yukawa Lagrangian in the unitary gauge takes the simpler form

$$\mathcal{L}_Y = -(1 + \frac{H}{v}) \{ \bar{\mathbf{d}}'_L \mathbf{M}'_d \mathbf{d}'_R + \bar{\mathbf{u}}'_L \mathbf{M}'_u \mathbf{u}'_R \} + \bar{\mathbf{l}}'_L \mathbf{M}'_\ell \mathbf{l}'_R + h.c., \quad (2.39)$$

where  $\bar{\mathbf{d}}'$ ,  $\bar{\mathbf{u}}'$  and  $\bar{\mathbf{l}}'$  denote vectors in the 3-dimensional generation space, and the corresponding mass matrices are given by

$$(\mathbf{M}'_d)_{ij} \equiv -c_{ij}^{(d)} \frac{v}{\sqrt{2}}, \quad (\mathbf{M}'_u)_{ij} \equiv -c_{ij}^{(u)} \frac{v}{\sqrt{2}}, \quad (\mathbf{M}'_\ell)_{ij} \equiv -c_{ij}^{(\ell)} \frac{v}{\sqrt{2}}. \quad (2.40)$$

Therefore, the spontaneous symmetry breaking mechanism generates fermion masses, which in turn fix all Yukawa couplings. In general the mass matrices in Eq. 2.40 are not

diagonal, Hermitian, or symmetric. Thus, to identify the physical mass eigenstates  $d_j$ ,  $u_j$ , and  $\ell_j$ , which are linear combinations of the corresponding weak eigenstates  $d'_j$ ,  $u'_j$ , and  $\ell'_j$ , it is necessary to diagonalize the matrices by separate unitary transformations on the left- and right-handed fermion fields. This is achieved as follows. The matrix  $\mathbf{M}'_d$  can be decomposed as  $\mathbf{M}'_d = \mathbf{H}_d \mathbf{U}_d = \mathbf{S}_d^\dagger \mathcal{M}_d \mathbf{S}_d \mathbf{U}_d$ , where  $\mathbf{H}_d \equiv \sqrt{\mathbf{M}'_d \mathbf{M}'_d^\dagger}$  is an hermitian positive-definite matrix, while  $\mathbf{U}_d$  is unitary. The  $\mathbf{H}_d$  matrix can be diagonalized by a unitary matrix  $\mathbf{S}_d$ ; the resulting matrix  $\mathcal{M}_d$  is diagonal, hermitian and positive definite. Similarly, one has  $\mathbf{M}'_u = \mathbf{H}_u \mathbf{U}_u = \mathbf{S}_u^\dagger \mathcal{M}_u \mathbf{S}_u \mathbf{U}_u$ . In terms of the diagonal mass matrices

$$\mathcal{M}_d = \text{diag}(m_d, m_s, m_b), \quad \mathcal{M}_u = \text{diag}(m_u, m_c, m_t), \quad \mathcal{M}_\ell = \text{diag}(m_e, m_\mu, m_\tau) \quad (2.41)$$

the Yukawa Lagrangian takes the simpler form

$$\mathcal{L}_Y = -(1 + \frac{H}{v}) \{ \bar{\mathbf{d}} \mathcal{M}_d \mathbf{d} + \bar{\mathbf{u}} \mathcal{M}_u \mathbf{u} + \bar{\mathbf{l}} \mathcal{M}_\ell \mathbf{l} \} \quad (2.42)$$

where the mass eigenstates are defined by

$$\begin{aligned} \mathbf{d}_L &\equiv \mathbf{S}_d \mathbf{d}'_L, & \mathbf{u}_L &\equiv \mathbf{S}_u \mathbf{u}'_L, & \mathbf{l}_L &\equiv \mathbf{S}_\ell \mathbf{l}'_L, \\ \mathbf{d}_R &\equiv \mathbf{S}_d \mathbf{U}_d \mathbf{d}'_R, & \mathbf{u}_R &\equiv \mathbf{S}_u \mathbf{U}_u \mathbf{u}'_R, & \mathbf{l}_R &\equiv \mathbf{S}_\ell \mathbf{U}_\ell \mathbf{l}'_R, \end{aligned} \quad (2.43)$$

One observes that the Higgs interactions (Fig. 2.1) have a very characteristic form: they are always proportional to the squared mass of the coupled boson or fermion. All Higgs couplings are therefore determined by  $M_H$ ,  $M_W$ ,  $M_Z$ , the mass  $m_f$  of fermions, and the vacuum expectation value  $v$ .

### 2.1.5 Observation of a particle compatible with the standard model Higgs boson

The SM Higgs boson production cross sections at a proton-proton collider is shown in Fig. 2.2(a) as a function of the Higgs mass hypothesis and for the different leading production mechanisms. In addition, in Fig. 2.3, the corresponding Leading Order (LO) Feynman diagrams are shown. Gluon fusion process ( $gg \rightarrow H$ ) is the dominating Higgs production mechanism over the entire mass range accessible at the LHC. In the vector boson fusion process ( $qq' \rightarrow qq'H$ ), which is about one order of magnitude weaker than gluon fusion, the Higgs boson is produced through a direct coupling with vector bosons (W or Z), which are irradiated by a pair of incoming quarks from the proton beams. The associated production with a W or Z boson ( $q\bar{q}' \rightarrow WH$ ,  $q\bar{q} \rightarrow ZH$ ) have a smaller cross section than the previous mechanisms but, the presence of the vector boson helps in reconstructing the events reducing the contamination from other SM processes. The associated production with  $t\bar{t}$  pairs ( $qq, gg \rightarrow t\bar{t}H$ ) has the smallest cross section, however, it allows for a direct access to the Higgs coupling to top quarks, representing thus an important process. Depending on the Higgs boson mass hypothesis, different decay channels (Fig. 2.2(b)) can be exploited to detect it. The Higgs boson does not couple to photons and gluons at LO, but such processes can arise via fermion or vector boson loops, giving a sizable contribution in the low mass region.

The search for the massive Higgs boson has been long and tedious. However, in Summer 2012, the ATLAS and the CMS collaborations announced the observation of a new particle in data taken in 2011 and 2012 [17, 18]. A combination of the measurements targeting its decay into fermions ( $b\bar{b}$ ,  $\tau\tau$ ) or vector bosons ( $ZZ^*$ ,  $WW^*$ ,  $\gamma\gamma$ ) and all the different production modes, led to an excess of events above the expected background around a mass

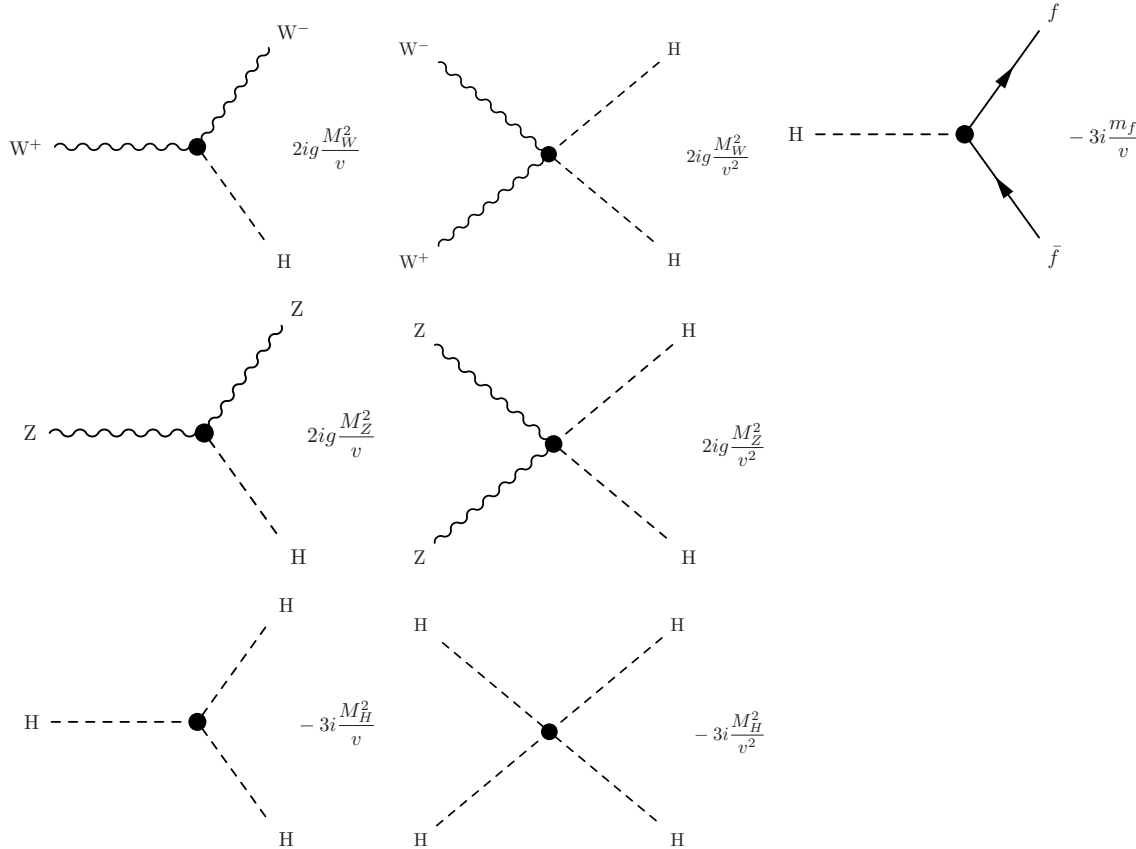


**Figure 2.1:** Higgs interaction vertices in the standard model.

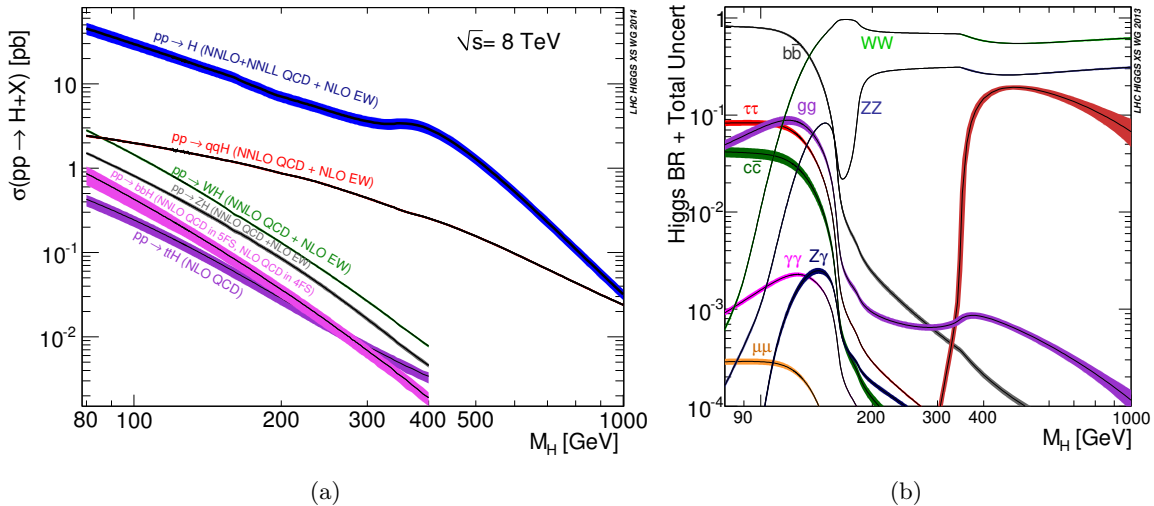


**Figure 2.2:** (a) The SM Higgs production cross-sections at  $\sqrt{s} = 8$  TeV for the different production mechanisms [16]. (b) Decay branching ratios of the SM Higgs boson in the different channels as a function of the mass hypothesis [16].

of 125 GeV. The CMS result yields a local significance of  $5.0\sigma$  with a global significance of  $4.6\sigma$  in the Higgs mass search range of  $115 < m_H < 130$  GeV (Fig. 2.4(a)). For ATLAS, the local significance is found to be  $5.9\sigma$  with a global significance of  $5.1\sigma$  in the range  $100 < m_H < 600$  GeV (Fig. 2.4(b)). A simultaneous fit to the reconstructed invariant mass

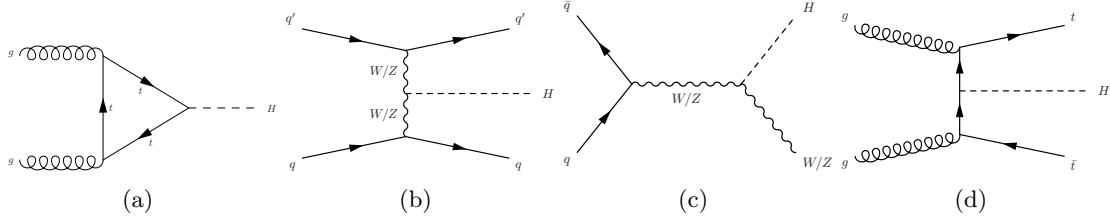


**Figure 2.3:** Leading order Feynman diagrams for the most important production processes of the SM Higgs boson: (a) gluon fusion, (b) vector boson fusion, (c) Higgs-strahlung and (d)  $t\bar{t}$  associated production.

peaks in the two channels with the highest mass resolution,  $H \rightarrow ZZ^* \rightarrow 4\ell$  and  $H \rightarrow \gamma\gamma$ , and for the two experiments has been performed. The resulting combined measured mass of the Higgs boson is  $m_H = 125.09 \pm 0.21(\text{stat.}) \pm 0.11(\text{syst.}) \text{ GeV}$  (Fig. 2.5) [19]. Subsequent studies on production and decay rates [20] and spin-parity [21–23] of the new boson showed that its properties are compatible with those expected for the SM Higgs boson.

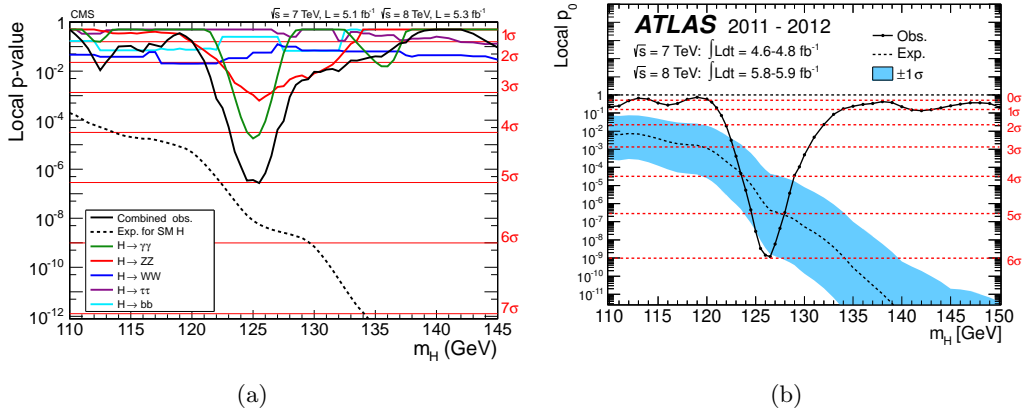


**Figure 2.4:** The observed (solid) local p-value as a function of the Higgs boson mass  $m_H$  for (a) the CMS and (b) ATLAS experiments. In (a) the results for each individual channel are also shown. The dashed curve shows the expected local p-value under the hypothesis of a SM Higgs boson signal at that mass. The horizontal red lines indicate the p-values corresponding to significances of 1 to 6 $\sigma$ .

Finally, the Higgs boson couplings to SM particles are investigated simultaneously in different production and decay processes, including the possibility of the Higgs boson to be coupled to BSM particles [20]. To test possible deviations from the SM predictions, the coupling modifiers,  $k_j^2 = \sigma_j / \sigma_j^{\text{SM}}$  and  $k_j^2 = \Gamma_j / \Gamma_j^{\text{SM}}$ , for production and decay rates, are introduced. However, to directly measure the individual coupling modifiers, an assumption about the Higgs boson width  $\Gamma_H$  is necessary. Thus, another modifier is introduced and defined as  $k_H = \sum_j \mathcal{B}_j^{\text{SM}} k_j^2$ , where  $\mathcal{B}_j^{\text{SM}}$  are the branching fractions for the Higgs boson decay to the final state  $f$  as predicted by the SM. In the case where the SM decays of the Higgs boson are the only ones allowed, the relation  $k_H^2 = \Gamma_H / \Gamma_H^{\text{SM}}$  holds. If instead deviations from the SM are introduced in the decays, the width can be expressed as:

$$\Gamma_H = \frac{k_H^2 \Gamma_H^{\text{SM}}}{1 - B_{\text{BSM}}}, \quad (2.44)$$

where  $B_{\text{BSM}}$  indicates the total branching fraction into BSM decays. The two possible scenarios are considered: the first leaves  $B_{\text{BSM}}$  free, provided that  $B_{\text{BSM}} \geq 0$ , whereas the

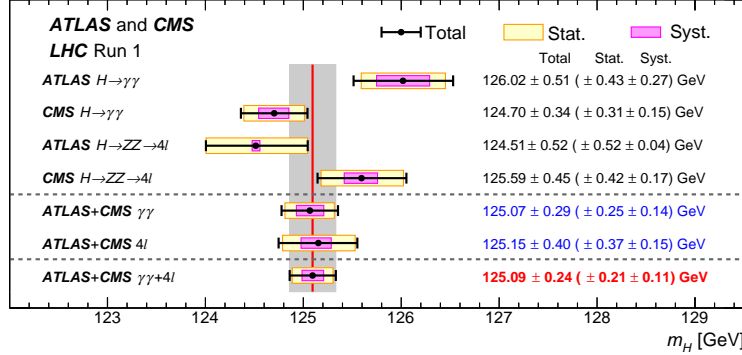


**Figure 2.5:** Summary of Higgs boson mass measurements from the individual analyses of ATLAS and CMS and from their combination. The magenta and yellow bands correspond to the systematic and statistical uncertainties, respectively. The total uncertainties are also indicated as black error bars. The red vertical line and corresponding gray shaded column indicate the central value and the total uncertainty of the combined measurement, respectively [19].

second assumes  $B_{\text{BSM}} = 0$ . The parameters of interest in the fits to data are thus the seven independent coupling modifiers,  $k_Z$ ,  $k_W$ ,  $k_t$ ,  $k_\tau$ ,  $k_b$ ,  $k_g$ , and  $k_\gamma$ , one for each SM particle involved in the production processes and decay modes studied, plus  $B_{\text{BSM}}$  in the case of the first scenario. The results of the two fits are shown in Fig. 2.6. The overall branching fraction of the Higgs boson into BSM decays is determined to be less than 34% at 95% CL. This constraint applies to invisible decays into BSM particles, decays into BSM particles that are not detected as such, and modifications of the decays into SM particles that are not directly measured by the experiments.

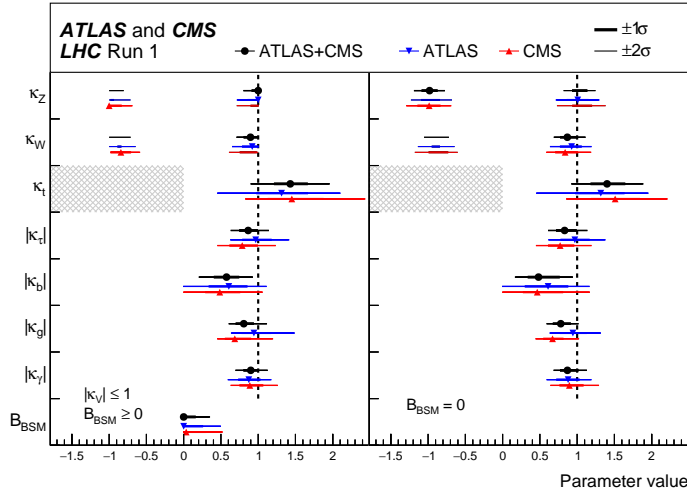


**Figure 2.6:** Fit results for two parameterizations: the first one assumes that  $B_{\text{BSM}} \geq 0$ , and the second one assumes that there are no additional BSM contributions to the Higgs boson width ( $B_{\text{BSM}} = 0$ ). The measured results for the combination of ATLAS and CMS are reported together with their uncertainties, as well as the individual results from each experiment [19].

### 2.1.6 Quantum chromodynamics

Quantum Chromodynamics (QCD) is the gauge theory of strong interactions, describing the dynamics of colored quarks and gluons. The QCD represents the  $SU(3)_C$  component of the standard model, where  $C$  denotes the color. After applying the principle of gauge invariance to the free Lagrangian for the quark fields holding color  $\alpha$  that runs from 1 to 3 (usually identified with red, green, blue), and flavor  $q$ , one obtains the following expression for the final gauge invariant QCD Lagrangian

$$\mathcal{L}_{\text{QCD}} = \sum_q \bar{\psi}_{q,\alpha} (i\gamma^\mu \partial_\mu \delta_{\alpha\beta} - g_s \gamma^\mu t_{\alpha\beta}^a \mathcal{A}_\mu^a - m_q \delta_{\alpha\beta}) \psi_{q,b} - \frac{1}{4} G_{\mu\nu}^a G_a^{\mu\nu}. \quad (2.45)$$

In the equation above, the quark fields are represented by the spinors  $\psi$ . The fields  $\mathcal{A}_\mu^a$  corresponds to the eight gluon fields, since  $C$  runs from 1 to  $N_C^2 - 1 = 8$ . Each gluon carries one unit of color and one unit of anticolor. The eight  $3 \times 3$  matrices  $t_{\alpha\beta}^a$  are the  $SU(3)_C$  generators and rotate the quark color in the  $SU(3)_C$  space in a quark-gluon interaction. The field tensor is

$$G_{\mu\nu}^a = \partial_\mu \mathcal{A}_\nu^a - \partial_\nu \mathcal{A}_\mu^a - g_s f_{abc} \mathcal{A}_\mu^b \mathcal{A}_\nu^c, \quad (2.46)$$

where  $f_{abc}$  are the structure constants of the  $SU(3)$  group. As  $[t^a, t^b] = i f_{abc} t^c$  the group is non-Abelian. Owing this property,  $G_{\mu\nu}^a G_a^{\mu\nu}$  term generates the cubic and quartic gluon self-interactions. The fundamental parameters of QCD are the *strong coupling constant*  $g_s$ , often written in terms of  $\alpha_s = g_s^2/4\pi$ , and the quark masses  $m_q$ . All interactions appearing in Eq. 2.44 have strength given by  $g_s$  (Fig. 2.7).

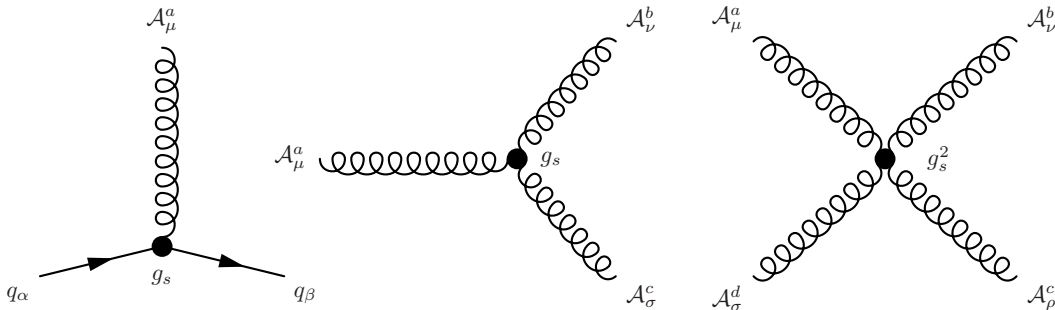


**Figure 2.7:** Interaction vertices of the QCD Lagrangian.

The QCD has the property of *asymptotic freedom*, i.e. the coupling becomes weak at high energies or short distances, and for energies approaching zero or for very large distances, it tends to infinity. As a consequence, the further away a quark is pulled from another one, the stronger the force gets, such that quarks cannot exist as free particles. Because of this phenomenon, referred to as *confinement*, quarks form bound color-singlet states called hadrons, consisting of either a quark and an antiquark (mesons) or three quarks or antiquarks (baryons). In the regime of very high momentum transfer interactions, the perturbation theory is a very satisfactory description of QCD physics observables, giving precise predictions about what can be tested in collider experiments. This approach is called perturbative-QCD, or pQCD. In this framework, QCD predictions are calculated using the formalism of the Feynman rules which are derived from the  $\mathcal{L}_{\text{QCD}}$ . The transition amplitudes for a given process from a set of initial state particles to a set of final state particles are computed by sorting the diagrams by the factors of the coupling constants and calculating them up to a certain

order. However, higher order diagrams generally contain loops which contribute and lead to divergencies. In order to obtain finite predictions for the cross sections, a renormalization of the theory is performed, resulting in a cancellation of the divergent terms. The predictions for observables are then expressed in terms of the renormalized coupling  $\alpha_s(\mu_R^2)$ , a function of the renormalisation scale  $\mu_R$ . The coupling satisfies the renormalisation group equation:

$$\mu_R^2 \frac{d\alpha_s}{d\mu_R^2} = \beta(\alpha_s) = -(b_0\alpha_s^2 + b_1\alpha_s^3 + b_2\alpha_s^4 + \dots) \quad (2.47)$$

where the  $b_i$  are the  $i$ -loop coefficients of the  $\beta$  function. They depend on the number of quark flavors  $n_f$ , and for sixteen or less flavors the strong coupling gets smaller for processes that involve large momentum transfer, leading to the asymptotic freedom. Choosing  $\mu_R$  close to the typical scale of the process of interest  $Q^2$ , the  $\alpha_s(\mu_R)$  represents the effective strength of the strong interaction between particles under study. Neglecting all the  $b_i$  coefficients but  $b_0$ , an exact leading order expression for the running coupling  $\alpha_s$  can be obtained

$$\alpha_s(\mu_R^2) = \frac{1}{b_0 \log \left( \frac{\mu_R^2}{\Lambda_{\text{QCD}}^2} \right)} = \frac{12\pi}{(33 - 2n_f) \log \left( \frac{\mu_R^2}{\Lambda_{\text{QCD}}^2} \right)} \quad (2.48)$$

where  $\Lambda_{\text{QCD}}$  is the perturbative cut-off over the renormalization's integrals, and is not predicted by the theory. The meaning of this cut-off is the validity of the perturbative regime approximation, beyond which the integrals would diverge. For many experimental studies, the strong coupling is evaluated at a fixed energy scale, typically of the order of the electroweak scale,  $\mu_R \simeq M_Z$  (Fig. 2.8).

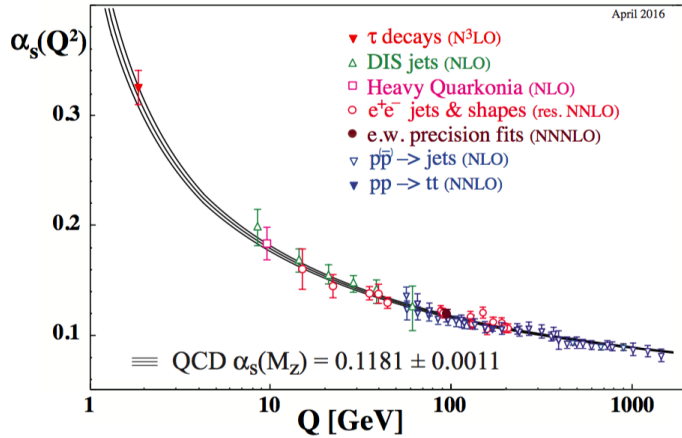


**Figure 2.8:** Summary of measurements of the running coupling  $\alpha_s$  as a function of the energy scale  $Q$  of the process [3].

## 2.2 Limitations of the standard model

The standard model has been remarkably confirmed by experimental data collected over the last few decades, which validated all its predictions. The ultimate verification of the model has been provided by the latest discovery of a scalar particle at the LHC (Section 2.1.5), whose properties are largely compatible with the SM predictions for the Higgs boson. Nevertheless, there are fundamental physical phenomena in nature that cannot be adequately explained by the SM. Furthermore, some features of the model represent *ad hoc* additions to the theory

and, although providing predictions that have been confirmed, imply a lack of understanding, making the framework theoretically unsatisfactory. Some of the main unresolved issues of the SM are briefly described in the following.

### The hierarchy problem

This issue arises from the observation of a large discrepancy between the electroweak and gravity scales. This is reflected in the mass difference between the masses of the W and Z bosons that define the scale of electroweak interactions ( $\mathcal{O}(10^2 \text{ GeV})$ ), and the Planck mass ( $M_{\text{Pl}} = \sqrt{\hbar c/G_{\text{Newton}}} = \mathcal{O}(10^{19})$ ), that defines the scale beyond which gravity must be described by quantum mechanics. More technically, the question is why the Higgs boson of mass  $m_H$  (Eq. 2.37) is so much lighter than the Planck mass. The problem is that  $m_H^2$  receives enormous quantum corrections from the virtual effects of every particle that couples, directly or indirectly, to the Higgs field. There are three types of radiative corrections to the Higgs mass that arise from the diagrams in Fig. 2.9. Each of them gives a correction to the Higgs mass:

$$\begin{aligned} \text{top loop} & - \frac{3}{8\pi^2} \lambda_t \Lambda^2 \\ \text{gauge loop} & + \frac{1}{16\pi^2} g^2 \Lambda^2 \\ \text{Higgs loop} & + \frac{1}{16\pi^2} \lambda^2 \Lambda^2 \end{aligned} \quad (2.49)$$

where  $\Lambda$  is a momentum cut-off representing the scale up to which the SM remains valid, and beyond which new physics enters to alter the high-energy behavior of the theory. Each of the leptons and quarks of the SM also contribute, however the largest correction arises from the top quark. If  $\Lambda$  is of the order of  $M_{\text{Pl}}$ , then this quantum correction to  $m_H^2$  is about 30 orders of magnitude larger than the measured value of  $m_H$  of 125 GeV. Thus, in order to obtain such a small value for the Higgs boson mass an incredible fine-tuning cancellation must occur between the quadratic radiative corrections and the physical mass. Avoiding such a miraculous cancellation can only happen if the cut-off scale  $\Lambda \simeq \mathcal{O}(1 - 10 \text{ TeV})$  rather than the Planck scale, that is, if new physics shows up at that energy. This is only directly a problem for corrections to the Higgs scalar boson squared mass, because quantum corrections to fermion and gauge boson masses do not have the direct quadratic sensitivity to  $\Lambda$  found in Eq. 2.49. However, the quarks and leptons and the electroweak gauge bosons of the SM all obtain masses from the Higgs boson, so that the entire mass spectrum of the theory is directly or indirectly sensitive to the cut-off  $\Lambda$ .

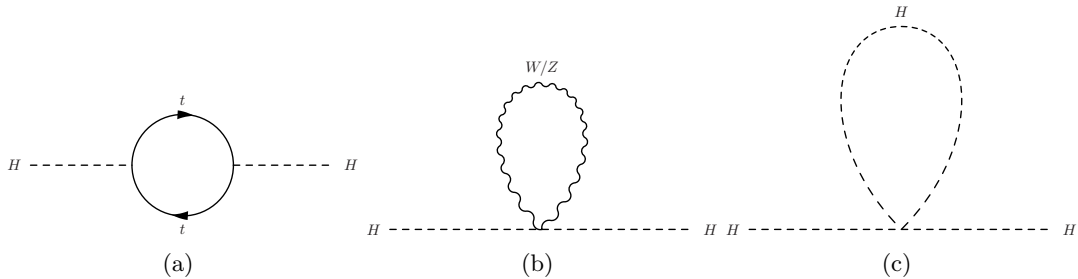


**Figure 2.9:** Radiative corrections to the Higgs squared mass parameter  $m_H^2$  due to: (a) Yukawa coupling with the top quark; (b) gauge boson loop; (c) Higgs quartic self-interaction.

Many extensions of the SM suggest new physics at the TeV scale to address the hierarchy

problem. Models of *supersymmetry* [24, 25] introduce a new heavy scalar called *stop* as *superpartner* of the SM top quark, which cancels out the top quark loop corrections to the Higgs mass. Non-supersymmetric models have also been proposed, which predict heavier partners to the top quark. Another possibility to address the hierarchy problem is to assume the Higgs boson to be a composite particle as in the *composite Higgs* models (Section 2.3.2), rather than an elementary particle as predicted in the SM.

## Dark matter and dark energy

Several cosmological observations showed that the standard model only describes 5% of the total content of the Universe. First, the measured orbital velocities of stars around their galaxy center is incompatible with the observed matter density in the space. In particular, assuming the gravitational mass is due to only visible matter, stars far from the center of galaxies have much higher velocities than expected. The easiest way to account for this discrepancy is to postulate the existence of another kind of matter, called *dark matter*, that does not interact through electromagnetic or strong interactions. A second major result in cosmology is the discovery that the Universe is in accelerated expansion: it was measured that in average galaxies recede from each other and that this escape rate increases with the distance. Such a feature cannot be achieved with usual particles or with dark matter, whereas a new type of energy with a negative pressure, called *dark energy*, has to be added to the Universe content. To account for the experimental observations, dark matter and dark energy have been estimated to compose respectively 26% and 69% of the total Universe content [26], but their fundamental nature remains nowadays a mystery. The most widely accepted hypothesis on the form for dark matter is that it is composed of weakly interacting massive particles (WIMPs) that interact only through gravity and the weak force. The searches from the point of view of experimental and theoretical dark matter hunting is one of the major efforts in particle physics. There are two fronts: direct searches in cosmic rays by underground experiments, and searches at hadron colliders, where dark matter would be produced in pairs of neutral particles that may be predicted by different models. No dark matter particle has been conclusively identified by any of these experiments.

## Gravity

The standard model does not include the fourth fundamental interaction, gravity. In fact, gravity is by many aspects very different from the three other forces, and establishing a common framework to describe both raises several challenges. In the decades after the discovery of general relativity, it was realized that general relativity is incompatible with quantum mechanics. It is possible to describe gravity in the framework of quantum field theory like the other fundamental forces, such that the attractive force of gravity arises due to exchange of virtual spin-2 *gravitons*, in the same way as the electromagnetic force arises from exchange of virtual photons. The theory arising from this approach is known as *quantum gravity*. This theory is known not to be renormalizable, as the loop corrections including a graviton induce divergencies that cannot be reabsorbed through the renormalisation procedure, as opposed to the electroweak and chromodynamics quantum theories. Thus, quantum gravity cannot be used to make meaningful physical predictions. Moreover, quantum gravitational effects are only expected to become apparent near the Planck scale, a scale far smaller in distance (equivalently, far larger in energy) than what is currently accessible at high energy particle accelerators. Several theoretical approaches to the problem of quantum gravity have been proposed, being one of the most popular the *string theory* [27].

It has to be noted than most of these approaches only attempt to describe the quantum

behavior of the gravitational field and should not be confused with the objective of unifying all fundamental interactions into a single mathematical framework. However, the present understanding of gravity would aid further work towards unification.

## 2.3 Theories of new physics

The standard model of particle physics has been very successful in describing observations. However, as explained in the previous section, this framework leaves several unanswered fundamental questions. Many extensions to the standard model have been proposed that attempt to address the open issues and to achieve a more fundamental theory that could explain the entirety of current phenomena. These new theoretical developments are referred to as *beyond standard model* (BSM) theories. In this section, three specific BSM scenarios are reviewed, which are of particular interest because of their highly predictive features. Specifically, with the aim of addressing the hierarchy problem of the SM, they predict the existence of new resonances with masses in the TeV range, which can be produced at hadron colliders. Furthermore, since the new resonances can decay into pairs of well-known standard model particles, their existence and properties can be directly probe by collider experiments. In particular, the decay modes into a pair of electroweak bosons W, Z or H, can provide striking signatures, as new techniques have been developed by the experiments to efficiently reconstruct the decay and mass of the bosons in the final state.

### 2.3.1 Warped extra dimensions

A class of theories beyond the standard model are those postulating the existence of new compactified spatial dimensions. They attempt to explain the apparent weakness of gravity by assuming that SM particles are confined in a (3+1)-dimensional hypersurface called *3-brane*, as opposed to gravity which is allowed to propagate in a (4+n)-dimensional *bulk*. In this scenario, the strength of gravity is diluted in the extra dimensions (thereby weakening our perception of gravity), while the other fundamental forces would not.

The basic idea comes from the so-called *large extra dimensions* scenario proposed by Arkani-Hamed, Dimopoulos and Dvali (ADD model) [28]. If spacetime has 4+n dimensions, then the effective 4-dimensional (reduced) Planck scale,  $\overline{M}_{\text{Pl}} = M_{\text{Pl}}/\sqrt{8\pi}$ , is determined by the fundamental (4+n)-dimensional Planck scale,  $M_*$ , and the geometry of the extra dimensions:

$$\overline{M}_{\text{Pl}}^2 = V_n M_*^{n+2} \simeq R^n M_*^{n+2}, \quad (2.50)$$

where  $V_n$  is the volume of the  $n$ -dimensional compactified space and  $R$  its radius. The hierarchy problem is thus eluded if  $M_* \sim 1 \text{ TeV}$ , which turns into a condition on the size  $R$  of the extra dimensions. Assuming  $n = 1$ , one can solve Eq. 2.50 and obtain  $R \sim 10^8 \text{ m}$ . This is a scale of the order of the Earth-Sun distance, over which we know that the  $1/r^2$  Newton's law of gravitational attraction works very well. Thus,  $n = 1$  is excluded. For  $n = 2$ , one obtains  $R \sim 100 \mu\text{m}$  or  $R^{-1} \sim 10^{-4} \text{ eV}$ , which is close to the limit of current table top experimental searches for deviations from the Newton's law [29].

The purpose of this model was to eliminate the hierarchy problem, i.e. to remove the large ratio between the weak scale  $v$  and the true fundamental scale  $\overline{M}_{\text{Pl}}$ , hence the requirement  $M_* \sim 1 \text{ TeV}$ . However, it introduces a new hierarchy, namely that between the compactification scale  $\mu_c = 1/R$  and  $v$ . Thus, the ADD really only trades one large ratio for another and does not really eliminate the hierarchy problem. An alternative solution,

represented by the so-called *warped extra dimensions* (WED) scenario, has been proposed by Randall and Sundrum (RS) [30].

The basic RS model, referred to as RS1, assumes the existence of only one extra dimension with size  $r_c$ . This fifth, extra dimension is labelled by the coordinate  $\phi \in [-\pi, \pi]$ , such that it can be described by a line segment between two 4-dimensional branes (or 3-branes), known as the *Planck* and *TeV* brane, located, respectively, at the  $\phi = 0$  and  $\phi = \pi$  boundary of the fifth dimension (Fig. 2.10). In the simplest version of the RS model, it is assumed, like in the ADD case, that the SM fields live on the *TeV* brane, while gravity lives everywhere. The *Planck* brane is where gravity is a relatively strong force. The classical action describing the above set-up is given by the sum of the gravitational action in the bulk,  $\mathcal{S}_{gravity}$ , and on the two branes,  $\mathcal{S}_{TeV}$  and  $\mathcal{S}_{Planck}$ ,

$$\begin{aligned} \mathcal{S} &= \mathcal{S}_{gravity} + \mathcal{S}_{TeV} + \mathcal{S}_{Planck}, \\ \mathcal{S}_{gravity} &= \int d^4x \int_{-\pi}^{+\pi} d\phi \sqrt{-G} - \Lambda + 2M_*^3 R, \\ \mathcal{S}_{TeV} &= \int d^4x \sqrt{-G(x^\mu, \phi = \pi)} \Lambda, \\ \mathcal{S}_{Planck} &= \int d^4x \sqrt{-G(x^\mu, \phi = 0)} \Lambda. \end{aligned} \quad (2.51)$$

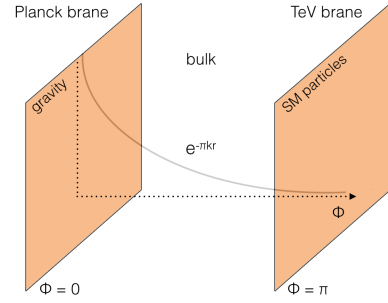


**Figure 2.10:** Set-up of the five dimensions in the RS model. The *Planck* and *TeV* branes are the 4-dimensional boundaries of the extra dimension  $\phi$  compactified in an interval  $[0, \pi]$ .

In the above equation,  $G$  is the 5-dimensional metric  $G_{\mu\nu}$ ,  $\Lambda$  a cosmological constant, and  $R$  the 5-dimensional Ricci tensor. By requiring a solution of the 5-dimensional Einstein's equation for the above action that respects the 4-dimensional Poincaré invariance in the  $x^\mu$  coordinates, one finds that the 5-dimensional metric must take the form

$$ds^2 = e^{-2\sigma(\phi)} \eta_{\mu\nu} dx^\mu dx^\nu + r_c^2 d\phi, \quad (2.52)$$

where  $\eta_{\mu\nu} = \text{diag}(1, -1, -1, -1)$  is the usual Minkowski metric and  $\sigma(\phi)$  is some a priori unknown function. This type of geometry is called “non-factorizable”, because the metric of the 4-dimensional subspace is  $\phi$ -dependent. Solving the 5-dimensional Einstein's equations provides a unique solution for  $\sigma(\phi)$ :

$$\sigma(\phi) = \sqrt{\frac{-\Lambda}{24M_*^3}} \equiv r_c |\phi| k, \quad (2.53)$$

where  $k$  is referred to as the *curvature factor*. By plugging the solution back into the original action and integrating out the extra dimension  $\phi$ , one finds that the 4-dimensional Planck mass is given by

$$\overline{M}_{\text{Pl}} = \frac{M_*^3}{k} (1 - e^{-2\pi k r_c}). \quad (2.54)$$

It is assumed that  $k \sim M_* \sim \overline{M}_{\text{Pl}}$  in order to avoid producing strong hierarchy between the mass scales of the theory. However, the electroweak energy scale  $v$  or any physical mass  $m$  in the *TeV* brane is exponentially suppressed compared to the 5-dimensional energy  $v_0$  or mass  $m_0$ :

$$m = e^{-\pi kr_c} m_0, \quad v = e^{-\pi kr_c} v_0. \quad (2.55)$$

This means that by taking  $v_0$  of the order of the 5-dimensional fundamental mass scale  $M_*$ , the separation between the Planck mass and electroweak scales is produced by the metric when  $kr_c \sim 11$  (small hierarchy). Such factor indeed would already suppress a parameter with value of order  $10^{18}$  GeV to only 1 TeV. The hierarchy is thus naturally established by the warp factor  $e^{-\pi kr_c}$ . This Planck-electroweak hierarchy explanation is the most celebrated achievement of WED scenarios.

A distinctive novel feature of the RS scenario is the existence of a so-called tower of Kaluza–Klein (KK) excitations of a spin-2 field, the KK graviton, arising from tensor fluctuations around the 4-dimensional part of the metric. Scalar fluctuations around the fifth extra dimension give rise to a spin-0 field called *radion*. Massive graviton excitations appear, with 4-dimensional effective masses given by

$$m_G^{(n)} = kx_n e^{-\pi kr_c}, \quad (2.56)$$

where  $x_n$  is the  $n$ -th root of the Bessel function  $J_1$ . These masses are of order of a TeV, so that Kaluza–Klein gravitons can be detected as massive resonances in collider experiments. The zero-mode of the graviton field corresponds to the mediator of gravitational interaction, and its wave function is highly peaked at  $\phi = 0$ . Gravity is thus localized on the *Planck* brane, while on the *TeV* brane we feel only the tail of the graviton wave-function.

The coupling of an excited graviton to matter is described by the Lagrangian

$$\mathcal{L} = -\frac{1}{\Lambda_\pi} T^{\mu\nu} \sum_{n>0} h_{\mu\nu}^{(n)}, \quad (2.57)$$

where  $T^{\mu\nu}$  is the energy-momentum tensor of the matter field,  $h_{\mu\nu}^{(n)}$  is the  $n$ -th excitation of the graviton, and  $\Lambda_\pi = \bar{M}_{\text{Pl}} e^{-\pi kr_c}$  is of order of TeV. It is interesting to note that this model has only two free parameters: the mass of the first (lightest) KK-graviton excitation,  $m_1$ , and the ratio  $\tilde{k} \equiv k/\bar{M}_{\text{Pl}}$ , which controls the widths of the new resonances:

$$\Gamma_n = \rho m_n x_n^2 \tilde{k}^2, \quad (2.58)$$

where  $\rho$  is a constant depending on the number of open decay channels. The RS model in its simplest form is thus highly predictive.

In the original RS1 model the SM matter is localized on the *TeV* brane, as the Higgs field. A well-motivated extension of the original RS1 model explored an alternative scenario, in which SM fields propagate in the warped bulk, except for the Higgs field which is required on the *TeV* brane to avoid hierarchy. This extension is referred thereafter as the *bulk scenario* [31, 32]. Similarly to the KK-graviton excitations, in the bulk scenario a KK expansion is applied to each SM field. The zero-mode of each KK tower represents the correspondent SM particle. The first and second generation fermions are localized near the *Planck* brane, leading to the small Yukawa couplings to the Higgs field which is localized on the *TeV* brane. Similarly, the top quark can be localized near the *TeV* brane to account for its large Yukawa coupling. In the original RS1 scenario all the particles are localized on the *TeV* brane, therefore the strength of the couplings between KK-graviton and SM particles are democratic. As a consequence, the RS gravitons are produced via both  $q\bar{q}$  annihilation and gluon fusion processes. In the bulk scenario, couplings of KK gravitons to light fermions are highly suppressed since, as mentioned above, KK gravitons are localized

near the *TeV* brane, whereas light fermions are localized near the *Planck* brane. As a result,  $q\bar{q}$  annihilation at hadron collider for KK graviton production is negligible in this case. In contrast, SM gluons have a flat localization in the bulk, so that the coupling of gluons to KK gravitons and hence KK graviton production via gluon fusion is dominant. Furthermore, decays of KK graviton into top quarks and Higgs bosons are enhanced due to their profile being near the *TeV* brane, resulting in couplings to KK gravitons (which are also localized there) being only  $\sim$  TeV-suppressed just like in the original RS1 model (Eq. 2.57). Another crucial point of the bulk scenario is that before symmetry-breaking, the W and Z gauge bosons start out with flat localization in the bulk. However, after symmetry-breaking, the gauge bosons eat a Higgs, and their wave functions are still mostly flat in the bulk but fall sharply near the brane. Thus, in the bulk scenario, branching fractions for decays into pair of vector bosons are the same size as those for decays into Higgs bosons or top quarks. The branching fractions for the different decay modes of the graviton in both the bulk and RS1 scenarios are shown in Fig. 2.11 as a function of the graviton mass. It can also be shown that in RS1 scenario the graviton decays preferentially to transverse polarized vector bosons, whereas in the bulk scenario it decays preferentially to longitudinally polarized modes, making those two benchmarks an excellent framework to study the sensitivity of the vector boson identification techniques used at the collider experiments to the polarization (Chapter 7).

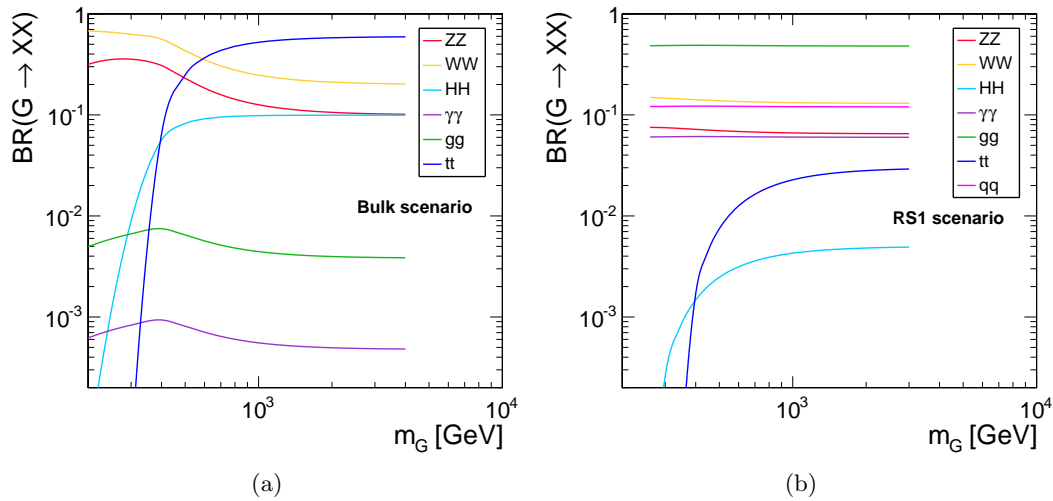


**Figure 2.11:** Branching fractions for the different decay modes of the graviton in the (a) bulk and (b) RS1 scenarios, as a function of the graviton mass.

### 2.3.2 Compositeness

One of the approaches to the hierarchy problem compatible with observations is based on the assumption that the Higgs boson is a composite particle, a bound state of more fundamental constituents held together by a new strong force. In composite Higgs models [33–35],  $\Lambda$  is the energy scale where the composite nature of the Higgs boson becomes important, which roughly coincides with the confinement scale of the new strong interaction. Thus, the solution to the hierarchy problem is that there is no elementary scalar, and beyond  $\Lambda$  an experiment becomes sensitive to the underlying “partons” that compose the Higgs boson. However, precision electroweak data rule out new strong interactions at scales below about 10 TeV. One key question is therefore the lightness of the Higgs boson with respect to such scale.

By comparing with the QCD sector, one observes that the strong coupling scale is  $\Lambda_{\text{QCD}} \sim \mathcal{O}(300 \text{ MeV})$ , whereas most bound states, such as the  $\rho$  meson and proton, are at least as heavy as this. However, a counter-example in QCD is given by the existence of the pions, which are all lighter than  $\Lambda_{\text{QCD}}$ , although only by a  $\mathcal{O}(1)$  factor. The reason for the pions to be appreciably lighter than the other QCD bound states is found in the chiral perturbation theory. In fact, the pions represent the Goldstone bosons of the spontaneously broken  $SU(2)_L \times SU(2)_R$  flavor symmetry coming from chiral rotations of the up and down quarks. The spontaneous symmetry breaking of the flavor symmetry into the vectorial isospin subgroup  $SU(2)_V$ , is induced by a non-perturbative QCD vacuum state, characterized by a non-vanishing quark condensate  $\langle \bar{q}_L^a q_R^b \rangle \sim \delta^{ab} \Lambda_{\text{QCD}}^3$ . However, because of the non-vanishing and differing masses of the quarks, the  $SU(2)_L \times SU(2)_R$  is only an approximate symmetry, and therefore the pions are not massless, but have small masses, so that they are *pseudo-Goldstone bosons*.

In composite Higgs models, a similar structure is assumed, where the Higgs is a pseudo-Goldstone boson of some symmetry with strong coupling scale  $\Lambda \approx 4\pi f$ , where  $f$  is the scale at which the symmetry is spontaneously broken. The main idea is that the Higgs mass parameter is protected against quadratic quantum corrections up to the compositeness scale because it is a pseudo-Goldstone boson. Above the scale of compositeness, it is simply not an elementary scalar. Furthermore, the pseudo-Goldstone nature of the Higgs is an explanation for why the Higgs mass is so much lighter than the other bound states in the strongly coupled sector.

Such models start with a large global symmetry group  $G$ , analogous to the “large”  $SU(2)_L \times SU(2)_R$  global symmetry of low energy QCD. The strong dynamics spontaneously breaks  $G$  to a subgroup  $H$ , similarly to the QCD chiral symmetry breaking  $SU(2)_L \times SU(2)_R \rightarrow SU(2)_V$ . In a minimal composite Higgs model  $G = SO(5) \rightarrow H = SO(4)$ . The SM electroweak group  $SU(2)_L \times U(1)_Y$  is a subgroup of  $H$ , thus introducing a preferred orientation in the coset space  $SO(5)/SO(4)$  with respect to the global  $SO(4)$ . In this way, the electroweak scale  $v$  is distinct from the  $G \rightarrow H$  symmetry breaking scale  $f$ . The parameter  $\xi = (v/f)^2$  is introduced to characterize this separation of scales and to quantify the degree of vacuum misalignment. In a theory with little hierarchy  $\xi \sim 1$ , while a small amount of fine-tuning can give rise to  $\xi \ll 1$ . In particular, compatibility with the constraints coming from electroweak precision tests and Higgs coupling measurements generically implies  $\xi \lesssim 0.2$ . This bound places the scale  $f$  at about 1 TeV, resulting in a strong coupling scale  $\Lambda \approx 4\pi f \sim 10 \text{ TeV}$ . Such large value results in a large one-loop contribution to the Higgs mass parameter (Eq. 2.49), so that a generic composite Higgs set up still requires some tuning between the  $v$  and  $f$  scales. One way to generate a “little hierarchy” is through the mechanism of *collective symmetry breaking* as in *Little Higgs* (LH) scenarios [36–40], which is now a key ingredient in composite Higgs models. The main idea of this approach is that one can separate the scales  $v$  and  $f$  by introducing new particles, which cancel the quadratic divergences at one-loop order. In particular, the quadratic divergence induced by the SM gauge boson loops are canceled by the quadratic divergence induced by heavy gauge bosons at one loop level. Heavy fermionic states are also introduced, which couple to the Higgs field such that the one-loop quadratic divergence induced by the top-quark Yukawa coupling to the Higgs boson is canceled. Furthermore, extra Higgs fields exist as the Goldstone boson multiplets from the global symmetry breaking. This is achieved by enlarging the simple global group  $G$  and embedding two parallel global symmetries  $G_1 \times G_2$ , such that  $G \supset G_1 \times G_2 = [SU(2)_1 \times U(1)_1] \times [SU(2)_2 \times U(1)_2]$ . A specific implementation, called the *littlest Higgs* [39, 40], starts with the global symmetry  $G = SU(5)$ , which is spontaneously broken down at the scale  $\Lambda$  to its subgroup  $SO(5)$  via a vacuum expectation value of order  $f$ .

At the same time, the gauge symmetry  $[SU(2) \times U(1)]^2$  is also broken into  $[SU(2)_L \times U(1)_Y]$ , identified as the SM gauge group. The global symmetry breaking leaves 14 massless Goldstone bosons, which become the longitudinal components of the  $W'^{\pm}$  and  $Z'$  gauge bosons associated with the broken gauge groups, giving them masses of the order  $f$ :

$$M(W'^{\pm}) \simeq M(Z') = \frac{g}{\sin 2\theta} f, \quad (2.59)$$

where  $\theta$  is given by the gauge couplings of the two broken  $SU(2)$  groups:  $\tan \theta = g_1/g_2$ . The partial decay widths are computed using the formalism of Feynman rules:

$$\begin{aligned} \Gamma(W'^{\pm} \rightarrow \ell\nu) &\simeq \Gamma(Z' \rightarrow \ell\ell) = \frac{g^2 \cot^2 \theta}{96\pi} M \\ \Gamma(W'^{\pm} \rightarrow q\bar{q}') &\simeq \Gamma(Z' \rightarrow q\bar{q}) = \frac{g^2 \cot^2 \theta}{32\pi} M \\ \Gamma(W'^{\pm} \rightarrow WH) &\simeq \Gamma(Z' \rightarrow ZH) = \frac{g^2 \cot^2 2\theta}{192\pi} M \\ \Gamma(W'^{\pm} \rightarrow WZ) &\simeq \Gamma(Z' \rightarrow WW) = \frac{g^2 \cot^2 2\theta}{192\pi} M \end{aligned} \quad (2.60)$$

where  $M$  is the mass of the  $V'$  triplet given by Eq. 2.59. Summing over all the quark and lepton channels results in a total width

$$\Gamma_{\text{tot}} = \frac{g^2}{96\pi} (\cot^2 2\theta + 24 \cot^2 \theta) M. \quad (2.61)$$

One can immediately observe that the fermionic decay modes dominate for  $\cot \theta \geq 1/2$ , while bosonic decay modes become significant only below this value. However, since the  $V'$  resonances are produced mainly via the Drell-Yan process  $q\bar{q}^{(\prime)} \rightarrow V'$ , one should notice that the production cross section would be at the same time suppressed for the enhanced bosonic channels. Thus, the interactions of the new predicted particles is described within these theories, and detailed predictions of their properties are made. Furthermore, they provide distinct signatures that can be searched for at the hadron collider.

### 2.3.3 Heavy vector triplet

New heavy spin-1 resonances are predicted by several extensions of the standard model, such as the Composite Higgs and Little Higgs models described in the previous section. A model-independent strategy has been proposed in Ref. [41] to study these resonances, based on a simplified phenomenological Lagrangian, which reproduces a large class of explicit models. The main reason for introducing a simplified model is that the experimental searches for new resonances are typically not sensitive to all the details and the free parameters of the chosen benchmark model, but only to those parameters or combinations of parameters that control the mass of the resonance and the interactions involved in its production and decay. Therefore one can employ a simplified description of the new phenomena, where only the relevant couplings and mass parameters are retained. In turn, the experimental results expressed in terms of the phenomenological parameters can be easily translated into the free parameters of any explicit model by computing the phenomenological/explicit parameter relations.

In this approach, a new real vector in the  $SU(2)_L$  representation is introduced in addition to the SM fields, describing one charged and one neutral heavy spin-1 particle (heavy vector triplet or HVT) with the charge eigenstate fields given by

$$V_\mu^\pm = \frac{V_\mu^1 \mp i V_\mu^2}{\sqrt{2}} \quad V_\mu^0 = V_\mu^3. \quad (2.62)$$

The dynamics of the new vector is described by a simple phenomenological Lagrangian

$$\begin{aligned} \mathcal{L}_V = & -\frac{1}{4} \mathcal{D}_{[\mu} V_{\nu]}^a \mathcal{D}^{[\mu} V^{\nu]a} + \frac{m_V^2}{2} V_\mu^a V^{\mu a} \\ & + ig_V c_H V_\mu^a H^\dagger \tau^a \overleftrightarrow{\mathcal{D}}^\mu H + \frac{g^2}{g_V} c_F V_\mu^a J_F^{\mu a} \\ & + \text{extra terms} \end{aligned} \quad (2.63)$$

where  $g$  denotes the gauge coupling. The first line of the above equation contains the kinetic and mass terms for the field  $V$ , plus trilinear and quadrilinear interactions with the vector bosons from the covariant derivatives. The second line contains direct interactions of  $V$  with the Higgs current in the first term, and with the SM left-handed fermionic currents  $J_F^{\mu a}$  in the second term. The Higgs current term with coefficient  $c_H$  leads to vertices involving the physical Higgs field and the three unphysical goldstone bosons. Since the goldstone bosons represent the longitudinally polarized SM vector bosons W and Z, the parameter  $c_H$  controls the interactions of  $V$  with the SM vector bosons and with the Higgs boson, and in particular its decay modes into these electroweak particles. Similarly, the parameter  $c_F$  describes the direct interaction with fermions, which is responsible for both the resonance production via  $q\bar{q}$  annihilation and for its fermionic decays. One observes that a universal coupling of the new field  $V$  to fermions is assumed in Eq. 2.63 for simplicity, such that  $c_F$  represents the couplings to leptons ( $c_\ell$ ), light quarks ( $c_q$ ) and the third quark family ( $c_3$ ). The third line of the equation contains new operators and free parameters, which however have a sub-leading effect on the phenomenology of interest for resonant searches, and therefore to a first approximation they can be neglected.

In the adopted simplified description, the free parameter  $g_V$  represents the typical strength of  $V$  interactions, while the dimensionless coefficient  $c_H$  parametrizes the departure from the typical strength. Such parametrization is found convenient because, although the coefficient  $c_F$  is of order one in most of the explicit models, the parameter  $c_H$  is of order one in the strongly-coupled scenario (e.g., Composite Higgs models) but can be reduced in a weakly coupled case (e.g., extensions of the SM gauge group [42, 43]). The coefficients are never larger than one in all cases, whereas the coupling  $g_V$  can vary over a large range in different scenarios, from  $g_V \sim g \sim 1$  in the typical weakly-coupled case up to  $g_V \sim 4$  in the strong limit. Therefore, it is more convenient to factor it out of the parametrization, although it is not a fundamental parameter of the model. For the purpose of presenting experimental results, the combinations  $g_V c_H$  and  $g^2 c_F / g_V$  that enter in the vertices are instead treated as fundamental parameters, as they control production and decay rates.

After electroweak symmetry breaking the heavy vector acquires mass and one finds that the charged and neutral  $V$ 's are practically degenerate ( $M_\pm \simeq M_0 \simeq M_V$ ), and therefore they are expected to have comparable production and decay rates at the hadron collider. The partial widths are as well immediately computed in this framework:

$$\begin{aligned} \Gamma_{V^\pm \rightarrow f\bar{f}'} &\simeq 2\Gamma_{V^0 \rightarrow f\bar{f}} \simeq N_c[f] \left( \frac{g^2 c_F}{g_V} \right)^2 \frac{M_V}{48\pi} \\ \Gamma_{V^\pm \rightarrow WZ} &\simeq \Gamma_{V^0 \rightarrow WW} \simeq \frac{g_V^2 c_H^2 M_V}{192\pi} \\ \Gamma_{V^\pm \rightarrow WH} &\simeq \Gamma_{V^0 \rightarrow ZH} \simeq \frac{g_V^2 c_H^2 M_V}{192\pi}, \end{aligned} \quad (2.64)$$

where  $N_c[f]$  is the number of colors and is equal to three for the diquark and to 1 for the dilepton decays. It can be observe that through the partial width to  $\text{qq}$ , the parameter  $c_F = c_q$  controls the Drell-Yan production rate. The channels which are not reported in Eq. 2.64 are either forbidden, like  $\text{HH}$  and  $\gamma\gamma$  decays, or suppressed like the decays to transverse polarizations or to  $\text{W}\gamma$ .

Two exemplary benchmark models, called A and B, are studied in Ref. [41], which correspond to two explicit models describing heavy vectors, namely those in Refs. [42] and [34], respectively. The  $c_F$  and  $c_H$  coefficients are fixed to specific values in these models, and the only free parameters are the resonance coupling  $g_V$  and its mass  $M_V$ . Moreover, since models A and B are inspired, respectively, by weakly coupled extensions of the SM gauge group and strongly coupled scenarios, i.e. Composite Higgs models, the two benchmark models are considered in different regions of  $g_V$ , relatively small,  $g_V \lesssim 3$ , and relatively large,  $g_V \gtrsim 3$ , respectively. In particular, the branching fractions for the different decay modes of the neutral spin-1 resonance in models  $A_{g_V=1}$  and  $B_{g_V=3}$  are shown in Fig. 2.12 as a function of the resonance mass. For these values of  $g_V$ , model A predicts comparable branching fractions for decay modes into fermions and bosons, as expected from Eq. 2.64. In model B, on the contrary,  $c_H$  is unsuppressed, and therefore the dominant branching fractions are into dibosons, whereas the fermionic decays are extremely suppressed.

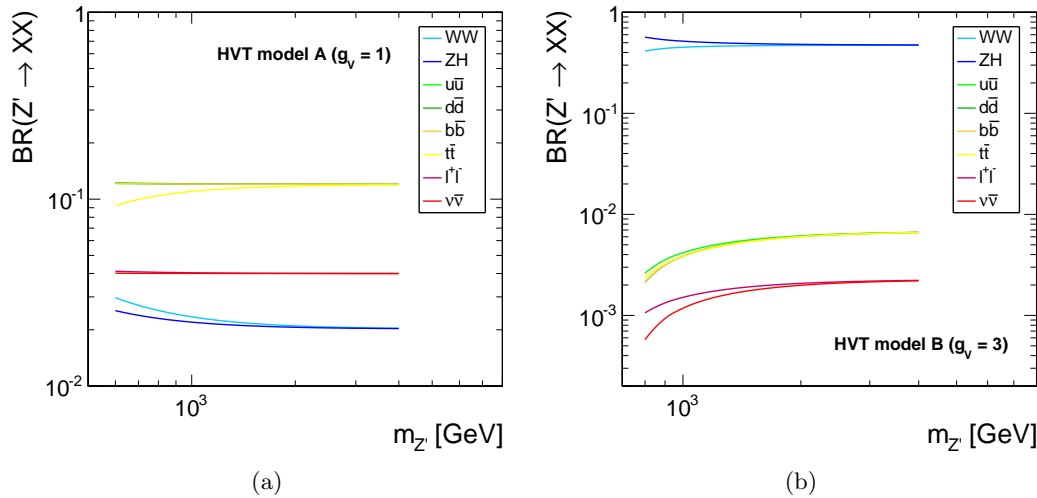


**Figure 2.12:** Branching fractions for the different decay modes of the neutral spin-1 resonance  $Z'$  ( $V^0$ ) for the benchmarks (a)  $A_{g_V=1}$  (a) and (b)  $B_{g_V=3}$ , as a function of the resonance mass.

It has to be noted that the prediction of this simplified model are only valid for sufficiently narrow resonances. In fact, several effects due to new physics, not included in this simplified framework, might contribute to the tail and radically change its prediction. As a consequence, the results of an experimental search which is sensitive to the tail cannot be easily translated into bounds on the phenomenological parameter space.

# The CMS experiment at the LHC

---

## 3.1 The Large Hadron Collider

The Large Hadron Collider (LHC) [44] is a proton-proton (pp) collider located at the European Particle Physics Laboratory (CERN) near Geneva, Switzerland. It is situated in the former CERN Large Electron-Positron Collider (LEP) tunnel with a circumference of 27 km about 100 m under ground crossing the border between France and Switzerland. A hadron collider has been chosen to allow higher center-of-mass energies ( $\sqrt{s}$ ) compared to electron-positron colliders, the latter limited by synchrotron radiation due to the low mass of the particles to be accelerated. High center-of-mass energies are required for the production of heavy SM particles such as the top quark and the Higgs boson, and to search for new BSM interactions at the TeV scale. For this purpose, the LHC is designed to produce pp collisions up to a  $\sqrt{s} = 14$  TeV, superseding previous high energy hadron colliders, such as Tevatron, by a factor of 7. Higher center-of-mass energies lead to larger cross sections for the production of the physics processes of interest in parton-parton interactions (Fig. 3.1), maximizing the sensitivity to new discoveries. In addition to colliding protons, the LHC is also capable of accelerating and colliding heavy nuclei, which is, however, not considered in this work.

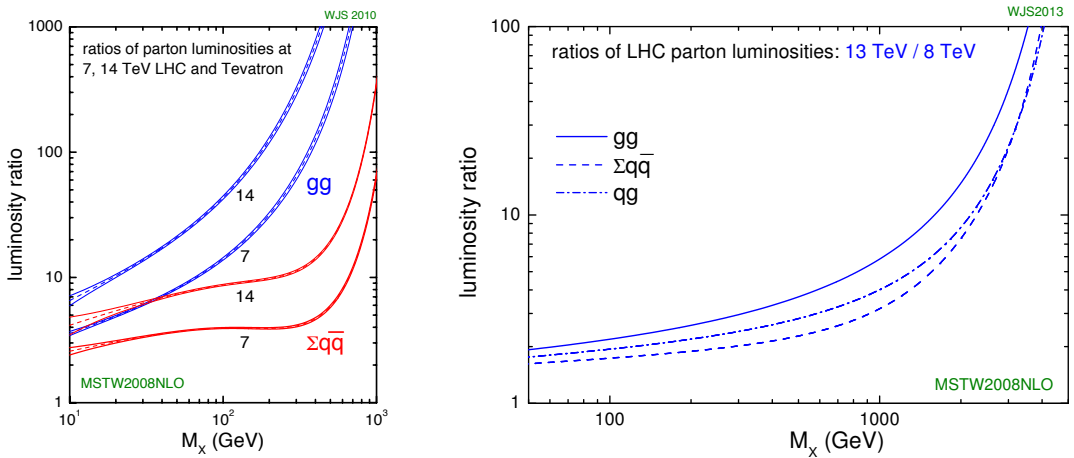


**Figure 3.1:** (left) Parton luminosity ratios of pp collisions at LHC at  $\sqrt{s} = 7, 14$  TeV and  $p\bar{p}$  collisions at Tevatron at  $\sqrt{s} = 1.96$  TeV. (right) Parton luminosity ratios of pp collisions at LHC at  $\sqrt{s} = 13$  TeV and at  $\sqrt{s} = 8$  TeV [45].

The LHC is the final element in a succession of machines that accelerate protons to increasingly higher energies. Protons, obtained from a hydrogen source, are first accelerated by a linear accelerator (LINAC 2) to energies of 50 MeV. The beam is then injected into the Proton Synchrotron Booster (PSB), which accelerates the protons to 1.4 GeV, followed by the Proton Synchrotron (PS), which pushes the beam to 25 GeV. Protons are then sent to the

Super Proton Synchrotron (SPS) where they are accelerated to 450 GeV. Finally, the beam is injected in the LHC ring, where it completes several revolutions to reach the targeted energy. The LHC ring and the acceleration chain are sketched in Fig. 3.2.

Inside the ring, the two proton beams circulate in opposite directions in two tubes kept at ultrahigh vacuum, referred as beam pipes. The acceleration of protons inside LHC is made by radio-frequency cavities (400 MHz), giving a 492 keV energy gain per revolution, with a 7 keV loss per turn due to synchrotron radiation. It takes 4 minutes and 20 seconds to fill each LHC ring, and 20 minutes for the protons to reach their maximum energy of 7 TeV. The maximum energy of the protons is limited by the strength of the magnetic field required for keeping the protons inside the ring. For 7 TeV-protons a magnetic field of 8.3 T has to be produced, which can only be reasonably obtained by superconducting magnets. The ring is equipped with 1232 dipole magnets for bending and 392 quadrupole magnets for focussing made of niobium-titanium (NbTi), which are cooled down to a temperature of 1.9 K with the help of super-fluid helium. After acceleration the protons move through the ring in separate bunches of protons with a fixed spatial separation.

The LHC ring has four interaction points at which the two counter rotating beams are made to cross and located in the center of the four LHC experiments. Just prior to collision, particles from the incoming beams must be squeezed closer together in order to maximize the chances of interaction. For this purpose, a system of three quadrupole magnets, so-called inner triplet, is located at both sides of each interaction point, which squeeze the beams and lead them to collisions in the center of the detector. Inner triplets tighten the beam, making it 12.5 times narrower from 0.2 mm down to 16  $\mu\text{m}$  across.

Besides the high center-of-mass energy required for the production of heavy particles, a high event rate has to be obtained to allow the discovery of processes with low production cross sections. The instantaneous luminosity  $\mathcal{L}$  characterizes the interaction rate. For a process with a cross section  $\sigma$ , the interaction rate is given by

$$\frac{dN_{ev}}{dt} = \sigma \mathcal{L}. \quad (3.1)$$

The instantaneous luminosity depends only on the beam parameters and can be written for a Gaussian beam distribution as:

$$\mathcal{L} = \frac{N_b^2 n_b f_{\text{rev}} \gamma_r}{4\pi \sigma_x \sigma_y}, \quad (3.2)$$

where  $N_b$  is the number of particles per bunch,  $n_b$  the number of bunches per beam,  $f_{\text{rev}}$  the revolution frequency,  $\gamma_r$  the relativistic gamma factor, while  $\sigma_x$  and  $\sigma_y$  characterize the widths of the transverse beam profiles in the horizontal and vertical direction, respectively. The number of interaction events in a period of running time of the collider can be derived as

$$N_{ev} = \sigma \int \mathcal{L} dt = \sigma L, \quad (3.3)$$

where  $L$  is called the integrated luminosity. It is a measurement of the collected data size and it is usually expressed in inverse of cross section.

The LHC beams can reach very high luminosity with a high frequency bunch crossing and a high density of protons per bunch. In the ring, 2808 bunches of  $1.15 \times 10^{11}$  protons are circulated, with an average length of 7.5 cm, a width of about 16  $\mu\text{m}$  and a bunch spacing of 25 ns (collision frequency of 40 MHz). This corresponds to the design instantaneous luminosity of  $10^{34} \text{ cm}^{-2} \text{ s}^{-1}$  for pp collisions, which supersedes by a factor of 100 the luminosity reached by previous hadron colliders.

Proton collisions take place in four points of the LHC tunnel where the four main experiments are located: ATLAS (*A Toroidal LHC ApparatuS*) [46], CMS (*Compact Muon Solenoid*) [47], LHCb (*LHC beauty experiment*) [48] and ALICE (*A Lead Ion Collider Experiment*) [49]. ATLAS and CMS are general purpose experiments, designed to get an extensive study of SM and BSM physics and to operate at the design luminosity. The LHCb experiment is instead optimized for bottom quark physics studies while the ALICE experiment is dedicated to the study of the lead-lead collisions at the design luminosity of  $10^{27} \text{ cm}^{-2} \text{ s}^{-1}$ .

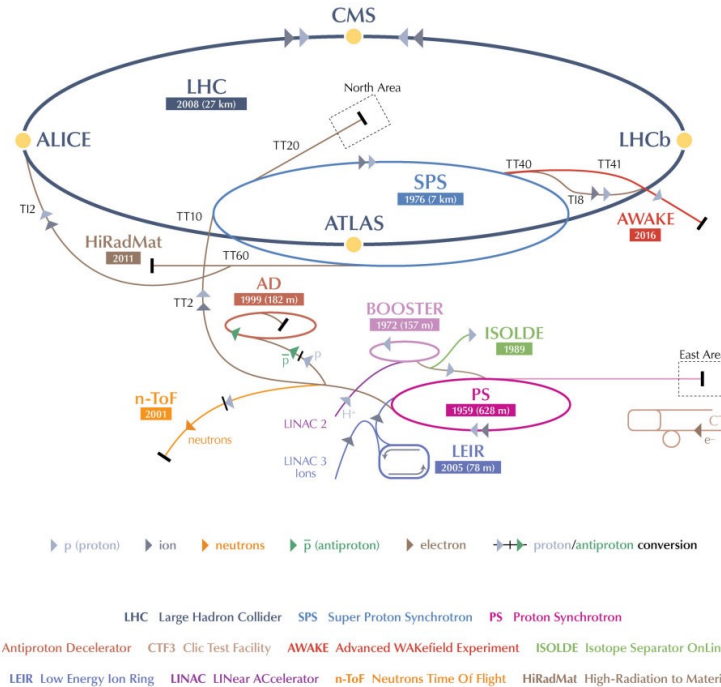


**Figure 3.2:** The CERN accelerator complex showing the chain of injection of protons into the LHC ring and the locations of the four main experiments ATLAS, CMS, LHCb and ALICE [50].

LHC operation officially started at the beginning of September 2008 but it was interrupted after a short period, due to the breakdown of superconducting magnets. The collider has been reactivated in November 2009 with first pp collisions at  $\sqrt{s} = 900 \text{ GeV}$ , officially starting a new era in the particle physics experiments. The operating center-of-mass energies in pp collisions have so far been 7 TeV in 2010-2011, 8 TeV in 2012 and 13 TeV in 2015-2016. The 7 and 8 TeV periods together make out the *LHC Run 1*, while the 13 TeV period is called the *LHC Run 2*. The work presented in this document is based on data sets collected with pp collisions at 8 TeV in 2012 and at 13 TeV in 2015.

During the whole Run 1, the LHC operated with a 50 ns bunch spacing. The peak of instantaneous luminosity in 2011 has been  $\approx 0.4 \times 10^{34} \text{ cm}^{-2} \text{ s}^{-1}$  with a total delivered integrated luminosity of  $6.1 \text{ fb}^{-1}$  [51]. In 2012 the beam energy increased to 4 TeV per beam with a peak luminosity of  $\approx 0.8 \times 10^{34} \text{ cm}^{-2} \text{ s}^{-1}$  and  $23.3 \text{ fb}^{-1}$  delivered integrated luminosity by the end of that year [51]. The increment of the instantaneous luminosity leads to a no more negligible number of simultaneous interactions per bunch crossing, the so-called *pileup* (PU) events. It depends on the cross section of inelastic collisions (75 mb at  $\sqrt{s} = 8 \text{ TeV}$  [52]) and it is directly linked to the instantaneous luminosity. The average PU of the data collected in 2012 is equal to 21 (Fig. 3.3) while it has been around 15 in 2011 [51].

A long shut-down period for the LHC (LS1) occurred during the whole 2013 and 2014, where upgrades and technical improvements have been performed in order to reach the designed instantaneous luminosity and center-of-mass energy. On March, 21st 2015 the first pp collisions at  $\sqrt{s} = 13$  TeV has been obtained, a new record-breaking energy. For the first three months the machine operated with 50 ns bunch spacing while, from August 2015, it has been reduced to the designed 25 ns and the number of bunches per beam has been increased. The first part of this Run 2 phase ended on November 2015 with a total delivered integrated luminosity of  $4.2 \text{ fb}^{-1}$  and a peak luminosity of  $\approx 0.5 \times 10^{34} \text{ cm}^{-2} \text{ s}^{-1}$  with an average pileup of 12 [51].

The LHC Run 2 has been restarted in April 2016, after an end-of-the-year technical stop, reaching a peak luminosity of  $\approx 1.5 \times 10^{34} \text{ cm}^{-2} \text{ s}^{-1}$ . The machine has remained in operation at  $\sqrt{s} = 13$  TeV for the whole year with a total delivered integrated luminosity of  $40 \text{ fb}^{-1}$ . Accordingly to the current LHC schedule, the Run 2 will proceed up to the end of 2018 with a total expected integrated luminosity of  $\approx 150 \text{ fb}^{-1}$ . The data collected in 2016 are not considered in this work.

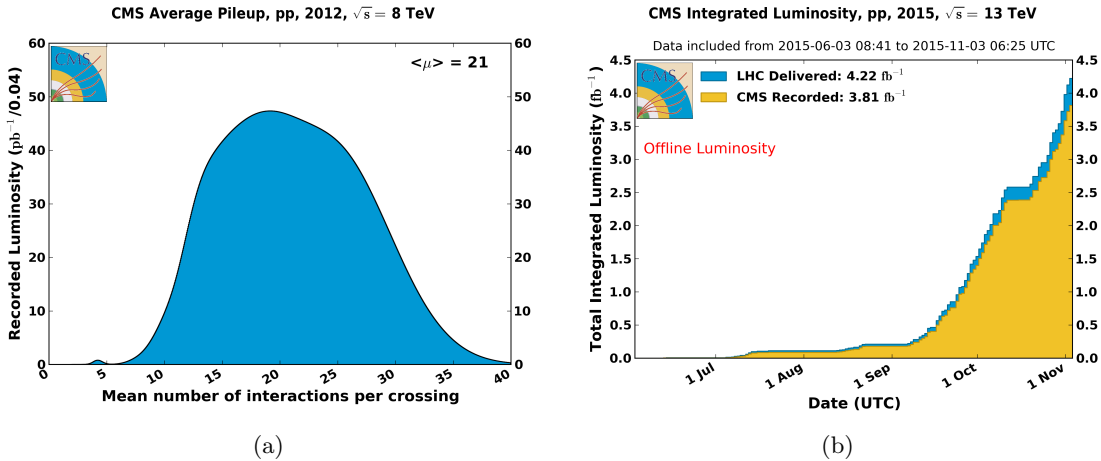


**Figure 3.3:** (a) Number of simultaneous interactions per bunch crossing in data collected in 2012 by the CMS experiment at LHC. (b) Cumulative luminosity versus day delivered by LHC (blue) in 2015; the offline luminosity recorded by the CMS experiment is also reported (orange). [51]

## 3.2 The CMS detector

The CMS detector is a general purpose detector installed 100 m underground at the LHC interaction point 5 (P5) near the village of Cessy in France. It has been designed to exploit the different properties of the wide range of particles and phenomena produced in high-energy collisions at the LHC.

The design of this detector is driven by the challenges of a physics experiment in the LHC environment. Many of the physics processes of interest have a small cross section and the background from QCD jet production is overwhelmingly dominant. In order to achieve high rejection power with an optimal efficiency for rare channels, the detector has to be able to reconstruct the primary interaction entirely and to reduce the influence of overlapping events. Therefore, one needs to collect all possible information on the particles passing through the detector. Since these have different properties, a mixture of subdetectors is required

for a complete event reconstruction. The reconstruction of lepton signatures is essential for the extraction of rare processes and an excellent muon and electron identification and momentum resolution is desired. A precise measurement of secondary vertices and track impact parameters is fundamental for an efficient identification of heavy flavor quarks and  $\tau$  leptons. Moreover, a large hermetic geometric coverage is preferred, which allows for a precise estimate of the transverse momentum carried away by invisible particles through the sum of all visible particles.

The high peak luminosities of LHC lead to large pileup imposing further challenges to the design. As a consequence of pileup, the products of an interaction under study may be confused with those from other interactions in the same bunch crossing. This effect can be reduced by using high-granularity detectors resulting in low occupancy. In addition, the short bunch crossing requires fast response time and good time resolution of each detector element. Hence, a large number of detector channels and an excellent synchronization among them are necessary. Another challenge arises from the large flux of particles near the interaction point which leads to high radiation levels and the need of radiation hard detectors and front-end electronics.

Figure 3.4 shows the layout of the CMS detector. The detector is built in a cylindrical structure composed of a barrel in the center and endcaps at both sides. This structure is 21.6-m-long, 14.6 m in circumference and 12500-tons-heavy. The detector design and layout was driven by the choice of the magnetic field configuration. Large bending power is needed for a precise measurement of the momentum of high-energy charged particles. Within the CMS detector this is achieved by a superconducting solenoid with a length of 12.9 m and an inner diameter of 5.9 m generating a magnetic field of 4 T. The bore of the magnet coil is large enough to accommodate the inner tracker and the calorimetry inside. The inner tracker consists of a pixel and a strip detector both made out of Silicon, representing the key component of CMS to measure the momenta of charged particles and identify primary and secondary vertices. The calorimetry system comprises a crystal electromagnetic calorimeter (ECAL) and a brass and scintillator hadronic calorimeter (HCAL), which provide information on the energies and directions of all charged and neutral particles. Outside the magnet are the large muon detectors, which, integrated inside the return yokes of the magnet, provide identification of muons and measurement of their momenta.

For the description of the CMS detector the following coordinate system is used. The origin is centered at the nominal collision point inside the experiment with the  $y$ -axis pointing vertically upward, the  $x$ -axis pointing radially inward toward the center of the LHC, and the  $z$ -axis points along the beam direction. The azimuthal angle  $\phi$  is measured from the  $x$ -axis in the  $x$ - $y$  plane. The polar angle  $\theta$  is measured from the  $z$ -axis. Pseudorapidity is defined as  $\eta = -\ln \tan(\theta/2)$ . Thus, the momentum and energy measured transverse to the beam direction, denoted by  $p_T$  and  $E_T$ , respectively, are computed from the  $x$  and  $y$  components.

In the following sections the three main components of the CMS detector will be described together with a section on the triggering system.

### 3.2.1 Tracking detectors

The tracking system of CMS (Fig. 3.5) is designed to provide a precise and efficient measurement of the trajectories of charged particles emerging from the LHC collisions, as well as a precise reconstruction of secondary vertices [53]. It surrounds the interaction point and has a length of 5.8 m and a diameter of 2.5 m providing coverage up to  $|\eta| < 2.5$ . In order

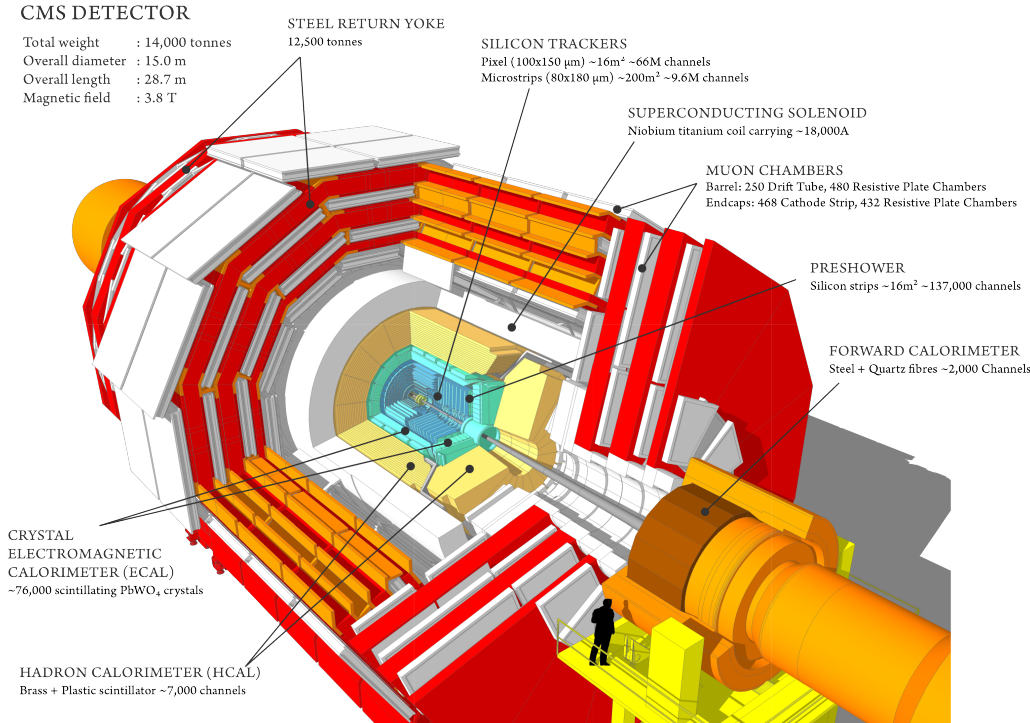


**Figure 3.4:** Layout of the CMS experiment and its subdetectors.

to achieve high tracking efficiency at the high luminosities of LHC, a detector technology featuring granularity, speed and radiation hardness is required. Furthermore, the material budget of the tracking system has to be as low as possible in order to avoid a worsening of the tracking efficiency and resolution due to material interaction effects of the charged particle, such as multiple scattering, bremsstrahlung, photon conversion or nuclear interactions. These requirements lead to a tracker design entirely based on silicon detector technology. With about  $200\text{ m}^2$  of active silicon area the CMS tracker is the largest silicon tracker ever built. It is divided into a pixel detector close to the interaction region and a strip detector in the outer region. The motivations for this layout are explained in what follows.

At LHC design luminosity more than 1000 particles are hitting the tracking volume in each bunch crossing. This leads to a hit rate density of  $1\text{ MHz/mm}^2$  at a radius of 4 cm which imposes severe challenges to the design of the tracking detectors. With a pixel size of  $100 \times 150\text{ }\mu\text{m}^2$  in  $r\text{-}\phi$  and  $z$ , respectively, an occupancy of the order of  $10^{-4}$  per pixel and LHC bunch crossing can be achieved. The hit rate density falls with the distance from the interaction point to  $60\text{ kHz/mm}^2$  at a radius of 22 cm and to  $3\text{ kHz/mm}^2$  at a radius of 115 cm. Therefore, at intermediate radii (20–55 cm), silicon micro-strip detectors are used, with a typical cell length of 10 cm and a pitch of  $80\text{ }\mu\text{m}$ . At the outermost radii (55–110 cm) the strip size can be further increased to  $25\text{ cm} \times 180\text{ }\mu\text{m}$ . With this choice an occupancy of less than 3% is maintained in the strip detector. However, the strip capacitance scales with its length and therefore the electronics noise is a linear function of the strip length as well, becoming not negligible in the outermost region where the strip size is the largest. In order to maintain a good signal to noise ratio well above 10, CMS uses thicker silicon sensors for the outer tracker region ( $500\text{ }\mu\text{m}$  thickness as opposed to the  $320\text{ }\mu\text{m}$  in the inner tracker) with correspondingly higher signal. To mitigate the radiation damage effects and prolong the lifetime of the detector modules, the tracking detectors are designed to run at subzero

temperatures. The cooling is established using a mono-phase liquid cooling system with  $\text{C}_6\text{F}_{14}$  as cooling fluid. The whole tracker system operated at  $+4^\circ \text{ C}$  during Run 1. After this phase, several improvements have been implemented and an operative temperature of  $-15^\circ \text{ C}$  is currently maintained for Run 2.

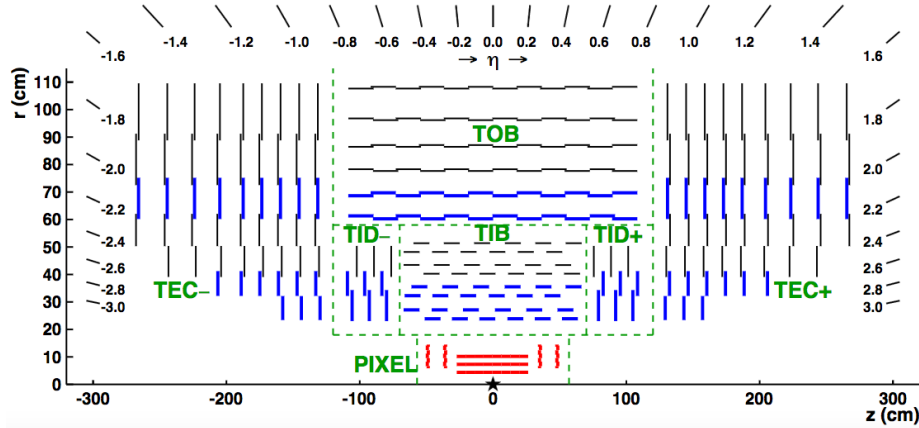


**Figure 3.5:** Longitudinal section of half of the CMS silicon tracker system; the different detector types are indicated.

The pixel detector is built from 3 barrel layers at radii of 4.4, 7.3 and 10.2 cm (BPix) and two end disks (FPix) on each side at a distance of  $z = \pm 34.5, \pm 46.5 \text{ cm}$  from the interaction point. It consists of 1440 segmented silicon sensor modules with a total of 66 million readout channels covering an area of about  $1 \text{ m}^2$ . The pixel detector is essential for the reconstruction of secondary vertices from the decay of bottom quarks and  $\tau$  leptons. It provides precise track point measurements in  $r$ - $\phi$  and  $z$  and therefore guarantees a small impact parameter resolution important for good secondary vertex reconstruction. This is achieved thanks to the readout of the analog pulse height information. The sensor surface in the barrel layers is parallel to the magnetic fields, hence the charge carriers produced by a particle traversing experience a Lorentz drift, which leads to charge spreading over more than one pixel. The analog pulse height information can be used to calculate a center of gravity of the charge distribution improving the hit information. The forward detectors are tilted at  $20^\circ$  in a turbine-like geometry to induce charge-sharing. As shown in Fig. 3.6, a spatial resolution of  $10 \mu\text{m}$  in the transverse plane and  $30 \mu\text{m}$  in the longitudinal plane can be achieved for BPix. For FPix a spatial resolution of  $20 \mu\text{m}$  is obtained. A detailed description of the design and the functioning of the CMS pixel barrel detector is given in Chapter 14.

The strip detector occupies the radial region between 20 cm and 1.16 m. As illustrated in Fig. 3.5, it is composed of four subsystems: the four-layer Tracker Inner Barrel (TIB), the six-layer tracker outer barrel (TOB) and on each side three-disk Tracker Inner Disks (TID) and nine-disk Tracker Endcaps (TEC). The silicon micro-strip sensors have strips parallel to the beam axis in the barrel and radial on the disks. The modules in the first two layers and rings, respectively, of TIB, TID, and TOB as well as rings 1, 2, and 5 of the TECs carry a second micro-strip detector module which is mounted back-to-back with a stereo angle of 100 mrad in order to provide a measurement of the second coordinate ( $z$  in the barrel and  $r$  on the disks). This tracker layout ensures at least 9 hits in the silicon strip tracker in the full range  $|\eta| < 2.4$  with at least 4 of them being two-dimensional measurements. The

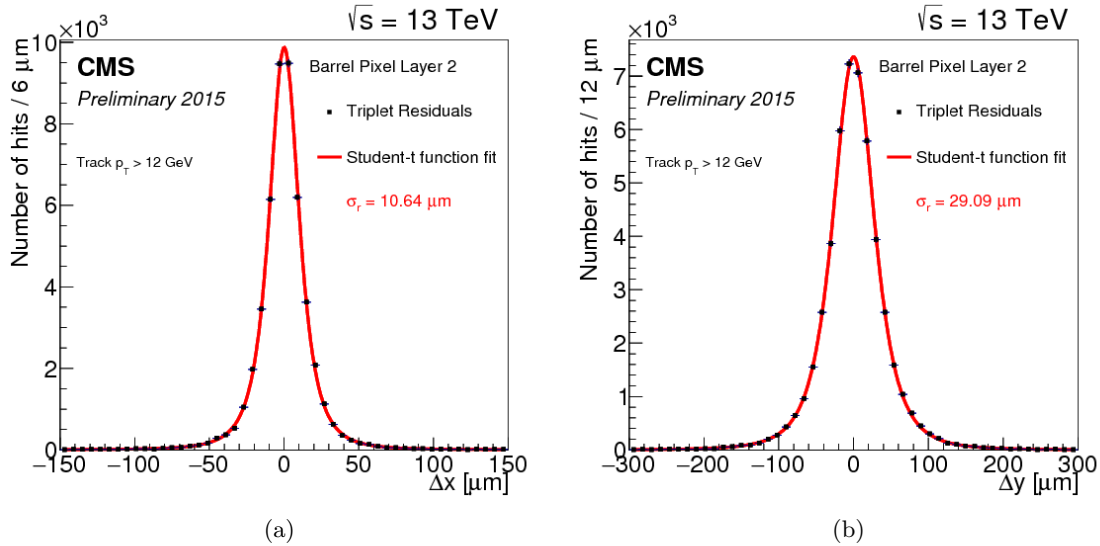


**Figure 3.6:** Distributions of the hit residuals on the pixel barrel layer 2 in the transverse (a) and longitudinal (b) direction with respect to the beam. The distributions are fitted with a Student’s t-function. The fitted width parameter  $\sigma_r$  is reported on the plot [54].

total number of silicon sensors in the strip tracker is 24244, making up a total active area of  $198 \text{ m}^2$ , with about 9.3 million of strips.

### 3.2.2 Calorimetry

The calorimeter measures the energies and directions of all neutral and charged particles traversing the detector, with the exception of muons and neutrinos. It consists of two parts, the electromagnetic calorimeter (ECAL) [55] and the hadronic calorimeter (HCAL) [56].

The goal of ECAL is to measure precisely the energy of electrons and photons which generate electromagnetic showers inside it. It is a hermetic and homogeneous calorimeter with a large pseudorapidity coverage up to  $|\eta| < 3$ . As illustrated in Fig. 3.7, ECAL is divided into barrel and endcap detectors consisting of scintillation crystals made from lead tungstate ( $\text{PbWO}_4$ ). The choice of this material is motivated by its high density ( $8.28 \text{ g/cm}^3$ ), short radiation length ( $X_0 = 0.89 \text{ cm}$ ) and small Molière radius ( $2.2 \text{ cm}$ ), resulting in a high stopping power, fine granularity and therefore a compact calorimeter able to fit inside the solenoid. The ECAL comprises 61200 crystals in the barrel and 7324 crystals in each of the 2 endcaps, for a total volume of  $8.14 \text{ m}^3$  and  $2.9 \text{ m}^3$ , respectively. The crystals have a tapered shape and are mounted in a quasi-projective geometry. The barrel extends radially between 1.29 and 1.75 cm covering the region  $|z| < 3.05 \text{ m}$  and  $|\eta| < 1.479$ . The crystals have a front face cross-section of  $22 \times 22 \text{ mm}^2$  and a length of 2.3 cm ( $25.8 X_0$ ). They are organized in 36 identical supermodules each covering  $20^\circ$  in  $\phi$ . The crystals are contained in a thin-walled glass-fibre alveola structures (“submodules”) with  $2(\phi) \times 5(\eta)$  crystals per each resulting in a granularity 360-fold in  $\phi$  and  $2 \times 85$ -fold in  $\eta$ . The endcaps are placed at a distance of 3.14 m from the interaction point and they extend radially between 3.16 and 17.11 cm, covering the region  $1.479 < |\eta| < 3.0$ . The crystals have a front face cross section of  $28.6 \times 28.6 \text{ mm}^2$  and a length of 2.2 cm ( $24.7 X_0$ ). A preshower detector with a thickness of  $3 X_0$  is placed in front of the endcaps ( $1.653 < |\eta| < 2.6$ ) to guarantee a reliable discrimination of single photons

and photons produced in pairs in neutral pion decays. The relatively low light yield of the crystals ( $30 \gamma/\text{MeV}$ ) requires use of photodetectors with intrinsic gain that can operate in a magnetic field. Silicon avalanche photodiodes (APDs) are used as photodetectors in the barrel and vacuum phototriodes (VPTs) in the endcaps. The light output and the amplification have a strong temperature dependence. The response to an incident electron changes by  $(3.8 \pm 0.4)\%/\text{ }^\circ\text{C}$  which in turn means that the temperature has to be closely monitored and kept stable to a precision of  $\pm 0.05\text{ }^\circ\text{C}$ . The nominal operating temperature of the ECAL is  $18\text{ }^\circ\text{C}$  and is provided by a water cooling system.

The energy resolution of the electromagnetic calorimeter can be parametrized by the following expression:

$$\frac{\sigma_E}{E} = \frac{S}{\sqrt{E(\text{GeV})}} \oplus \frac{N}{E(\text{GeV})} \oplus C. \quad (3.4)$$

The first term is stochastic including contributions from the shower containment, the number of photoelectrons and the fluctuations in the gain process. The second contribution corresponds to the noise term, which includes noise in the readout electronics and fluctuations in pileup. The third term is a constant dominating the energy resolution for high-energy electron and photon showers. It depends on non-uniformity of the longitudinal light collection, energy leakage from the back of the calorimeter, single-channel response uniformity and stability. The value of the three coefficients were determined by measurements with electron beam in a matrix of  $3 \times 3$  crystals to be  $S = 2.8\%$ ,  $N = 12\%$  and  $C = 0.3\%$  [57].

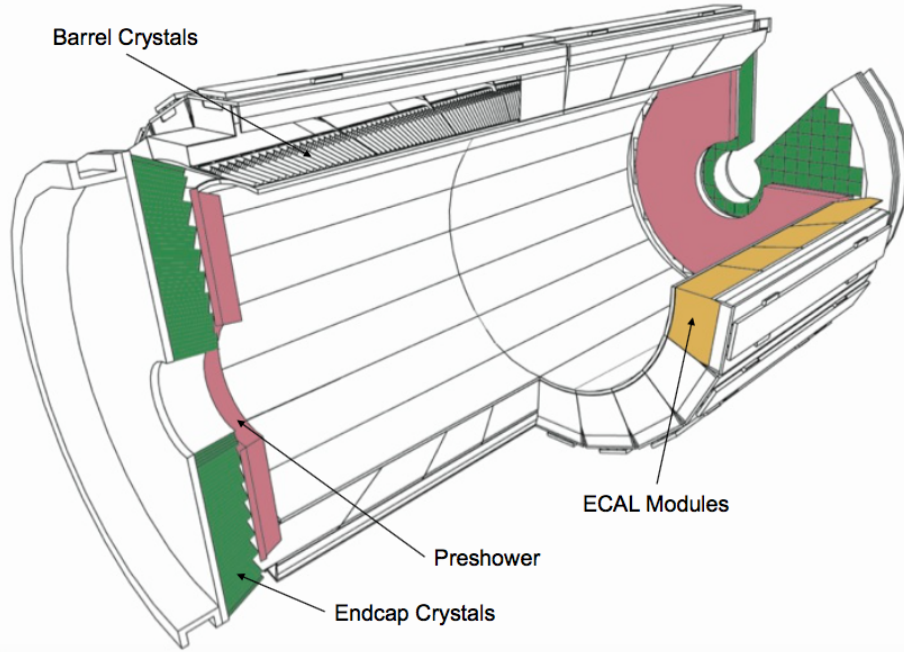


**Figure 3.7:** Schematic view of the CMS electromagnetic calorimeter [47].

The energy measurement of the ECAL is complemented by the measurement of the hadronic calorimeter. The HCAL is designed to be as near to hermetic around the interaction region as possible to allow events with missing energy to be identified. It is a sampling calorimeter composed of layers of brass absorber interlaced with tiles of plastic scintillators

as active material to detect the showers generated by the hadrons in the brass. The energy released in the scintillator tiles causes them to emit blue-violet light, a fraction of which is absorbed and re-emitted by embedded wavelength-shifting fibres in the green region of the spectrum. The green light is then carried by special fibre-optic waveguides to the readout system. The photodetection readout is based on multi-channel hybrid photodiodes (HPDs), which are photodetectors configured especially for CMS that can provide gain and operate in a high magnetic field.

Figure 3.8 shows a schematic cross section of the HCAL detectors. The hadron barrel (HB) and endcaps (HE) calorimeters sit behind the tracker and the electromagnetic calorimeter as seen from the interaction point. The HB is radially restricted between the outer extent of the electromagnetic calorimeter ( $r = 1.77\text{ m}$ ) and the inner extent of the magnet coil ( $r = 2.95\text{ m}$ ). This constrains the total amount of material which can be put in to absorb the hadronic shower. Therefore, an Outer Hadron (HO) calorimeter is placed outside the solenoid complementing the barrel calorimeter. The HO uses the solenoid as additional absorbing material and provides sufficient containment for hadronic showers with a thickness of 11.8 interaction lengths ( $\lambda_l$ ). The first scintillators are placed in front of the first absorber plate in order to sample showers developing in the material between the ECAL and the HCAL, while the last scintillators are installed after the last absorber plate to correct for late developing showers leaking out. A total amount of 70000 and 20916 scintillator tiles are installed in the HB and the HE, respectively. The HB and HE cover the region  $|\eta| < 1.3$  and  $1.3 < |\eta| < 3.0$ , respectively. Beyond  $|\eta| = 3$ , the Hadron Forward (HF) calorimeter placed at 11.2 m from the interaction point extends the pseudorapidity coverage down to  $|\eta| = 5.2$ . The HF is a sampling calorimeter made from steel absorber plates composed of 5 mm thick grooved plates with quartz fibers inserted as active medium. The signal is generated when charged shower particles above the threshold generate Cherenkov light in the quartz fibres, thereby rendering the calorimeter mostly sensitive to the electromagnetic component of showers. The calorimeter is segmented and arranged in towers as summarized in Table 3.1.

The HCAL energy resolution is

$$\frac{\sigma_E}{E} = \frac{a}{\sqrt{E(\text{GeV})}} \oplus 5\% \quad (3.5)$$

where  $a$  is 65% in the barrel, 85% in the endcaps and 100% in the forward calorimeter.

**Table 3.1:** Tower segmentation in azimuthal and polar angle for the hadronic barrel, endcap and forward calorimeters.

	HB/HO	HE ( $ \eta  \leq 2.5$ )	HE ( $ \eta  > 2.5$ )	HF ( $ \eta  \leq 4.7$ )	HF ( $ \eta  > 4.7$ )
$\Delta\phi \times \Delta\eta$	$0.087 \times 0.087$	$0.087 \times 0.087$	$0.175 \times 0.175$	$0.175 \times 0.175$	$0.175 \times 0.35$

### 3.2.3 Muon detectors

The muon system is the outermost part of the CMS detector. It is located in the steel return yoke of the solenoid, covering the pseudorapidity region  $|\eta| < 2.4$ . This is possible because muons are hardly affected by this large material budget. The coil acts as a shield from electromagnetic and hadronic particles escaping the calorimeters and the yoke provides a magnetic field between consecutive muon stations, allowing a momentum measurement independent from the inner tracker. The muon system is designed for three major functions: robust and fast identification of muons, good resolution of momentum measurement, and integration to a fast and reliable trigger system. The gaseous detectors have been chosen

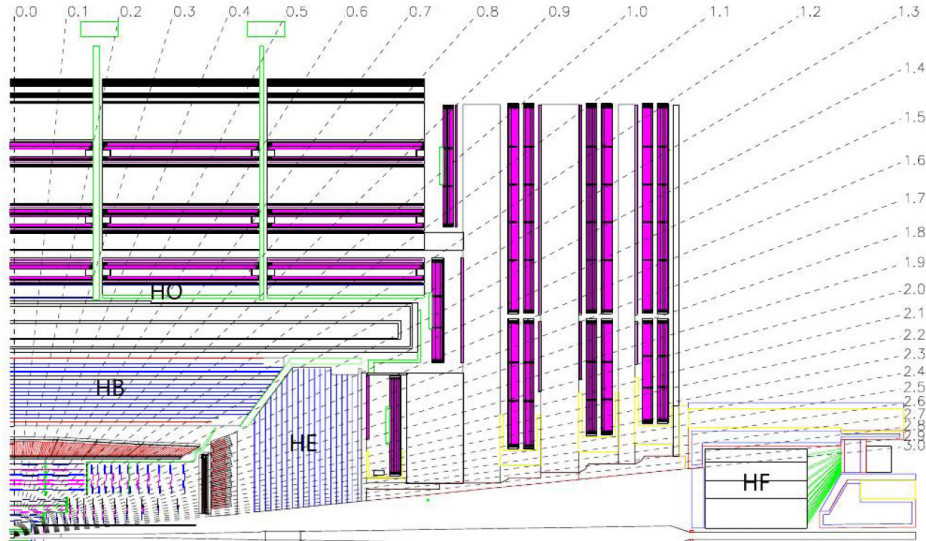


**Figure 3.8:** Longitudinal view of the CMS detector showing the locations of the hadron barrel (HB), endcap (HE), outer (HO) and forward (HF) calorimeters [47].

since they are robust and with a relative fast response. Furthermore, the area to be covered is extremely wide and a gaseous detector system allows to reduce the cost and the amount of readout channels. The muon system is thus composed of three types of gaseous detectors arranged in barrel and endcap sections, as shown in Fig. 3.9: Drift Tubes (DTs), Resistive Plate Chambers (RPCs) and Cathode Strip Chambers (CSCs). The choice of different detector topologies lies essentially in the different expected particle rates.

In the barrel region, where the neutron-induced background is small, the muon rate is low, and the 4-T magnetic field is uniform, DTs with standard rectangular drift cells are used covering the pseudorapidity region  $|\eta| < 1.2$ . A DT cell is a 4 cm wide gas tube with a positively charged stretched wire inside. The barrel DT chambers are organized in five separate wheels. Each wheel is divided into 12 sectors, each covering a  $30^\circ$  azimuthal angle. In each of the 12 sectors there are 4 chambers per wheel which are concentric around the beam line and separated by the iron return yoke. Each DT chamber, on average  $2\text{ m} \times 2.5\text{ m}$  in size, consists of 12 layers of DT cells, arranged in three groups of four. For the first 3 stations in each wheel, the middle group measures the  $z$  coordinate while the two outside groups measure the  $r\phi$  coordinate. The fourth and outermost station does not contain the  $z$ -measuring planes. Each one of the 250 DT chambers has a resolution of  $\approx 100\text{ }\mu\text{m}$  in  $r\phi$  and up to  $150\text{ }\mu\text{m}$  in  $z$ , and can measure the particle direction with 1 mrad accuracy.

In the two endcap regions of CMS, where the muon rates and background levels are high and the magnetic field is large and non-uniform, CSCs are used with their fast response time, fine segmentation, and radiation resistance, covering the pseudorapidity region between 0.9 and 2.4. Each CSC is trapezoidal shaped multiwire proportional chambers which consists of 6 gas gaps, each gap having a plane of radial cathode strips and a plane of anode wires running almost perpendicularly to the strips. The gas ionization and subsequent electron avalanche caused by a charged particle traversing each plane of a chamber produces a charge on the anode wire and an image charge on a group of cathode strips. Thus, each CSC provides a two-dimensional position measurement, where the  $r$  and  $\phi$  coordinates are determined by the cathode strips and the anode wires, respectively. A total amount of 540 CSC are arranged in 4 disks per endcaps divided in concentric rings (3 rings in the innermost station, 2 in the

others). Each chamber has a spatial resolution of about 200 mm in  $r$ , and  $75 \times 150 \mu\text{m}$  in the  $r\phi$  coordinate.

In addition, there is a total of 610 RPCs added in both the barrel and endcap regions to provide a fast, independent, and highly-segmented trigger over a large portion of the rapidity range ( $|\eta| < 1.6$ ) of the muon system. They produce a fast response, with good time resolution ( $\approx 2$  ns) but coarser position resolution than the DTs or CSCs. RPCs are made from two high resistive plastic plates with a voltage applied and separated by a gas volume. The signal generated by the muon when passing through the gas volume is detected by readout strips mounted on top of one of the plastic plates. Six layers of RPCs are installed in the barrel muon system, two layers in each of the first two stations and one layer in each of the last two stations. One layer of RPCs is built into each of the first three stations of the endcap.

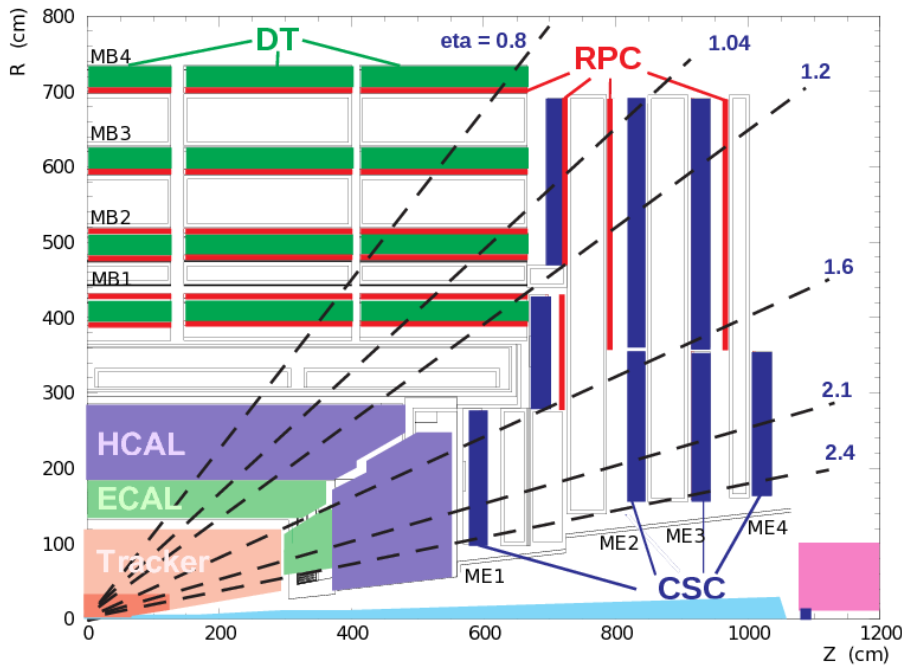


**Figure 3.9:** A longitudinal view of one quarter of the CMS experiment; the three muon detectors detector types are highlighted.

### 3.2.4 The trigger system

The LHC provides proton-proton and heavy-ion collisions at unprecedented high luminosity and interaction rates. Given the high segmentation of the CMS detector, about 100 million readout channels are present and this corresponds to an enormous volume of data at the detector front-ends. At the design luminosity and collision frequency, each crossing produces approximately 1 MB of zero-suppressed data resulting in a raw data rate of about 40 TB per second. These figures are many orders of magnitude larger than the archival storage capability of  $\approx 1$  kHz at data rates of  $\mathcal{O}(10^2)$  MB/s. Technical difficulties in handling, storing and processing such extremely large amounts of data impose a reduction factor on the rate of events that can be written to permanent storage. This task is performed by the trigger system, which is the baseline of the physics event selection process. The key point of the trigger system is a fast time rejection of all the “non-interesting” events. This can be done

by exploiting event topologies common to group of physics processes, such as the presence of one or more leptons in the event. The trigger system needs to be as inclusive as possible, in order to collect data for all the physics searches that can be performed with pp collisions, but it has also to operate within the CMS time restriction and avoid the saturation of the storage capability. The required rejection power of  $\mathcal{O}(10^5)$  is too large to be achieved in a single processing step, if a high efficiency has to be maintained for the physics phenomena that CMS plans to study. For this reason, the full selection task is split into two steps. The first step (Level-1 Trigger) is designed to reduce the rate of events accepted for further processing to less than 100 kHz. The second step (High-Level Trigger or “HLT”) is designed to reduce this maximum L1 accept rate of 100 kHz to a final output rate of 1 kHz.

The L1 Trigger is built from custom designed, programmable electronics and is housed partly on the detectors, partly in the underground control room located at a distance of approximately 90 m from the experimental cavern. It is designed to take a fast accept/reject decision every bunch crossing, on the basis of a rough reconstruction of the event. The detector information used at L1 are coarsely segmented data from the calorimeters and the muon system only. Within a time budget of  $3.2 \mu\text{s}$ , it has to decide if an event is discarded or kept, and transfer this decision back to the subdetectors, which in the meantime keep the high resolution data in the front-end electronics. Figure 3.10 shows the L1 Trigger architecture: it has local, regional and global trigger components.

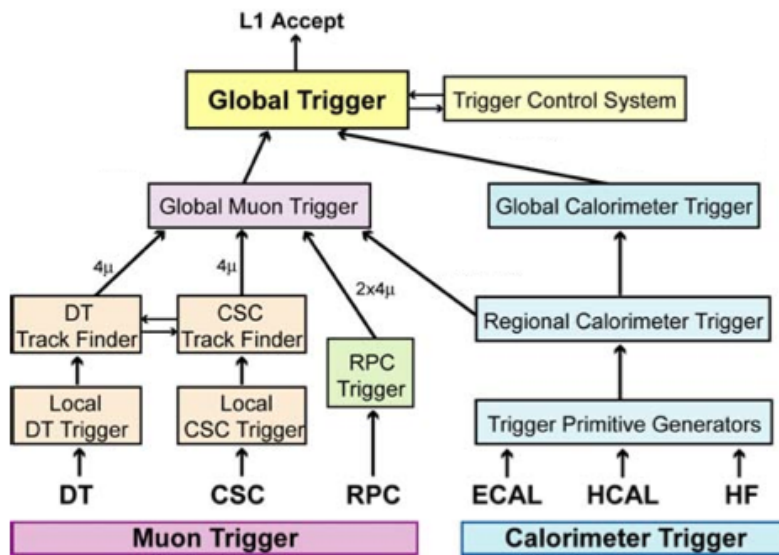


**Figure 3.10:** Architecture of the Level-1 Trigger [47].

Trigger primitives are generated by calculating the transverse energy of a trigger tower and assigning it to the correct bunch crossing. A regional calorimeter trigger then determines regional electron, photon and jet candidates and information relevant for muon and  $\tau$  lepton identification. The global calorimeter trigger provides information about the jets, the total transverse energy and the missing energy in the event and identifies the highest-ranking trigger candidates.

In the muon system all three types of detectors take part in the trigger decision. The DT chambers provide track segments in the projection and hit pattern in  $\eta$ , while the CSC determine three-dimensional track segments. The track finders in the DT chambers and the

CSCs calculate the transverse momentum of a track segment and its location and quality. The RPCs deliver an independent measurement derived from regional hit patterns. The global muon trigger receives up to four candidates from each subsystem (DT, barrel RPC, CSC and endcap RPC) together with the isolation information from the global calorimeter trigger. The aim is to improve the efficiency and to reduce the rate by making use of the complementarity and the redundancy of the subsystems. In the end, the global muon trigger selects a maximum of four muon trigger candidates and determines their momentum, charge, position and quality.

The trigger objects extracted by the global calorimeter trigger and the global muon trigger are sent to the global trigger where the decision to accept or reject an event is taken and distributed to the subdetectors. The simplest triggers are in general those based on the presence of one object with an  $E_T$  or  $p_T$  above a predefined threshold (single-object triggers) and those based on the presence of two objects of the same type (di-object triggers) with either symmetric or asymmetric thresholds. Other requirements are those for multiple objects of the same or different types (“mixed” and multiple-object triggers). Up to 128 algorithms can be executed in parallel. The decision is also based on the readiness of the subdetectors and the data acquisition system (DAQ), which is supervised by the Trigger Control System (TCS). The Level-1 Accept (L1A) decision is communicated to the subdetectors through the Timing, Trigger and Control (TTC) system.

If an event is accepted by the L1 trigger, the full detector information ( $\approx 1$  MB) is readout by the DAQ system and passed to the HLT system for further analysis. The HLT is a special part of the CMS software which runs on a farm of several thousand processors performing high-level object reconstruction and analysis. Each processor works on the reconstruction of one event at a time, to get to a trigger decision within on average 100 ms. Since the time budget for one event is much larger than at the L1 trigger, more complicated algorithms, including tracking, can be executed at the HLT. Once an event is accepted, it is stored on disk and fully reconstructed offline at a later time.

The full detector readout is available at HLT, but in order to meet the timing requirements given by the input rate from L1, events are discarded before being fully reconstructed, as soon there is enough reconstructed information to take the decision. Therefore the selection is organized in a sequence of logical steps. The Level-2 uses the full information from calorimeters and muon detectors to reconstruct the physical objects and to reduce the event rate by roughly one order of magnitude. The data from the silicon tracker represent almost 80% of the event size and require complex and time consuming algorithms for the reconstruction. For this reason this information is used only during the Level-3 selection.

The HLT consists of approximately 400 trigger paths. Each trigger path starts from the seed provided by the L1 trigger and it is built from reconstruction modules and filter modules. After some parts of the data are reconstructed, a filter module decides if the reconstructed objects pass the thresholds and the next step in reconstruction is started, or if the event is not accepted by the path. In the later case, the execution of the path is stopped and the following reconstruction steps and filter steps are not performed to save computation time. If an event is not accepted by a path, it can still be accepted by a different path.

If, for some paths with low thresholds, the acceptance rate is too high, they can be prescaled to lower the rate. A prescale value of ten means, for example, that the path is executed only for every tenth event that was accepted by the L1 trigger, and, consequently, the trigger rate for that path is ten times smaller. The prescale value for one trigger path has several predefined levels, depending on the instantaneous luminosity of the LHC machine. During an LHC fill, the instantaneous luminosity decreases, and the prescale values can be

changed during a CMS run to keep the global trigger rate at an optimal level.

## **Part I**

# **Search for diboson resonances with CMS**

# Diboson resonances as signature for new physics

---

This part of the thesis is dedicated to the description and discussion of searches for new physics in proton-proton collision data collected with the CMS experiment at LHC. As pointed out in Chapter 2, the remarkable compatibility of the discovered scalar resonance by the ATLAS and CMS collaborations with the SM predictions for the Higgs boson, force physicists to deeply understand the role of naturalness in the dynamics of this particle. Several theoretical extensions to the SM have been proposed offering a concrete realization of naturalness, where new particles with masses in the TeV range generate loop corrections with the necessary cancellations to stabilize the Higgs boson mass. This means that the attention can be restricted to direct experimental manifestations of new physics represented by the production of reasonably narrow new particles. More natural solutions can therefore be probed at the LHC through the direct discovery of these new particles in final states with SM objects with known properties. The research described in this work follows exactly this approach and it is focused on the direct search for new massive resonances ( $M_X > 800 \text{ GeV}$ ) decaying to pairs of vector bosons (WW, WZ, or ZZ) or to a vector boson and a Higgs boson (WH or ZH). These decay modes can have large branching fractions in several BSM models. Popular examples include the bulk scenario of the Randall–Sundrum warped extra-dimensions described in Section 2.3.1, as well as the composite Higgs and Littlest Higgs models discussed in Section 2.3.2. Furthermore, the HVT model (Section 2.3.3) generalizes a large class of explicit theories that predict new heavy spin-1 vector bosons, adopting a simplified model strategy. The properties of the above benchmark models studied in this thesis are summarized in Table 4.1.

**Table 4.1:** Summary of the properties of the heavy resonance models considered in this work. The polarization of the produced W/Z boson in all considered models is mostly longitudinal.

model	particles	spin	charge	main production	main decay
HVT model A, $g_V = 1$	W' singlet	1	$\pm 1$	$q\bar{q}^{(\prime)}$	$q\bar{q}^{(\prime)}$
HVT model A, $g_V = 1$	Z' singlet	1	0	$q\bar{q}$	$q\bar{q}$
HVT model A, $g_V = 1$	W' + Z' triplet	1	0, $\pm 1$	$q\bar{q}/q\bar{q}^{(\prime)}$	$q\bar{q}/q\bar{q}^{(\prime)}$
HVT model B, $g_V = 3$	W' singlet	1	$\pm 1$	$q\bar{q}^{(\prime)}$	WZ, WH
HVT model B, $g_V = 3$	Z' singlet	1	0	$q\bar{q}$	WW, ZH
HVT model B, $g_V = 3$	W' + Z' triplet	1	0, $\pm 1$	$q\bar{q}/q\bar{q}^{(\prime)}$	WW, WZ, ZH
RS bulk scenario, $\tilde{k} = 0.5$	$G_{\text{bulk}}$	2	0	$gg$	WW, ZZ

The signal under investigation is a narrow resonance, referring to the assumption that the resonance's natural width is smaller than the experimental resolution, covering a large fraction of the parameter space of the reference models considered. This assumption allows a “model-independent” type of search, where the description of the resonance mass distribution can be restricted to the detector effects only and hence, independently from the chosen benchmark model.

The semi-leptonic final states are considered, where one of the two bosons is a W decaying into a charged lepton ( $\ell$ ) and a neutrino ( $\nu$ ). The lepton can be either a muon ( $\mu$ ) or an electron (e), however, the results include the  $W \rightarrow \tau\nu$  contribution from the decay  $\tau \rightarrow \ell\nu\bar{\nu}$ . However, the gain in sensitivity from  $\tau$  leptons is limited by the small branching fractions involved. The second boson in the final state decays into hadrons, and can be either a vector boson  $V = W$  or  $Z$ , or a Higgs boson. In the first case, the final state is labelled as  $\ell\nu q\bar{q}$  including  $W \rightarrow q\bar{q}^{(\prime)}$  and  $Z \rightarrow q\bar{q}$  decays (Figures 4.1(a), 4.1(b) and 4.1(c)). For the Higgs boson, the final state is labeled as  $\ell\nu b\bar{b}$  referring to the Higgs boson decay into a bottom quark-antiquark pair (Fig. 4.1(d)).

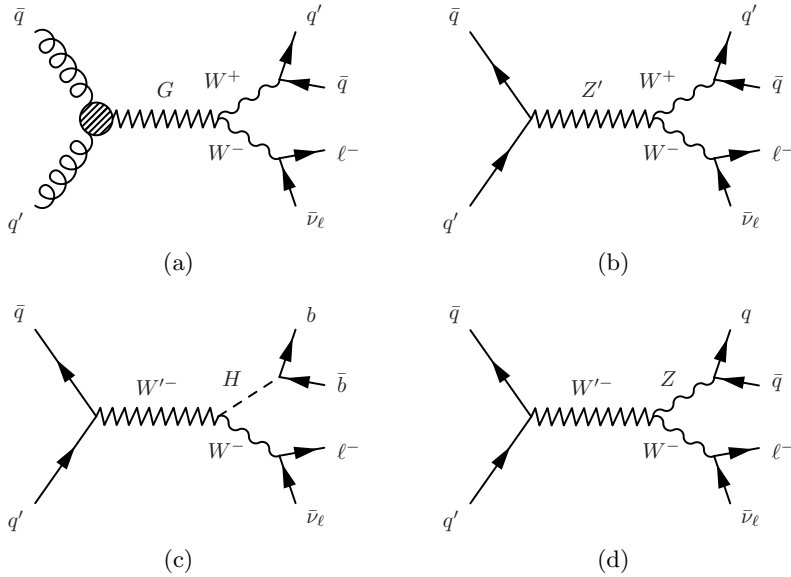


**Figure 4.1:** Feynman diagrams for the production of a neutral spin-2  $G$  (a), and a neutral  $Z'$  (b) and charged  $W'$  (c and d) spin-1 resonances. All resonances decay to a pair of bosons (WW, WZ, or WH) with their subsequent semi-leptonic decay.

The search in the  $\ell\nu b\bar{b}$  final state is based pp collision data at  $\sqrt{s} = 8$  TeV collected in 2012 and corresponding to an integrated luminosity of  $19.7 \text{ fb}^{-1}$ . The second analysis described in this thesis and focused on the  $\ell\nu q\bar{q}$  final state is instead based on the pp collision data at  $\sqrt{s} = 13$  TeV collected in 2015 and corresponding to an integrated luminosity of  $2.3 \text{ fb}^{-1}$ . Although different algorithms are used for the reconstruction and identification of the hadronically decaying boson, the analysis strategy is similar in the two searches.

The key challenge of these analyses is the reconstruction of the highly energetic decay products. Since the resonances under study have masses of  $\approx$  TeV, their decay products, i.e. the bosons, have on average transverse momenta of several hundred GeV or more. As a consequence, the particles emerging from the boson decays are very collimated. In particular, the jet-decay products of the bosons cannot be resolved using the standard algorithms, but are instead reconstructed as a single jet object. Dedicated techniques, so-called jet “V tagging” and “H tagging” techniques, are applied to exploit the substructure of such jet objects, and can help resolve jet decays of massive bosons. These techniques also help to suppress SM background, which mainly originates from the production of W bosons in association with jets (W+jets). Further discrimination is achieved in the  $\ell\nu b\bar{b}$  analysis channel exploiting the specific characteristics of jets arising from the hadronization of bottom quarks.

The aim is to reconstruct the full event to be able to search for a localized enhancement in the invariant mass of the WV or WH system on the top of a smoothly falling SM background distribution. The background mainly comprises W+jets production, although another significant contribution is represented by events involving pair produced top quarks ( $t\bar{t}$ ). Other minor backgrounds are represented by single top quark and SM diboson (WW, WZ or ZZ) production processes.

The invariant mass of the WV and WH system is determined by estimating the neutrino transverse momentum with the measured missing transverse energy in the event, while an estimate of the neutrino longitudinal momentum is derived by imposing the constraint of the W mass on the invariant mass of the  $\ell\nu$  system. In the following, the diboson invariant mass will be labelled either  $m_{\ell\nu+\text{jet}}$ , or  $m_{\text{WV}}$  and  $m_{\text{WH}}$  for the  $\ell\nu q\bar{q}$  and  $\ell\nu b\bar{b}$  final states, respectively. The mass spectrum for the dominant W+jets background is determined from observed events with a reconstructed jet mass not compatible with the V or H hypothesis. This strategy partially relies on the simulation of the background processes. Furthermore, simulated events are used for the optimization of the analysis selection aimed at maximizing the discrimination of the signal against the background and hence the analysis sensitivity.

This part of the thesis is organized as follows. Chapter 5 gives an overview of the methods used to simulate the physics processes happening in pp collisions at the LHC together with a description of the specific simulated background and signal events used in this analysis, as well as a discussion about the data sets analyzed. Chapter 6 provides a detailed description of the algorithms used in CMS for the reconstruction of the event and of the physics objects expected in the semi-leptonic final states under investigation. Particular attention is given to the V and H tagging algorithms representing the key feature of this analysis and therefore, separately discussed in Chapter 7. The analysis strategy, already outlined here, is explained in details in Chapter 8. This includes the final event selection and categorization optimized to enhance the analysis sensitivity, as well as the strategy for the estimation of the expected background, the modelling of the signal and the related systematic uncertainties which will be used as input to the statistical analysis of the diboson invariant mass distribution observed in data. The final results are discussed in Chapters 9 and 10 for the 8 and 13 TeV data analysis, respectively. Eventually, these results are combined with limits derived in companion CMS searches for resonances decaying to a pair of bosons in several different final states, with data collected in both LHC Run 1 and Run 2. These analyses use the same V and H tagging techniques as presented here to separate the signal from the large multijet or V+jets background. The statistical combination represent the last piece of this work and it is presented in Chapter 11.

# Data sets and simulated samples

---

The simulation of pp collisions is usually performed by means of Monte Carlo (MC) event generators, providing an accurate modelling of the event kinematics and topology at parton and hadron level. The hard inelastic scattering has to be fully calculated: from the hard interaction between the partons inside the protons, where perturbative QCD calculations (Section 2.1.6) can be used, to the formation of particle jets from the outgoing partons. Furthermore, it is fundamental to understand the exact response of the detector to the outgoing particles produced in pp collisions. Consequently, the stable outgoing particles are fed to a full detector simulation that models the interaction of those particles with the detector material and the corresponding detector response. The raw detector data are then subject to the same reconstruction algorithms that are also used for real data. In this chapter, MC event generators are described in detail, followed by a brief description of the CMS detector simulation. Finally, few details are given in the last section on the pp collision data sets used to perform the searches described in this thesis.

## 5.1 Simulation of proton-proton collisions

### 5.1.1 Monte Carlo event generators

The generation of hard inelastic pp collisions is factorized into different steps ordered by the timescale on which they happen, as illustrated in Fig. 5.1, and described in the following.

The basis of theoretical event generation at the LHC is a parametrisation of the incoming partons (quarks, anti-quarks and gluons) stemming from the proton, which is given by the parton density functions (PDF). They describe the probability to find a quark or gluon with a given proton momentum fraction  $x$  in the pp collision taking place at the LHC. In QCD the PDFs depend on a factorization scale  $\mu_F^2$  at which the proton is probed. All interactions between quarks and gluons happening at scales below the scale  $\mu_F^2$  are absorbed into the PDFs. Therefore at small  $\mu_F^2$  the proton is observed basically as a combination of its three valence quarks  $uud$ . At higher scales, however, it is dominated by sea quarks and gluons.

A collision between two partons, one from each side, gives the hard process of interest, which can be due to physics within or beyond the standard model. Using the incoming partons as input, the simulation of the hard process is performed by the event generator. It produces hypothetical events with the distributions and rates predicted by theory based on the cross section formulae of the physics process of interest. Using the cross section formula the phase space is sampled and candidate events are defined by choosing values for the degrees of freedom from a uniformly distributed random number generator.

The cross section can be calculated by means of the so called *factorization theorem* [59]. According to the theorem, the hadron itself is described by the whole particle composition interacting on a soft binding energy scale, whereas the collisions occur between the partons on a hard energy scale with large transverse momenta. The cross section for the process is then given by the convolution of the PDF  $f_i(x, Q^2)$ , integrated over the proton momentum

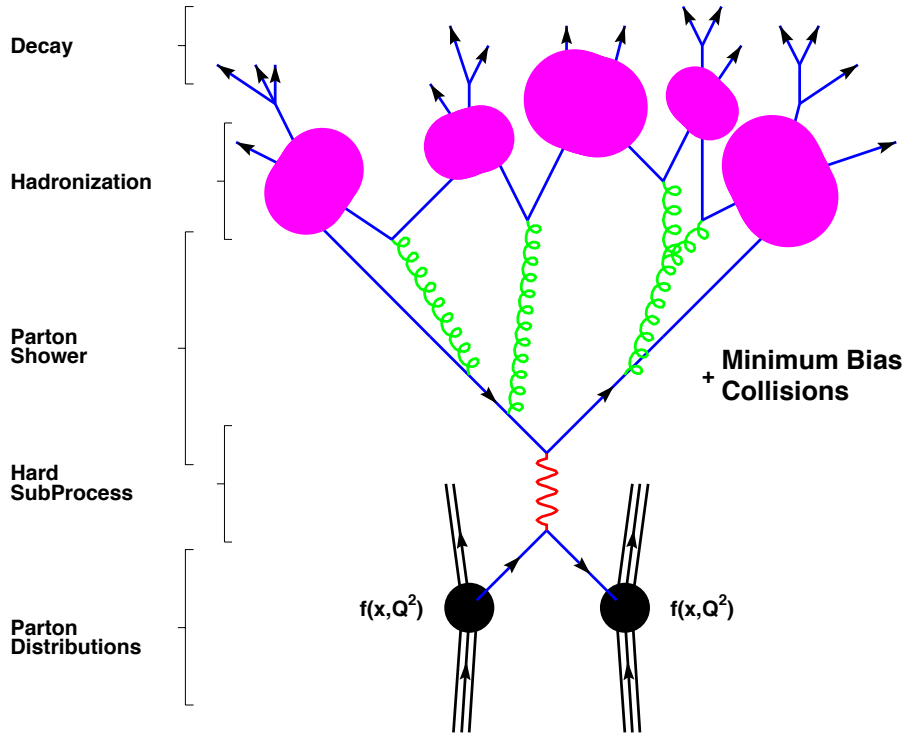


**Figure 5.1:** Steps of Monte Carlo event generation as described in the text evolving in time from bottom to top [58].

fraction  $x$ , for the colliding protons (A, B) at an energy scale  $Q^2$ , and the hard parton-parton cross sections  $\hat{\sigma}_{ij} \rightarrow X$  for all combinations of two partons i and j:

$$\sigma(AB \rightarrow X) = \sum_{q,g=0}^n \alpha_S^n(\mu_R^2) \sum_{ij} \int dx_i dx_j f_{i,A}(x_i, \mu_F^2) f_{j,B}(x_j, \mu_F^2) \cdot \hat{\sigma}_{ij \rightarrow X}^{(n)}(s; x_i, x_j, \mu_R^2, \mu_F^2). \quad (5.1)$$

In this equation the index  $n$  runs over the perturbative order and  $s$  is the squared center-of-mass energy of the collision. The tree-level process, where no emission of gluons or quarks happens, is called “Leading Order” (LO) and takes place when  $n = 0$ . Further orders are called “Next-to-Leading Order” (NLO,  $n = 1$ ), “Next-to-Next-to-Leading Order” (NNLO,  $n = 2$ ) and so on.

As it can be seen from the formula, the PDFs play a fundamental role in the description of the hard process, and it is very important to have several experimental tests to access their values. In fact, perturbative QCD cannot predict the PDFs, since they contain also the low energy (non-perturbative) information about the scattering. As a consequence, PDFs distributions are extracted from data, in deep-inelastic scattering experiments. Most of the parametrizations of proton PDFs now used for the LHC have been extracted from the ZEUS [60] and H1 [61] experiments in electron-proton collisions at the HERA collider and fixed target experiments. The more recent parametrizations also take into account vector boson production and single-inclusive jet production from the Tevatron experiments, as well as LHC data. Once measured for a certain momentum fraction  $x_i$  at an energy scale  $Q^2$ , they can be extrapolated to another scale using the DGLAP (Dokshitzer-Gribov-Lipatov-Altarelli-Parisi) evolution equation [62]. The PDF sets used for the simulation of signal

samples in these analyses are provided by the CTEQ/CT group [63, 64]. This set especially incorporates the effects of Tevatron Run I jet production data on the gluon distribution and is therefore expected to describe the mainly gluon based LHC processes realistically. The CT sets additionally include measurements from HERA-1 data, new data on the asymmetry in the rapidity distribution of the charged lepton from W boson decay from CDF, and rapidity distributions of Z bosons from both CDF and DØ. The NNPDF sets [65] are calculated with an approach based on neural network and the newest versions include LHC data as well. An example of the most important parton distributions inside the proton is shown in Fig. 5.2.

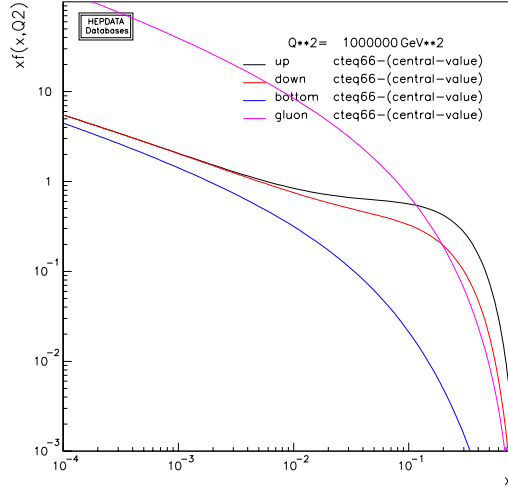


**Figure 5.2:** CTEQ6.6 central value parton distribution functions at the typical mass scale of a new diboson resonance ( $Q^2 = (1000 \text{ GeV})^2$ ) for up, down and bottom quarks, and gluons in the proton in double-logarithmic scale.

An accurate description of the process must take into account radiative corrections to the tree-level or LO description of the process of interest. In particular, one has to include the effects of real and virtual higher-order corrections in perturbation theory. This is achieved by computing the matrix element between the initial and final states as the sum of contributions with increasing powers of  $\alpha_S$ . For instance, the LO contribution to the W boson production process can be calculated from the diagram in Fig. 5.3. The diagrams contributing at NLO to this process and corresponding to the real and virtual radiative corrections at the first order are shown in Fig. 5.4.

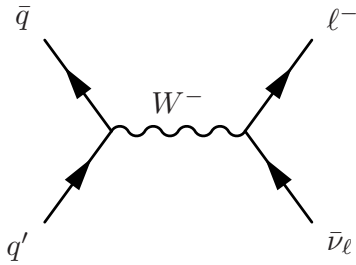


**Figure 5.3:** (top) Feynman diagram contributing to the W boson production at leading order. The charge conjugate production mode is implied. Only the leptonic decay of the W boson is considered.

Perturbative calculations in QCD are limited to processes in which the coupling constant  $\alpha_S$  is small, and by the complexity of higher order calculations preventing their evaluation.

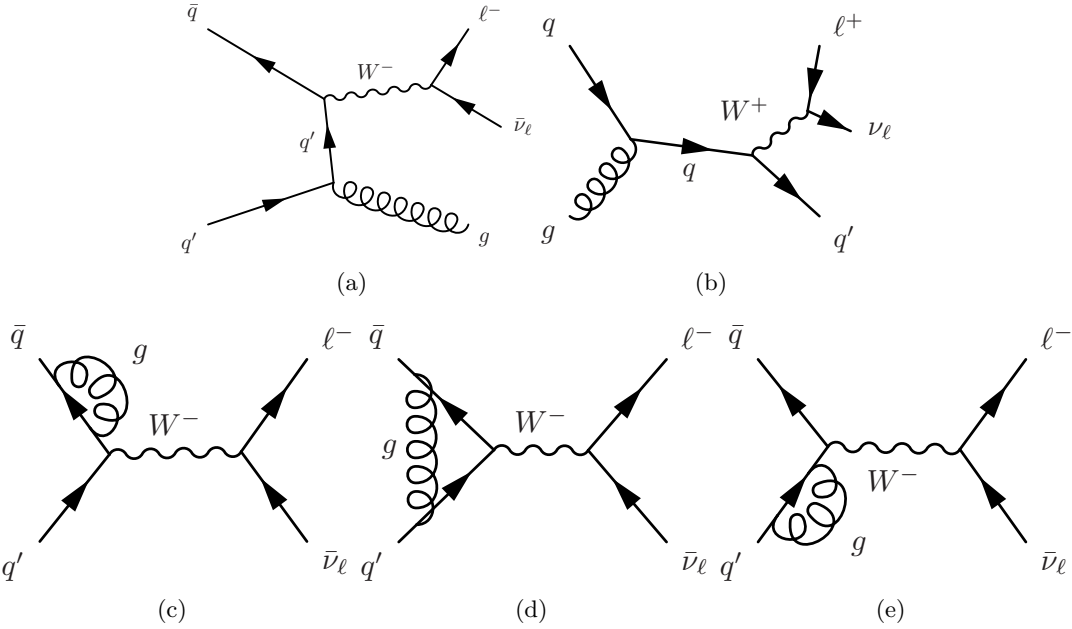


**Figure 5.4:** Feynman diagrams contributing at next-to-leading order to the W boson production and corresponding to the first order real (top) and virtual (bottom) radiative corrections. The charge conjugate production modes are implied. Only the leptonic decay of the W boson is considered.

Consequently, the current generators are only able to treat a limited number of partons in the final state. Parton showering algorithms extend the fixed order calculations beyond these limiting factors by calculating emissions of additional partons from the in- and outgoing partons of the main interaction. This approach in principle takes into account emissions of an unlimited number of partons, but, as opposed to full higher order calculations, does not take into account loop diagrams. Parton showering algorithms start from the hard process allowing the partons to split (or branch) into pairs of other partons. These again may also branch and so on, so that an event then consists of a large number of elementary particles, including quarks and gluons. The cascade of splittings is stopped once the energy scale reaches values where the coupling constant  $\alpha_S$  becomes large.

At this stage, quarks and gluons, which carry colour, cannot be considered as free anymore and recombine to form neutral hadrons, through the so called *hadronization* process. The formation of color-neutral hadrons from the colored partons is treated in phenomenological non-perturbative models. Eventually, many short-lived resonances will be present after hadronization which are then decayed.

The showering and hadronization programs often bring along the possibility to add underlying events. The underlying event arises from the colored remains of the protons that did not take part in the hard collisions, the so-called beam remnants. They are usually included in the hadronization process, because they might be colour-connected to the hard subprocess. The produced hadrons will however carry a very small transverse momentum and will be very forward. The probability for colour reconnection to take place between two partons can also be adjusted based on experimental data. It is also possible that more than one parton interact with the other proton. This phenomenon, called multiple parton interaction, and it is usually added to the description of the process.

As last step the pileup is also accounted for. Additional simulated minimum-bias interactions are added to the generated events to match the additional particle production due to

pileup. The exact number of average collisions per bunch crossing in the data is estimated by multiplying the instantaneous luminosity, continuously monitored, by the total inelastic cross section. One can then reconstruct the distribution of the number of pileup interactions in the data for the complete data taking. The corresponding distributions for the 2012 and 2015 data are shown in Figs. 5.5(a) and 5.5(c), respectively, together with the corresponding simulated pileup scenarios. Simulated events are then reweighted such that they match the data distribution. The description of the pileup by the simulation can be verified by counting the number of reconstructed vertices in the event as illustrated in Figs. 5.5(b) and 5.5(d).

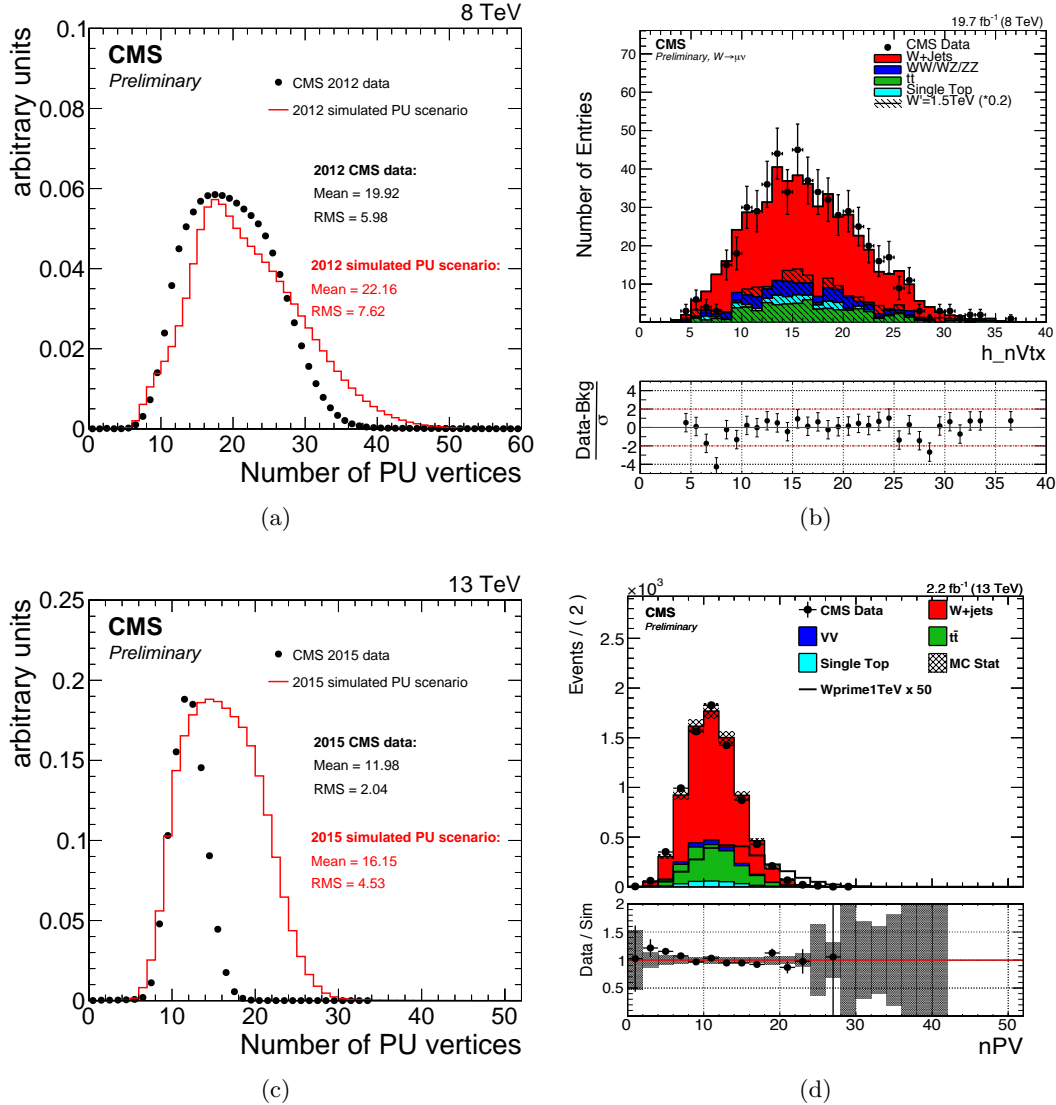


**Figure 5.5:** Distributions of the estimated average number of pileup collisions in the full data set of pp collisions recorded at  $\sqrt{s} = 8$  TeV in 2012 (a) and at  $\sqrt{s} = 13$  TeV (c), together with the corresponding simulated pileup scenarios. Also shown are the distributions of the number of reconstructed primary vertices in 8 TeV (b) and 13 TeV (d) data (black dots) and in various simulated samples after pileup reweighting, for lepton+jet events.

Currently, NLO available calculations included in MC event generators cover a wide range of physics processes, starting with two particles annihilation to a maximum of five

final state objects. A popular generator is PYTHIA [66, 67], a general purpose program which, in addition to the hard process, also takes care of the parton showering, the hadronization, and the description of the underlying event. For the matrix element calculation, PYTHIA only considers the leading order hard subprocess (diagram in Fig. 5.3 for the W production case), and higher order effects are added by “evolving” the event using the parton shower. A more accurate approach is followed by MADGRAPH [68] where the hard real radiative corrections are included in the matrix element (Fig. 5.4). This generator is well suited to study processes such as W or Z produced in association with hard jets. Since it does not completely simulate the events, it needs an additional program, typically PYTHIA, to perform the parton shower after the calculation of the matrix element. It has to be noted that matrix element generators as well as shower and hadronization generators are usually treated independently: the matrix element generators compute the hard process at fixed-order and the parton shower processes the soft and collinear emissions. However, this fails to correctly represent higher order processes in which an additional parton is emitted at the hard scale because parts of this process overlap with the soft one. Combining an NLO matrix element program with a parton shower program therefore leads to double-counting of events. The NLO matrix element generators, such as POWHEG [69] and MC@NLO [70], take special care of the merging of soft and collinear emissions and hard ones.

### 5.1.2 CMS detector simulation

For a detailed understanding on how interactions in pp collisions at the LHC are observed by the CMS detector, a dedicated simulation of the whole detector is needed. Both the propagation of particles through the detector material as well as the response of the active detector components and their digital output need to be simulated. The input to the detector simulation are collections of particles produced by MC event generators. The output is the digital signal from all detector components in the same format that is used for real data.

The CMS simulation is based on the GEANT4 [71] toolkit. The program calculates the trajectory of the various particles generated during the collision, simulates their electromagnetic and hadronic interaction with the crossed material and the signal they will produce in the various subdetectors. The detector geometry is given as an input to the program, and to obtain a description as close as possible to the reality, any available information such as the existence of insensitive materials or dead channels and their position, is included. The electronic readout of the hits produced by particles is simulated, taking into account resolution and detector response effects. The same algorithms as for real data are then used to reconstruct the various physical objects (Chapter 6)

## 5.2 Simulated samples

### 5.2.1 Simulation of signal processes

For the 8 TeV data analysis, the signal hypothesis has been simulated at LO accuracy with a  $W'$  boson produced via quark-antiquark annihilation and decaying into W and Higgs bosons in the  $\ell\nu q\bar{q}$  final state with  $q = b, c$  or  $g$  and  $\ell = e, \mu$  or  $\tau$ . Resonance masses in the range 0.8–2.5 TeV are considered in this analysis. The events are generated at parton level using a model of a generic narrow spin-1  $W'$  resonance implemented with MADGRAPH. Showering and hadronization are performed using PYTHIA6 using the Z2\* tune [72, 73]. It has been verified that the kinematic distributions obtained with the implementation of the generic model agree with those predicted by implementations of the LH, composite Higgs and HVT

models in MADGRAPH. The resonance width differs in the three models, but in each case it is found to be negligible with respect to the experimental resolution.

The full simulation of the detector has been done privately following the standard CMS procedure described in Section 5.1.2. This emulation has been validated comparing the private production with samples from the MC production campaign carried out centrally for the whole collaboration.

The following parameters are used to compute the cross sections:  $g_V = 3$ ,  $c_H \simeq -1$ , and  $c_F \simeq 1$  in the HVT model B (Section 2.3.3) and  $\cot 2\theta = 2.3$ ,  $\cot \theta = -0.20799$  in the LH model, where  $\theta$  is a mixing angle parameter that determines  $W'$  couplings (Section 2.3.2) such that  $\cot 2\theta$  and  $\cot \theta$  can be directly related to  $c_H$  and  $c_F$ .

The intrinsic width and cross section for both models are listed in Table 5.1 for the resonance masses considered. The widths for the HVT model B are computed by means of Eq. 2.64, while the cross sections were obtained using the online tools provided by the authors of the simplified model described in Section 2.3.3.

**Table 5.1:** Intrinsic total widths ( $\Gamma$ ) and cross sections for  $\sqrt{s} = 8$  TeV ( $\sigma$ ) for the LH model and HVT model B for different masses of a resonance  $W'$  decaying to  $WH$ . The  $WH \rightarrow \ell\nu b\bar{b}$  branching fraction is not included in the calculation.

Resonance mass [TeV]	LH model		HVT model B	
	$\Gamma$ [GeV]	$\sigma$ [pb]	$\Gamma$ [GeV]	$\sigma$ [pb]
0.8	7.22	$5.09 \times 10^{-1}$	24.1	$3.37 \times 10^{-1}$
0.9	8.12	$3.03 \times 10^{-1}$	27.1	$2.48 \times 10^{-1}$
1.0	9.02	$1.87 \times 10^{-1}$	30.1	$1.71 \times 10^{-1}$
1.1	9.92	$1.18 \times 10^{-1}$	33.1	$1.16 \times 10^{-1}$
1.2	10.8	$7.65 \times 10^{-2}$	36.1	$8.05 \times 10^{-2}$
1.3	11.7	$5.06 \times 10^{-2}$	39.1	$5.59 \times 10^{-2}$
1.4	12.6	$3.39 \times 10^{-2}$	42.2	$3.88 \times 10^{-2}$
1.5	13.5	$2.29 \times 10^{-2}$	45.2	$2.51 \times 10^{-2}$
1.6	14.4	$1.56 \times 10^{-2}$	48.2	$1.87 \times 10^{-2}$
1.7	15.3	$1.08 \times 10^{-2}$	51.2	$1.30 \times 10^{-2}$
1.8	16.2	$7.43 \times 10^{-3}$	54.2	$9.03 \times 10^{-3}$
1.9	17.1	$5.17 \times 10^{-3}$	57.2	$6.27 \times 10^{-3}$
2.0	18.0	$3.61 \times 10^{-3}$	60.2	$4.25 \times 10^{-3}$
2.1	19.0	$2.53 \times 10^{-3}$	63.2	$3.02 \times 10^{-3}$
2.2	19.8	$1.76 \times 10^{-3}$	66.2	$2.10 \times 10^{-3}$
2.3	20.8	$1.24 \times 10^{-3}$	69.2	$1.46 \times 10^{-3}$
2.4	21.6	$8.67 \times 10^{-4}$	72.2	$1.01 \times 10^{-3}$
2.5	22.6	$6.07 \times 10^{-4}$	75.3	$7.31 \times 10^{-4}$

Figure 5.6 shows the ratio between the resonance's natural width and mass for a  $W'$  in the LH and the HVT model B. The width is less than 5% for the following parameter values:  $0.95 < g_V < 3.76$ ,  $c_H = -1$ , and  $c_F = 1$ ;  $g_V < 3.9$ ,  $c_H = -1$ , and  $c_F = 0$ ; or  $g_V < 7.8$ ,  $c_H = 0.5$ , and  $c_F = 0$ . The widths for the LH model have been computed by means of Eq. 2.61, and they are less than 5% for values of  $0.084 < |\cot \theta| < 1.21$ . Hence, in both models the resonance's natural width can be considered to be negligible compared to the experimental resolution.

For the 13 TeV data analysis, the bulk graviton model and HVT models are used as benchmark signal processes. In these models, a resonance is simulated which decays only to pairs of vector gauge bosons in the  $\ell\nu q\bar{q}^{(\prime)}$  final state, with  $\ell = e, \mu$ , and  $\tau$ . The vector gauge

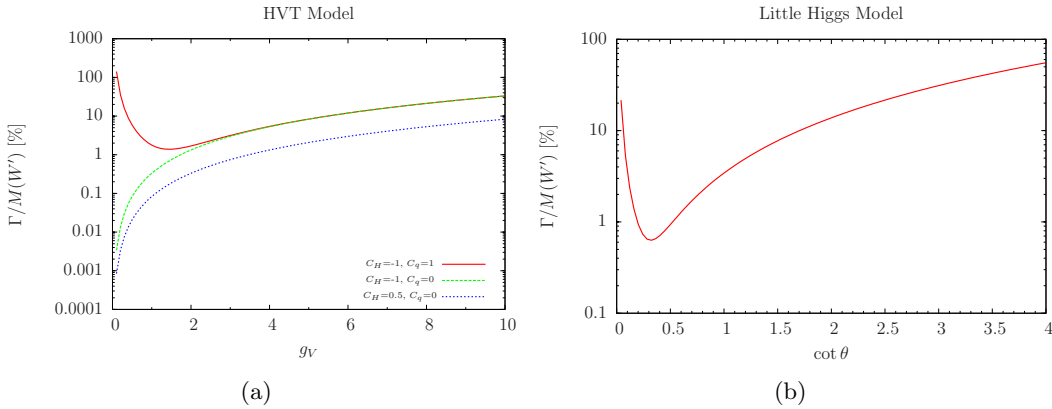


**Figure 5.6:** Ratio between the resonance's natural width and mass for a  $W'$  in the LH and the HVT model B.

bosons are produced with a longitudinal polarization in more than 99% of the cases. For each resonance hypothesis, masses are considered in the range 0.6 to 4.0 TeV. Simulated signal events are generated at LO accuracy with MADGRAPH5\_AMC@NLO with a relative resonance width of 0.1%.

The natural width of a bulk graviton as a function of the curvature parameter  $\tilde{k}$  and for different mass hypotheses is shown in Fig. 5.7. For cases in which  $\tilde{k} \leq 0.5$  the relative width of the graviton resonance ( $\Gamma_G/M_G$ ) is predicted to be below 1%. Hence, it can be neglected when compared to the detector resolution over the whole explored mass range.

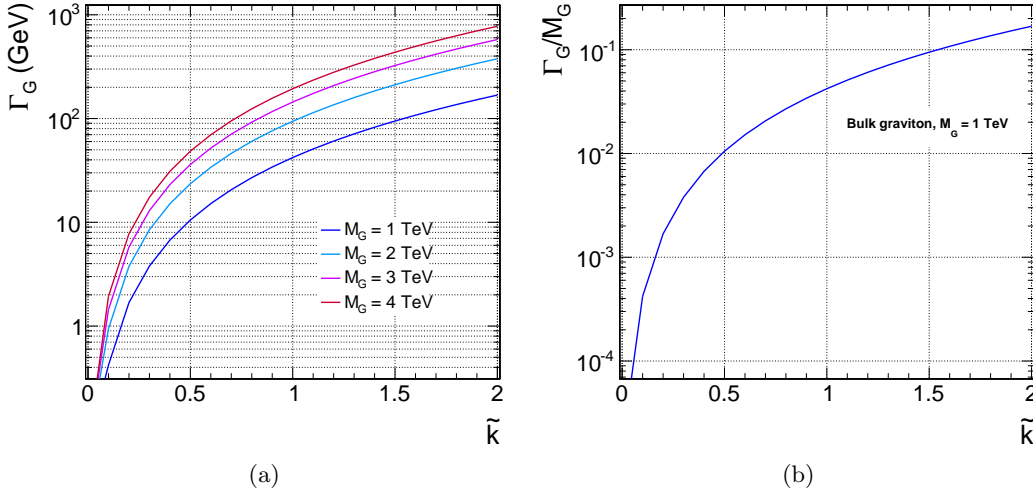


**Figure 5.7:** (a) Natural width of a bulk graviton as a function of the coupling constant  $\tilde{k}$  and for various mass hypotheses. (b) The same dependence is expressed as relative fraction of the signal width with respect to a reference graviton mass of 1 TeV.

Figure 5.8 compare the production cross sections  $\sigma(pp) \rightarrow X$  of the resonance for  $\sqrt{s} = 8$  and 13 TeV, for the bulk graviton with  $\tilde{k} = 0.5$ , and  $W'$  and  $Z'$  in the HVT model B, as a function of the resonance mass. Cross sections for the bulk graviton model are computed with MADGRAPH with the model used for the even generation, while values for the HVT model B are obtained using the online tools provided by the authors of Ref. [41] using the

same parameters as for the 8 TeV data analysis.

For a resonance mass of 2 TeV, the production rates at for  $\sqrt{s} = 13$  TeV are expected to increase of a factor  $\approx 17$  for a resonance produced via gluon-gluon fusion such as the graviton; a smaller factor of  $\approx 7$  is expected instead for resonances produced via quark-antiquark annihilation such as  $W'$  and  $Z'$ .

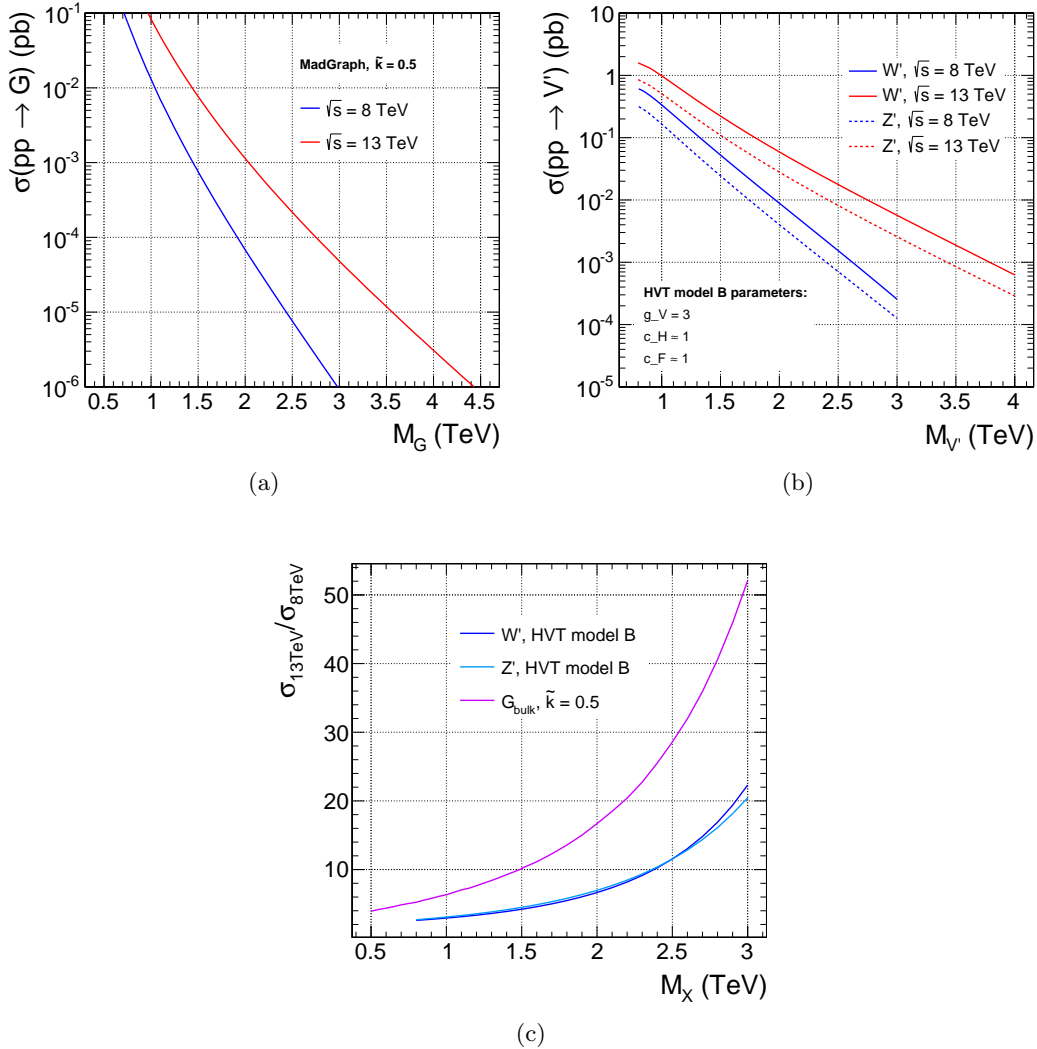


**Figure 5.8:** Comparison of the production cross sections of the resonance for  $\sqrt{s} = 8$  and 13 TeV for the bulk graviton (a), and  $W'$  and  $Z'$  in the HVT model B (b), as a function of the resonance mass. (c) Ratio of the production cross sections for  $\sqrt{s} = 8$  and 13 TeV for all models.

### 5.2.2 Simulation of background processes

For the 8 TeV data analysis, the background is modelled using the MADGRAPH5 v1.3.30 event generator to simulate the production of  $W$  boson in association with jets at LO, the POWHEG 1.0 r1380 package to generate  $t\bar{t}$  and single top quark events at NLO accuracy, and PYTHIA6 v424 for SM diboson ( $WW$ ,  $WZ$ , and  $ZZ$ ) production at LO. All simulated event samples are generated using the CTEQ6L1 PDF set with  $\alpha_S$  also at LO, except for the POWHEG  $t\bar{t}$  sample, for which the CT10 NNLO PDF set is used. All the samples are then processed

further by PYTHIA6, using the Z2\* tune for simulation of parton showering and subsequent hadronization, and for simulation of the underlying event. All simulated background samples are normalized to the integrated luminosity of the recorded data, using inclusive cross sections determined at NLO, or NNLO when available, calculated with the cross section integrators MCFM [74–77] and FEWZ [78], except for the  $t\bar{t}$  sample, for which TOP++ [79] is used. The NNLO cross section for the W+jets process is obtained by rescaling the LO value given by the generator to the NNLO cross section derived from the inclusive production by means of a flat  $k$ -factor = NNLO/LO = 1.3. The simulated samples used in the 8 TeV data analysis described in this work are listed in Table 5.2 together with the corresponding cross sections.

**Table 5.2:** Summary of the MC generated samples for background processes used for the 8 TeV data analysis. The cross sections used to normalize the samples are also indicated.

Process	Cross section (pb)	Generator	PDF set
W+jets, $W \rightarrow \ell\nu, p_T^W > 180 \text{ GeV}$	29.0 (NNLO)	MADGRAPH	CTEQ6L1
$t\bar{t}$ (inclusive)	252.9 (NNLO+NNLL)	POWHEG	CT10
single t quark (t-channel, inclusive)	54.9 (NNLO)	POWHEG	CTEQ6L1
single $\bar{t}$ quark (t-channel, inclusive)	29.7 (NNLO)	POWHEG	CTEQ6L1
single t quark (tW-channel, inclusive)	11.2 (NNLO)	POWHEG	CTEQ6L1
single $\bar{t}$ quark (tW-channel, inclusive)	11.2 (NNLO)	POWHEG	CTEQ6L1
single t quark (s-channel, inclusive)	3.8 (NNLO)	POWHEG	CTEQ6L1
single $\bar{t}$ quark (s-channel, inclusive)	1.8 (NNLO)	POWHEG	CTEQ6L1
WW (inclusive)	54.8 (NLO)	PYTHIA6	CTEQ6L1
WZ (inclusive)	33.2 (NLO)	PYTHIA6	CTEQ6L1
ZZ (inclusive)	8.1 (NLO)	PYTHIA6	CTEQ6L1

For the 13 TeV analysis, the W+jets SM process is simulated with MADGRAPH5\_AMC@NLO at LO accuracy. The  $t\bar{t}$ , single top quark and diboson events are generated with both POWHEG and MADGRAPH5\_AMC@NLO at NLO accuracy. Parton showering and hadronization are implemented through PYTHIA8 using the CUETP8M1 tune [80, 81]. The NNPDF 3.0 PDFs with  $\alpha_S$  at NLO, are used for all simulated samples. The simulated background is normalized using inclusive cross sections calculated at NLO, or NNLO order in QCD where available, using MCFM and FEWZ, except for the  $t\bar{t}$  sample, for which TOP++ [79] is used. A  $k$ -factor = 1.21 is used to rescale the W+jets simulation to the NNLO cross section.

The simulated samples used in the 13 TeV data analysis described in this work are listed in Table 5.3 together with the corresponding cross sections.

### 5.3 Data sets

Two independent data sets are analyzed in this work to search for diboson resonances decaying to two different final states.

The analysis focused on the  $\ell\nu b\bar{b}$  final state is performed with the complete set of data recorded in 2012 by the CMS detector and corresponding to an integrated luminosity of  $19.7 \text{ fb}^{-1}$  of pp collisions at  $\sqrt{s} = 8 \text{ TeV}$ . The recorded events are divided into 4 run periods (runs A, B, C, D).

The second analysis described in this work is focused on the  $\ell\nu q\bar{q}'$  final state and it is performed with only the largest part of the full set of data recorded in 2015 by the CMS

**Table 5.3:** Summary of the MC generated samples for background processes used for the 13 TeV data analysis. The cross sections used to normalize the simulated events are also indicated. The NNPDF 3.0 PDFs are used for all simulated samples

Process	Cross section (pb)	Generator
W+jets, $W \rightarrow \ell\nu$ , $100 < H_T < 200$ GeV	1627.5 (NNLO)	MADGRAPH5_AMC@NLO
W+jets, $W \rightarrow \ell\nu$ , $200 < H_T < 400$ GeV	435.2 (NNLO)	MADGRAPH5_AMC@NLO
W+jets, $W \rightarrow \ell\nu$ , $400 < H_T < 600$ GeV	59.2 (NNLO)	MADGRAPH5_AMC@NLO
W+jets, $W \rightarrow \ell\nu$ , $600 < H_T < 800$ GeV	14.6 (NNLO)	MADGRAPH5_AMC@NLO
W+jets, $W \rightarrow \ell\nu$ , $800 < H_T < 1200$ GeV	6.7 (NNLO)	MADGRAPH5_AMC@NLO
W+jets, $W \rightarrow \ell\nu$ , $1200 < H_T < 2500$ GeV	1.6 (NNLO)	MADGRAPH5_AMC@NLO
W+jets, $W \rightarrow \ell\nu$ , $H_T > 2500$ GeV	0.04 (NNLO)	MADGRAPH5_AMC@NLO
$t\bar{t}$ (inclusive)	831.8 (NNLO+NNLL)	POWHEG
single t quark (t-channel), $W \rightarrow \ell\nu$	44.5 (NNLO)	POWHEG
single $\bar{t}$ quark (t-channel), $W \rightarrow \ell\nu$	26.5 (NNLO)	POWHEG
single t quark (tW-channel, inclusive)	35.9 (NNLO)	POWHEG
single $\bar{t}$ quark (tW-channel, inclusive)	35.9 (NNLO)	POWHEG
single $t+\bar{t}$ quark (s-channel), $W \rightarrow \ell\nu$	3.7 (NNLO)	MADGRAPH5_AMC@NLO
$WW \rightarrow \ell\nu q\bar{q}'$	50.0 (NNLO)	POWHEG
$WZ \rightarrow \ell\nu q\bar{q}$	10.7 (NLO)	MADGRAPH5_AMC@NLO
$ZZ \rightarrow \ell\ell q\bar{q}$	3.22 (NLO)	MADGRAPH5_AMC@NLO

detector corresponding to an integrated luminosity of  $2.3 \text{ fb}^{-1}$  of pp collisions at  $\sqrt{s} = 13 \text{ TeV}$ . During 2015, there have been three running periods labeled from B to D. In fact, after a short period of 50 ns operation (period B), the machine collected data with a bunch spacing of 25 ns (period C and D). However, since the first two periods only add a tiny contribution to the total integrated luminosity of 2015 collisions, the decision was made to base the analysis on period D only, corresponding to the largest data set.

All events that are accepted by a specific set of high level triggers enter one specific data set, so that the choice of a trigger for the analysis defines which data set has to be used. As discussed in the next chapter (Sections 6.3.2 and 6.2.2), events are collected with a trigger requiring either one muon or one electron passing given  $p_T$  and  $\eta$  selections. Hence, the data sets used in these analyses are the so called “SingleMuon” and ”SingleElectron” primary data sets listed in Table 5.4.

Even though stable run periods are chosen for the analyses, not all runs can be used. This analysis requires the whole detector to be functional since the objects employed are reconstructed from all parts of the detector as described in the next chapter. Therefore, only data-taking runs and luminosity blocks during which the detector was in a state sufficiently good for further analysis are used.

**Table 5.4:** Data sets used in this analysis.

$\sqrt{s}$	Year	Data set	Run period	Run range	$\mathcal{L} [\text{pb}]^{-1}$
8 TeV	2012	SingleMuon	A	190456–193621	889.362
			B	193833–196531	4424
			C	198022–203742	7144
			D	203777–208686	7307
		Total	190456–208686	19764	
	2012	SingleElectron	A	190456–193621	889.362
			B	193833–196531	4422
			C	198022–203742	7080
			D	203777–208686	7314
		Total	190456–208686	19705	
13 TeV	2015	SingleMuon	D	256630–260627	2320
		SingleElectron	D	256630–260627	2320

# Object and event reconstruction

---

In the pp collisions at the LHC a large number of particles are produced which must be properly reconstructed and identified. These particles travel through the CMS detector and they are classified in objects depending on their specific signature in each subdetector. This chapter covers the reconstruction of physics objects that are needed for the identification of signal events in the lepton plus jet event topology described in Chapter 4.

The measurement of a track in the tracker detector for charged particles and the reconstruction of the primary vertices represent key aspects of the reconstruction of the various objects and are detailed in Section 6.1. In this analysis  $\tau$  leptons are reconstructed as electrons (Section 6.2) or muons (Section 6.3) and accounted to the respective channel if they decay leptonically, or as jets (Section 6.4) if they decay hadronically. However, only the leptonic decay mode contributes to the analysis since at least one muon or electron has to be reconstructed in the event. In addition to leptons and jets, the last type of particle present in the final state is the neutrino, whose presence can be inferred from an imbalance of the transverse energy (Section 6.5). The identified lepton and the missing transverse energy in the event are associated with the  $W \rightarrow \ell\nu$  candidate which is entirely reconstructed through the algorithm described in Section 6.6.

## 6.1 Tracks and vertices

The reconstruction of tracks of charged particles allows for their momentum measurement and aids in particle identification as described in the following. The reconstruction of the tracks' vertices is important to distinguish the primary interaction, i.e. the hard interaction, from additional interactions that might take place in the event and also for the identification of secondary vertices of jets that contain c or b quarks called c-/b-tagging (see Sec. 6.4.3).

### 6.1.1 Track reconstruction

The track reconstruction at CMS [82] is based on information coming from the silicon tracker system. A charged particle passing through a tracker layer can in general induce a signal in more than one pixel or more than one strip. The first step of the tracking procedure is the assembly of nearby tracker channels into one hit cluster. The particle position and its uncertainty is then inferred from the relative signal amplitudes in each channel.

Because of the magnetic field, charged particles travel through the tracking detectors on a helix trajectory which is described by 5 parameters: the curvature  $k$ , the track azimuthal angle  $\phi$  and polar angle  $\theta$ , the signed transverse impact parameter  $d_0$  and the longitudinal impact parameter  $z_0$ . The transverse (longitudinal) impact parameter of a track is defined as the transverse (longitudinal) distance of closest approach of the track to the primary vertex.

The trajectories of charged particles are reconstructed through a iterative procedure consisting in multiple iterations of the *Combinatorial Track Finder algorithm* (CTF) [83], which uses the reconstructed hits in the silicon detectors to determine the track parameters. In the first iterations the algorithm searches for tracks of relative large  $p_T$  and produced near the interaction region. Then, hits associated to high quality tracks are iteratively removed

from the input list to reduce the combinatorial complexity of the next iterations, and to allow the more difficult reconstruction of low  $p_T$  or displaced tracks. Each iteration of the CTF algorithm is made of four steps: track seeding, track finding and track fitting.

In the first step, a first estimate of the helix parameters and of its covariance matrix is provided using only pairs or triplets of hits compatible with the hypothesis of a track coming from the pp interaction region. Track candidates are best seeded from hits in the pixel detector because of the low occupancy, high efficiency and unambiguous 3-dimensional position information.

The track finding stage associates new hits in the next tracker layers to the trajectory obtained from seeds using a standard Kalman Filter (KF) pattern recognition approach [84,85], which takes into account the effect of multiple scattering in the tracker layers. The current trajectory is extrapolated to the next tracker layer and compatible hits are assigned to the track on the basis of the  $\chi^2$  between the predicted and measured positions. In case multiple compatible hits are found when extrapolating the helix to a single layer, the algorithm creates one trajectory candidate for each hit and they are propagated independently. Furthermore, in order to take into account possible inefficiencies, one additional candidate is created without including any hit information. A quality index is assigned to the tracks, based on the  $\chi^2$ , the number of missing hits, and how compatible they are with originating from a primary interaction vertex. Only the best quality tracks are kept for further propagation and ambiguities are resolved between tracks during and after track finding. In case two tracks share more than 50% of their hits, the lower quality track is discarded. The fake rate, defined as the fraction of reconstructed tracks not associated with a charged particle, is substantially reduced by these quality requirements.

For each trajectory the finding stage results in an estimate of the track parameters. However, since the full information is only available at the last hit and constraints applied during trajectory building can bias the estimate of the track parameters, all valid tracks are refitted using the KF to determine the most accurate estimate of the helix parameters. The usual fit starting from the interaction point to the end of the tracker is complemented with a second fit running backward from the outermost tracker layer to the interaction point. This approach is found to improve the accuracy of the  $p_T$  and impact parameter measurement by 0.5% and 1%, respectively.

The performance of the track reconstruction is shown in Fig. 6.1 for simulated muons, electrons and pions. For isolated muons with  $1 < p_T < 100 \text{ GeV}$ , the track reconstruction efficiency is  $> 99\%$  over the full  $\eta$ -range of tracker acceptance, and does not depend on  $p_T$  (Fig. 6.1(a)). The fake rate is completely negligible. For pions and electrons the efficiency is in general lower along with a higher fake rate because of interactions with the material in the tracker. The material budget of the CMS tracker in units of radiation length is presented in Fig. 6.2.

In Fig. 6.3(a) the transverse momentum resolution for muon tracks with  $p_T = 1, 10$ , and  $100 \text{ GeV}$  is shown. At high transverse momentum ( $100 \text{ GeV}$ ), the resolution is 2–3% up to  $|\eta| = 1.6$ . The material of the tracker accounts for 20–30% of the transverse momentum resolution. At lower momenta, the resolution is dominated by multiple scattering and its distribution reflects the amount of material traversed by the track. The resolutions of the track impact parameter in the transverse and longitudinal plane are also shown in Fig. 6.3. At high momentum the transverse impact parameter resolution is fairly constant and is dominated by the hit resolution in the first pixel layer. It is progressively degraded by multiple scattering at lower momenta. The same applies to the longitudinal impact parameter resolution. The improvement of the  $z_0$  resolution up to  $|\eta| = 0.5$  is due to the charge sharing

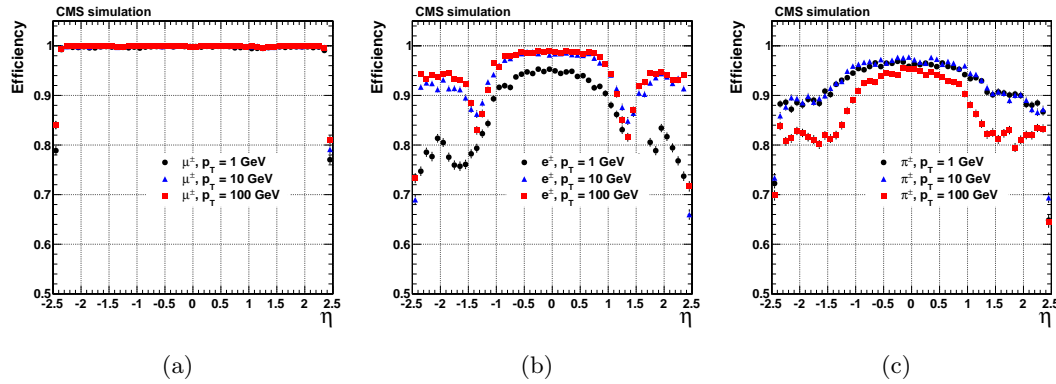


**Figure 6.1:** Track reconstruction efficiency for simulated muons (a), electrons (b), and pions (c) passing the high-purity quality requirements as a function of  $\eta$  and for  $p_T = 1, 10$ , and  $100$  GeV [82].

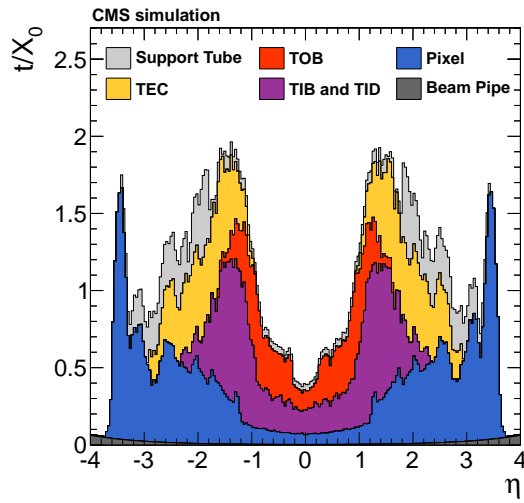


**Figure 6.2:** Material budget of the CMS tracker in units of radiation length  $X_0$  as a function of pseudorapidity divided into the contributions of the different subdetectors [82].

effects among neighboring pixels.

### 6.1.2 Vertex reconstruction

The identification of vertices is essential to distinguish the primary vertex associated with the hard interaction from additional pileup vertices that might be present in the event. This became even more important at the highest LHC luminosity reached at the end of 2016 where an average of 25 pp interactions took place simultaneously.

In the primary-vertex reconstruction [86], the measurements of the location and uncertainty of an interaction vertex are computed from a given set of reconstructed tracks. The prompt tracks originating from the primary interaction region are selected based on the transverse impact parameter significance with respect to the beam line, number of strip and pixel hits, and the normalized track  $\chi^2$  from a fit to the trajectory. The selected tracks are then clustered on the basis of their  $z$ -coordinates at their point of closest approach to the center of the beam spot using a *deterministic annealing* (DA) algorithm [87]. This clustering allows for the

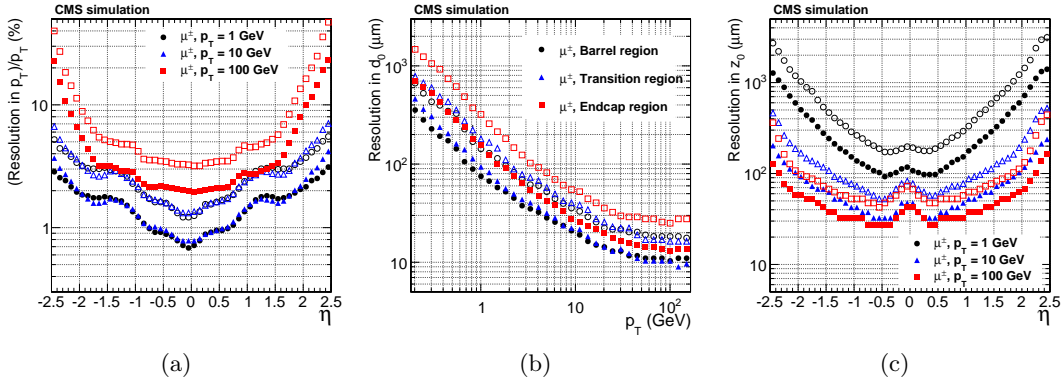


**Figure 6.3:** Resolution of track transverse momentum (a), transverse (b) and longitudinal (c) impact parameter for simulated muons passing the high-purity quality requirements as a function of  $\eta$  and for  $p_T = 1, 10$ , and  $100 \text{ GeV}$  [82].

reconstruction of any number of pp interactions in the same LHC bunch crossing. Vertices are resolved with separations of about 1 mm, appropriate for a multiplicity of interactions per bunch crossing up to 20, as the longitudinal RMS spread of the luminous region is about 6 cm.

After identifying candidate vertices based on the DA clustering in  $z$ , those candidates containing at least two tracks are then fitted using an *adaptive vertex fitter* [88], to compute the best estimate of vertex parameters, including its  $x$ ,  $y$ , and  $z$  position, and covariance matrix. This algorithm addresses the issue of secondaries and fake tracks in the cluster by iteratively down-weighting the tracks which are not compatible with the fitted common vertex. The primary vertex, where the hard process of interest takes place, is chosen as the vertex with the highest sum of  $p_T^2$  of the clustered tracks.

The primary vertex spatial resolution depends on the event topology and on the number of tracks related to the vertex, as shown in Fig. 6.4. For minimum-bias events, the resolutions in  $x$  and  $z$  are, respectively, less than  $20 \mu\text{m}$  and  $25 \mu\text{m}$ , for primary vertices reconstructed using at least 50 tracks. The resolution is better for the jet-enriched sample where tracks have significantly higher mean  $p_T$  resulting in higher resolution in the track impact parameter, and consequently better vertex resolution. For these events, the resolutions approach  $10 \mu\text{m}$  in  $x$  and  $12 \mu\text{m}$  in  $z$  for primary vertices using at least 50 tracks.

In the analysis described in this work, all events are required to have at least one primary vertex reconstructed within a 24 cm window along the beam axis, with a transverse distance from the nominal pp interaction region of less than 2 cm.

## 6.2 Electrons

### 6.2.1 Electron reconstruction

The electron reconstruction in CMS [90] is based on the association of an energy deposit in the ECAL with a track reconstructed in the silicon tracker system. Electrons lose energy primarily through bremsstrahlung when interacting with the tracker layers, and consequently they suffer from large energy losses. Given the non-Gaussian properties of the energy loss distributions, the standard track reconstruction algorithm based on the KF is not appropriate

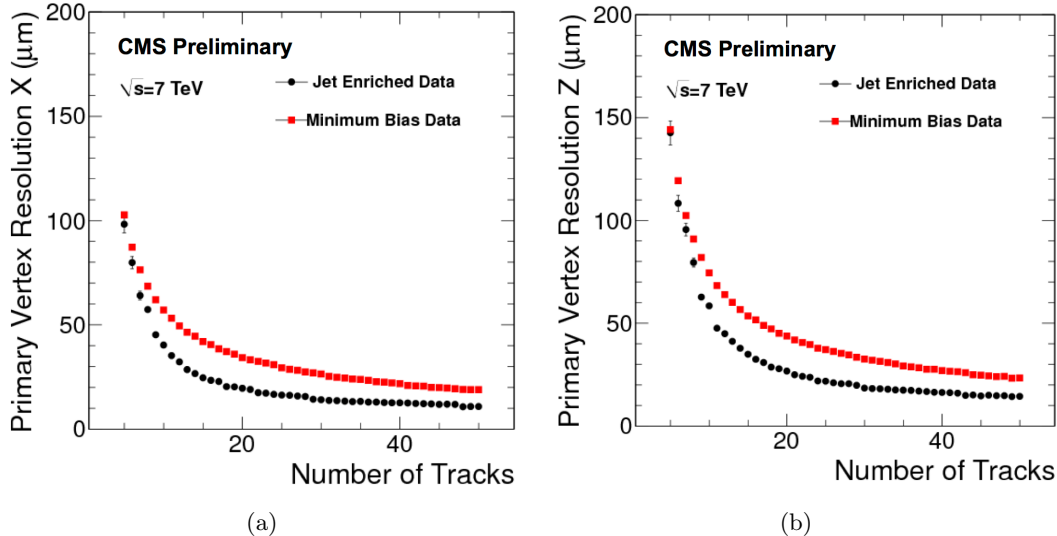


**Figure 6.4:** Primary-vertex resolution in  $x$  (a) and  $z$  (b) as a function of the number of tracks at the fitted vertex, for two kinds of events with different average track  $p_T$  values. The results in  $y$  are almost identical to the one in  $x$  [89].

and leads in general to a reduced hit-collection efficiency, as well as to a poor estimation of track parameters. A better performance for electron reconstruction is achieved by using dedicated techniques that make use of information, not only from the tracker, but also from the ECAL, as described in the following.

The electron reconstruction starts by searching for clusters of energy in the ECAL. As the electrons are degraded in energy, the effect of the magnetic field is to enhance the bending of their trajectories, resulting in a spread of irradiated photons along the  $\phi$  coordinate. To recover this radiated energy, ECAL superclusters are formed, by merging clusters of similar  $\eta$  over some range of  $\phi$ . Because of the different geometry of the detector in barrel and endcap, different clustering algorithms are used in different regions.

For the electron track reconstruction two approaches are used. In the first one, referred to as “ECAL driven”, the supercluster energy and position, and the assumption that the electron originated near the center of the beam spot, are used to extrapolate the electron trajectory in the tracker. Tracker seeds compatible with the predicted trajectory are sought in the first or second layer of the pixel detector (and also in the TEC to improve efficiency in the forward region). This method is designed for isolated electrons with  $p_T > 5 \text{ GeV}$ .

A second approach, referred to as “tracker driven”, complements the electron track reconstruction, especially for low- $p_T$  or non isolated electrons, as well as for electrons in the barrel-endcap transition region. This method is developed as part of the particle-flow (PF) reconstruction algorithm [91, 92] described in Section 6.4.2. It takes the standard track collection reconstructed with the KF algorithm and attempts to identify a subset of these tracks that are compatible with being electrons. Electrons that suffer only little bremsstrahlung loss can be identified by searching for tracks extrapolated to the ECAL that pass close to an ECAL PF cluster. Electrons that suffer large bremsstrahlung loss can be identified by the fact that the fitted track will often have poor  $\chi^2$  or few associated hits. The track seeds originally used to generate these electron-like tracks are retained.

The seed collections obtained by using these two methods are merged, and used to initiate electron track finding. This procedure is similar to that used in standard tracking, except

that the  $\chi^2$  threshold, used by the KF to decide whether a hit is compatible with a trajectory, is weakened. This is to accommodate tracks that deviate from their expected trajectory because of bremsstrahlung.

To obtain the best estimate of the track parameters, the final track fit is performed using a modified version of the KF method, called the Gaussian Sum Filter (GSF) [93]. The fractional energy loss of an electron, as it traverses a layer of material, follows a Bethe–Heitler distribution. This distribution is non-Gaussian, making it unsuitable for use in a conventional KF algorithm. The GSF technique solves this by approximating the Bethe–Heitler energy-loss distribution as the sum of several Gaussian functions. This method is then a generalization of the KF where the trajectory in each tracker layer is described by a weighted sum of KF components for which the energy loss follows a Gaussian law with a given width. The propagation of each component is done separately from one layer to another and the weights are then updated given the measurement in the new site. The allowed window to search for a hit in the next tracker layer is larger than for the usual KF track. This procedure is iterated until the last tracker layer, unless no hit is found in two subsequent layers. A minimum of five hits is finally required to create a track. A GSF electron candidate is finally built by associating an ECAL supercluster with a GSF track with compatible  $\eta$  and  $\phi$  positions.

The electron transverse energy  $E_T$  is equal to the transverse energy of the correspondent ECAL energy deposit (or supercluster)  $E_T^{\text{SC}}$ , and defined as  $E_T = E \sin \theta$ , where  $\theta$  is the polar angle of the supercluster (ST) relative to the beam axis, and  $E$  the energy measured in the supercluster.

The performance of the GSF electron reconstruction are studied using a “tag-and-probe” (T&P) method [94]. The method uses a known SM resonance mass and decay (e.g.  $Z \rightarrow e^+ e^-$ ) to select particles of the desired type and probe the efficiency of a particular selection criterion on those particles. In general the “tag” is an object that passes a set of very tight selection criteria designed to isolate the required particle type (in this case an electron, though the method is not strictly limited to this case). A generic set of the desired particle type (i.e. with potentially very loose selection criteria) known as “probes”, is selected by pairing these objects with tags such that the invariant mass of the combination is consistent with the mass of the resonance. Combinatorial backgrounds are usually eliminated through a variety of background subtraction methods. The definition of the probe object depends on the specifics of the selection criterion being examined. The efficiency itself is measured by counting the number of “probe” particles that pass the desired selection criteria. It is found that the estimated efficiencies are almost insensitive to any specific definition of the tag. The GSF electron reconstruction efficiency measured with this method is above 95% for electrons in the ECAL barrel with  $E_T > 35 \text{ GeV}$ , as shown in Fig. 6.5(a). Slightly lower efficiencies are obtained for electrons reconstructed in the ECAL endcaps (Fig. 6.5(b)). A good agreement is found between data and simulation, resulting in scale factors consistent with unity almost in the entire range. The performance are presented here for the electron reconstruction in Run 1 but similar results are obtained in CMS for Run 2.

Once a GSF electron candidate is reconstructed, the energy measurement provided by electromagnetic calorimeter can be combined with the tracker momentum measurement to improve the estimate of electrons with energies below 35 GeV as shown in Fig. 6.6. At energies above 35 GeV however, the momentum measurement is completely driven by the supercluster.

### 6.2.2 Electron trigger

As explained in Section 3.2.4, the events of interest for physics analyses are selected by the trigger system in two steps, namely, the L1 and HLT. At the L1, where the tracker information

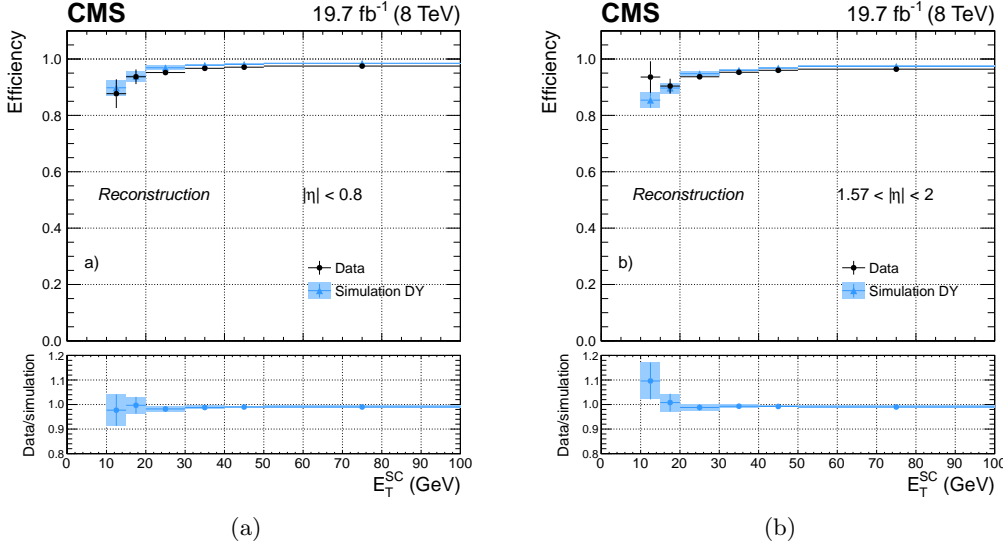


**Figure 6.5:** Electron reconstruction efficiency measured in dielectron events in data (dots) and Drell-Yan simulation (triangles), as a function of the  $E_T$  for electrons reconstructed in the ECAL barrel (a) and endcaps (b). The bottom panels show the corresponding data-to-simulation scale factors [95].

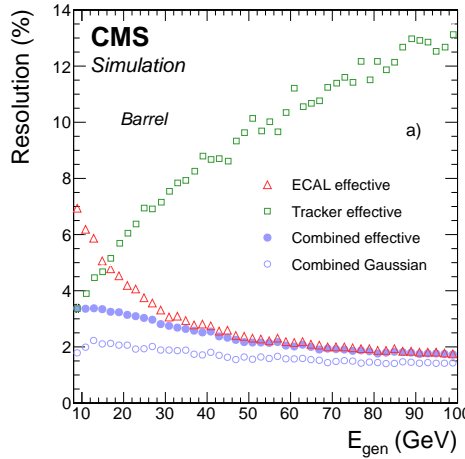


**Figure 6.6:** Expected resolution in  $E_T$  for isolated electrons in the ECAL barrel as a function of the electron generated energy, obtained from the ECAL, the tracker and the combined estimates [95].

is not available, electrons and photons are indistinguishable and based on calorimeter trigger towers, consisting, in the barrel, of a  $5 \times 5$  matrix of ECAL crystals and the corresponding HCAL tower, while a more complex definition of the tower is used in the endcaps. A L1 candidate is formed combining the highest-energy central trigger tower together with its next-highest adjacent tower. At this stage, the trigger choice is based on the energy distribution among the central and neighbouring towers, on the amount of energy in the HCAL downstream the central tower, and on the  $E_T$  of the  $e/\gamma$  candidate. Events passing L1 are then filtered by the HLT. Here, the pixel tracker information is used to separate electrons from photons. The starting point of any electron HLT selection consists of building

a supercluster and a trajectory as described in Section 6.2.1. Many different triggers involving electrons are designed at the HLT level and various additional identification and isolation requirements on the electrons are made for each of them. They consist of conditions on:

- transverse profile of the cluster of energy in the ECAL;
- the amount of energy in the HCAL downstream the ECAL cluster;
- the existence of a KF or GSF track matching the supercluster position;
- quality of association between the track and the ECAL cluster;
- activity in the ECAL, HCAL, or tracker around the candidate.

The conditions used and their severity depend on the number of electrons requested by the trigger and their transverse energy threshold, each trigger being designed to have a rate of accepting events of 50 Hz or less. Practically, all the HLT steps and criteria involving only calorimeters information are done first, while the time consuming steps involving track reconstruction are only performed at the end for events passing the previous criteria. The L1 and HLT triggers used to collect the data analyzed in this thesis are listed in Tables 6.1 and 6.2 for the 8 and 13 TeV data sets, respectively. The tables also detail the conditions imposed on several variables described in Section 6.2.3. Figure 6.7 shows the L1 trigger efficiencies for different  $E_T$  thresholds as a function of the electron  $E_T$ . The curves exhibit the typical turn on behaviour in correspondence of the imposed  $E_T$  threshold.

**Table 6.1:** The L1 and HLT single-electron triggers used to collect the 8 TeV data analyzed in this thesis together with the imposed requirements on the electron candidate.

Trigger	Name	Selections
Level 1	L1_SingleEG20	1 e/ $\gamma$ candidate $E_T > 20$ GeV
HLT	HLT_Ele80_CaloIdVT_GsfTrkIdT OR L1_SingleEG40	1 GSF electron: $E_T > 80$ GeV $ \Delta\eta_{in}  < 0.008$ $ \Delta\phi_{in}  < 0.07$ (barrel) or 0.05 (endcaps) $H/E < 0.05$ $\sigma_{i\eta i\eta} < 0.011$ (barrel) or 0.031 (endcaps)

**Table 6.2:** The L1 and HLT single-electron triggers used to collect the 13 TeV data analyzed in this thesis together with the imposed requirements on the electron candidate.

Trigger	Name	Selections
Level 1	L1.SingleEG35 OR L1.SingleEG40	1 e/ $\gamma$ candidate $E_T > 35$ GeV OR $E_T > 40$ GeV
HLT	HLT_Ele105_CaloIdVT_GsfTrkIdT OR HLT_Ele115_CaloIdVT_GsfTrkIdT	1 GSF electron: $E_T > 105$ GeV OR $> 115$ GeV $ \Delta\eta_{in}  < 0.008$ $ \Delta\phi_{in}  < 0.07$ (barrel) or 0.05 (endcaps) $H/E < 0.05$ $\sigma_{i\eta i\eta} < 0.011$ (barrel) or 0.031 (endcaps)

Both the L1 and HLT triggers require one electron (or  $\gamma$ ) candidate. The  $E_T$  thresholds imposed for the data collected in pp collisions at 13 TeV are higher compared to the one used

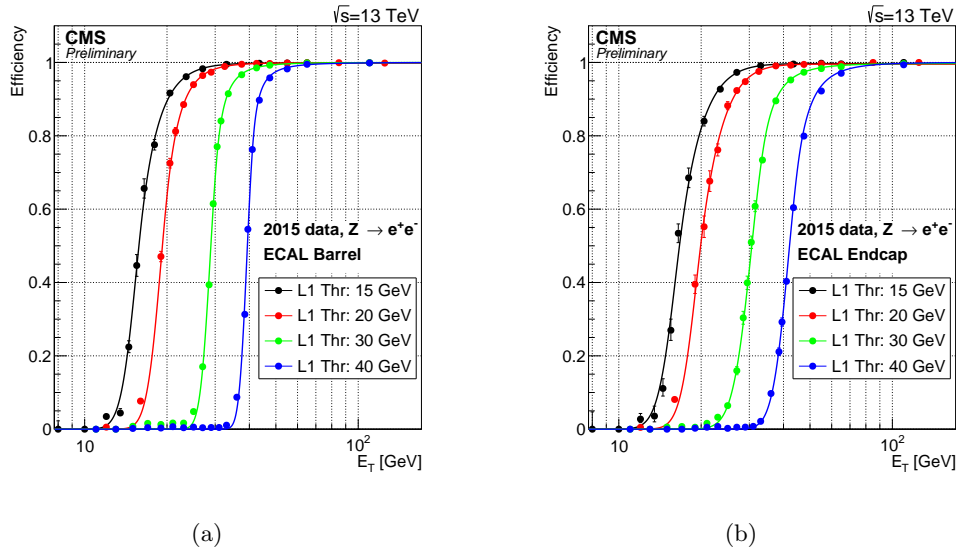


**Figure 6.7:** L1 electron triggering efficiency in ECAL barrel (a) and endcaps (b) as a function of the offline reconstructed electron  $E_T$ . The efficiency is shown for the 15, 20, 30, 40 GeV EG trigger thresholds [96].

in Run 1, in order to keep low trigger rates given the higher production rates of low-energy multijet background expected in Run 2. The chosen HLT triggers require a reconstructed GSF track whose association to the ECAL cluster has to pass tight quality criteria ( $|\Delta\eta_{in}|$  and  $|\Delta\phi_{in}|$ ). Requirements are also applied at this level on the transverse profile of the cluster of energy in the ECAL ( $\sigma_{in in}$ ) and on the amount of energy in the HCAL downstream the ECAL ( $H/E$ ). There are no requirements imposed on the electron candidate isolation. In general, this results in high fake rates of jets misreconstructed as electrons from multijet background, and, as a consequence, in high trigger rates which would require a prescale. However, the high  $E_T$  threshold allows for an unprescaled trigger, as jets from multijet background are characterized by low momentum. In addition, the kinematic region of the analyses presented in this thesis is located at very high lepton  $p_T$  and the signal efficiency is mainly affected at very low resonance masses ( $< 1 \text{ TeV}$ ) with a loss in efficiency of 20–25%.

The efficiency for an electron passing the high- $E_T$  selections described in Sec. 6.2.3 to fire the HLT triggers of Tables 6.1 and 6.2 have been measured in data with T&P method and are found to be 98–99% for electrons with  $E_T$  in the trigger plateau, with data-to-simulation scale factors close to unity.

### 6.2.3 Electron identification

All the physics analyses in CMS involving one or two electrons in the final state start with the general electron reconstruction algorithm presented in Section 6.2.1. A high efficiency in any kinematical conditions is therefore needed and, as a consequence, the probability for other particles to be reconstructed as electrons is sizeable. For instance, a charged pion can mimic the signature of an electron if it interacts early and leaves most of its energy in the ECAL. Moreover electrons can emerge in a jet through the weakly decay of a hadron containing a c or b quark. Finally, in addition to jets, photons can also lead to GSF electron candidates. This happens if the photon converts into a dielectron pair in one of the first layers of the tracker detector. If one of the electron takes most of the photon momentum, a GSF electron

candidate is likely to be reconstructed. An analysis dependent selection, which takes into account the specific kinematics and background level, has therefore to be applied on top of the electron reconstruction. This thesis focuses on the search for massive resonances decaying to pairs of SM bosons where one of the bosons is a W decaying leptonically, with a highly energetic electron or muon in the final state. A high and stable selection efficiency for  $E_T$  above 100 GeV is therefore an important requirement. Since this is a common feature of many searches for new physics, a specific cut based selection has been developed in CMS [97], consisting of requirements on several variables that exploit the characteristics of high- $E_T$  electrons. Only GSF electron candidates with  $E_T > 35$  GeV and well reconstructed in the tracker and ECAL sensitive regions are selected. Candidates in the ECAL transition region ( $1.442 < |\eta_{SC}| < 1.56$ ) and beyond the  $\eta$  coverage ( $|\eta_{SC}| > 2.5$ ) of the tracker are therefore discarded. A different selection is applied for candidates reconstructed in the ECAL barrel ( $|\eta_{SC}| < 1.442$ ) and endcaps ( $1.56 < |\eta_{SC}| < 2.5$ ). For Run 2 the values of  $\eta_{SC}$  have been slightly adjusted to match the acceptance of the detector more accurately. The selections are summarized in Tables 6.3 and 6.4, for the 8 and 13 TeV data analysis, respectively, and discussed in the following.

**Table 6.3:** List of the variables used in the high- $E_T$  electron selections for the 8 TeV data analysis, together with the corresponding requirements for electrons reconstructed in the ECAL barrel and endcaps.

Variable	ECAL barrel	ECAL endcaps
ECAL-driven	yes	yes
$E_T$	$> 35$ GeV	$> 35$ GeV
$ \eta_{SC} $	$< 1.442$	$1.56\text{--}2.5$
$ \Delta\eta_{in} $	$< 0.005$	$< 0.007$
$ \Delta\phi_{in} $	$< 0.06$	$< 0.06$
Relative track isolation	5%	5%
Calorimeter isolation	$< 2 + 0.03E_T + 0.28\rho$	$< 2.5 + 0.28\rho$ if $E_T < 50$ $< 2.5 + 0.03(E_T - 50) + 0.28\rho$ if $E_T \geq 50$
Transverse shower shape	$E_{2\times 5}/E_{5\times 5} > 0.94$ OR $E_{1\times 5}/E_{5\times 5} > 0.83$	$\sigma_{in\eta} < 0.03$
$H/E$	$< 0.05$	$< 0.05$
$ d_{xy} $	$< 0.02$	$< 0.05$
Inner layer lost hits	$\leq 1$	$\leq 1$

As a starting point, electrons are selected if the reconstruction was seeded in the ECAL (Section 6.2.1). In fact, while useful for low-energy and non-isolated electrons, the PF algorithm is less suitable for high-energy electrons.

The difference in  $\eta$ ,  $\Delta\eta_{in}$ , and in  $\phi$ ,  $\Delta\phi_{in}$ , between the track position as measured in the inner layers, extrapolated to the interaction vertex and to the calorimeter, and the position of the supercluster, are required to be  $< 0.005$  and  $< 0.06$ , respectively. In fact, for jets, the position of the center of the ECAL deposit can be far from the track position, as all of the constituents can leave an energy deposit in the ECAL. The  $\Delta\phi_{in}$  distribution is however much broader than  $\Delta\eta_{in}$ , because of the wider spread of the energy in  $\phi$  due to photons from bremsstrahlung, resulting in a looser requirement. The distributions of  $\Delta\phi_{in}$  and  $\Delta\eta_{in}$  become narrower with increasing  $E_T$ , and therefore a higher discrimination power can be achieved with a tighter requirement at high  $E_T$  compared to the usual selections for low or intermediate energetic electrons. The reason of this behaviour comes from the fact that bremsstrahlung photons are more collinear to the electron at higher  $E_T$ . The definition of  $\Delta\eta_{in}$  has been changed for Run 2 to use instead the  $\eta$  of the seed cluster of the supercluster

**Table 6.4:** List of the variables used in the high- $E_T$  selections for the 13 TeV data analysis, together with the corresponding requirements for electrons reconstructed in the ECAL barrel and endcaps.

Variable	ECAL barrel	ECAL endcaps
ECAL-driven	yes	yes
$E_T$	$> 35 \text{ GeV}$	$> 35 \text{ GeV}$
$ \eta_{SC} $	$< 1.4442$	$1.566\text{--}2.5$
$ \Delta\eta_{in} $	$< 0.004$	$< 0.006$
$ \Delta\phi_{in} $	$< 0.06$	$< 0.06$
Relative track isolation	5%	5%
Calorimeter isolation	$< 2 + 0.03E_T + 0.28\rho$	$< 2.5 + 0.28\rho \text{ if } E_T < 50$ $< 2.5 + 0.03(E_T - 50) + 0.28\rho \text{ if } E_T \geq 50$
Transverse shower shape	$E_{2\times 5}/E_{5\times 5} > 0.94$ OR $E_{1\times 5}/E_{5\times 5} > 0.83$	$\sigma_{i\eta i\eta} < 0.03$
$H/E$	$< 1/E + 0.05$	$< 5/E + 0.05$
$ d_{xy} $	$< 0.02$	$< 0.05$
Inner layer lost hits	$\leq 1$	$\leq 1$

which is found to provide a more accurate indication of the  $\eta$  of the original electron before bremsstrahlung.

To suppress the misidentification of jets as electrons, the sum of the  $p_T$  of all other tracks in a cone of  $\Delta R < 0.3$  around the track of the electron candidate is required to be less than 5 GeV, imposing an isolation condition on the electron candidate track. To be used in the calculation of the isolation of the candidate track, the tracks have to be within 0.2 cm, in the  $z$  direction, of the primary vertex with which the electron candidate is associated. This requirement reduces the impact of pileup and it does not show a dependency with the electron  $E_T$  for values above 100 GeV. For electrons with  $E_T$  much lower than 100 GeV, the efficiency decreases up to 10% depending on the region of the detector in which the electrons are detected.

A calorimeter-based isolation is applied and defined as the sum of:

- ECAL isolation: sum of the  $E_T$  of the energy deposits in the ECAL calorimeter in a cone of  $\Delta R < 0.3$  around the track of the electron candidate excluding those associated with the candidate;
- HCAL1 isolation: sum of the  $E_T$  of the energy deposits in the first layer of the HCAL calorimeter in a cone of  $\Delta R < 0.3$  around the track of the electron candidate excluding those associated with the candidate.

The isolation variable so defined, is required to be less than 3% (plus a small  $\eta$ -dependent offset) of the candidate  $E_T$ . This sum, which allows a selection on the isolation of the electron candidate, is corrected for the average energy density in the event,  $\rho$ , to minimize the dependence of the efficiency of this selection criterion on pileup. This requirement differs from the selection usually applied for electrons of low or intermediate  $E_T$ . For these cases, a PF-based isolation is generally used, which merges the information of the tracker, the ECAL and the HCAL allowing to measure the contribution to the isolation from charged hadrons, neutral hadrons and photons separately. One of the main advantage of the PF-based isolation is that the energy deposit in the calorimeters associated to a charged hadron produced in another interaction, characterized by a different primary vertex, can be removed from the isolation sum. For very high energy ( $> 1 \text{ TeV}$ ) electrons, however, the PF algorithm might fail to recognize an electron from a GSF electron candidate and assigns all its energy deposit

to the photon isolation. Furthermore, the PF isolation is generally required to be below a fixed fraction of the electron  $E_T$  independently on its value. However, for high  $E_T$  values the background rejection can be improved while keeping an acceptable efficiency by following the  $E_T$  dependence of the ECAL+HCAL1 isolation variable. In fact, this isolation tends to increase for high- $E_T$  electrons due to the extension of the shower.

Further suppression of the misidentification of jets as electrons is achieved by requiring that the ratio  $H/E$  of the energy in the HCAL towers in a cone of  $\Delta R < 0.15$  centered on the electron candidate position, to the electromagnetic energy of the electron candidate supercluster is required to be less than 5%. This requirement is tighter compared with the threshold applied for low- or medium-energy electrons, where it becomes quite inefficient for a high number of pileup interactions. For Run 2, the selection on this variable has been increased. Additionally, the transverse profile of the energy deposition in the ECAL is required to be consistent with that expected for an electron, being defined by the following variables:

- $E_{1\times 5}/E_{5\times 5}$ : ratio of the energy contained in the  $1\times 5$  matrix in  $\eta \times \phi$  in the barrel ( $x \times y$  in the endcaps) centered on the seed crystal of the supercluster over the energy of the  $5 \times 5$  matrix centered on the seed crystal;
- $E_{2\times 5}/E_{5\times 5}$ : ratio of the energy contained in the most energetic  $2\times 5$  matrix in  $\eta \times \phi$  in the barrel ( $x \times y$  in the endcaps) centered on the seed crystal of the supercluster over the energy of the  $5 \times 5$  matrix centered on the seed crystal;
- $\sigma_{in\eta}$  : measure of the spread in  $\eta$  in units of crystals of the electrons energy in the  $5 \times 5$  block centered on the seed crystal.

In the barrel, the best performance are obtained applying a selection on both  $E_{1\times 5}/E_{5\times 5}$  and  $E_{2\times 5}/E_{5\times 5}$ . The two variables are indeed complementary: while  $E_{1\times 5}/E_{5\times 5}$  is well designed for electrons hitting the center of a crystal,  $E_{2\times 5}/E_{5\times 5}$  allows to recover electrons that hit the crystal close to its edge. Combining the two variables instead of using just one of them allows to set a tight requirement on both and thus well reject background while keeping a high efficiency on simulated electrons. The distributions of these variables are much broader for electrons in the endcaps and a higher discrimination power is obtained applying a selection on the variable  $\sigma_{in\eta}$ .

Two additional requirements are applied to reject photons that convert into a electron-positron pair in the tracker. First, the track associated with the cluster is required to have no more than one hit missing in the pixel layers. IN fact, the signature arising from photon conversion process is very similar to the one from real electrons, and the gain in discrimination using shower shape variables is limited. However, one of the main differences is the absence of hits in the first layers of the tracker, before the conversion happens. Furthermore, the transverse impact parameter  $d_{xy}$ , defined as the closest distance, in the transverse plane, between the primary vertex and the track of the electron candidate, is required to be  $< 0.02$  cm (barrel) or  $0.05$  cm (endcaps). The distribution of the transverse impact parameter is usually wider in the endcaps due to the poorer resolution of the track position in that region.

The efficiency of the high- $E_T$  electron selection measured with the T&P method in pp collisions at  $\sqrt{s} = 8$  TeV and in simulation as a function of the electron  $p_T$  is shown in Fig. 6.8, for electrons reconstructed in the ECAL barrel and endcaps. Similar results are obtained using 13 TeV data. The efficiencies and data-to-simulation scale factors are summarized in Tables 6.5 and 6.6, as measured in 8 and 13 TeV data and simulation, respectively. The scale

factors are close to unity, indicating a good agreement between data and simulation. They are used in the analysis presented in this thesis to correct the normalization of simulations.

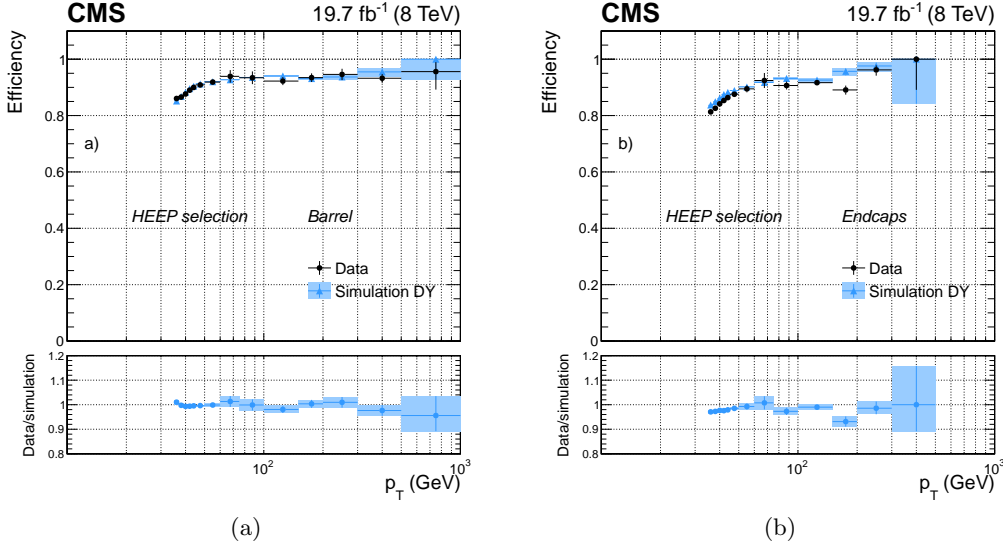


**Figure 6.8:** Efficiency of the high- $E_T$  electron selection as a function of electron  $p_T$  for dielectron events in pp collisions at  $\sqrt{s} = 8$  TeV (dots) and in DY simulation (triangles) for electrons reconstructed in the ECAL barrel (a), and endcaps (b) [95].

**Table 6.5:** Efficiencies and data-to-simulation scale factors for the high- $E_T$  electron selection, as measured in pp collisions at  $\sqrt{s} = 8$  TeV for electrons with  $E_T > 90$  GeV. The quoted uncertainties are statistical.

	ECAL barrel	ECAL endcaps
Efficiency simulation	$90.2\% \pm 0.2\%$	$92.2\% \pm 0.5\%$
Efficiency data	$88.7\% \pm 0.2\%$	$90.7\% \pm 0.6\%$
Data/simulation scale factor	$0.983 \pm 0.004$	$0.984 \pm 0.010$

**Table 6.6:** Efficiencies and data-to-simulation scale factors for the high- $E_T$  electron selection as measured in pp collisions at  $\sqrt{s} = 13$  TeV for electrons with  $E_T > 120$  GeV. The quoted uncertainties are statistical.

	ECAL barrel	ECAL endcaps
Efficiency simulation	$91.4\% \pm 0.10\%$	$84.4\% \pm 0.3\%$
Efficiency data	$91.6\% \pm 0.04\%$	$82.3\% \pm 0.1\%$
Data/simulation scale factor	$1.002 \pm 0.001$	$0.975 \pm 0.004$

## 6.3 Muons

### 6.3.1 Muon reconstruction

The CMS detector is specifically designed for the optimization of muon detection, as its name clearly states. In general, muons will not be absorbed by the calorimeters, as it happens with electrons, so a specific muon detection system (Section 3.2.3) is needed in order to identify

and correctly measure its momentum.

In the standard CMS reconstruction [98], tracks are first reconstructed independently in the inner tracker (tracker track) and in the muon system (standalone-muon track). A standalone-muon track is reconstructed from pre-built track segments (i.e. a set of aligned DT or CSC hits) in the muon chambers. The state vector associated to the segments found in the innermost chambers is used to seed the muon trajectory, from inside out, using the KF technique: the predicted state vector at the next measurement surface is compared with existing hits and updated accordingly. A suitable  $\chi^2$  cut is applied to reject bad hits and the procedure is iterated until the outermost surface of the muon system is reached. Finally, the track is extrapolated to the nominal interaction point and a vertex-constrained fit is performed. The magnetic field, the multiple scattering inside the steel yoke, and the energy losses are taken into account.

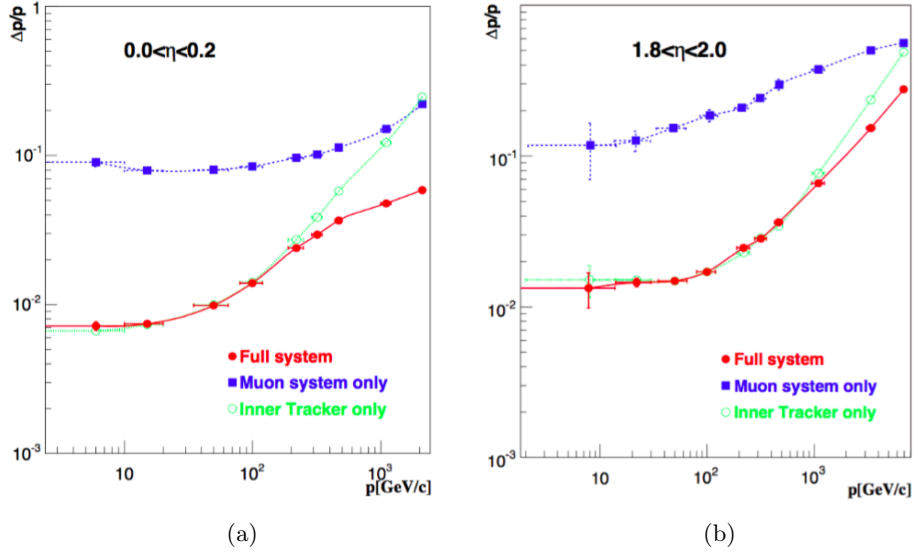
Based on reconstructed standalone-muon and tracker tracks, two reconstruction approaches are then used:

- **global-muon reconstruction (outside-in)**: each standalone-muon track is extrapolated to the tracker and a search is performed in a cone around it to match a tracker track; a global-muon track is fitted combining hits from the tracker track and standalone-muon track, using the KF technique;
- **tracker-muon reconstruction (inside-out)**: all tracker tracks with  $p_T > 0.5 \text{ GeV}$  are considered as possible muon candidates and are extrapolated to the muon system while searching for a match with at least one muon segment.

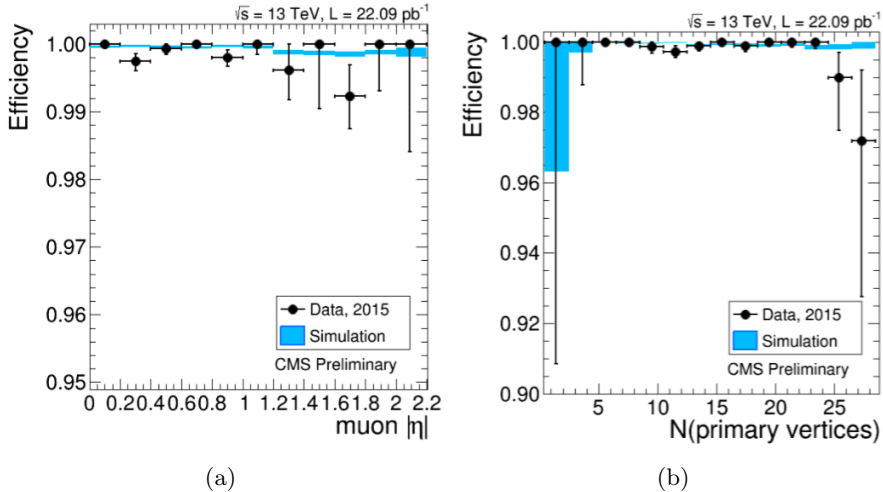
Tracker-muon reconstruction is more efficient than the global-muon reconstruction at low momenta,  $p_T \leq 5 \text{ GeV}$ , because it requires only a single muon segment in the muon system, whereas global-muon reconstruction is designed to have high efficiency for muons penetrating through more than one muon station, and typically requires segments in at least two muon stations. However, given the high efficiency of both the tracker track and muon segments reconstruction, about 99% of muons produced within the geometrical acceptance of the muon system and having sufficiently high momentum ( $p_T \geq 5 \text{ GeV}$ ) are reconstructed by both methods. As shown in Fig. 6.9 the additional information provided by the muon system is precious for the momentum reconstruction of high-energy muons ( $p_T \geq 200 \text{ GeV}$ ), for which the tracker-only momentum measurement degrades. In fact, as a particle's momentum increases and the curvature of its corresponding track decreases, the momentum resolution in the tracker becomes limited by position measurement resolution. One can then benefit from the large lever arm and 3.8 T magnetic field in the region between the tracker and the muon system by including hits in the muon chambers. For lower momenta, instead, the resolution of the tracking system is dominating.

Figure 6.10 shows the muon tracking efficiency as a function of the  $\eta$  of the probe muon and the number of primary vertices for 13 TeV data and simulation, evaluated using the T&P method described in Section 6.2.1. In the region  $|\eta| < 2.2$  and for events with number of reconstructed primary vertices lower than 25, the measured tracking efficiency for isolated muons is  $> 99\%$  in both data and simulation. The efficiency is constant as a function of the number of vertices in the event, hence it does not depend on the pileup.

The combination of different algorithms provides robust and efficient muon reconstruction. After the completion of both algorithms, the reconstructed stand-alone, global, and tracker muons are merged into a single software object, with the addition of further information, like



**Figure 6.9:** Relative resolution of the muon momentum measurement for the reconstruction with the inner tracker only, the muon system only and for the combination of the inner tracker and the muon system, for simulated muons emitted in the central (a) and forward (b) regions [99].



**Figure 6.10:** Tracking efficiency measured with a T&P technique, for muons from Z decays, as a function of the muon  $\eta$  (a) and the number of primary vertices (b), for 2015 data (black dots) and simulation (blue bands) [100].

isolation and energy collected in matching calorimeter towers. This information can be used for further identification, in order to achieve a balance between efficiency and purity of the muon sample as described in Section 6.3.3.

The performance of the reconstruction for high- $p_T$  muons is strongly affected by radiative processes and by the muon detector alignment. Electromagnetic showers and large energy losses can arise as the muon traverses the steel layers of the magnet return yoke, producing additional segments in the muon chambers. These events can affect the measurement done in the muon detectors. Therefore, specialized reconstruction algorithms for high- $p_T$  muons, known as “TeV-muon” refits, have been developed in CMS as described in the following.

The *tracker-plus-first-muon-station* fit (TPFMS) only uses hits from the tracker and the innermost muon station with hits, to reduce the sensitivity to possible showering starting deeper in the muon system. The *Picky* fit uses all tracker hits, while a selection is applied to muon hits. Hits from chambers with a high probability of shower contamination (determined from the hit occupancy) are required to be compatible with the extrapolated trajectory by applying a  $\chi^2$  cut. The *dynamic truncation* algorithm (DYT) starts from the idea that the muon track reconstruction should be stopped after a large energy loss, as hits produced after that can only bias the momentum measurement. For every global muon trajectory the algorithm starts from the corresponding tracker track and propagates it out to the muon stations. Compatible segments (or hits) in the muon chambers are found by using an estimator which takes into account the propagation of the tracker covariance matrix through the material and the magnetic field, and the covariance matrices of the candidate muon segments (or hits).

Momentum assignment is then performed by the *Cocktail* algorithm which combines the above methods to further improve the resolution at high  $p_T$  reducing the tails of the momentum resolution distribution. In particular, the algorithm chooses, on track-by-track basis, the best muon reconstruction. For Run 1, the Cocktail-algorithm decision is taken between the tracker-only, TPFMS, and Picky fits. This version of the algorithm is also known as the *Tune P* algorithm. It starts with the Picky fit, then switches to the tracker-only fit if the goodness of fit ( $\chi^2/\text{n.d.f.}$ ) of the latter is significantly better. Then it compares the  $\chi^2/\text{n.d.f.}$  of the chosen track with that of TPFMS; TPFMS is chosen if it is found to be better. For high- $p_T$  muons, TPFMS and Picky algorithms are selected by Tune P in most of the cases, in approximately equal amounts, while the tracker-only fit is selected only in a few percent of events.

For Run 2, the Tune P algorithm was extended to include also the DYT fit. The selection is still made on a track-by-track basis, but using both the  $\chi^2/\text{n.d.f.}$  of the track and the relative error of the  $p_T$  measurement. The algorithm starts with the Picky fit, then switches to DYT if the DYT track has a lower relative  $p_T$  error. It then compares the  $\chi^2/\text{n.d.f.}$  of the chosen track with that of the tracker-only fit and picks tracker-only if its  $\chi^2/\text{n.d.f.}$  is significantly better. Then the  $\chi^2/\text{n.d.f.}$  of the chosen track and TPFMS are compared and the one giving the best result is kept. At the end, if the final candidate track has  $p_T$  lower than 200 GeV or the tracker-only  $p_T$  is lower than 200 GeV, the tracker-only track is selected.

The momentum resolution obtained with the Tune P algorithm for muons with  $p_T$  in the range  $350 < p_T < 2000$  GeV is found to be  $\approx 6\%$ , as measured with cosmic-ray muon data [98, 101].

### 6.3.2 Muon trigger

The Level-1 muon trigger uses signals from all three CMS muon detector systems: DT, CSC, and RPC. It has a latency of  $3.2\ \mu\text{s}$  and reduces the rate of the readout of events with muon candidates at the detector front-end electronics to a few kHz by applying selections on the estimated muon  $p_T$  and quality. In the muon HLT, first a Level-1 trigger object is used as a seed to reconstruct a standalone-muon track in the muon system, leading to an improved  $p_T$  estimate. At this point,  $p_T$  threshold filters are applied to the standalone-muon (also called Level-2 muon). Then seeds in the inner tracker are generated in the region around the extrapolated Level-2 muon, and tracker tracks are reconstructed. If a successful match is made between a tracker track and the Level-2 muon, a global fit combining tracker and muon hits is performed, yielding a Level-3 muon track on which the final  $p_T$  requirements are applied. In this way, the rate of recorded inclusive muon events is reduced to a few tens of Hz. The average processing time of the HLT reconstruction is about 50 ms.

The L1 and HLT trigger used to collect the data analyzed in this thesis are listed in Tables 6.7 and 6.8 for the 8 and 13 TeV data analysis, respectively. For both analyses the HLT used to select the events is the unprescaled single-muon trigger with the lowest  $p_T$  threshold that does not include muon isolation requirements. In fact, although muons produced by the leptonic decay of a high- $p_T$  W boson tend to be isolated, their high momentum enhances the production of electromagnetic showers, that can mimic a non-isolated muon candidate. Therefore, only requirements on the muon  $p_T$  and  $\eta$  are applied at this stage. The efficiency of the L1 single-muon trigger with the 16 GeV threshold is shown in Fig. 6.11 as a function of the offline reconstructed muon  $p_T$  and  $\eta$ . In 2012 the efficiency for this trigger was greater than 90%. A similar result is obtained in 2015.

**Table 6.7:** The L1 and HLT single-muon triggers used to collect the 8 TeV data analyzed in this thesis together with the imposed requirements on the muon candidate.

Trigger	Name	Selections
Level 1	L1_SingleMu16_eta2p1	1 global muon with: $p_T > 16 \text{ GeV}$ $ \eta  < 2.1$
HLT	HLT_Mu40_eta2p1	1 global muon with: $p_T > 40 \text{ GeV}$ $ \eta  < 2.1$

**Table 6.8:** The L1 and HLT single-muon triggers used to collect the 13 TeV data analyzed in this thesis together with the imposed requirements on the muon candidate.

Trigger	Name	Selections
Level 1	L1_SingleMu25	1 global muon with: $p_T > 25 \text{ GeV}$
HLT	HLT_Mu45_eta2p1	1 global muon with: $p_T > 45 \text{ GeV}$ $ \eta  < 2.1$

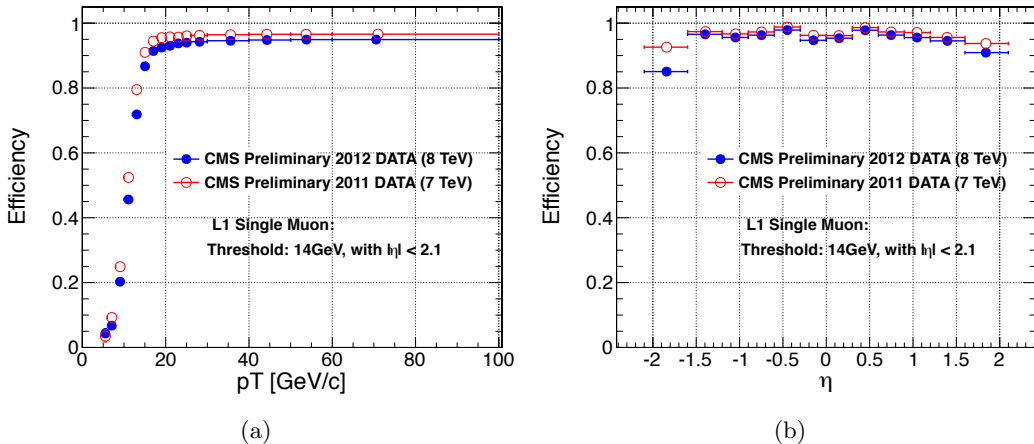


**Figure 6.11:** Efficiency of the L1 single-muon trigger with a threshold of 14 GeV on the muon  $p_T$  (a) and  $\eta$  (b) [102].

The efficiency for a muon passing the high- $p_T$  selections described in Section 6.3.3 to fire the HLT single-muon triggers have been measured in data with T&P method and are summarized in Tables 6.9 and 6.10.

**Table 6.9:** Efficiencies and scale factors for the single-muon HLT trigger used in the 8 TeV analysis for muons with  $p_T > 50 \text{ GeV}$ ,  $|\eta| < 2.1$ , and satisfying the high- $p_T$  and isolation selections described in Section 6.3.3. The quoted uncertainties are statistical.

	$0 <  \eta  < 0.9$	$0.9 <  \eta  < 1.2$	$1.2 <  \eta  < 2.1$
Efficiency simulation	$95.10\% \pm 0.03\%$	$87.01\% \pm 0.03\%$	$81.56\% \pm 0.03\%$
Efficiency data	$92.90\% \pm 0.02\%$	$83.14\% \pm 0.06\%$	$80.27\% \pm 0.05\%$
Data/simulation scale factor	$0.9768 \pm 0.0004$	$0.956 \pm 0.001$	$0.984 \pm 0.001$

**Table 6.10:** Efficiencies and scale factors for the single-muon HLT trigger used in the 13 TeV analysis for muons with  $p_T > 53 \text{ GeV}$ ,  $|\eta| < 2.1$ , and satisfying the high- $p_T$  and isolation selections described in Section 6.3.3. The quoted uncertainties are statistical.

	$0 <  \eta  < 0.9$	$0.9 <  \eta  < 1.2$	$1.2 <  \eta  < 2.1$
Efficiency simulation	$97.6\% \pm 0.1\%$	$93.4\% \pm 0.4\%$	$94.8\% \pm 0.2\%$
Efficiency data	$94.6\% \pm 0.2\%$	$89.7\% \pm 0.4\%$	$91.8\% \pm 0.2\%$
Data/simulation scale factor	$0.969 \pm 0.002$	$0.961 \pm 0.006$	$0.968 \pm 0.003$

### 6.3.3 Muon identification

The standard CMS muon reconstruction provides additional information for each muon, useful for muon quality selection and identification in physics analyses [98]. In general, particles detected as muons are produced in pp collision from different sources which lead to different experimental signatures. The so-called *prompt muons* arise either from decays of W, Z, and promptly produced quarkonia states, or other sources such as Drell-Yan processes or top quark production. Real muons are also produced in the decay of heavy flavour particles, such as beauty or charmed mesons, as well as in light hadron (pions or kaons) decays. Less frequently, muons might be originated from a calorimeter shower or a product of a nuclear interaction in the detector. Furthermore, the so called “punch-through” effect, i.e. hadron shower remnants penetrating through the calorimeters and reaching the muon system, can lead to the reconstruction of a muon candidate. Most of the physics analyses in CMS studying SM processes or searching for BSM signals use prompt muons, while all the other categories constitute the background. These analyses exploit the same set of information, although the applied selections might be different depending on the interesting signature and the expected background. In this section only the specific selection developed for high- $p_T$  muons are described. One of the main difference with respect to the low- and medium- $p_T$  muon selection is that this particular identification procedure does not use the PF algorithm. It is aimed at the best reconstruction of the muon track parameters without relying on external information on the event. Moreover, the goodness of the global-muon track fit selection, based on the  $\chi^2$  of the track, is not requested, but an additional selection based on the relative  $p_T$  resolution for the track used for momentum determination is applied.

The high- $p_T$  muon selection criteria are described in the following and they have not been changed since Run 1:

- The muon must be reconstructed both as a tracker- and a global-muon. This is

effective against decays-in-flight, punch-through and accidental matching (with noisy or background tracks or segments).

- Number of pixel hits in the tracker track  $\geq 1$ . To further suppress muons from decays in flight.
- Number of tracker layers involved in the measurements  $\geq 6$ . This guarantees a good  $p_T$  measurement, for which some minimal number of measurement points in the tracker is needed. It also suppresses muons from decays in flight.
- Number of muon-chamber hits included in the global-muon track fit  $\geq 1$ . This requirement assures that the global muon is not an accidental match between the information from the muon system and the tracker. This could happen in particular for non-prompt muons or fake muons from punch-through.
- The muon track is required to have muon segments in at least 2 muon stations. To further suppress punch-through and accidental track-to-segment matches. This selection is furthermore consistent with the logic of the single-muon trigger, which requires segments in at least two muon stations to obtain a meaningful estimate of the muon  $p_T$ .
- Transverse impact parameter of the muon track  $< 2 \text{ mm}$ . This assures the compatibility of the muon track with the interaction point hypothesis and it is effective against cosmic background and further suppress muons from decays in flight.
- Longitudinal impact parameter of the muon track  $< 5 \text{ mm}$ . To further suppress cosmic muons, muons from decays in flight and tracks from pileup.
- Relative  $p_T$  error  $< 30\%$ . To further suppress mis-reconstructed muons.

In addition to these identification criteria, an isolation requirement is applied to the well-identified muons. In particular, the muon must pass a relative tracker-only isolation selection: the scalar sum of the  $p_T$  of all other tracks in a cone of  $\Delta R < 0.3$  around but not including the muon tracker track must be less than 10% of the muon  $p_T$ , also as measured by the tracker. To be used in the calculation of the tracker-based isolation, tracks have to be within 2 mm, in the  $z$  direction, of the primary vertex with which the muon candidate is associated. These additional criteria help suppress the effect of tracks originating from pileup on the reconstructed quantities.

The efficiency and data-to-simulation scale factors for the high- $p_T$  muon identification and isolation criteria measured with the T&P method in 8 and 13 TeV data are summarized, respectively, in Tables 6.11 and 6.12. The scale factors are close to unity, indicating a good agreement between data and simulation. They are used in the analyses presented in this thesis to correct the normalization of simulations.

## 6.4 Jets

Particles carrying a color charge, such as quarks, cannot exist in free form because of QCD confinement which only allows for colorless states (Section 2.1.6). Quarks and gluons interact with pairs of quarks and anti-quarks produced from the vacuum until the formation of stable colourless hadrons. The ensemble of the final colourless objects is called a *jet* and it is reconstructed in the detector from energy depositions and charged particle momenta. The jets point back to the primary interaction, i.e. to the partons the jets originated from, but a correction for hadronization and detector effects is needed. Jet clustering algorithms have been

**Table 6.11:** Efficiencies and scale factors for the high- $p_T$  muon identification and isolation criteria used in the 8 TeV data analysis for muons with  $p_T > 50$  GeV and  $|\eta| < 2.1$ .

Muon $ \eta $	$0 <  \eta  < 0.9$	$0.9 <  \eta  < 1.2$	$1.2 <  \eta  < 2.1$
High- $p_T$ muon identification			
Efficiency simulation	$96.51\% \pm 0.02\%$	$96.61\% \pm 0.04\%$	$95.54\% \pm 0.03\%$
Efficiency data	$95.54\% \pm 0.02\%$	$95.87\% \pm 0.04\%$	$95.06\% \pm 0.03\%$
Data/simulation scale factor	$0.9900 \pm 0.0003$	$0.992 \pm 0.001$	$0.9949 \pm 0.0004$
Tracker-based muon isolation			
Efficiency simulation	$99.49\% \pm 0.01\%$	$99.58\% \pm 0.01\%$	$99.59\% \pm 0.01\%$
Efficiency data	$99.46\% \pm 0.01\%$	$99.51\% \pm 0.01\%$	$99.56\% \pm 0.01\%$
Data/simulation scale factor	$0.9996 \pm 0.0001$	$0.9994 \pm 0.0001$	$0.9997 \pm 0.0001$

**Table 6.12:** Efficiencies and scale factors for high- $p_T$  muon identification and isolation criteria used in the 13 TeV data analysis for muons with  $p_T > 53$  GeV and  $|\eta| < 2.1$ .

Muon $ \eta $	$0 <  \eta  < 1.2$	$1.2 <  \eta  < 2.1$
High- $p_T$ muon identification		
Efficiency simulation	$97.6\% \pm 0.2\%$	$99.81\% \pm 0.2\%$
Efficiency data	$96.7\% \pm 0.4\%$	$1.0\% \pm 0.7\%$
Data/simulation scale factor	$0.991 \pm 0.005$	$1.002 \pm 0.007$
Tracker-based muon isolation		
Efficiency simulation	$99.8\% \pm 0.1\%$	$99.6\% \pm 0.1\%$
Efficiency data	$99.7\% \pm 0.1\%$	$99.7\% \pm 0.1\%$
Data/simulation scale factor	$0.999 \pm 0.001$	$1.001 \pm 0.001$

developed to cluster particles (at parton, particle or detector level) into jets and reconstruct the energy and direction of the original parton. The task of a jet clustering algorithm is to allow comparisons between theoretical predictions, which are usually described by perturbative calculations, and experimental data. This is achieved reducing the complex structure of particle jets from a scattered parton to a simple four-momentum, which represents the main property of particle jets. In order to guarantee a meaningful calculation of theory predictions, jet clustering algorithms are characterized by two important properties. Clustering algorithms need to be infrared-safe, which means that the emission of infinitesimally-low-energy partons from partons inside a jet does not affect the jet properties. Furthermore, they need to be collinear-safe, which means that jet properties are not affected by the splitting of a parton inside a jet into two collinear partons. Jet algorithms for hadron colliders can be divided into two classes: cone [103] and sequential clustering [104–108] algorithms. The main algorithms used by LHC experiments belong to the second class and are the anti- $k_t$  [108] (AK) and the Cambridge–Aachen (CA) [104, 106] algorithms. In fact, they are found to fulfil theory requirements and to exhibit good properties for experimental measurements. For this work both algorithms are used and described in the following.

#### 6.4.1 Jet clustering algorithms

In sequential jet clustering algorithms, jets are defined through sequential, iterative procedures that combine four-vectors of input pairs of particles until certain criteria are satisfied and jets are formed. In particular, for each pair of particles  $i$  and  $j$ , a distance variable between the two particles ( $d_{ij}$ ), and the so-called “beam distance” for each particle ( $d_{iB}$ ), are computed:

$$d_{ij} = \min(p_{Ti}^{2n}, p_{Tj}^{2n}) \frac{\Delta R^2 ij}{R^2} , \quad d_{iB} = p_{Ti}^{2n} , \quad (6.1)$$

where  $p_{Ti}$  and  $p_{Tj}$  are the transverse momenta of particles  $i$  and  $j$ , respectively, “ $\min$ ” refers to the smaller of the two  $p_T$  values, the integer  $n$  depends on the specific jet algorithm,  $\Delta R^2 ij$  is the distance between  $i$  and  $j$  in  $\eta$  and  $\phi$ , and  $R$  is a free distance parameter, with all angles expressed in radians. The particle pair  $(i, j)$  with smallest  $d_{ij}$  is combined into a single object. All distances are recalculated using the new object, and the procedure is repeated until, for a given object  $i$ , all the  $d_{ij}$  are greater than  $d_{iB}$ . Object  $i$  is then classified as a jet and not considered further in the algorithm. The process is repeated until all input particles are clustered into jets.

The distance parameter  $R$  is responsible for defining the angular size of the jet. The parameter  $n$  governs the topological properties of the jets and depending on its value three different classes of clustering algorithms are distinguished. For  $n = 1$  the procedure is referred to as the  $k_t$  algorithm (KT), which clusters soft objects before harder ones are added to the final jet. The KT jets tend to have irregular shapes and are especially useful for reconstructing jets of lower momentum [108]. For this reason, they are also sensitive to the presence of low- $p_T$  pileup contributions. For  $n = 0$ , the procedure corresponds to the CA algorithm. This relies only on angular information, and, like the KT algorithm, provides irregularly-shaped jets. The CA algorithm is useful in identifying jet substructure as described in Chapter 7. For  $n = -1$ , the procedure corresponds to the AK algorithm, which compares the inverse square of the transverse momenta. The AK algorithm is used extensively in LHC experiments and by the theoretical community for finding well-separated jets. The use of inverse square of the  $p_T$  as a weight in the  $d_{ij}$  distances has the advantage that hard objects collect adjacent soft ones before these are clustered among themselves into harder objects, figuratively reproducing in reverse the parton fragmentation and gluon emission processes. This property makes the algorithm independent on soft radiation preserving infrared-safety. The AK algorithm is also collinear-safe as the clustering is driven by the angular distance between two particles. Gluons emitted at small angles are picked up by the algorithm in early steps of the iteration and therefore do not affect the jet properties. Furthermore, this algorithm tends, by construction, to form almost circular jets allowing for straight-forward calibration and understanding of the detector acceptance. The behaviours of the CA and AK jet algorithms are illustrated in Fig. 6.12.

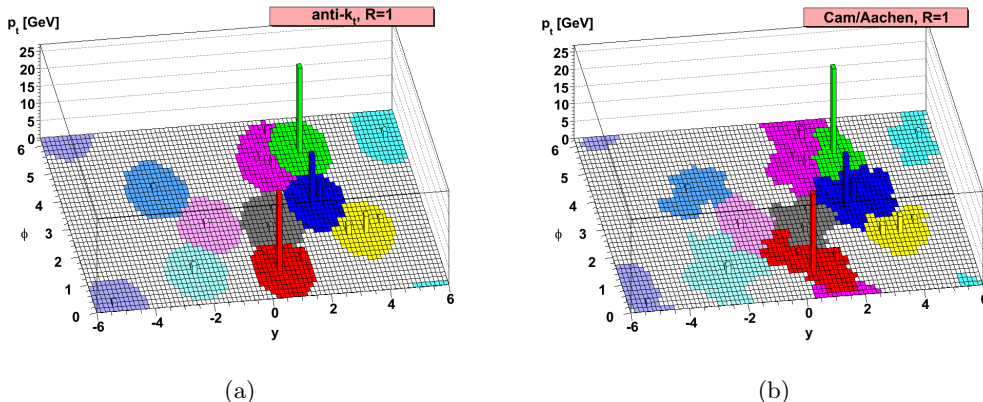


**Figure 6.12:** An example of jet clustering with the AK (a) and CA (b) algorithms. The reconstructed jets are shown as colored regions [108].

The choice of the distance parameters  $R$ , generally depends on the analysis. While large cone size jets collect all energy from the scattered parton, they also pick up a large contribution of background energy from the underlying event or pileup interactions. Small cone size jets pick up little contamination, but may not collect all energy from the scattered parton. The default choice in CMS for physics analyses in Run 1 and Run 2 uses the KT algorithm with  $R = 0.5$  (AK5) and  $R = 0.4$  (AK4), respectively, since more collimated jets are expected at higher  $\sqrt{s}$ . However, a larger value of  $R$  increases the efficiency to entirely reconstruct the highly energetic products in the decays into hadrons of boosted V and Higgs bosons. In fact, the average angular distance between the decay products is inversely proportional to the  $p_T$  of the mother particle. The default choice in CMS for physics analyses involving boosted V or Higgs bosons decaying hadronically is  $R = 0.8$ . In particular, CA8 and AK8 jets are used for Run 1 and Run 2 analyses, respectively. The chosen value of  $R$  provides a high efficiency for V or Higgs bosons with small boost and ensures that no efficiency is lost in the transition from the classical reconstruction in two small jets at low boson  $p_T$  to the reconstruction as a single large-cone jet at higher values. Another point to consider when choosing the value of  $R$ , is the  $t\bar{t}$  data sample available for validating highly boosted W jets (Section 7.2). If  $R$  is chosen too large, the b quark from the  $t \rightarrow Wb$  decay tends to merge into the W jet. The chosen value of  $R$  is the result of a compromise between high efficiency for V or Higgs bosons with small boost and a sufficiently large sample of W jets in  $t\bar{t}$  data for validating the boosted boson jet identification procedure. Figure 6.13 shows the  $p_T$  range of W bosons for which the CA8 algorithm is efficient and compares this to the efficiency for reconstructing W bosons from two AK5 jets. Above a  $p_T$  of 200 GeV, the CA8 jet algorithm, used to identify W jets, becomes more efficient than the reconstruction of a W boson from two AK5 jets.

The AK5 or AK4 algorithms are used in this analysis to put requirements on additional b jets in the event selection (Section 8.1), along with the b tagging algorithm described in Section 6.4.3.

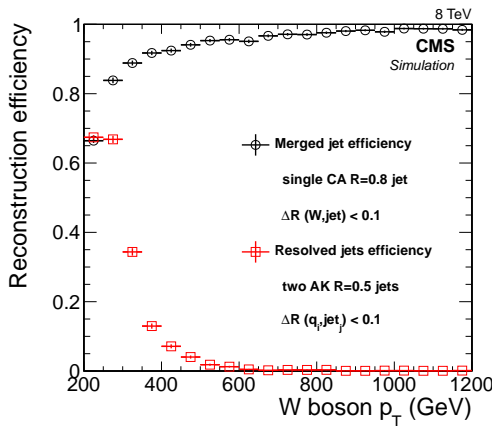


**Figure 6.13:** Efficiency to reconstruct a CA8 jet within  $\Delta R < 0.1$  of a generated W boson, and the efficiency to reconstruct two AK5 jets within  $\Delta R < 0.1$  of the generated quarks in the W boson decay, as a function of the  $p_T$  of the W boson [109].

#### 6.4.2 Jet reconstruction and calibration

In CMS several standard methods for jet reconstruction are available which make use of different detector components, e.g. the tracker and the calorimeters, and give different reconstructed objects as input to the above explained jet clustering algorithms. In this

work, only jets reconstructed with the PF algorithm are used and referred to as “PF jets”. As sketched in Fig. 6.14, the PF algorithm aims at reconstructing all the stable particles produced in an event, combining the information coming from all CMS sub-detectors to optimize particle identification, direction and energy determination. These particles are classified in several types: charged hadrons, photons, neutral hadrons, electrons and muons. Jets are typically composed by 65% charged hadrons, 25% photons, 10% neutral hadrons (Fig. 6.15). The PF algorithm is optimized to identify all these different components inside the jet, contrary to a calorimetric-only reconstruction. Typically, photons correspond to ECAL deposits not compatible with a tracker track. Charged hadrons correspond to HCAL and/or ECAL deposits matched to a inner track and not compatible with an electron, whereas neutral hadrons are identified as HCAL deposits not matched to any track. While the momentum of neutral particles is measured in the calorimeters, the momentum of charged particles is measured by the tracker with a better resolution. Hence, both the position and energy measurements are greatly improved with respect to calorimeter jets as this algorithm makes use of the tracking detectors and high granularity of the ECAL which is much higher than that of the HCAL. Once all the PF candidates in the event are reconstructed, they are used as input to the jet clustering algorithms described in the previous section and a PF jet is formed.

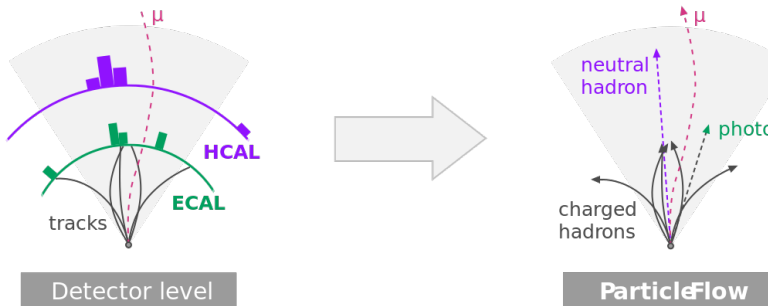


**Figure 6.14:** Sketch of the CMS particle-flow algorithm.

The jet momentum is determined as the vectorial sum of all PF candidates in the formed jet providing its “raw” estimate. At this stage, the reconstructed jet energy has a large uncertainty due to the several intrinsic limitations of the system, such as the non-linear response of the calorimeters, the detector segmentation, the presence of material in front of calorimeters, electronic noise and pileup. The raw jet energy and resolution are thus corrected for several factors in order to obtain the energy value as close as possible to the true energy of the initial parton. CMS has adopted a factorized approach [111] to the problem of jet energy corrections, where each level of correction takes care of a different effect as described in the following.

The first step in this approach is a correction to the jet energies to mitigate pileup effects. The additional pp collisions occurring within the same bunch-crossing as the primary hard interaction produce additional tracks in the tracker and deposit energy in the calorimeters. This contribution is usually referred to as in-time pileup. Due to the finite signal decay time in the calorimeters, the pp collisions occurring in the previous and subsequent beam crossings also contribute to calorimetric energy in the same time window as the primary hard interaction. This contribution is called out-of-time pileup. The out-of-time contribution is mitigated at the level of signal processing, while the in-time one is partially removed using tracking information. This is achieved identifying which vertex the charged PF candidates originate

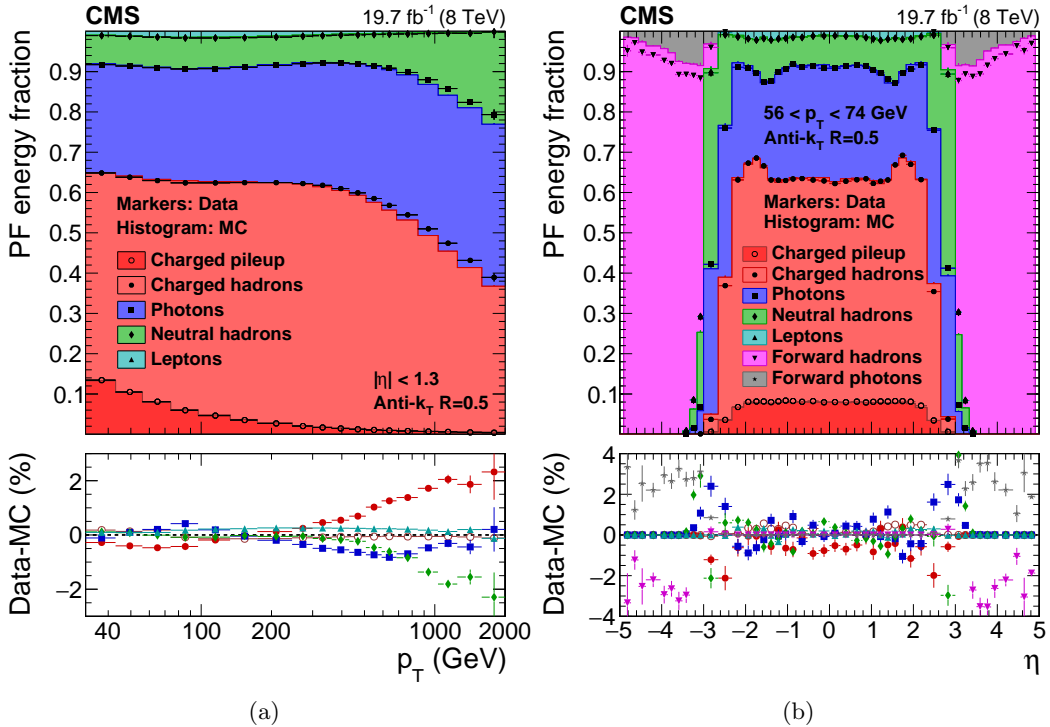


**Figure 6.15:** PF jet composition in data and simulation as a function of jet  $p_T$  for jets with  $|\eta| < 1.3$  (a), and as a function of  $\eta$  for jets with  $p_T$  in the range  $56 < p_T < 74 \text{ GeV}$  (b) [110].

from, and removing those unambiguously associated with pileup vertices before clustering jets. This method is referred to as *charged-hadron subtraction* (CHS), and represents the reference standard method for jet reconstruction in CMS for Run 1 and beginning of Run 2. For the second part of Run 2, other pileup mitigation techniques in addition to CHS have been developed and tested in CMS [112–114] but they are not used in this work. The CHS jets are then corrected to subtract residual contributions from neutral pileup particles, overlapping inside the jet cone. These corrections are determined from the simulation of a sample of QCD dijet events processed with and without pileup contaminations. This correction is usually parametrized as a function of the pileup energy density ( $\rho$ ) [115,116], the jet area (A) [117], jet  $p_T$  and  $\eta$ . The pileup offset corrections, defined as the mean value of the difference between the  $p_T$  of the reconstructed jet in events with and without pileup contamination, for AK5 CHS jets as a function of the corrected jet  $p_T$  and  $\eta$  are shown in Fig. 6.16, estimated for typical 2012 (8 TeV) conditions with an average number of additional pileup interactions  $\langle \mu \rangle = 20$ . The typical offset correction for a AK5 jet without CHS is 0.75 for a corrected jet  $p_T$  of 30 GeV, while a correction of 0.85 is obtained for AK5 CHS jets with same  $p_T$  value. This indicates that CHS removes approximately half of this offset before jet clustering by matching tracks to pileup vertices, reducing the residual offset correction. Roughly one third of the remaining pileup is from PF charged hadrons that have not been matched to good pileup vertices, and much of the rest is from PF photons.

Secondly, a simulation driven jet energy response correction is applied. The detector simulation takes into account effects due to particles deflected by the magnetic field, energy lost when traversing the detector material, particle conversions, and a detailed detector geometry. In this step the aim is to correct for non-uniformities in the different CMS subdetectors, by comparing the reconstructed jet  $p_T$  to the particle-level one using simulated events only. The

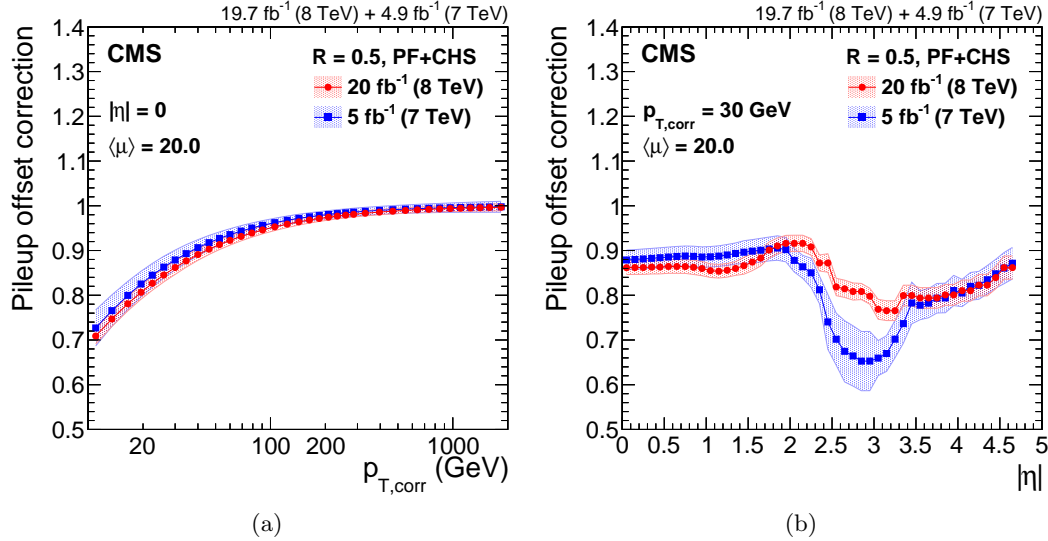


**Figure 6.16:** Pileup offset correction for AK5 CHS jets estimated for the typical 2012 condition of  $\langle \mu \rangle = 20$ . Corrections are shown for jets at  $|\eta| = 0$  as a function of the corrected jet  $p_T$  (a), and for jets with  $p_T = 30$  GeV as a function of the jet  $|\eta|$  [110].

corrections are derived as a function of jet  $p_T$  and  $\eta$  and make the response uniform over these two variables. The simulated particle response corrections are summarized in Fig. 6.17 for 7 and 8 TeV data. The response is quite flat at  $p_T > 50$  GeV, where the competing effects of increasing calorimeter response and falling tracking efficiency within the jet core compensate each other. In the barrel and endcap regions, the corrections rise with  $|\eta|$ , due to the increasing amount of material located in front of the calorimeters, which leads to effects such as an increased rate of nuclear interactions in the tracker. The corrections are higher around  $|\eta| = 1.3$  and 3.0 due to the degradation of the response in the transition regions.

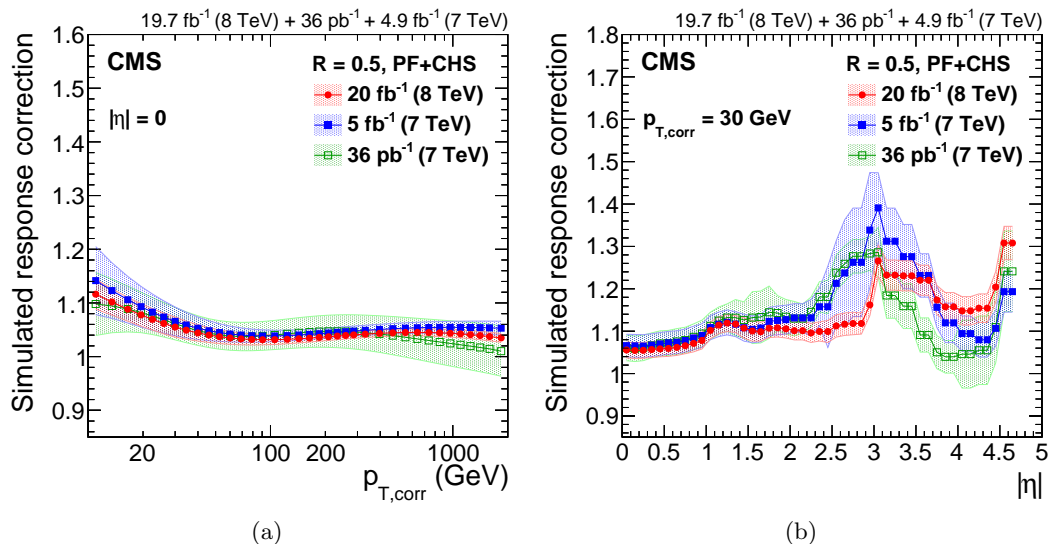


**Figure 6.17:** Detector response correction factors for AK5 CHS jets estimated for the 8 TeV data collected in 2012. Corrections are shown for jets at  $|\eta| = 0$  as a function of the corrected jet  $p_T$  (a), and for jets with  $p_T = 30$  GeV as a function of the jet  $|\eta|$  [110].

Finally data-driven residual corrections are applied to correct for any measurable difference between the detector simulation and the jets measured in data. This correction is done in two steps. At first, an additional correction for the non homogeneous response of the detector with  $\eta$  is derived from dijet events, in which the  $p_T$  response of a probe jet, outside the barrel region, is balanced to the one in the reference tag region ( $|\eta| < 1.3$ ) as a function of the average  $p_T$  of the dijet system. Only events with back-to-back dijets and little additional activity in the event are used, to avoid any impact from unbalanced events. The jet energy is calibrated as a function of transverse momentum using a combination of  $Z(\rightarrow \ell\ell) + \text{jet}$ ,  $\gamma + \text{jet}$ , and multijet events for jets in the reference barrel region ( $|\eta| < 1.3$ ). The basic idea, in all the considered topologies, is to exploit the transverse momentum balance between the jet to be calibrated and a well reconstructed and calibrated reference object ( $Z$  or  $\gamma$ ). The jet energy response is studied using two approaches. In one method the jet response is evaluated by comparing the reconstructed jet momentum ( $p_{T,\text{jet}}$ ) directly to the momentum of the reference object ( $p_{T,\text{ref}}$ ), while the second, more advanced, method takes into account the missing energy measured in the calorimeters to balance the reference object and jet momenta. In this method the additional event activity is taken into account by the missing energy. Therefore, additional jets in the event have only a small impact on the measurement. The residual corrections are summarized in Fig. 6.18 for 8 TeV data. The residual response corrections are less than 3% in the barrel, less than 10% in the endcaps, and about 10% in the forward detector.

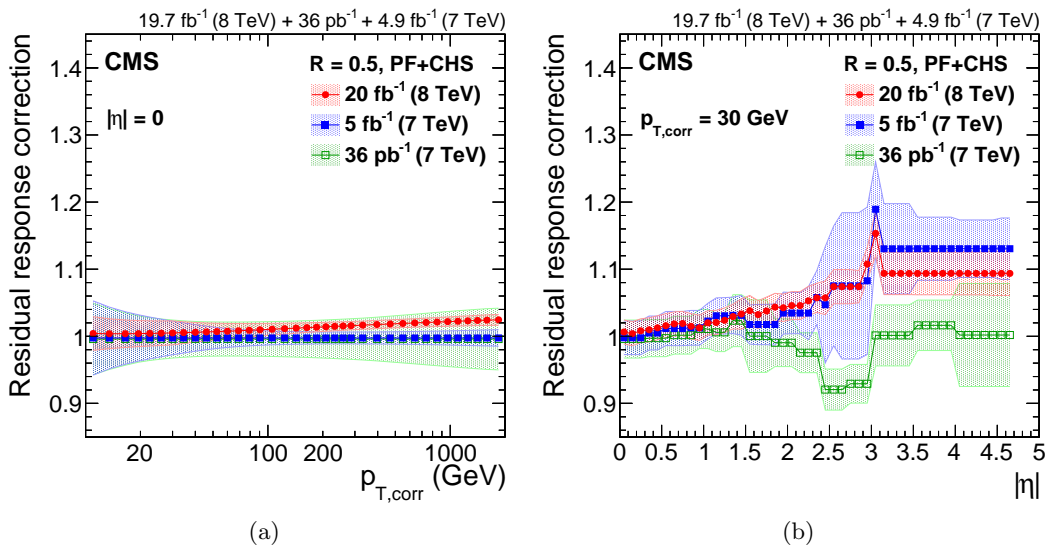


**Figure 6.18:** Residual data/simulation response correction factors for AK5 CHS jets for the 8 TeV data collected in 2012. Corrections are shown for jets at  $|\eta| = 0$  as a function of the corrected jet  $p_T$  (a), and for jets with  $p_T = 30 \text{ GeV}$  as a function of the jet  $|\eta|$  (b) [110].

The fully calibrated PF jets are finally obtained in both data and simulation by multiplying all the above correction factors to the raw jet  $p_T$  as follows:

$$p_{T,\text{corr}} = p_{T,\text{raw}} \times C_{\text{pu}}(p_{T,\text{raw}}, \eta, \rho, A) \times C_{\text{sim}}(C_{\text{pu}} \cdot p_{T,\text{raw}}, \eta) \times C_{\text{res}}(C_{\text{pu}} \cdot C_{\text{sim}} \cdot p_{T,\text{raw}}, \eta) \quad (6.2)$$

where  $C_{\text{pu}}$  represents the pileup correction,  $C_{\text{sim}}$  is the simulated response correction and  $C_{\text{res}}$  is the global residual correction applied only on jets in data. Figure 6.19 shows the overall uncertainty on the corrections to the jet energy scale for AK5 and AK4 CHS jets for

8 and 13 TeV data, respectively. In both cases, the final uncertainties are below 3% across the phase space of this analysis.

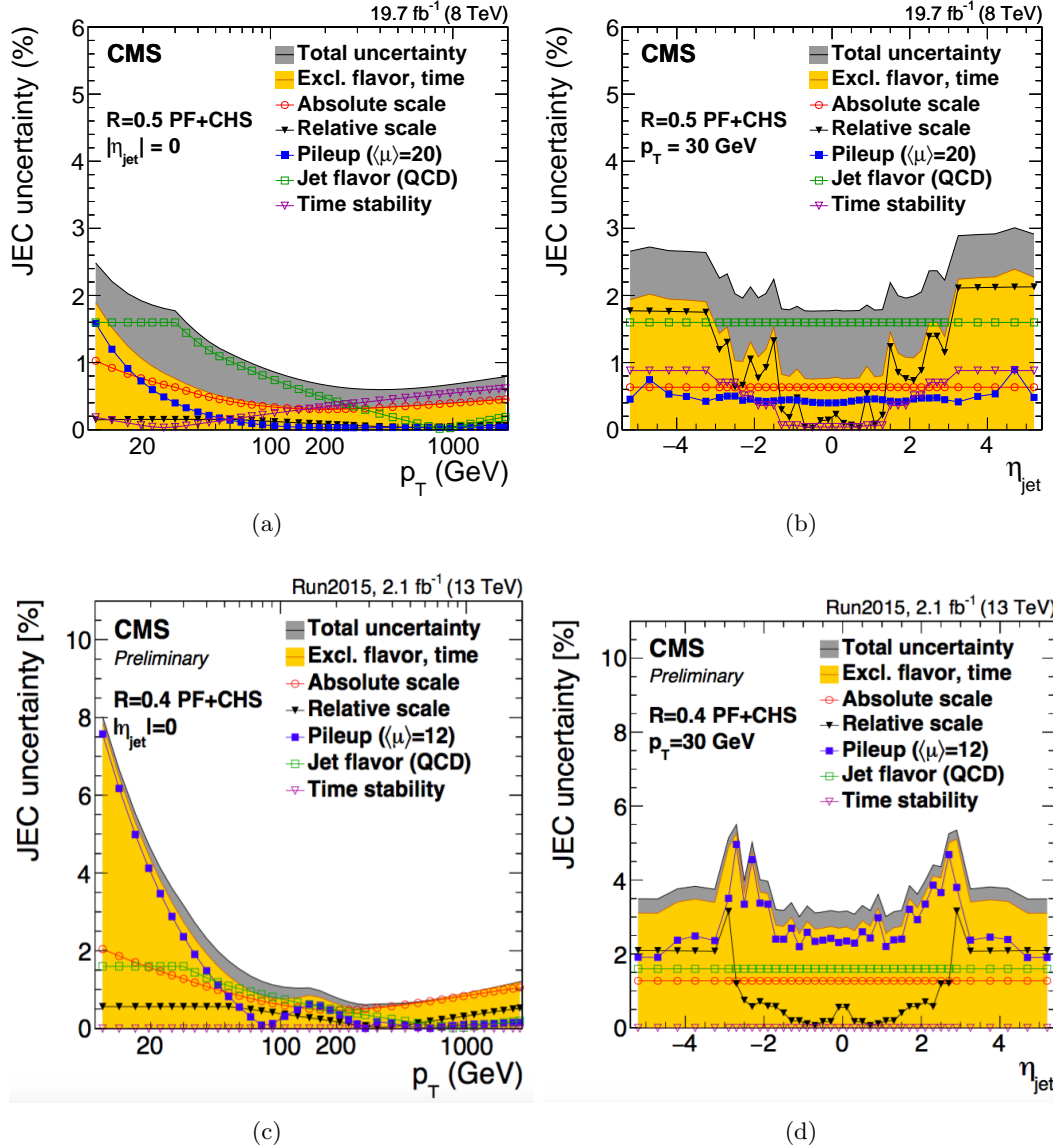


**Figure 6.19:** Summary of jet energy scale systematic uncertainties for the 8 TeV data collected in 2012 for AK5 CHS jets (upper plots) and for the 13 TeV data collected in 2015 for AK4 CHS jets (lower plots). Uncertainties are shown for jets at  $|\eta| = 0$  as a function of the corrected jet  $p_T$  (left), and for jets with  $p_T = 30$  GeV as a function of the jet  $|\eta|$  (right) [110,118].

The energy resolution of jets is relatively poor compared to the resolution of other physics objects (electrons, muons, photons), and the biases caused by jet resolution smearing is important for steeply falling spectra and for resonance decays. Hence, calibrations are evaluated to correct the jet energy resolution in addition to the corrections to the jet energy scale described above. The measurements are performed with methods which are extensions of the methods used for measuring jet energy scales, but instead of looking at the mean of the response distribution, the width is the interesting parameter. Furthermore, corrections have to compensate for effects that do not produce an overall shift in the mean, but that can widen the distribution. As shown in Fig. 6.20, the jet energy resolution in data is worse than

in the simulation by 10–20% depending on  $\eta$ , and the jets in simulation need to be smeared accordingly.

Jets used in this analysis are requested to pass loose identification criteria, in order to reject spurious jet-like features originating from isolated noise patterns in the calorimeters or the tracker. The efficiency of these requirements is above 99% for real jets.

For the 13 TeV data analysis described in this work, all AK4 and AK8 jets must have corrected  $p_T > 30 \text{ GeV}$  and  $> 200 \text{ GeV}$ , respectively, and  $|\eta| < 2.4$  to be considered in the subsequent steps of the analysis. Furthermore, the AK4 and AK8 jets are required to be separated from any well-identified muon or electron (Sections 6.3 and 6.2) by  $\Delta R > 0.3$  and  $> 0.8$ , respectively. This requirement is applied to clean the jet collection used in the analysis from leptons mis-identified as jets. Finally, AK4 jets are required to be separated from the AK8 jet representing the  $V \rightarrow q\bar{q}^{(\prime)}$  candidate by  $\Delta R > 0.8$  since an overlap is expected between the two reconstructions. The same selections are applied for AK5 and CA8 jets in the 8 TeV data analysis. For this case an additional selection is applied to the pseudorapidity of CA8 jets. In particular, CA8 jets are not used in the analysis if their pseudorapidity falls in the region  $1.0 < |\eta| < 1.8$ , thus overlapping the barrel-endcap transition region of the silicon tracker. In fact, in Run 1 it has been found that in this region, ‘noise’ can arise when the tracking algorithm reconstructs many fake displaced tracks associated with the jet. This issue in the reconstruction has been studied in details in the context of this work. The studies, presented and discussed in Appendix A, resulted in the choice of the  $\eta$  region to be excluded. In particular, the simulation does not sufficiently describe the full material budget of the tracking detector in that region, thus it does not accurately describe this effect. Without this requirement, a bias can be introduced in the b tagging, jet substructure and missing energy information, making this analysis systematically prone to that noise. As a consequence of these results, other analyses involving similar kinematic cuts and identification algorithms have been affected [119]. However, this problem has been fixed for Run 2 and this additional fiducial cut does not have to be applied in 13 TeV data analyses.

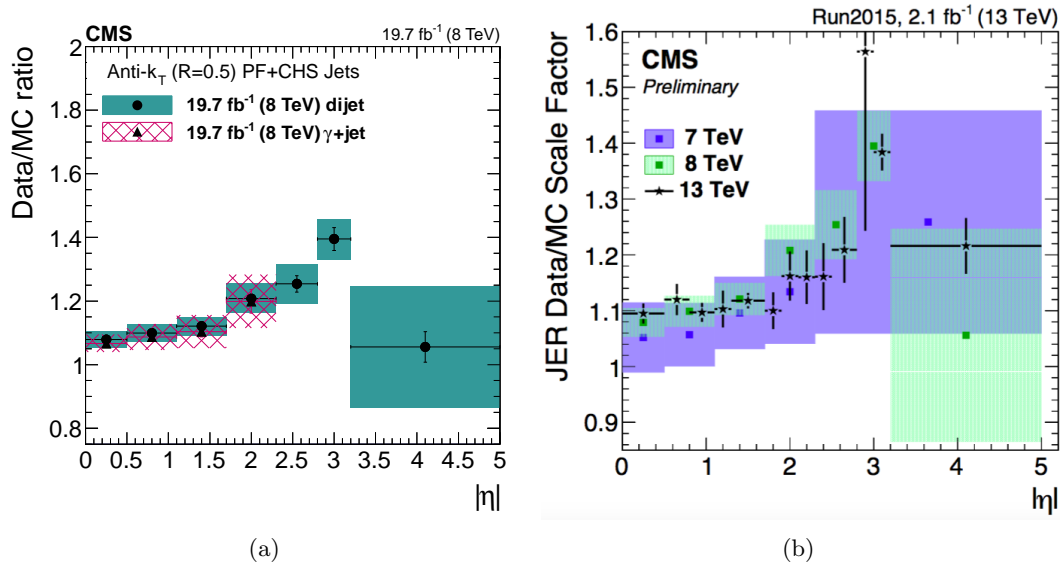


**Figure 6.20:** Data/MC scale factors for the jet  $p_T$  resolution for AK5 CHS jets as a function of  $|\eta|$  determined from 8 TeV data collected in 2012 (a) and for AK4 CHS jets in 13 TeV data collected in 2015 (b) [110, 118].

### 6.4.3 Identification of b jets

The identification of jets originating from b quarks (“b jets”) is one of the key ingredients of the analysis described in this work, which aims at isolating events of new physics with H bosons decaying to  $b\bar{b}$ . The ability to identify b jets (“b tagging”) plays a crucial role in reducing background coming from processes involving jets from gluons and light-flavor quarks (u, d, s), and from c quark fragmentation.

Identifying b jets relies on the properties of the production and the weak decay of b hadrons. The most important property is the relatively long lifetime of b hadrons of about  $1.5 \text{ ps}$  ( $c\tau \equiv 450 \mu\text{m}$ ) corresponding to a flight distance that is observable with high resolution tracking detectors. A b hadron with  $p_T = 50 \text{ GeV}$  covers, on average, almost half a centimetre ( $Lc \sim \gamma\tau$ ) before decaying. As shown in Fig. 6.21, this leads to secondary vertices displaced from the primary event vertex and charged particle tracks incompatible with the primary vertex with sizeable impact parameter. In addition, b hadrons have a large mass and large multiplicity of charged particles in the final state (about five charged particles on average per b hadron decay). Because of the hard b-fragmentation function, the b hadron in a b jet carries a large fraction of the jet energy. Since b and c hadrons may decay semileptonically, in about 20% (per lepton species) of the cases an electron or muon is produced inside a b jet, if both direct and cascade decays are taken into account.

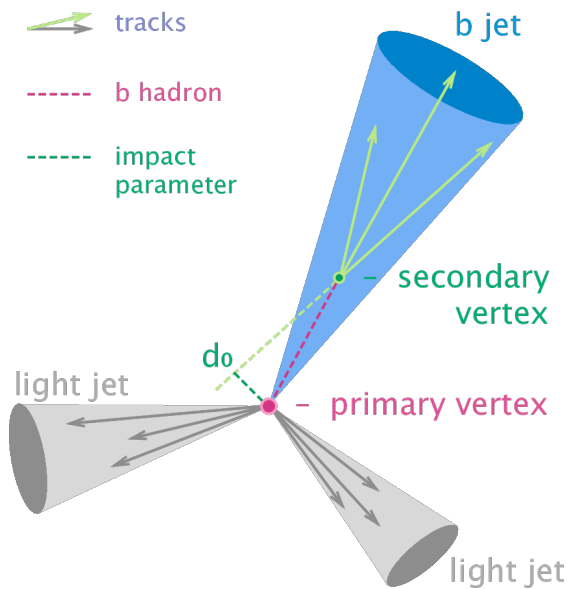


**Figure 6.21:** Representation of a b hadron decay and reconstructed b jet in the transverse plane.

A variety of algorithms has been developed in CMS [120] to identify b jets based on the b hadron properties described above. These algorithms use low-level physics objects, mainly jets and charged tracks. Only the tracking detectors offer the spatial resolution needed to measure the properties of b hadron decays such as their significant flight path. Efficient track reconstruction, and in particular precise spatial reconstruction close to the interaction point, is thus the key ingredient. Some of these algorithms use just a single observable, while others combine several of these objects to achieve a higher discrimination power. Each of these algorithms yields a single discriminator value for each jet. The minimum thresholds on these discriminators define loose (“L”), medium (“M”), and tight (“T”) operating points with a misidentification probability for light-flavor jets of 10%, 1%, and 0.1%, respectively, at

an average jet  $p_T$  of about 80 GeV.

The jets used for b tagging are reconstructed with the PF algorithm and calibrated as described in Section 6.4.2. A sample of well-reconstructed tracks of high purity is required as input to each of the b tagging methods. In addition to selection applied in the iterative tracking procedure described in Section 6.1.1, specific requirements are imposed:

- the fraction of misreconstructed or poorly reconstructed tracks is reduced by requiring  $p_T > 1 \text{ GeV}$ ;
- at least 8 tracker hits (including pixel) must be associated with the track;
- at least 2 hits are required in the pixel system since track measurements in the innermost layers provide most of the discriminating power;
- the normalised  $\chi^2$  is required to be  $< 5$  to ensure a good-quality fit;
- the absolute value of the transverse and longitudinal impact parameter of the track must be  $< 0.2$  and  $< 17 \text{ cm}$ , respectively, to reject charged particle tracks having their origin from sources with large displacement from the primary vertex (e.g. photon conversions and nuclear interactions in the beam pipe or the first layers of the pixel detector);
- tracks are associated to jets in a cone  $\Delta R < 0.3$  around the jet axis, where the jet axis is defined by the primary vertex and the direction of the jet momentum;
- in order to reject tracks from pileup the distance to jet axis, defined as the distance of closest approach of the track to the axis, is required to be  $< 700 \mu\text{m}$ ;
- the point of closest approach between the track trajectory and the jet axis, must be within 5 cm of the primary vertex.

Two algorithms for reconstructing secondary vertices are exploited. For the first algorithm, the tracks associated to jets and fulfilling the above selection requirements are used in the *adaptive vertex reconstruction* (AVR) algorithm [121] based on the adaptive vertex fitter described in Section 6.1.1. This is the secondary vertex reconstruction algorithm used for b tagging methods in CMS during Run 1. A number of selection criteria are applied to remove vertices that are less likely to originate from a b hadron decay.

- at least 2 tracks must be associated to the secondary vertex;
- the fraction of tracks shared with the primary vertex is required to be  $< 65\%$ ;
- the distance between the primary vertex to the secondary vertex in the transverse plane, the 2D flight distance, must be in the range 0.1–25 mm;
- the 2D flight distance divided by its uncertainty or so-called 2D flight distance significance has to be  $> 3$ ;
- the invariant mass of charged particles associated to the vertex is required to be  $< 6.5 \text{ GeV}$  and not compatible with the mass of the  $K_S^0$  hadron in a window of 50 MeV;
- the angular distance  $\Delta R$  between the jet axis and the secondary vertex flight direction is required to be less than the jet distance parameter;

In contrast with the AVR algorithm, the *inclusive vertex finder* (IVF) [122], is not seeded from tracks associated to the reconstructed jets. The IVF algorithm uses as input the collection of reconstructed tracks in the event and looser quality criteria are applied. The selected tracks are then used to identify clusters of nearby tracks based on their minimum distance and the angles between them. The clusters are fitted with the adaptive vertex fitter and a cleaning procedure is applied. At this stage, tracks can appear in multiple vertices and therefore, one of the vertices is removed based on the number of shared tracks and distance between the vertex and another one. Furthermore, tracks in the secondary vertex compatible with the primary vertex are removed. When there are at least 2 tracks associated to the secondary vertex after the track arbitration, the vertex is refitted and selection criteria similar to the case of the AVR vertices are applied.

The efficiency to reconstruct a secondary vertex for b (c) jets using the IVF algorithm is about 10% (15%) higher compared to the efficiency to reconstruct a secondary vertex with the AVR algorithm. However, for light-flavour jets the probability to find a secondary vertex also increases by about 8%. Independently of the jet flavour, around 60% of the jets with an AVR vertex also have an IVF vertex.

In this analysis the *Combined Secondary Vertex* (CSV) b tagging algorithm is used, which combines the information of displaced tracks with the information of secondary vertices associated to the jet. This allows the algorithm to avoid limitations due to inefficiencies in the secondary vertex reconstruction. Jets are divided in three vertex-dependent exclusive categories: the presence of a reconstructed secondary vertex; at least two tracks with impact parameter significance larger than 2; none of the previous. The following set of variables with high discriminating power and low correlations are considered:

- the secondary vertex category;
- the 2D flight distance significance of the secondary vertex;
- the number of tracks in the jet
- the number of tracks associated to the secondary vertex;
- the secondary vertex mass;
- the ratio of the energy carried by tracks at the vertex with respect to all tracks in the jet;
- the  $\eta$  of the tracks at the vertex with respect to the jet axis;
- the 2D impact parameter significance of the first track that raises the invariant mass above the charm threshold of 1.5 GeV when subsequently summing up tracks ordered by decreasing impact parameter significance;
- the 3D signed impact parameter significance for each track in the jet.

Two likelihood ratios are built from these variables used to discriminate between b and c jets and between b and light-flavor jets and combined with prior weights of 0.25 and 0.75, respectively. Figure 6.22(a) shows the distribution of the CSV discriminator value in a multijet sample for 8 TeV data and for simulation, for jets clustered with the AK5 algorithm.

The CSV algorithm was further optimized for Run 2 and the new version is referred to as CSV version 2 (CSVv2) [124]. The main differences with respect to the Run 1 version of the CSV algorithm are the different vertex reconstruction algorithm used, the number of

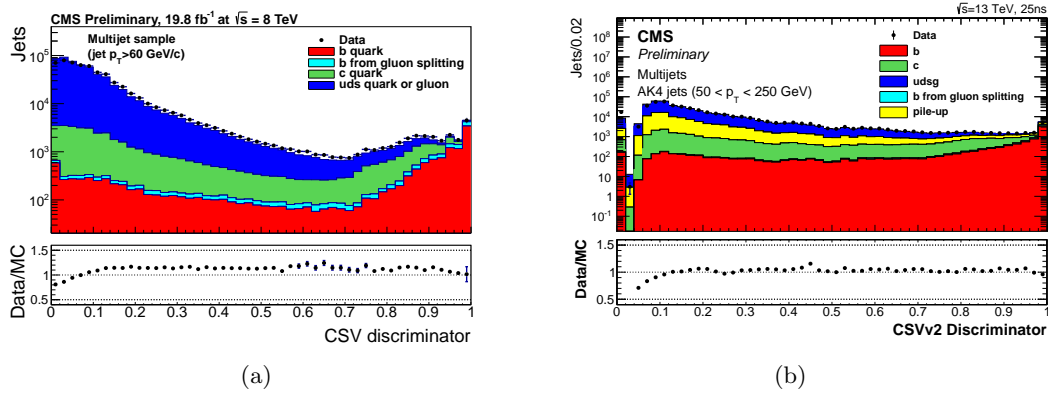


**Figure 6.22:** (a) Distribution of the CSV discriminator value in a multijet sample for data collected at 8 TeV and for simulation [123], for jets reconstructed with the AK5 algorithm. (b) Distribution of the CSVv2 discriminator value in a multijet sample for data collected at 13 TeV and for simulation, for jets clustered with the AK4 algorithm [124].

input variables and the way those are combined. In the newest version the input variables are combined using a multivariate technique. In fact, the likelihood-based method previously used, limited the amount of input variables since correlation between those could not be taken into account properly. In addition, the secondary vertex information is obtained with the IVF method described above. Figure 6.22(b) shows the distribution of the CSVv2 discriminator value in a multijet sample for 13 TeV data and for simulation, for jets clustered with the AK4 algorithm.

The performance of the CSVv2 tagger is presented in Fig. 6.23 as the b jet identification efficiency versus the misidentification probability for jets in simulated  $t\bar{t}$  events requiring jet  $p_T > 30$  GeV. A comparison is shown with the Run 1 version of the CSV algorithm trained for 8 TeV pp collisions using AK5 jets. The absolute improvement of the CSVv2 algorithm with respect to the CSV is of the order of 2 to 4% in b jet identification efficiency when comparing at the same misidentification probability for light-flavour jets. The improvement of using IVF vertices with respect to using AVR vertices in the CSVv2 algorithm is of the order of 1 to 2%.

The value of the discriminator threshold for the b tagging algorithms used in this analysis and the corresponding efficiencies are presented in Table 6.13. In this analysis the medium working point is used to identify and reject  $t\bar{t}$  events where a real b jet is expected in addition to the large-cone jet used to reconstruct the  $V \rightarrow q\bar{q}^{(\prime)}$  or  $H \rightarrow bb$  candidate, representing instead the signal. The same b tagging algorithm but together with the loose working point is used to identify whether the CA8 jet comes from a H boson decaying into bottom quarks, as described in Section 7.3.

The mismodelling of the b tagging variables in simulation is taken into account by reweighting simulation event-by-event with the ratio of the b tagging efficiency in data and simulation, determined in a sample enriched with b jets and depending on the jet  $p_T$  and  $\eta$ . The correction factors as a function of the b jet  $p_T$  are shown in Fig. 6.24(a) and 6.24(b) for the CSVM and CSVv2M operating points respectively, as measured in 8 and 13 TeV data. In a similar way, correction factors are also derived and applied to correct the misidentification probability in simulation. These factors are shown in Fig. 6.25(a) and 6.25(b) as a function of the jet  $p_T$  for the CSVM and CSVv2M operating points.

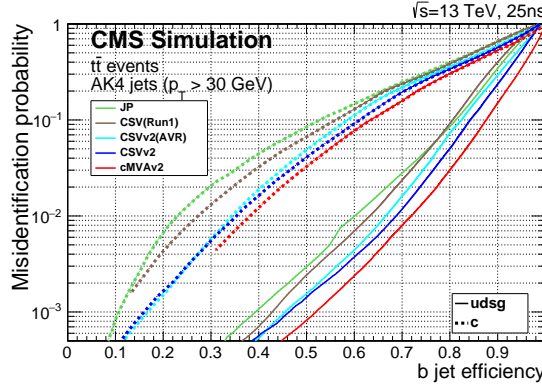


**Figure 6.23:** Performance of the CSVv2 algorithm showed as the probability for non-b jets to be misidentified as b jet as a function of the efficiency to correctly identify b jets. The improvement of this algorithm with respect to the Run 1 version is also shown [124].

**Table 6.13:** B taggers and discriminator threshold used in CMS for Run 1 and Run 2 and corresponding efficiency for b jets with  $p_T > 30$  GeV in simulated  $t\bar{t}$  events.

Algorithm	operating point	discriminator value	b tagging efficiency (%)
CSV (Run 1)	CSVL	0.244	84
	CSVM	0.679	68
	CSVT	0.898	52
	CSVv2L	0.460	83
CSVv2 (Run 2)	CSVv2M	0.800	69
	CSVvsT	0.935	49

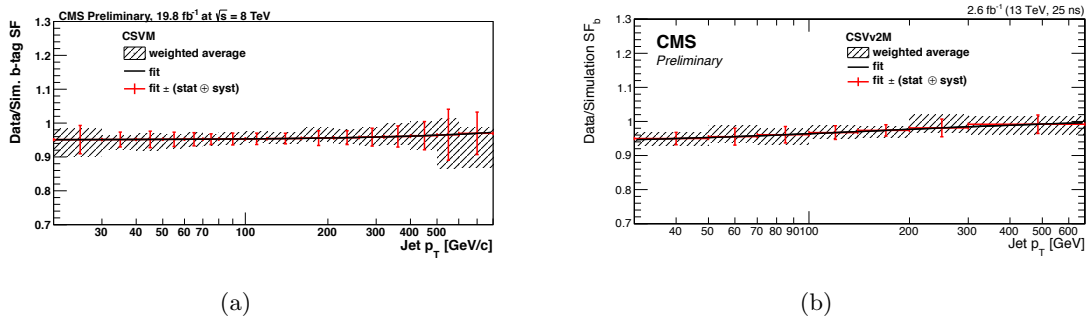


**Figure 6.24:** Data-to-simulation correction factors for the b tagging efficiency for the CSVM (a) and CSVv2M (b) algorithms as a function of the b jet  $p_T$  as measured in 8 and 13 TeV data [123, 124].

## 6.5 Missing transverse energy

CMS is a full coverage hermetic detector which identifies and reconstructs almost all stable or long-lived particles produced in pp collisions. The only exceptions are neutrinos and hypothetical neutral weakly interacting particles. Although these particles do not leave a signal in the detector, their presence can be inferred from the momentum imbalance in the transverse plane, a quantity known as missing transverse momentum and denoted by  $\vec{p}_T^{\text{miss}}$ .

Several standard methods are available in CMS for the reconstruction of  $\vec{p}_T^{\text{miss}}$ , which, as

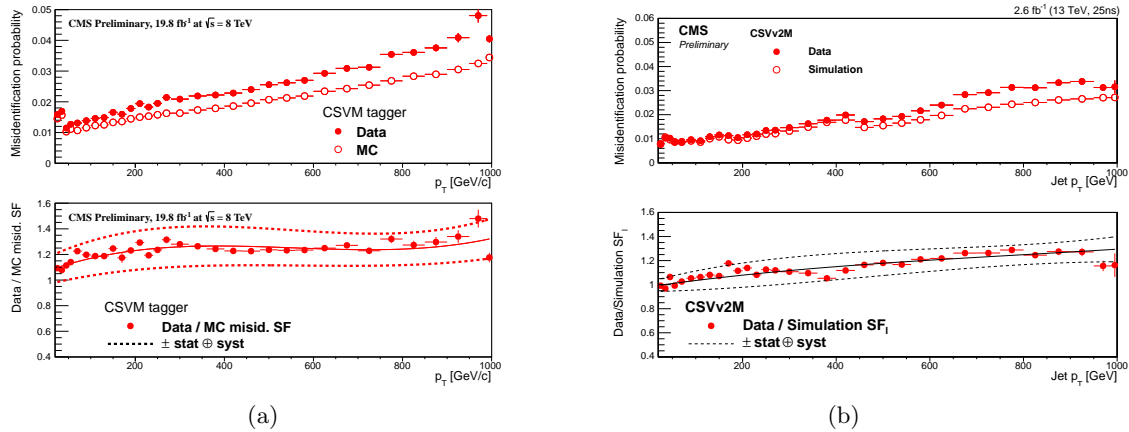


**Figure 6.25:** Data-to-simulation correction factors for the misidentification probability for the CSVM (a) and CSVv2M (b) algorithms as a function of the jet  $p_T$  as measured in 8 and 13 TeV data [123,124].

for the jet reconstruction, can be based on calorimeter information only, include also tracker information, or use the PF algorithm [125]. In this analysis, the PF  $\vec{p}_T^{\text{miss}}$  is used along with PF jets and it is calculated as the negative vector sum of the transverse momenta of all reconstructed PF candidates in a given event

$$\vec{p}_T^{\text{miss}} = - \sum_i^N \vec{p}_{T,i}. \quad (6.3)$$

Its magnitude is referred to as missing transverse energy and denoted by  $E_T^{\text{miss}}$ . The  $E_T^{\text{miss}}$  is an important variable in many searches for physics beyond the standard model such as the ones described in this thesis where a real highly energetic neutrino is expected in the final state. In addition, the precise measurement of  $E_T^{\text{miss}}$  plays a crucial role for measurements of standard model physics involving W bosons and top quarks. The  $\vec{p}_T^{\text{miss}}$  reconstruction is sensitive to pileup, detector malfunctions and to various reconstruction effects and a precise calibration of all reconstructed physics objects is crucial for its performance. The level of mismeasurement is significantly reduced after jet energy calibration, described in Section 6.4.2. A correction to the  $\vec{p}_T^{\text{miss}}$  is derived by propagating the jet energy scale corrections as described in the following.

The raw missing transverse momentum can be written as:

$$\vec{p}_T^{\text{miss,raw}} = - \sum_i^{N_{\text{jets}}} \vec{p}_{T,i}^{\text{raw}} - \sum_i^{N_{\text{uncl}}} \vec{p}_{T,i}, \quad (6.4)$$

where the first and second sum runs over the  $p_T$  of the PF candidates clustered as jets and unclustered, respectively, and the superscript ‘‘raw’’ indicates the uncorrected value. The correction to the  $\vec{p}_T^{\text{miss}}$  is then obtained by replacing the first sum with the vector sum of the transverse momenta of the jets to which jet energy scale corrections (JEC) are applied:

$$\vec{C}_T^{\text{JEC}} = \sum_i^{N_{\text{jets}}} \vec{p}_{T,i}^{\text{raw}} - \sum_i^{N_{\text{jets}}} \vec{p}_{T,i}^{\text{JEC}}, \quad (6.5)$$

where the sum is performed over all jets with corrected  $p_T > 10$  GeV.

Further corrections improve the performance of the  $\vec{p}_T^{\text{miss}}$  reconstruction in events with large numbers of pileup interactions. This is achieved as explained in the following.

The raw  $\vec{p}_T^{\text{miss}}$  can be written as a sum of the two contributions due to particles produced in the primary vertex (PV) and in pileup interactions (PU)

$$\vec{p}_T^{\text{miss,raw}} = - \sum_{i \in \text{PV}} \vec{p}_{T,i} - \sum_{i \in \text{PU}} \vec{p}_{T,i}. \quad (6.6)$$

Particles produced in the pileup interactions can be further classified into neutral (PUneu) and charged (PUch) particles so that the equation above can be expressed as

$$\vec{p}_T^{\text{miss,raw}} = - \sum_{i \in \text{PV}} \vec{p}_{T,i} - \sum_{i \in \text{PUch}} \vec{p}_{T,i} - \sum_{i \in \text{PUneu}} \vec{p}_{T,i}. \quad (6.7)$$

The contribution to the genuine  $\vec{p}_T^{\text{miss}}$  from such interactions is close to zero, as the probability to produce neutrinos is small in inelastic pp scattering interactions (e.g. neutrinos from Kaon decays). The vectorial  $\vec{p}_T$  sum of charged particles is therefore expected to be well balanced by that of neutral particles. However, the nonlinearity and minimum energy thresholds in the calorimeters cause  $\vec{p}_T^{\text{miss}}$  to point on average in the direction of the vectorial  $\vec{p}_T$  sum of neutral particles. Nevertheless, it can be assumed that the directions of neutral pileup particles is measured with high precisions from the positions of the calorimeter cells in which we observe the energy deposits, while their energies are systematically off by the same factor. At the same time, the CMS tracker can also measure very well the charged pileup particles from their large curvature due to the low  $p_T$  characterizing this type of processes. With these assumptions, the total contribution from pileup can be estimated as

$$\vec{\Delta}_{\text{PU}} = \sum_{i \in \text{PUch}} \vec{p}_{T,i} + \sum_{i \in \text{PUneu}} \vec{p}_{T,i} = \sum_{i \in \text{PU}} f(\vec{v}) \vec{v}, \quad (6.8)$$

where  $\vec{v}$  represents the sum of the transverse momenta of charged particles for each pileup interaction. The correction  $f(\vec{v})$  is parametrized as  $f(\vec{v}) = c_1(1.0 + \text{erf}(-c_2|\vec{v}^{c_3}|))$ , where the coefficients  $c_1$ ,  $c_2$ , and  $c_3$  are extracted from simulated minimum bias events. The corrected  $\vec{p}_T^{\text{miss}}$  is then obtained removing the additional contribution  $\vec{\Delta}_{\text{PU}}$  from Eq. 6.6

$$\vec{p}_T^{\text{miss,PUcorr}} = \vec{E}_T^{\text{miss,raw}} + \vec{\Delta}_{\text{PU}}. \quad (6.9)$$

Another type of correction is derived and applied to correct for a modulation in  $\phi$  in the  $\vec{p}_T^{\text{miss}}$  present not only in data but also in simulation. The distribution of genuine  $\vec{p}_T^{\text{miss}}$  is instead independent of  $\phi$  because of the rotational symmetry of the collisions around the beam axis. The possible causes of the modulation include imperfect detector alignment, inefficiencies, a residual  $p_T$  dependence of the calibration, and a shift between the center of the detector and the beam line. The correction for this effect can be expressed as a shift in the  $\vec{p}_T^{\text{miss}}$  components along the  $x$  and  $y$  detector coordinates, which increases approximately linearly with the number of reconstructed vertices. This correlation is used for a correction procedure as follows

$$\vec{E}_{T,x}^{\text{miss,phi corr}} = \vec{E}_{T,x}^{\text{miss,raw}} - (c_{x_0} + c_{x_s} N_{\text{vtx}}), \quad \vec{E}_{T,y}^{\text{miss,phi corr}} = \vec{E}_{T,y}^{\text{miss,raw}} - (c_{y_0} + c_{y_s} N_{\text{vtx}}), \quad (6.10)$$

where the coefficients are determined separately for data and simulated events.

Other more sophisticated missing energy determinations aimed at improving the resolution have been developed in CMS [126, 127] but will not be discussed in this section since they are

not used in this work.

The distributions of the PF  $E_T^{\text{miss}}$ , obtained after applying all the corrections described above, in  $Z \rightarrow \mu^+\mu^-$ ,  $Z \rightarrow e^+e^-$ , and prompt photon events are presented in Fig. 6.26 as measured in 8 TeV data and for simulation. Good agreement between data and simulation is observed in all distributions.

These events contain no genuine  $\vec{p}_T^{\text{miss}}$ , and thus a balance exists between the well-measured vector boson transverse momentum, denoted as  $\vec{q}_T$ , and the hadronic recoil, denoted as  $\vec{u}_T$ , which dominates the  $\vec{p}_T^{\text{miss}}$  measurement. The  $q_T$  can therefore be used as a reference to measure the scale and resolution of  $\vec{p}_T^{\text{miss}}$ . The hadronic recoil can be projected to the axis defined by  $q_T$ , yielding two signed components, parallel ( $u_{\parallel}$ ) and perpendicular ( $u_{\perp}$ ) to this axis. The parallel component is typically negative as the observed hadronic system is usually in the hemisphere opposite the boson. The scalar quantity  $-\langle u_{\parallel} \rangle / \vec{q}_T$  is referred to as the  $\vec{p}_T^{\text{miss}}$  response. The response curves, extracted from the data as a function of the vector boson boost  $\vec{q}_T$ , are shown in Fig. 6.27(a), where deviations from unity indicate a bias on the hadronic recoil energy scale which is fully recovered for  $\vec{q}_T > 40$  GeV. The resolution curves,  $\sigma(u_{\parallel})$  and  $\sigma(u_{\perp})$  as a function of  $q_T$ , are shown in Fig. 6.27(b) and 6.27(c), respectively, for each control sample. The resolution increases with increasing  $q_T$ , while the data and simulation curves are in good agreement for each control sample.

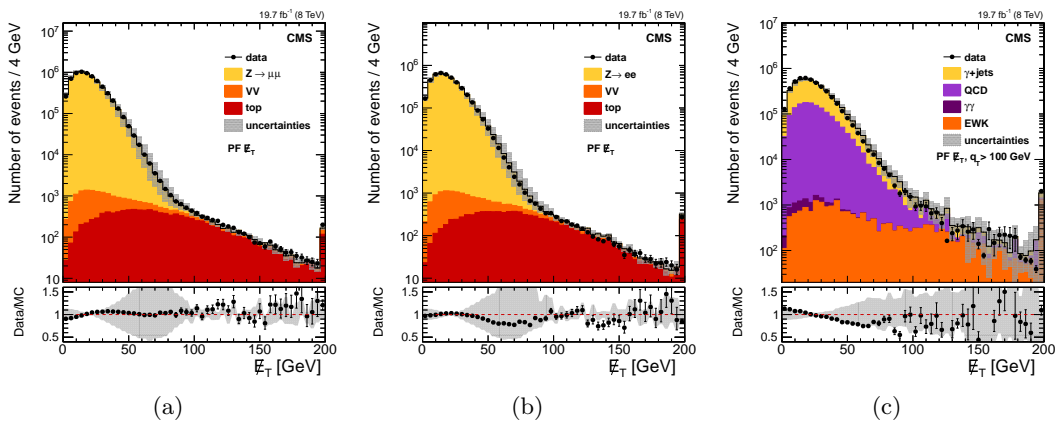


**Figure 6.26:** The PF  $E_T^{\text{miss}}$  distribution in  $Z \rightarrow \mu^+\mu^-$  (a),  $Z \rightarrow e^+e^-$  (b), and prompt photon (c) events for 8 TeV data and for simulation. The points in the lower panel of each plot show the ratio between data and simulation describing their agreement [126].

## 6.6 $W \rightarrow \ell\nu$ reconstruction

The identified muon or electron (see Section 6.2.3 and 6.3.3) is associated with the  $W \rightarrow \ell\nu$  candidate. The  $\vec{p}_T$  of the undetected neutrino is assumed to be equal to the  $\vec{p}_T^{\text{miss}}$ . The longitudinal momentum of the neutrino ( $p_z$ ) is obtained by solving a quadratic equation that sets the  $\ell\nu$  invariant mass to the known  $W$  boson mass [3]:

$$M_W^2 = m_\ell^2 + 2(E_\ell E_\nu - p_{x_\ell} p_{x_\nu} - p_{y_\ell} p_{y_\nu} - p_{z_\ell} p_{z_\nu}) = (80.4)^2 \quad (6.11)$$

In the case of two real solutions, the one with the smaller absolute value is chosen. If the discriminant becomes negative, or equivalently the  $W$  boson transverse mass  $M_T$  is larger

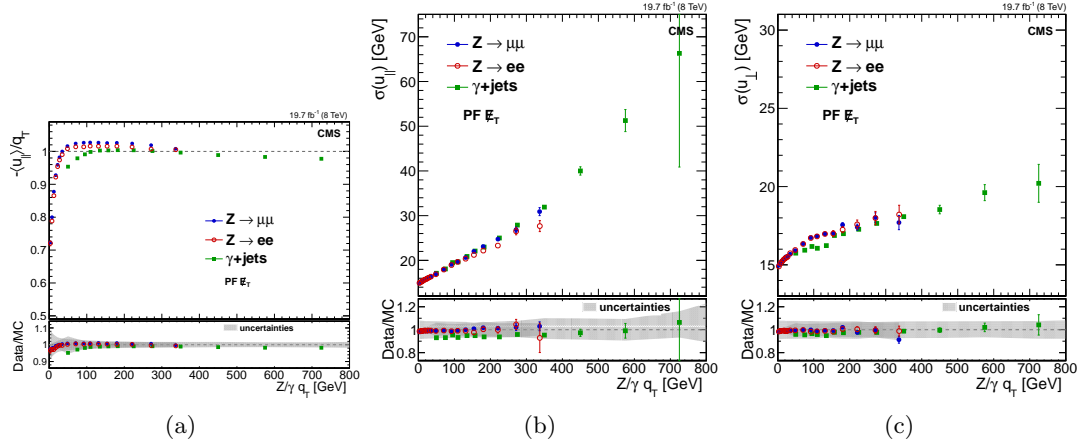


**Figure 6.27:** (a) Response curves for PF  $\vec{p}_T^{\text{miss}}$  in events with a Z-boson or prompt photon. Also shown are the resolution curves of the parallel (b) and perpendicular (b) recoil components as a function of the  $Z/\gamma q_T$ . In each plot the upper frame shows the response in 8 TeV data, while the lower one shows the ratio between data and simulation. [126].

than  $M_W$  used in the constraint, the solutions have an imaginary part. This happens because of the finite resolution of  $E_T^{\text{miss}}$ . Several schemes exist to deal with this situation. One technically simple method consists of taking the real part of the complex solutions but it leads to the wrong W boson mass. This method is used for the reconstruction of the  $W \rightarrow \ell\nu$  candidate in the 13 TeV data analysis described in this work. A second method has been studied, which eliminates the imaginary component by modifying the components of the missing transverse energy such to give  $M_T = M_W$ , still respecting equation 6.11 [128]. This method is used in the 8 TeV data analysis for the reconstruction of the  $W \rightarrow \ell\nu$  candidate and for the reconstruction of the mass of the leptonically decaying top quark in  $t\bar{t}$  events. The performance of the two methods are equivalent in terms of resolution of the reconstructed diboson or top quark invariant mass.

The four-momentum of the neutrino is used to reconstruct the four-momentum of the  $W \rightarrow \ell\nu$  candidate. The same procedure holds also for the cases where the W boson decays to  $\tau\nu$  and the  $\tau$  decays to one muon or electron and two neutrinos. In this case, the  $\vec{p}_T^{\text{miss}}$  represents the  $\vec{p}_T$  of the three-neutrino system.

# Identification of highly boosted $W/Z \rightarrow q\bar{q}^{(\prime)}$ and $H \rightarrow b\bar{b}$

---

Large-cone jets (Section 6.4), also referred to as “fat jets”, are used to reconstruct the  $W$  jet,  $Z$  jet, and  $H$  jet candidates resulting after the hadronization of the two quarks from the decay of highly boosted  $W$ ,  $Z$ , and Higgs boson, respectively. In fact, for the resonance mass range considered in this search, the two quarks from the  $V$  or Higgs boson decay would be separated by a small angle, resulting in the detection of a single “merged” jet after hadronization, instead of two separated jets. To discriminate against multijet backgrounds, the analysis exploits both the reconstructed jet mass, which is required to be close to the boson mass, and the jet substructure arising from the two jet cores that correspond to the two high- $p_T$  decay quarks. The techniques used to identify jets arising from the merged decay products of a single  $V$  or Higgs boson are referred to as “ $V$  tagging” or “ $H$  tagging”, respectively. They employ novel jet substructure algorithms, which are described in Section 7.1. The features of the  $V$  tagging algorithm are described in Section 7.2 and its performance in both data and simulation are discussed. Finally, in Section 7.3, a procedure tuned to the specific properties of the Higgs boson decay into a bottom quark-antiquark pair is presented.

## 7.1 Jet substructure observables

### 7.1.1 Pruned jet mass

As the mass of the  $V$  or Higgs boson is larger than the mass of a typical QCD jet, the jet mass is the primary observable that distinguishes them from a QCD jet. The bulk of the signal jet mass arises from the kinematics of the two jet cores that correspond to the two decay quarks. In contrast, the QCD jet mass arises mostly from large-angle and soft gluon radiation. As a first step in exploring potential substructure, the jet constituents are subjected to a jet grooming algorithm that improves the resolution in the jet mass and reduces the effect of pileup [109, 129]. The goal of jet grooming is to recluster the jet constituents, while applying additional requirements that eliminate soft, large-angle QCD radiation. This procedure shifts the jet mass of QCD jets to smaller values, while maintaining the mass for signal jets close to the boson mass. Furthermore, soft contributions from the underlying event and pileup, usually present in all jets, are removed. Different jet grooming algorithms have been explored at CMS and their performance on jets in multijet processes has been studied in detail [109, 129]. In this analysis, the *jet pruning* algorithm [130, 131] is used, as it was found to provide the best discrimination against QCD background as discussed in Ref. [109, 129].

Jet pruning reclusters each fat jet starting from all its original constituents, through the implementation of the CA algorithm, but applying two additional conditions beyond those given in 6.1. In particular, the softer of the two particles  $i$  and  $j$  to be merged is removed when the following conditions are met:

$$z_{ij} \equiv \frac{\min(p_{Ti} + p_{Tj})}{p_{Ti} + p_{Tj}} < z_{cut}, \quad \Delta R_{ij} > D_{cut} \equiv \alpha \frac{m_j}{p_T} \quad (7.1)$$

where  $m_j$  and  $p_T$  are the mass and transverse momentum of the originally-clustered jet, and  $z_{cut}$  and  $\alpha$  are parameters of the algorithm, chosen to be 0.1 and 0.5, respectively. In this particular choice of parameters, the algorithm removes the largest number of jet constituents, and can therefore be regarded as the most aggressive jet grooming technique. The resulting jet is the *pruned jet*. The pruned jet mass,  $m_{jet}$ , is computed from the sum of the four-momenta of the constituents that survive the pruning; it is then corrected by the same factor used to correct the jet  $p_T$  (Section 6.4). Figure 7.1(a) illustrates the effect of pruning on AK8 jets: the  $m_{jet}$  spectrum of the  $W$  jet candidate from the decay of highly boosted and longitudinally polarized  $W$  bosons is shown together with the distribution in  $m_{jet}$  for the simulated background of  $W+jets$ . Dashed and solid lines correspond to the distributions before and after the application of the pruning algorithm, respectively. Fully merged jets reconstructed from the  $W$  boson decay generate a distinctive peak around the  $W$  boson mass, which is narrowed by the pruning, while background jets acquire a smaller mass on average, enhancing the discrimination. Figure 7.1(b) compares the distributions in  $m_{jet}$  for  $W$ ,  $Z$  and  $H$  jet candidates from the decay of highly boosted  $W$ ,  $Z$  and Higgs bosons, respectively. The distribution in  $m_{jet}$  for the  $W+jets$  background is also shown. Not-full-merged signal jets give rise to a peak at low masses.

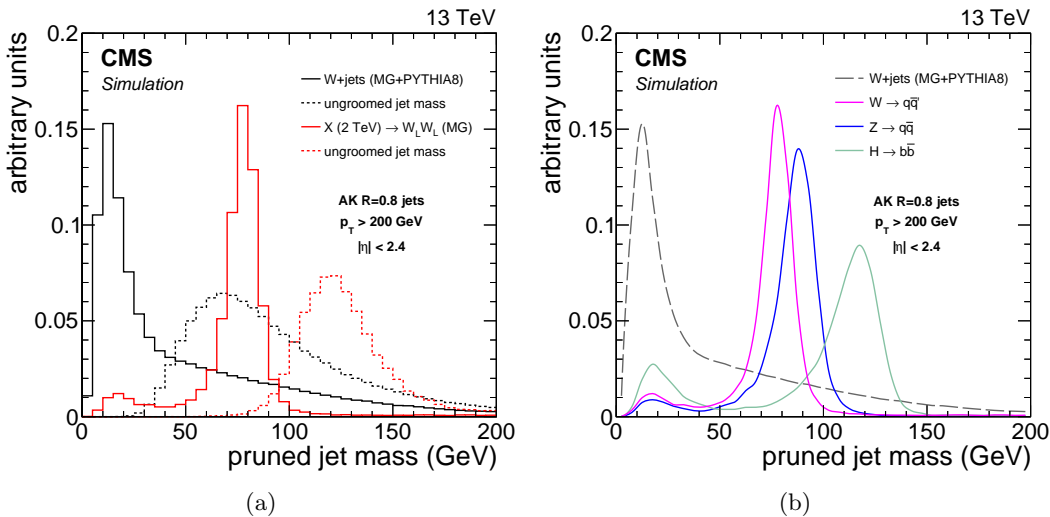


**Figure 7.1:** (a) Distribution in pruned jet mass  $m_{jet}$  for simulated events of highly boosted  $W$  bosons and inclusive QCD jets expected in the  $W+jets$  process. The ungroomed jet mass is shown as dotted lines to illustrate the effect of pruning. MG denotes the MADGRAPH generator. (b) Comparison of the distributions in  $m_{jet}$  for simulated events of highly boosted  $V$  and Higgs bosons.

### 7.1.2 N-subjettiness

In addition to the pruned jet mass, additional information about the jet shape is used to discriminate the signal against jets from gluon and single-quark hadronization. This information can be obtained from the quantity called *N-subjettiness* [132]. It takes advantage of the multi-body kinematics in the decay pattern of boosted hadronic objects, and it can be used to effectively “count” the number of subjets in a given jet.

The N-subjettiness is a generalized jet shape observable which defines a measure,  $\tau_N$ , for a jet to have  $N$  subjets. The constituents of the jet before the pruning procedure are reclustered using the  $k_T$  algorithm (Section 6.4), until  $N$  joint objects (subjets) remain in the iterative combination procedure of the algorithm. The observable  $\tau_N$  is then defined as

$$\tau_N = \frac{1}{d_0} \sum_k p_{T,k} \min\{\Delta R_{1,k}, \Delta R_{2,k}, \dots, \Delta R_{N,k}\}, \quad (7.2)$$

where  $k$  runs over the constituents of the jet, and the distances  $\Delta R_{n,k}$  are calculated relative to the axis of the  $n$ th subjet. The normalization factor  $d_0$  is taken as

$$d_0 = \sum_k p_{T,k} R_0, \quad (7.3)$$

where  $R_0$  is the characteristic jet radius used in the original jet clustering algorithm. The subjet axes are obtained by running the exclusive  $k_T$  algorithm [105], and reversing the last  $N$  clustering steps. The variable  $\tau_N$  quantifies the compatibility of the jet clustering with the hypothesis that exactly  $N$  subjets are present. Jets with  $\tau_N \approx 0$  have all their radiation aligned with the candidate subjet directions and therefore have  $N$  (or fewer) subjets. Jets with  $\tau_N \gg 0$  have a large fraction of their energy distributed away from the candidate subjet directions and therefore have at least  $N + 1$  subjets. The ratio between 2-subjettiness and 1-subjettiness,  $\tau_{21} = \tau_2/\tau_1$ , is found to be a powerful discriminant between jets originating from hadronic V decays and from gluon and single-quark hadronization. Jets from  $V \rightarrow q\bar{q}^{(\prime)}$  decays in signal events are characterized by lower values of  $\tau_{21}$  relative to QCD background. Figure 7.2 shows the  $N$ -subjettiness ratio  $\tau_{21}$  distribution for W jets and QCD jets after requiring  $60 < m_{\text{jet}} < 100$  GeV, demonstrating its discrimination power after the pruned jet mass selection.

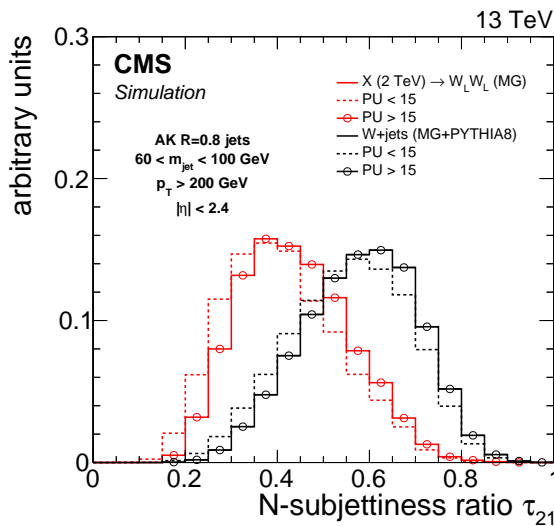


**Figure 7.2:** Distribution in N-subjettiness ratio  $\tau_{21}$  for simulated events of highly boosted and longitudinally polarized W bosons and inclusive QCD jets expected in the W+jet process. The distributions are shown after a selection on the pruned jet mass requiring  $60 < m_{\text{jet}} < 100$  GeV. The histograms are the expected distributions after full CMS simulation with pileup corresponding to an average number above and below 15 interactions.

## 7.2 The V tagging algorithm

The jet substructure observables described in the previous section are employed for identifying, or “tagging”,  $W$  and  $Z$  jets (“V jets”). The V tagging of the jets is obtained combining selections on both the pruned jet mass  $m_{\text{jet}}$  and N-subjettiness ratio  $\tau_{21}$  observables.

The selection criteria have been optimized in the context of searches for resonances decaying into diboson in the  $\ell\nu$ +jet and dijet final states [133–135]. The optimization, based on simulation, aims at maximizing the analysis sensitivity and it leads to slightly different working points for each analysis. In particular, the baseline selection values have been changed from Run 1 to Run 2. Typical signal efficiencies and mistagging rates of QCD jets obtained, respectively, from simulations and measurements with 8 and 13 TeV data are summarized in Table 7.1, for jets with  $p_T = 500$  GeV.

**Table 7.1:** Typical selection criteria for V tagging used in Run 1 and Run 2. The corresponding signal efficiency and mistagging rate of QCD jets are also reported for jets with  $p_T = 500$  GeV, obtained from 8 and 13 TeV data and from simulation.

Data sets	V tagging selections	signal efficiency	mistagging rate
8 TeV	$60 < m_{\text{jet}} < 100$ GeV $\tau_{21} < 0.5$	0.65	0.04
13 TeV	$65 < m_{\text{jet}} < 105$ GeV $\tau_{21} < 0.45$	0.55	0.03

The  $\ell\nu q\bar{q}$  analysis described in this work makes use of a looser  $\tau_{21}$  working point of 0.6 resulted from an optimization which takes into account signal efficiency and background rejection over a large jet  $p_T$  range. In fact, this channel is characterized by a low background rate and a  $\tau_{21}$  selection providing a higher signal efficiency over the whole jet  $p_T$  range is therefore preferred. This working point corresponds to a signal efficiency of 65% and a mistagging rate of 5%.

The V tagging performance at 8 TeV has been studied in detail in Ref. [109]. From simulation studies it is observed that the efficiency of the  $m_{\text{jet}}$  selection increases with  $p_T$  up to about 600 GeV since at higher  $p_T$  the showers from the  $W$  decay quarks are more likely to be reconstructed within a single fat jet. Above 600 GeV, the efficiency begins to decrease as a function of jet  $p_T$ , since at very large values the PF candidate reconstruction degrades in resolving the jet substructure, and the pruning algorithm therefore removes too large a fraction of the jet mass. For Run 2, the PF reconstruction has been optimized by exploiting the full potential of the CMS ECAL granularity to resolve jet substructure and a constant efficiency is maintained up to at least  $p_T = 2.5$  TeV [114, 136].

The efficiency of the additional  $\tau_{21}$  selection also drops as a function of  $p_T$ , thus a fixed working point will degrade the efficiency with increasing  $p_T$ . However, the same efficiency at an equivalent background rejection rate can be reached by adjusting the  $\tau_{21}$  selection as a function of  $p_T$ . This possibility has not been explored yet in any of the searches which employ V tagging.

The efficiency of the V tagging selection as a function of the number of reconstructed primary vertices (PV) has also been studied [114]. It is observed that the efficiency of the  $m_{\text{jet}}$  selection is constant as a function of PV, whereas the additional  $\tau_{21}$  selection efficiency drops from 60% at 0 PV to 40% at 30 PV. However, the mistagging of the background also decreases with pileup for the same selection, yielding similar discrimination. Efficiency and mistagging rate are affected by pileup in the same way, since additional pileup shifts the  $\tau_{21}$

distribution towards higher values (towards background like) for both signal and background (Fig. 7.2). Therefore, the same signal efficiency can be reached at the same background rejection rate for up to 30 reconstructed vertices by merely adjusting the  $\tau_{21}$  selection.

An important factor that influences the V tagging performance is the polarization of the reconstructed V bosons. In fact, the pruned jet mass selection is less efficient for transversely polarized ( $V_T$ ) V bosons. This can be explained by a higher asymmetry in the  $p_T$  of the two quarks from the  $V_T$  boson decay, such that the pruning algorithm in a considerable fraction of events rejects the particles from the lower  $p_T$  quark and yields a much lower jet mass. In addition, the  $\Delta R$  separation between the partons for pure longitudinally polarized ( $V_L$ ) V bosons is smaller on average than for  $V_T$  bosons and is more likely to be accepted by a large-cone jet. In the analysis presented in this work only  $V_L$  bosons are considered.

This analysis relies on the modelling of the jet substructure variables  $m_{\text{jet}}$  and  $\tau_{21}$  in simulation. The data/simulation discrepancies in  $m_{\text{jet}}$  and  $\tau_{21}$  can bias the signal efficiency estimated from simulated samples. Therefore, the modelling of signal efficiency is cross-checked in a signal-free sample with jets having characteristics that are similar to those expected for a genuine signal [114]. A pure sample of high- $p_T$  W bosons, that decay to quarks and are reconstructed as a single jet, is obtained selecting  $t\bar{t}$  and single top quark events. Scale factors for the  $\tau_{21}$  selection efficiency are extracted by estimating the selection efficiency on both data and simulation for the pure W jet signal. This is achieved by subtracting the background contribution. The generated W boson in the  $t\bar{t}$  simulation provides a model of the contribution from the W jet peak in the pruned jet mass. The contribution from combinatorial background is derived from  $t\bar{t}$  simulation as well. This signal plus background model is fitted directly in the distributions of data and in their simulation.

The pruned jet mass distribution of events that pass and fail the  $\tau_{21}$  selection are fitted simultaneously to extract the selection efficiency on the pure W jet component. The ratio of data and simulation efficiencies are taken as the V tagging efficiency scale factor. Figure 7.3 shows the fits obtained with 13 TeV data for the  $\tau_{21} < 0.45$  selection and similar results are obtained for the looser  $\tau_{21} < 0.6$  selection used in the  $\ell\nu q\bar{q}$  analysis presented in this work. The extracted scale factor for this selection is  $1.01 \pm 0.03$  and it is used to correct the total signal efficiency and the VV background normalization predicted by the simulation. The quoted uncertainty includes two systematic effects. One comes from the modelling of the nearby jets and  $p_T$  spectrum in  $t\bar{t}$  MC events, obtained by comparing the selection efficiency estimated from LO and NLO  $t\bar{t}$  simulation. The other is due to the choice of the models used to fit signal and background. The quadratic sum of these systematic uncertainties is found to be smaller than half of the statistical uncertainty on the scale factor. An additional uncertainty is calculated to account for the extrapolation of the scale factor from  $t\bar{t}$  events with an average jet  $p_T \sim 200$  GeV to higher momenta. This is estimated from the difference between PYTHIA8 and HERWIG++ [137] showering models with a resulting factor of  $4.53\% \times \ln(p_T/200 \text{ GeV})$ .

The peak position in the W jet mass and its resolution are also extracted to obtain data-to-simulation corrections on the pruned jet mass listed in Table 7.2, as obtained from 13 TeV data and from simulation. The quoted uncertainties are statistical. The W jet mass scale in data is  $\approx 1\%$  smaller than in simulation while its resolution is found to be larger by about 5%. In the simulation  $m_{\text{jet}}$  must therefore be shifted and enlarged by the above quantities to correct for the difference between data and simulation.

The mass peak position is slightly shifted relative to the W boson mass. The shift is found to be primarily due to extra radiation in the W jet from the nearby b quark, and additional effects are due to the presence of the extra energy deposited in the jet cone from pileup, underlying event, and initial-state radiation not completely removed in the jet pruning procedure.

Because the kinematic properties of  $W$  jets and  $Z$  jets are very similar, the same corrections are also used when the  $V$  jet is assumed to arise from a  $Z$  boson.

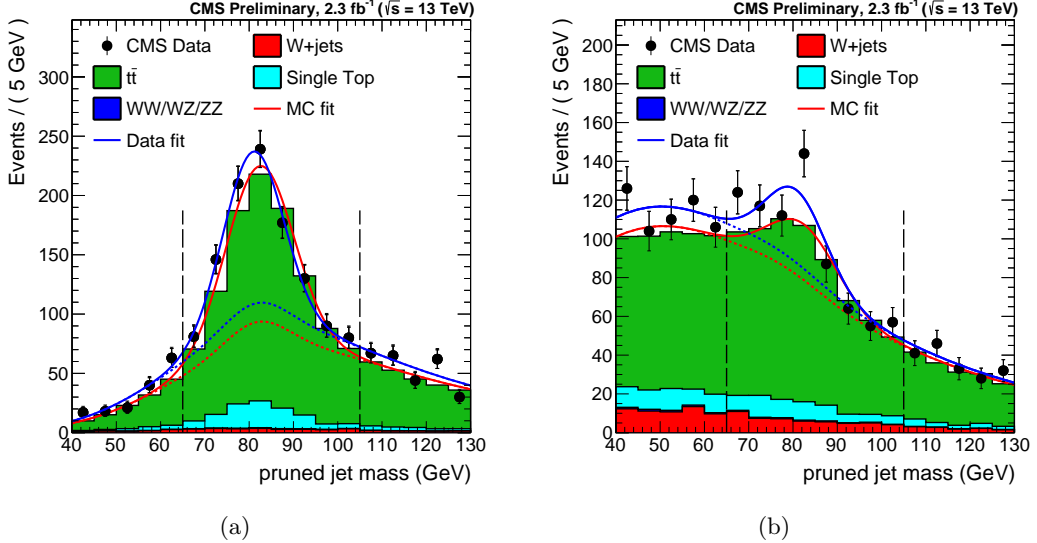


**Figure 7.3:** Distribution in pruned jet mass for events that (a) pass and (b) fail the  $\tau_{21} < 0.45$  selection in the  $t\bar{t}$  control sample. The result of the fit to data and simulation are shown, respectively, by the solid and long-dashed line and the background components of the fit are shown as dashed-dotted and short-dashed line [114].

**Table 7.2:**  $W$  jet mass peak position and resolution, as extracted from top quark enriched sample in 8 TeV data and from simulation, after applying the  $\tau_{21} < 0.5$  selection [109].

$\tau_{21} < 0.45$	$m_{jet} [\text{GeV}]$	Standard deviation [GeV]
Data	$84.1 \pm 0.4$	$8.4 \pm 0.6$
Simulation	$82.7 \pm 0.3$	$7.6 \pm 0.4$

### 7.3 The H tagging algorithm

As discussed in the previous sections boosted  $V$  bosons are reconstructed using jet substructure methods through the  $V$  tagging algorithm, providing large discrimination against multijet backgrounds. However, if one or more of the decay products is a  $b$  quark, adding  $b$  jet identification (Section 6.4) along with jet substructure information can significantly improve the sensitivity of these methods.

Two different approaches to identify boosted  $H \rightarrow b\bar{b}$  candidates have been explored and used at CMS [123]:

- application of  $b$  tagging to the fat jet (“fat jet  $b$  tagging”)
- application of  $b$  tagging to the subjets reconstructed within the fat jet (“subjets  $b$  tagging”)

Both approaches are based on the standard  $b$  tagging algorithms which take advantage of the tracking and vertexing information and are designed to identify jets from single  $b$  quarks.

As described in Section 6.4, the b tagging procedure starts with an association of tracks to jets, based on the angular distance between the tracks and the jet axis. The default b tagging algorithms use the selection  $\Delta R < 0.3$ . However, when applying this to a large-cone jet of size  $R = 0.8$ , the criteria is suboptimal. Hence, to apply b tagging to fat jets, this angular distance is enlarged to  $\Delta R < 0.8$ . For the application of b tagging to subjets, the angular distance remains at the default value of  $\Delta R < 0.3$ .

The H tagging technique starts requiring that the pruned jet mass of the H jet candidate lies in a window around the Higgs boson mass (Fig. 7.1(b)), as this requirement rejects a large fraction of QCD background as demonstrated in the previous sections. The subjets are then obtained by reversing the last step of the pruning recombination algorithm described in Section 7.1.1. In addition to the jet mass requirement, the b tagging is applied either to the whole fat jet or to the two subjets, where both subjets are required to pass the same selection on the CSV discriminator. The b tagging efficiency and misidentification probability of QCD jets after applying the selection  $75 < m_{\text{jet}} < 135 \text{ GeV}$  are shown in Fig. 7.4. The subjet b tagging outperforms the fat jet tagging for most of the phase space.

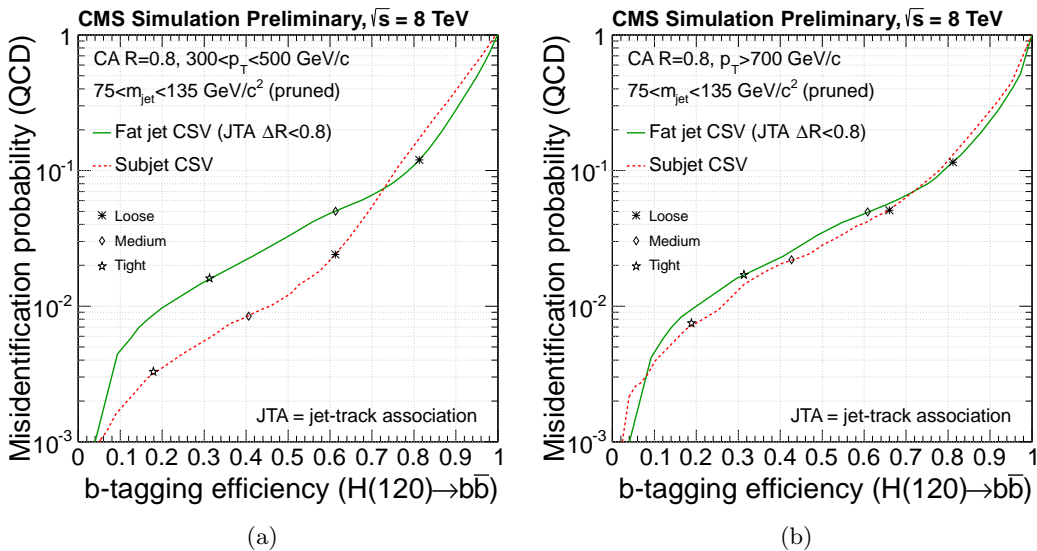


**Figure 7.4:** Misidentification probability as a function of b tagging efficiency for boosted  $H \rightarrow b\bar{b}$  jets and inclusive QCD jets for the CSV algorithm applied to CA8 jets and pruned subjets for jets with (a)  $300 < p_T < 500 \text{ GeV}/c$  and (b)  $p_T > 700 \text{ GeV}/c$ . Loose, medium, and tight operating points of the CSV discriminator are indicated [123].

The H tagging efficiency obtained combining the requirement on the pruned jet mass ( $75 < m_{\text{jet}} < 135 \text{ GeV}$ ) and the subjet b tagging at the CSVL operating point is between 40 and 50% for a H jet  $p_T$  range spanning from 300 GeV to 1 TeV, with a suppression of QCD background to about 0.4%.

The use of a fixed-size jet-track association cone inevitably leads to track sharing between the subjets of the jets once their angular separation becomes comparable or smaller than the size of the association cone. For boosted H jets the fraction of shared tracks, defined as the ratio of the number of tracks within  $\Delta R < 0.3$  from more than one subjet and the number of all tracks within  $\Delta R < 0.3$  from any of the subjets, ranges from a few percent at a jet  $p_T$  of 400 GeV and increases to 40% at a jet  $p_T$  of 700 GeV and to 80% at a jet  $p_T$  of

1 TeV. Because of track sharing, the b tagging probabilities for individual subjets deteriorate at large jet  $p_T$  and the subjet b tagging performance approach the fat jet b tagging one as can be seen in Fig. 7.4. The lost in efficiency is then recovered applying the two approaches depending on the  $\Delta R$  between the two subjets. In particular, the analysis involving boosted Higgs bosons such as the one presented in this work apply subjet b tagging and fat jet b tagging if  $\Delta R > 0.3$  and  $< 0.3$ , respectively. The distribution of the angular separation  $\Delta R$  of the two subjets reconstructed within the fat jet for different jet  $p_T$  ranges in simulated events of highly boosted Higgs bosons decaying to  $b\bar{b}$ , is shown in Fig. 7.5.

In this analysis a requirement on the pruned jet mass of the reconstructed H jet candidate given by  $110 < m_{\text{jet}} < 135$  GeV is applied. The  $m_{\text{jet}}$  window is chosen such that a contamination from possible signals with boosted V jets in the Higgs boson mass region is minimized. The b tagging is performed with the algorithm described above using the loose working point of the CSV discriminant. The total H tagging efficiency for these selections is about 35% for jet  $p_T$  of about 1 TeV with a mistagging probability below 1%.

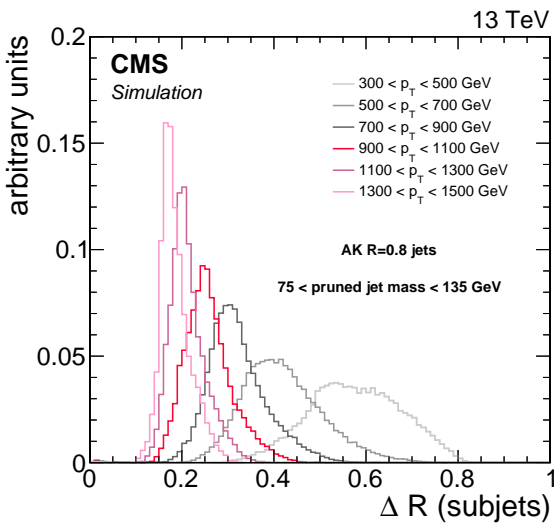


**Figure 7.5:** Distributions of the angular separation  $\Delta R$  of the two subjets reconstructed within the fat jet for simulated events of highly boosted Higgs bosons decaying to  $b\bar{b}$ . The distributions are compared for different ranges of the H jet  $p_T$ .

The validation of b tagging in boosted H jets is performed selecting events containing jets from gluon splitting to  $b\bar{b}$  ( $g \rightarrow b\bar{b}$ ) in which the b quarks hadronize inside the fat jet [123]. To enrich a sample of fat jets in  $g \rightarrow b\bar{b}$  component, used as an analogue of boosted  $H \rightarrow b\bar{b}$  jets, the fat jets are required to be double-muon-tagged with both subjets matched to distinct muon candidates within a cone of size  $\Delta R < 0.4$ . This sample is used to study the modelling of b tagging efficiencies in boosted  $H \rightarrow b\bar{b}$  topologies. The scale factors, given by the ratio between the efficiencies measured in data and simulation, are found to be in good agreement with those measured in the standard, non-boosted topologies, indicating that the simulation reproduces the b tagging performance in boosted and non-boosted environments equally well. These scale factors are used in the analysis to reweight the simulated events.

# Analysis strategy

---

This chapter describes in details the strategy followed in this search, that starting from the physics objects and identification algorithms described in the previous chapters, leads to the final results of the analysis. Although preliminary selections on the objects expected in the final state have already been discussed, tighter requirements and a categorization of the events are applied as described in Section 8.1 to maximize the analysis sensitivity to the signals under study. The final discriminating observable used to search for the signal is represented by the invariant mass of the diboson system. In fact, a possible signal would appear as a localized excess of data in one of the bins on the top of a smooth background. An accurate description of the expected background and signal distributions is therefore fundamental. A background estimation method for the main W+jets component, which makes use of data in sideband regions is used and described in Section 8.2. Another important source of background is represented by top quark production, which is estimated from data in a dedicated control region as discussed in Section 8.3. The background model together with the signal model presented in Section 8.4 is used to perform a maximum likelihood fit of the data in the statistical analysis. The systematic uncertainties in the signal and background predictions discussed in Section 8.5 are treated as nuisance parameters in the statistical interpretation. Finally, Section 8.6 describes the standard procedure for the statistical test of the new signal hypothesis commonly used by LHC experiments and originally developed for the Higgs boson search. The final results are presented in the next chapters.

## 8.1 Final event selection and categorization

Events are selected online with triggers requiring either one muon or electron (Sections 6.2.2 and 6.3.2). Several requirements are then applied offline to the selected events to enhance the analysis sensitivity as described in the following.

The two analyses described in this work feature the same selection strategy on the leptonic part of the final state. Both analyses require exactly one muon or one electron satisfying certain  $p_T$  and  $\eta$  requirements and passing the high- $p_T$  lepton identification criteria described in Sections 6.3.3 and 6.2.3. As summarized in Tables 8.1 and 8.2, the only difference is in the  $p_T$  threshold of the lepton which is higher for the 13 TeV data analysis to match the increase in the trigger threshold. The offline reconstructed  $p_T$  of the electron must be greater than 90 (120) GeV for the 8 (13) TeV data analysis, where the trigger reaches the plateau. This is required in order to avoid any bias on the distributions due to the turn-on of the trigger efficiency curve and its description in simulation. Reconstructed electrons must have  $|\eta| < 2.5$  and also be located outside of the overlap region between the ECAL barrel and endcaps, because the reconstruction of an electron object in this region is not optimal. In a similar way, the offline reconstructed  $p_T$  of the muon must be greater than 50 (53) GeV for the 8 (13) TeV analysis, and within  $|\eta| < 2.1$  as a consequence of the trigger criteria. Events with additional well-identified muons and/or electrons are rejected to avoid contamination from events containing  $Z \rightarrow ll$  decays.

**Table 8.1:** Summary of the final selection for the 8 TeV data analysis in the  $\ell\nu b\bar{b}$  final state.

Selection	Value
Lepton selection	
Electron	$p_T > 90 \text{ GeV}$ $ \eta  < 2.5$ except $[1.44, 1.57]$ range
Muon	$p_T > 50 \text{ GeV}$ $ \eta  < 2.1$
AK5 jet selections	
Jet $p_T$	$p_T > 30 \text{ GeV}$
Jet $\eta$	$ \eta  < 2.4$
$E_T^{\text{miss}}$ selections	
$E_T^{\text{miss}}$ (electron channel)	$E_T^{\text{miss}} > 80 \text{ GeV}$
$E_T^{\text{miss}}$ (muon channel)	$E_T^{\text{miss}} > 40 \text{ GeV}$
Boson selections	
$W \rightarrow \ell\nu$	$p_T > 200 \text{ GeV}$
$H \rightarrow b\bar{b}$ (CA8 jet)	$p_T > 200 \text{ GeV}$
Back-to-back topology	$ \eta  < 2.4$ except $[1.0, 1.8]$ range $\Delta R(\ell, H_{b\bar{b}}) > \pi/2$ $\Delta\phi(H_{b\bar{b}}, \vec{p}_T^{\text{miss}}) > 2$ $\Delta\phi(H_{b\bar{b}}, W_{\ell\nu}) > 2$
Diboson invariant mass	$m_{WH} > 0.7 \text{ TeV}$
H tagging selections	
Pruned jet mass	$110 < m_{\text{jet}} < 135 \text{ GeV}$
Combined b-tagging cut	2 CSVL b-tagged subjets if $\Delta R(\text{subjets}) > 0.3$ 1 CSVL b-tagged CA8 jet if $\Delta R(\text{subjets})$
$t\bar{t}$ rejection	
B-tag veto	no CSVM b-tagged AK5 jet within $\Delta R(H_{b\bar{b}}, AK5) = 0.8$
Top quark mass veto	$m_{\text{top}}^l < 120 \parallel m_{\text{top}}^l > 240$ $m_{\text{top}}^h < 160 \parallel m_{\text{top}}^h > 280$

The requirements  $E_T^{\text{miss}} > 40$  and  $> 80 \text{ GeV}$  are applied, respectively, in the muon and electron channels. The threshold is higher in the electron channel to further suppress the larger background from multijet processes expected at low values of  $E_T^{\text{miss}}$  due to jets misidentified as electrons. This background is expected to be negligible in the muon channel, for which a lower  $E_T^{\text{miss}}$  threshold can be used to preserve a higher efficiency for a low-mass signal. The identified lepton and the  $E_T^{\text{miss}}$  are used to reconstruct the  $W \rightarrow \ell\nu$  candidate as described in Section 6.6, which is required to have  $p_T > 200 \text{ GeV}$ .

A different strategy is instead used in the two analyses, for the hadronic part of the final state. As described in Section 6.4, the CA8 and AK8 algorithms are used to reconstruct the H and V jet candidates in the 8 and 13 TeV analysis, respectively. In both cases the jet is required to have  $p_T > 200 \text{ GeV}$  and  $|\eta| < 2.4$ . For CA8 jets, the pseudorapidity region  $1.0 < |\eta| < 1.8$  is excluded corresponding to the barrel-endcap transition region of the silicon tracker where the reconstruction of tracks is not optimal (Section 6.4.2). The probability of signal events with jets outside this region is 80% (92%) for a resonance mass of 1.0 (2.5) TeV.

The 8 TeV analysis aims at isolating events with a high- $p_T$  Higgs boson decaying to  $b\bar{b}$  and the H tagging algorithm described in Section 7.3 is applied. The H tagging requires the selected CA8 jet to have pruned mass in the range  $110 < m_{\text{jet}} < 135 \text{ GeV}$ . Furthermore, the subjets are required to be b-tagged with the CSVL algorithm if their angular distance  $\Delta R < 0.3$ . Otherwise, b tagging is applied to the whole CA8 jet using the same algorithm.

The 13 TeV analysis is instead focused on events with a high- $p_T$  V boson decaying to  $q\bar{q}$

**Table 8.2:** Summary of the final selection for the 13 TeV data analysis in the  $\ell\nu q\bar{q}$  final state.

Selection	Value
Lepton selection	
Electron	$p_T > 120 \text{ GeV}$ $ \eta  < 2.5$ except $[1.44, 1.57]$ range
Muon	$p_T > 53 \text{ GeV}$ $ \eta  < 2.1$
AK4 jet selections	
Jet $p_T$	$p_T > 30 \text{ GeV}$
Jet $\eta$	$ \eta  < 2.4$
$E_T^{\text{miss}}$ selections	
$E_T^{\text{miss}}$ (electron channel)	$E_T^{\text{miss}} > 80 \text{ GeV}$
$E_T^{\text{miss}}$ (muon channel)	$E_T^{\text{miss}} > 40 \text{ GeV}$
Boson selections	
$W \rightarrow \ell\nu$	$p_T > 200 \text{ GeV}$
$V \rightarrow q\bar{q}$ (AK8 jet)	$p_T > 200 \text{ GeV}$ $ \eta  < 2.4$
Back-to-back topology	$\Delta R(\ell, V_{q\bar{q}}) > \pi/2$ $\Delta\phi(V_{q\bar{q}}, \vec{p}_T^{\text{miss}}) > 2$ $\Delta\phi(V_{q\bar{q}}, W_{\ell\nu}) > 2$
Diboson invariant mass	$m_{VV} > 0.7 \text{ TeV}$
V tagging selections	
Pruned jet mass	$65 < m_{\text{jet}} < 105 \text{ GeV}$
2- to 1-subjettiness ratio	$\tau_{21} < 0.6$
$m_{\text{jet}}$ categories	
WW-enriched	$65 < m_{\text{jet}} < 85 \text{ GeV}$
WZ-enriched	$85 < m_{\text{jet}} < 105 \text{ GeV}$
$t\bar{t}$ rejection	
B-tag veto	no CSV b-tagged AK5 jet within $\Delta R(V_{q\bar{q}}, AK5) = 0.8$

and the V tagging algorithm described in Section 7.3 is applied in this case. The pruned jet mass window is shifted down to the V boson mass, requiring the selected AK8 jet to have pruned mass in the range  $65 < m_{\text{jet}} < 105 \text{ GeV}$ . Furthermore, the V jet is required to have  $\tau_{21} < 0.6$ . Finally, the V jet is deemed a W-boson candidate if its pruned mass falls in the range 65–85 GeV, while it is deemed a Z-boson candidate if it falls in the range 85–105 GeV instead. This categorization has been added on the top of the V tagging requirements on the  $m_{\text{jet}}$  to enhance discrimination between resonances with different charge and spin. Indeed, the first category, referred to as “WW-enriched”, has a higher sensitivity for resonances such as the neutral spin-2 graviton or the neutral spin-1  $Z'$  decaying to WW, where a W jet is expected. The second category, referred to as “WZ-enriched”, is instead optimized for resonances such as the charged spin-1  $W'$  decaying to WZ, where a Z jet is expected.

In addition, there are specific topological selection criteria chosen for both the analyses. It is required that the two V bosons from the decay of a massive resonance are approximately back-to-back: the  $\Delta R$  between the lepton and the signal jet is greater than  $\pi/2$ ; the  $\Delta\phi$  between the vector  $\vec{p}_T^{\text{miss}}$  and the signal jet, as well as between the  $W \rightarrow \ell\nu$  and signal jet candidates, are both greater than 2 radians.

To reduce the level of the  $t\bar{t}$  background, events with one or more reconstructed AK5 (or AK4) jets, not overlapping with the signal jet candidate are analyzed: if one or more of these jets is b-tagged with the CSV algorithm, the event is rejected. For the 8 TeV analysis additional selections are applied to further reduce contamination from  $t\bar{t}$  background. In

fact, the b tagging requirements in this analysis enhance the contribution from top quark production where real b jets are present. A leptonically decaying top quark candidate mass  $m_{\text{top}}^l$  is reconstructed from the lepton,  $E_T^{\text{miss}}$ , and the closest AK5 jet to the lepton using the method described in Section 6.6. A hadronically decaying top quark candidate mass  $m_{\text{top}}^h$  is also reconstructed, from the H jet candidate and the closest AK5 jet. Events with  $120 < m_{\text{top}}^l < 240 \text{ GeV}$  or  $160 < m_{\text{top}}^h < 280 \text{ GeV}$  are rejected. The chosen windows around the top quark mass are the result of an optimization carried out in this analysis, taking into account the asymmetric tails at larger values due to combinatorial background.

According to the above description of the final selections, the event categorization is based on 2 orthogonal classes of events for the 8 TeV data analysis in the  $\ell\nu bb$  final state, depending on the lepton flavour (muon or electron), and on 4 orthogonal classes of events for the 13 TeV data analysis in the  $\ell\nu q\bar{q}$  final state, depending on the lepton flavour and on the pruned jet mass category (WW or WZ).

The two boson candidates are combined into a diboson candidate, with presence of signal then inferred from the observation of localized excesses in the  $m_{\ell\nu+\text{jet}}$  distribution. When several diboson resonance candidates are present in the same event, only the one with the highest  $p_T$  V or H jet is kept for further analysis.

The reconstructed invariant mass of the resonance is required to be at least 0.7 TeV.

The distributions in  $p_T$  and N-subjettiness ratio  $\tau_{21}$  distributions for the V jet candidate in the  $\ell\nu q\bar{q}$  channel is shown in Fig. 8.1, after requiring  $65 < m_{\text{jet}} < 105 \text{ GeV}$ , for both simulation and 13 TeV data. Figure 8.2 shows the distribution in  $p_T$  for the H jet candidate after requiring  $40 < m_{\text{jet}} < 110 \text{ GeV}$ , for both simulation and 8 TeV data.

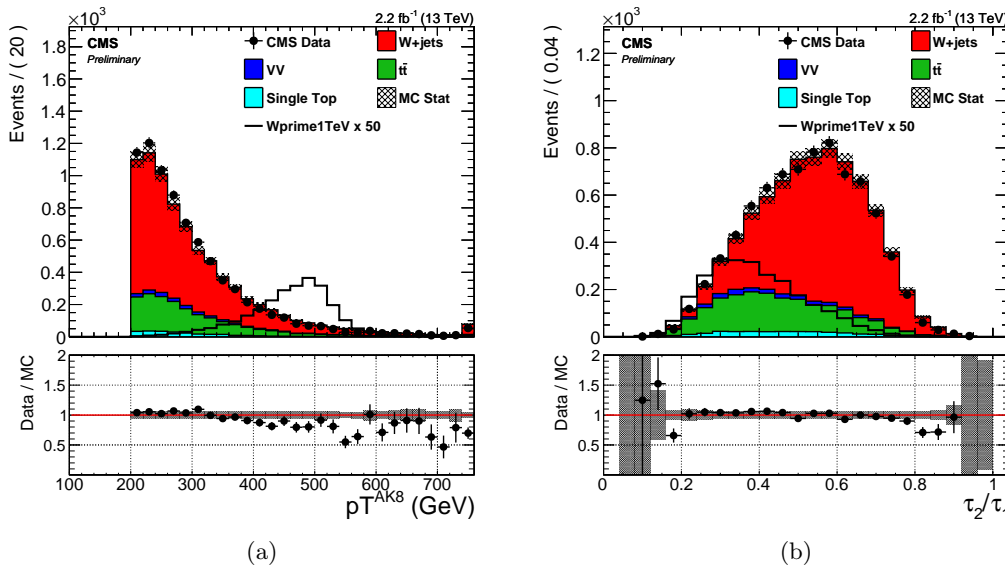


**Figure 8.1:** Distributions in  $p_T$  (a) and N-subjettiness ratio  $\tau_{21}$  (b) for the V jet candidate obtained requiring  $65 < m_{\text{jet}} < 105 \text{ GeV}$  after merging muon and electron channels. The SM diboson,  $t\bar{t}$ , and single top quark backgrounds are taken from simulation and are normalized to the integrated luminosity of the 13 TeV data sample. The  $W+jets$  background is rescaled to match the number of events in data.

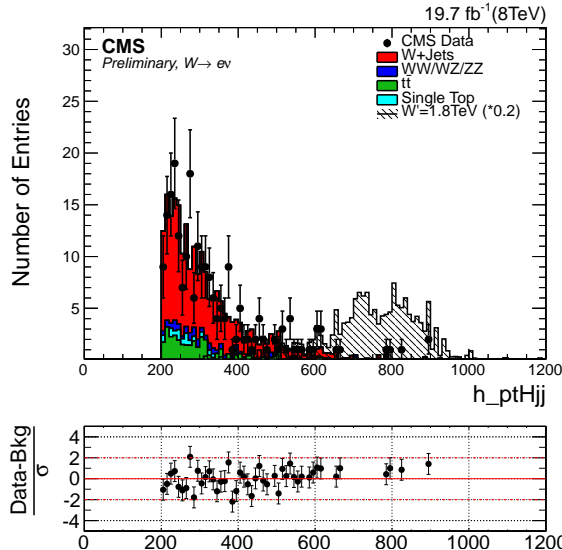


**Figure 8.2:** Distributions in  $p_T$  for the H jet candidate obtained requiring  $40 < m_{\text{jet}} < 110\text{ GeV}$  for events in the muon channel. The SM diboson,  $t\bar{t}$ , and single top quark backgrounds are taken from simulation and are normalized to the integrated luminosity of the 8 TeV data sample. The W+jets background is rescaled to match the number of events in data.

## 8.2 W+jets background estimate with $\alpha$ ratio method

The  $m_{\ell\nu+\text{jet}}$  distribution observed in data is dominated by SM background processes where single quark or gluon jets are falsely identified as signal jets. The dominant process is inclusive W boson production. Since both normalization and shape discrepancies are visible between data and simulation [129], a data driven method has been developed to estimate this background component, as described in the following. Sub-dominant backgrounds include  $t\bar{t}$ , single top quark, and non resonant diboson SM production, which are estimated from MC, after applying correction factors for residual data-to-simulation disagreement measured in control samples selected in data.

### 8.2.1 Description

The W+jets background is estimated through the so called  $\alpha$  *ratio* method. This method assumes that the correlation between  $m_{\text{jet}}$  and  $m_{\ell\nu+\text{jet}}$  for the dominant W+jets background can be adequately modelled by simulation. A signal-depleted control region (sideband) is defined by requiring the mass of the V or H jet to lie below or above the nominal selection; the  $m_{\ell\nu+\text{jet}}$  distribution observed in this region is then extrapolated to the nominal region through a transfer function estimated from simulation. Other minor sources of background, such as  $t\bar{t}$ , single top quark, and SM diboson production, are estimated using simulated events after applying correction factors based on control regions in data, as described in Sections 7.2 and 8.3. The sideband region is defined around the jet mass window that represents the analysis signal region (Section 8.1). The lower and upper sidebands for the two analyses are summarized in Table 8.3. For the 13 TeV analysis a “gap” is introduced between the signal region and the upper sideband, since the range defined by  $105 < m_{\text{jet}} < 135$  might include contribution from signals with highly Lorentz-boosted Higgs bosons in the final state. Since these types of searches at 13 TeV [138] have been performed simultaneously with the one described in this work, this region has been discarded to avoid introducing a bias in the shape and normalization extrapolation due to a possible signal. On the other hand,

the lower sideband of the 8 TeV  $\ell\nu b\bar{b}$  analysis includes the region where signals from highly Lorentz-boosted V bosons might occur. In fact, this analysis has been performed after the search for WV resonances in the semi-leptonic final state at 8 TeV discovered the signal region, where no deviation from the predicted SM background have been observed [133].

**Table 8.3:** Sideband regions used in the two analyses to estimate the contribution from the main W+jets background.

$m_{\text{jet}}$ sideband	final state	
	$\ell\nu b\bar{b}$	$\ell\nu q\bar{q}$
Low sideband (LSB)	40–110 GeV	40–65 GeV
High sideband (HSB)	135–150 GeV	135–150 GeV

### 8.2.2 Extraction of the W+jets normalization

The overall normalization of the W+jets background in the signal region is determined from a fit to the  $m_{\text{jet}}$  distribution in the lower and upper sidebands of the data. The analytical form of the fitting function is chosen from simulation studies, as are the contributions from minor backgrounds. A summary of the empirical functional forms used to parametrize each background contribution are listed in Table 8.4, and defined as follows:

$$\begin{aligned}
 F_{\text{Exp}}(x) &= e^{cx} \\
 F_{\text{ErfExp}}(x) &= e^{cx} \cdot \frac{1 + \text{Erf}((x - a)/b)}{2} \\
 F_{\text{ExpGaus}}(x) &= c_0 \cdot e^{cx} + c_1 \cdot \text{Gaus}(x, x_1, \sigma_1) \\
 F_{4\text{Gaus}}(x) &= c_1 \cdot \text{Gaus}(x, x_1, \sigma_1) + c_2 \cdot \text{Gaus}(x, x_2, \sigma_2) + c_3 \cdot \text{Gaus}(x, x_3, \sigma_3) + c_4 \cdot \text{Gaus}(x, x_4, \sigma_4) \\
 F_{\text{ErfExp2Gaus}}(x) &= e^{cx} \cdot \frac{1 + \text{Erf}((x - a)/b)}{2} + c_1 \cdot \text{Gaus}(x, x_1, \sigma_1) + c_2 \cdot \text{Gaus}(x, x_2, \sigma_2)
 \end{aligned} \tag{8.1}$$

**Table 8.4:** Summary of the empirical functional forms used to fit the  $m_{\text{jet}}$  spectra of each background component in the two analyses.

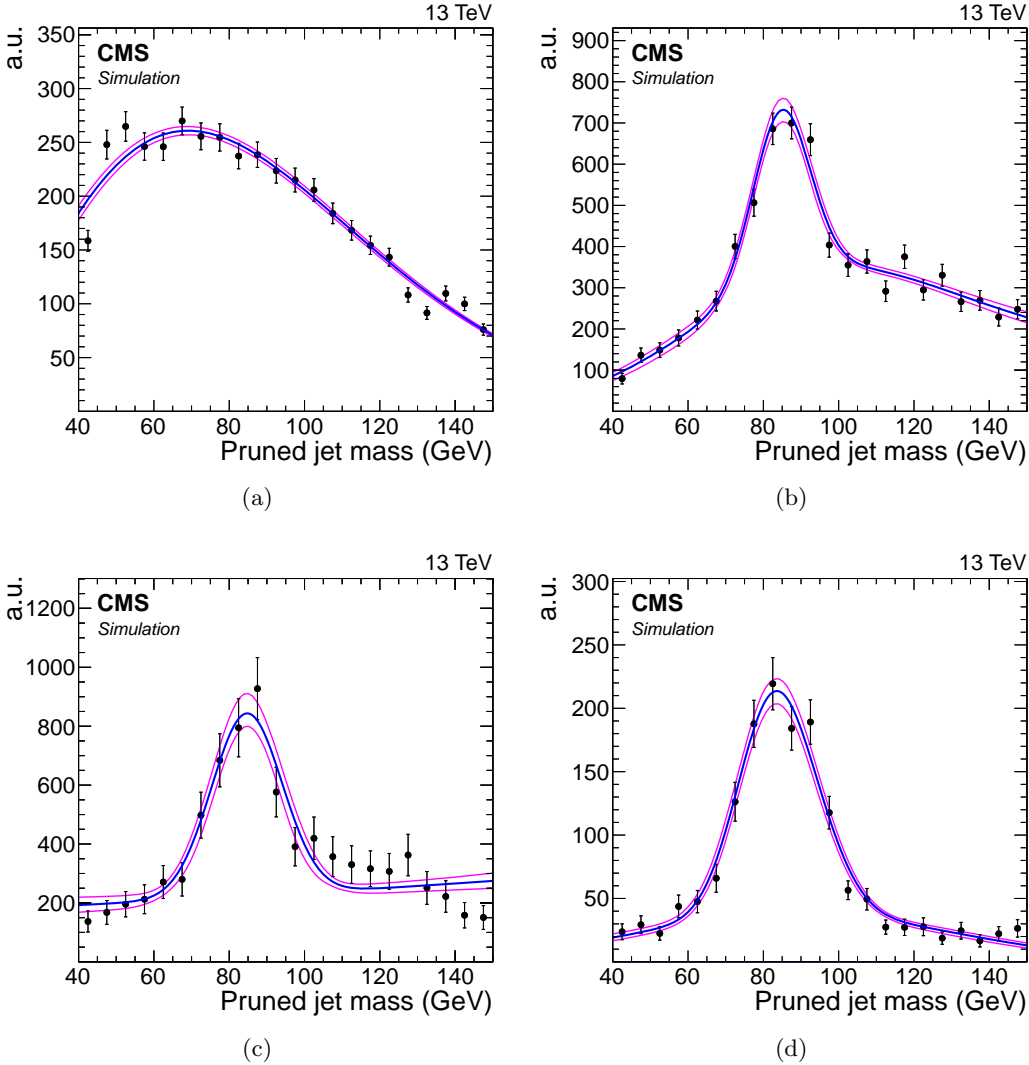
Final state	W+jets	$t\bar{t}$	single top quark	diboson
$\ell\nu b\bar{b}$	$F_{\text{ErfExp}}(x)$	$F_{\text{Exp}}(x)$	$F_{\text{Exp}}(x)$	$F_{\text{ExpGaus}}(x)$
$\ell\nu q\bar{q}$	$F_{\text{ErfExp}}(x)$	$F_{\text{ErfExp2Gaus}}(x)$	$F_{\text{ExpGaus}}(x)$	$F_{4\text{Gaus}}(x)$

Figure 8.3 shows the functional forms listed in Table 8.4 for the  $\ell\nu q\bar{q}$  channel, after fitting the simulation data of each background component, demonstrating that the chosen functions well reproduce the expected  $m_{\text{jet}}$  spectra.

The results of this fit procedure to extract the W+jets normalization are shown in Fig. 8.4 and 8.5 for the  $\ell\nu b\bar{b}$  and the  $\ell\nu q\bar{q}$  channel, respectively. The factors for correcting the simulated W-peak position and resolution to represent the observed data, taken from the top quark enriched control sample as described in Section 7.2, are included in the  $m_{\text{jet}}$  spectra of Fig. 8.5.

### 8.2.3 Extraction of the W+jets shape

The form of the  $m_{\ell\nu+\text{jet}}$  distribution for the W+jets background in the signal region (SR) is determined from the lower  $m_{\text{jet}}$  sideband, through the transfer function  $\alpha_{\text{MC}}(m_{\ell\nu+\text{jet}})$  obtained from the W+jets simulation, and defined as:



**Figure 8.3:** Functional forms describing the  $m_{\text{jet}}$  spectra for each background contribution after fitting the simulation data. (a) W+jets. (b)  $t\bar{t}$ . (c) Single top quark. (d) Diboson.

$$\alpha_{\text{MC}}(m_{\ell\nu+\text{jet}}) = \frac{F_{\text{MC,SR}}^{\text{W+jets}}(m_{\ell\nu+\text{jet}})}{F_{\text{MC,SB}}^{\text{W+jets}}(m_{\ell\nu+\text{jet}})}, \quad (8.2)$$

where  $F_{\text{MC,SB}}^{\text{W+jets}}$  and  $F_{\text{MC,SR}}^{\text{W+jets}}$  are the probability density functions used to describe the simulated  $m_{\ell\nu+\text{jet}}$  spectrum in the lower  $m_{\text{jet}}$  sideband and signal region, respectively. The upper  $m_{\text{jet}}$  sideband is not considered since the W+jets shape is different here compared to what expected in the lower sideband. Furthermore, the upper sideband suffers from a larger  $t\bar{t}$  background contamination.

Since the lower sideband region does not represent a perfectly pure sample of W+jets events in data, the presence of minor backgrounds is subtracted from the observed diboson invariant mass distribution to obtain an estimation of the W+jets contribution in the sideband control region of the data,  $F_{\text{data,SB}}^{\text{W+jets}}(m_{\ell\nu+\text{jet}})$ .

The  $m_{\ell\nu+\text{jet}}$  range used in the estimate of the background distribution determines the region of masses probed by these searches. This range is chosen to ensure a smoothly falling

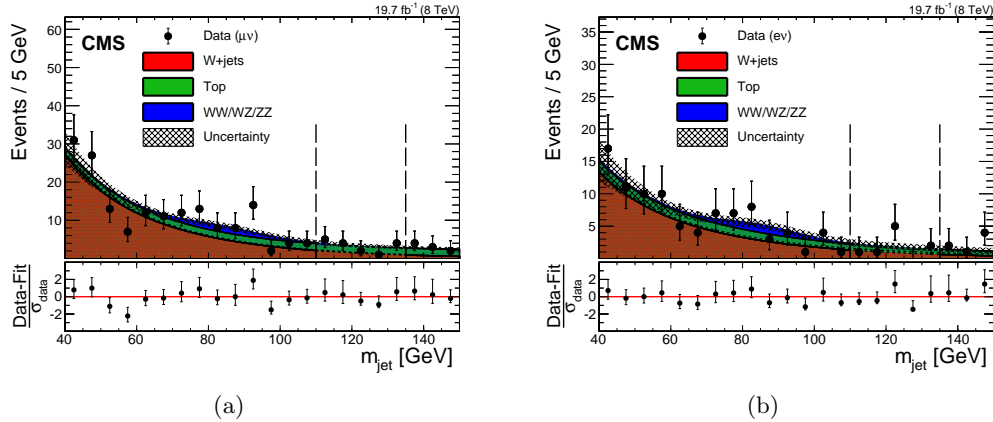


**Figure 8.4:** Distributions in pruned jet mass  $m_{\text{jet}}$  in the muon (a) and electron (b) channels for the  $\ell\nu b\bar{b}$  analysis at 8 TeV. All selections are applied except the requirement on the  $m_{\text{jet}}$  signal window. The signal region lies between the dashed vertical lines. The hatched region indicates the statistical uncertainty of the fit. At the bottom of each plot, the bin-by-bin fit residuals,  $(N_{\text{data}} - N_{\text{fit}})/\sigma_{\text{data}}$ , are shown.

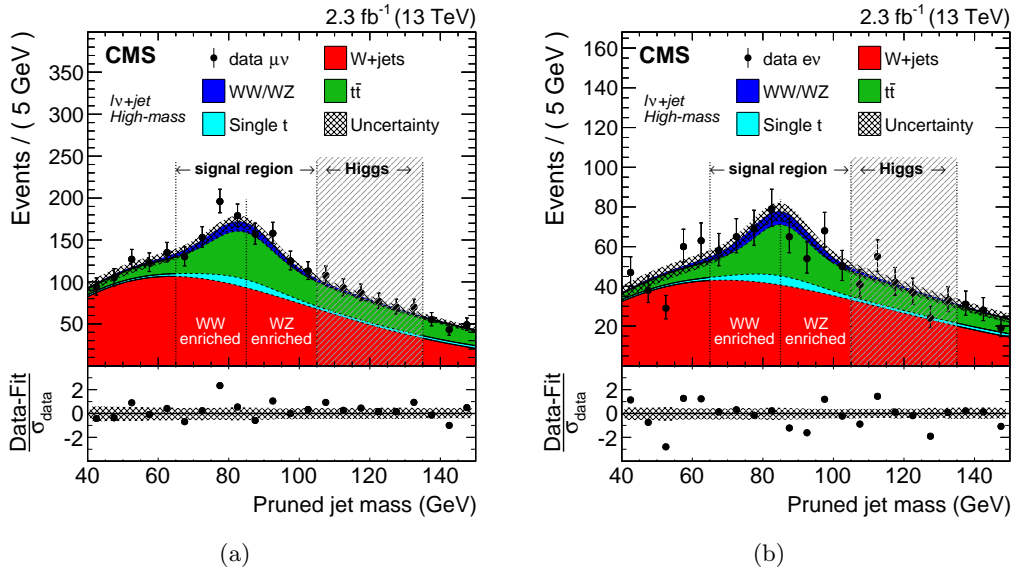


**Figure 8.5:** Distributions in pruned jet mass in the muon (a) and electron (b) channels for the  $\ell\nu q\bar{q}$  analysis at 13 TeV. All selections are applied except the requirement on the  $m_{\text{jet}}$  signal window. The signal regions and  $m_{\text{jet}}$  categories of the analysis are indicated by the vertical dotted lines. The shaded  $m_{\text{jet}}$  region 105–135 GeV is not used in the analysis. At the bottom of each plot, the bin-by-bin fit residuals,  $(N_{\text{data}} - N_{\text{fit}})/\sigma_{\text{data}}$ , are shown together with the uncertainty band of the fit normalized by the statistical uncertainty of data,  $\sigma_{\text{data}}$ .

background spectrum, and therefore far enough from the kinematic turn-on at low masses generated by the acceptance selections, allowing for a good stability and a robust control of the background estimation. For this reason the low edge of the range is chosen at 0.7 TeV while the high edge is chosen such that it is not too far from the last value where data are still present. Therefore, the fits are performed in the range  $0.7 < m_{\ell\nu+\text{jet}} < 4$  TeV for the 13 TeV analysis, while at 8 TeV no data are present above  $m_{\ell\nu+\text{jet}} \approx 3$  TeV and the chosen range is therefore  $0.7 < m_{\ell\nu+\text{jet}} < 3$  TeV.

To describe the smoothly falling W+jets background distribution, a parametrization of the form of a leveled exponential is adopted, defined as

$$F_{\text{ExpTail}}(x) = e^{-\frac{x}{a+bx}}. \quad (8.3)$$

This functional form is found to adequately describe the simulation in both the signal region and the low sideband as demonstrated in Fig. 8.6. Tests are performed with alternative functional forms, and the background prediction is found to agree with the one of the default function within the uncertainties. The minor background contributions are parametrized with a simple exponential functional form, except for the diboson contribution for which the  $F_{\text{ExpTail}}(x)$  defined above is used.

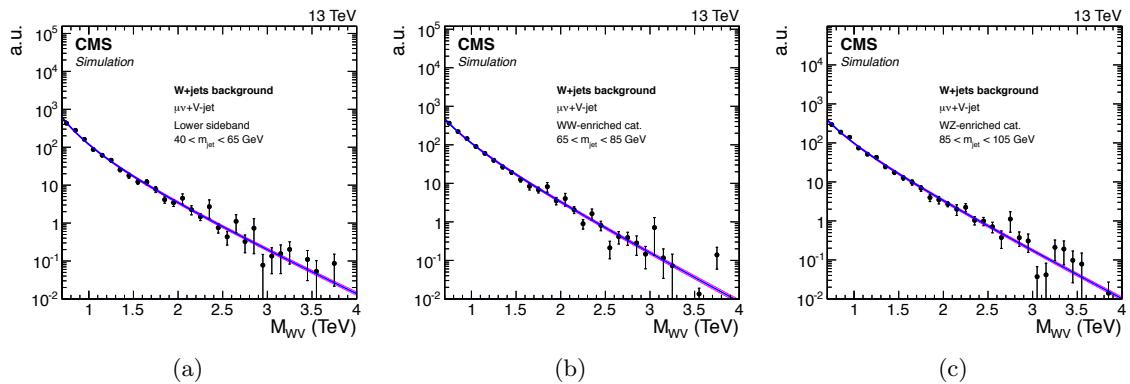


**Figure 8.6:** Functional form describing the diboson invariant mass spectrum of the W+jets background after fitting the simulation data. The distributions for the lower  $m_{\text{jet}}$  sideband (a), and the WW-enriched (b) and WZ-enriched (c) signal regions of the  $\ell\nu q\bar{q}$  analysis are shown.

For the  $\ell\nu q\bar{q}$  analysis, the  $\alpha_{\text{MC}}$  is computed independently for the two WW- and WZ-enriched categories, which are therefore treated as two different signal regions. Figure 8.7 shows the  $\alpha_{\text{MC}}$  for the two categories, obtained from a simultaneous fit of W+jets simulated data in the lower sideband and in the signal region defined by the category using the parametrization in Eq. 8.3. The blue and the red lines represent the probability density functions describing the W+jets background with  $m_{\text{jet}}$  in the lower sideband and signal region, respectively, and given by the leveled-exponential function of Eq. 8.3. A simultaneous fit is performed of the two distributions, where the parameters used to model the distribution in the signal region are correlated with the ones used to model the distribution in the sideband. The transfer function  $\alpha_{\text{MC}}$  is shown as a solid black line, while the dark (light) shaded region corresponds to the  $1\sigma$  ( $2\sigma$ ) statistical uncertainty of the fit. These uncertainties only represent the uncertainty in the modelling of the W+jets distribution. The bands have a size of approximately zero around 2 TeV as the  $\alpha_{\text{MC}}$  is the ratio of two probability density functions which have to cross in order to conserve the total probability. Similar results are obtained for the  $\ell\nu b\bar{b}$  analysis.

In Fig. 8.8, the result of the fit to the  $m_{\ell\nu+\text{jet}}$  distribution of the data with  $m_{\text{jet}}$  in the lower sideband is shown for the electron and muon channels of the  $\ell\nu q\bar{q}$  analysis. From this fit, an estimation of  $F_{\text{data},\text{SB}}^{\text{W+jets}}(m_{\ell\nu+\text{jet}})$  is obtained. Finally, the W+jets background distribution in the signal region is then extrapolated by rescaling  $F_{\text{data},\text{SB}}^{\text{W+jets}}$  by  $\alpha_{\text{MC}}$ . The minor backgrounds are then added to the W+jets background to obtain the total SM prediction in the signal region, which is given by

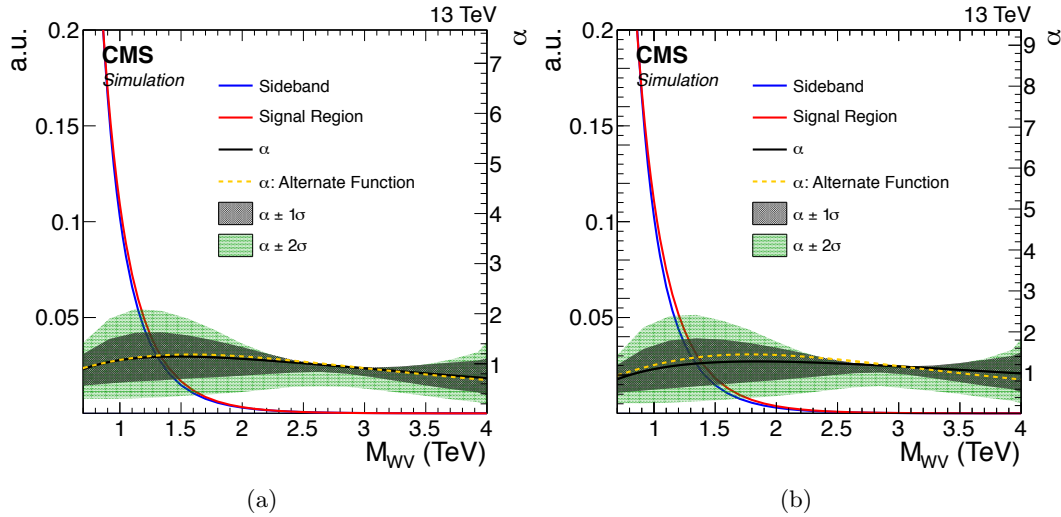


**Figure 8.7:** The transfer functions  $\alpha_{\text{MC}}$  from the lower  $m_{\text{jet}}$  sideband to the signal region defined by the WW-enriched (a) and WZ-enriched (b) category of the  $\ell\nu q\bar{q}$  analysis. The dark and light shaded areas represent the statistical uncertainty of the fit. The blue and the red lines represents the probability density functions describing the W+jets background with  $m_{\text{jet}}$  in the lower sideband and signal region, respectively. The  $\alpha_{\text{MC}}$  obtained fitting the W+jets with and alternative function is shown as yellow line.

$$N_{\text{SR}}^{\text{bkg}}(m_{\ell\nu+\text{jet}}) = N_{\text{SR}}^{\text{W+jets}} \times \alpha_{\text{MC}}(m_{\ell\nu+\text{jet}}) \times F_{\text{data,SB}}^{\text{W+jets}}(m_{\ell\nu+\text{jet}}) + \sum_k N_{\text{SR}}^k \times F_{\text{MC,SR}}^k(m_{\ell\nu+\text{jet}}). \quad (8.4)$$

In the above equation, the sum runs over the products of the normalization  $N_{\text{MC},\text{SR}}^k$  and probability density function  $F_{\text{MC},\text{SR}}^k$  of each minor background contribution  $k$ , while  $N_{\text{SR}}^{\text{W+jets}}$  and  $F_{\text{data,SB}}^{\text{W+jets}}$  represent the normalization and probability density function of the W+jets background derived from data as described previously in this chapter. The transfer function  $\alpha_{\text{MC}}$  accounts for small kinematic differences between the signal and the sideband regions.

Results of the final background extraction in the signal region will be presented in Chapters 9 and 10 or the  $\ell\nu b\bar{b}$  and  $\ell\nu q\bar{q}$  analysis, respectively.

#### 8.2.4 Validation of the $\alpha$ method

To test the validity and the robustness of the data driven method used to estimate the W+jets contribution and described previously in this section, a closure test is performed. In this test, the background is extracted to a signal free control region that allows to check the compatibility with data for both the distribution and normalization. In order to achieve this, the low mass sideband defined in Table 8.3 is divided into two regions:  $40 < m_{\text{jet}} < 55 \text{ GeV}$ , referred to as “region A”, is used as sideband, while  $55 < m_{\text{jet}} < 65 \text{ GeV}$ , referred to as “region B”, is used as signal region. The W+jets background normalization is then predicted in region B by performing a fit to the  $m_{\text{jet}}$  distribution of the data in region A and in the upper sideband (Table 8.3), while its distribution in  $m_{\ell\nu+\text{jet}}$  is extrapolated in region B with a fit of the data in region A and a suitable transfer function  $\alpha_{\text{MC}}$ . In this test, the  $\alpha_{\text{MC}}$  is defined as the ratio between the simulated W+jets background distributions in  $m_{\ell\nu+\text{jet}}$  in region B and A.

An example of the result of this test is presented in the following for the muon channel in

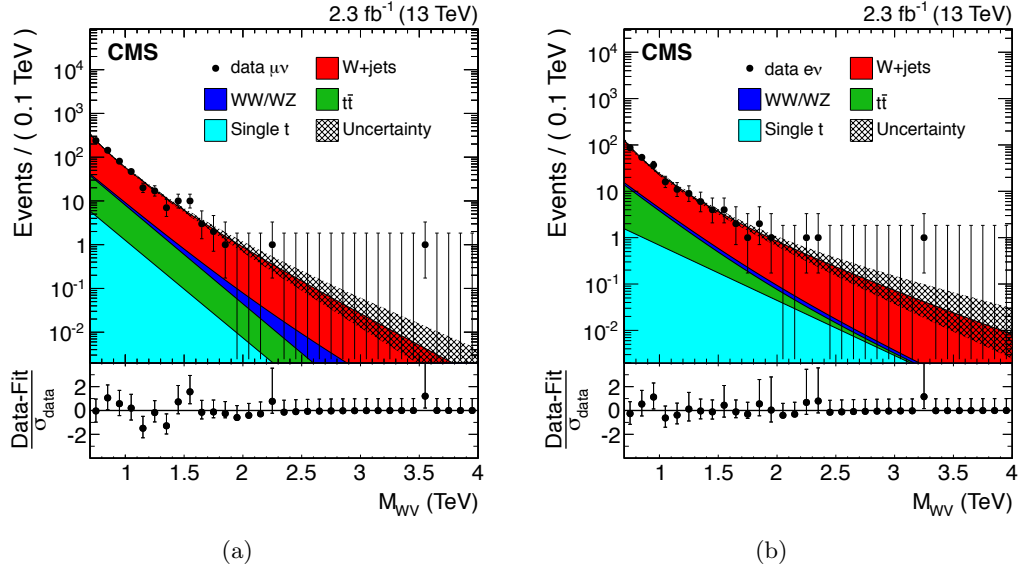


**Figure 8.8:** Results of the fit to the  $m_{WV}$  distribution of the data with  $m_{jet}$  in the lower sideband to estimate  $F_{data,SB}^{W+jets}$  for both muon (a) and electron (b) channels of the  $\ell\nu q\bar{q}$  analysis. Minor backgrounds are estimated from simulation, while the W+jets contribution is the result of the fit to the data.

the  $\ell\nu q\bar{q}$  analysis. Figure 8.9 shows the results of the fit to the  $m_{jet}$  distribution of the data inside the region A and the HSB, performed to extract the expected W+jets normalization inside the region B.

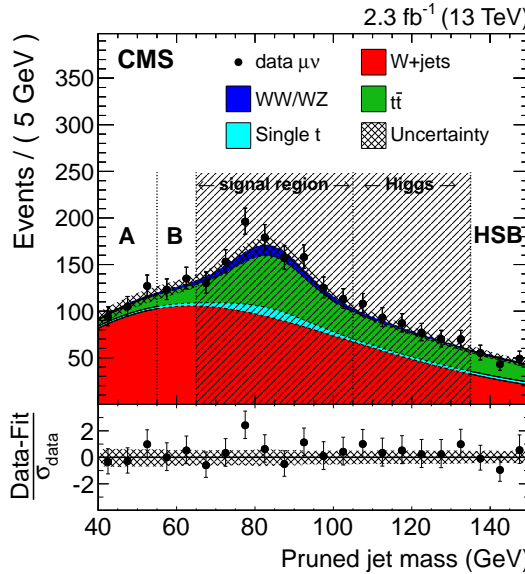


**Figure 8.9:** Result of the closure test for the muon channel in the  $\ell\nu q\bar{q}$  analysis. The plot shows the fit to the pruned jet mass distribution considering only events in data with  $m_{jet}$  in the ranges 40–55 GeV (A) and 135–150 GeV (HSB) performed to extract the W+jets normalization inside region B.

Figure 8.10(a) shows the transfer function  $\alpha_{MC}$  obtained from a simultaneous fit of W+jets simulated events in the region A and in the region B, using the leveled-exponential parametrization defined in Eq. 8.3. In Fig. 8.10(b), the result of the fit to the  $m_{\ell\nu+jet}$

distribution of the data with  $m_{\text{jet}}$  in the lower sideband is shown, where the W+jets shape is modelled through the same leveled-exponential function.

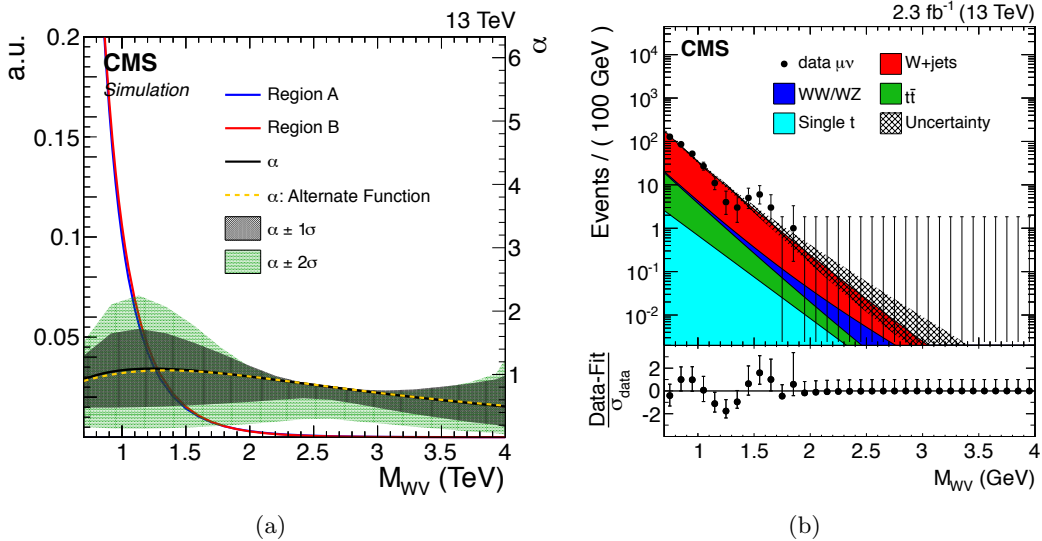


**Figure 8.10:** (a) The transfer function  $\alpha_{\text{MC}}$  obtained by simultaneously fitting the diboson invariant mass distributions of simulation data inside the sideband (A) and signal region (B). (b) Diboson invariant mass distribution for events with  $40 < m_{\text{jet}} < 55$  GeV (A). The W+jets shape is fitted, after subtracting contaminations from minor backgrounds, by means of a leveled-exponential function.

Finally, Fig. 8.11 shows a comparison between the total predicted background, obtained through Eq. 8.4, and the data inside the signal free region B. A good agreement is found over the whole  $m_{\ell\nu+\text{jet}}$  range. The test has been performed for both lepton flavours for the  $\ell\nu q\bar{q}$  analysis, as well as for the  $\ell\nu b\bar{b}$  analysis where slightly different definitions for region A and B are used. In all the cases, consistency between the predicted background and the data is observed, thus validating the proposed strategy for the W+jets background estimation.

### 8.3 Modelling of top quark production

The backgrounds from  $t\bar{t}$  and single top quark production in both analysis channels are estimated from data-based correction factors in the normalization of the simulation. A top quark enriched control sample is selected by applying all the analysis requirements except that the b jet veto is inverted by requiring, instead, at least one b-tagged AK4 (or AK5) jet in the event.

For the  $\ell\nu q\bar{q}$  channel, the comparison between data and simulation yields normalization correction factors for  $t\bar{t}$  and single top quark background processes evaluated in the pruned jet mass signal region  $65 < m_{\text{jet}} < 105$  GeV. The measured correction factors are  $0.87 \pm 0.04$  and  $0.83 \pm 0.07$  for the muon and electron channel, respectively, where the quoted uncertainty is only statistical. The disagreement is consistent with the difference between NLO and NNLO shape prediction for large top quark  $p_T$  [139].

For the  $\ell\nu b\bar{b}$  channel, a unique correction factor is calculated with a simultaneous fit to number of data events in the muon and electron channels in the pruned jet mass region  $40 < m_{\text{jet}} < 150$  GeV. The difference in normalization between data and simulation is found to be  $4.6 \pm 5.6\%$ , where the quoted uncertainty is only statistical.

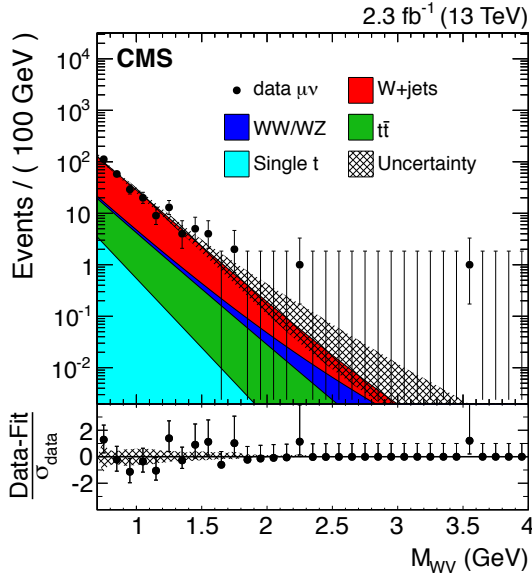


**Figure 8.11:** Distributions in diboson invariant mass for data and the expected backgrounds for events inside the pruned mass region defined by  $55 < m_{\text{jet}} < 65$  GeV (B). The W+jets background distribution is extracted using events within  $40 < m_{\text{jet}} < 55$  GeV (A).

These scale factors include both the W boson signal and the combinatorial components mainly due to events where the extra b jet from the top quark decay is in the proximity of the W, and are used to correct the normalization of the  $t\bar{t}$  and single top quark simulated background predictions in the signal regions. The relative uncertainties are used to quantify the uncertainty in the  $t\bar{t}$  and single top quark background normalization.

The  $m_{\text{jet}}$  distribution in the top quark enriched sample for the 13 TeV data  $\ell\nu q\bar{q}$  analysis and for simulation is shown in Fig. 8.12(a), while Fig. 8.12(b) shows the  $\tau_{21}$  distribution. The same distribution is also shown for the  $\ell\nu b\bar{b}$  analysis channel in Fig. 8.13, where 8 TeV data and simulation are compared. In all cases, the  $m_{\text{jet}}$  spectrum shows a clear peak for events with a W boson decaying to hadrons, including the combinatorial background, while a reasonable agreement between the shapes in data and simulation is observed. Comparisons of data and simulation are also shown in Fig. 8.14 for other distributions such as the reconstructed  $m_{\ell\nu+\text{jet}}$ , as well as  $m_{\text{top}}^l$  and  $m_{\text{top}}^h$ . In the latter a clear peak at the top quark mass is visible.

## 8.4 Signal modeling

The potential discovery and exclusion power of these analyses rely on the ability of finding a local enhancement on the top of a smoothly falling background. This is ultimately achieved through an unbinned likelihood fit of the signal + background model to the reconstructed diboson invariant mass, which depends on the accurate description of the signal shape.

An analytical parametrization of the signal shape is chosen such that it well reproduces the simulated resonance distributions. As stated in Section 5.2.1, simulated signal events are generated with a resonance natural width sufficiently small compared to the detector resolution. This makes the model used for generating the events independent from the detector effects on the signal shape, allowing a model independent search for narrow resonances where only the detector resolution has to be described. A double-sided Crystal-Ball (CB) function [140] (i.e. a Gaussian core with power law tails on both sides) is found to well serve this purpose. To

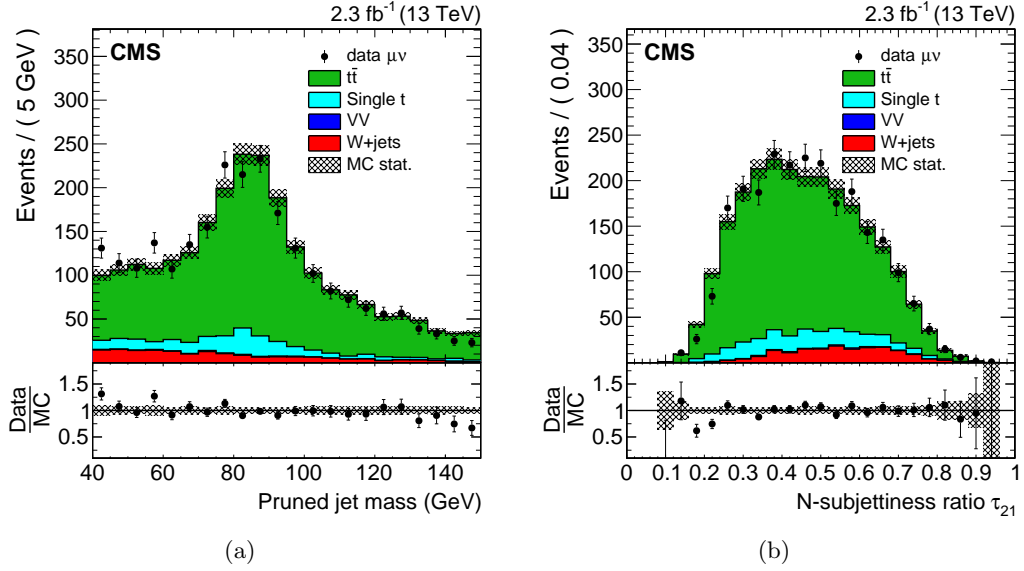


**Figure 8.12:** Distributions in the N-subjettiness ratio  $\tau_{21}$  (a) and pruned jet mass  $m_{\text{jet}}$  (b) from the top quark enriched control sample in the muon channel of the  $\ell\nu q\bar{q}$  analysis. The  $t\bar{t}$  background is rescaled such that the total number of background events matches the number of events in 13 TeV data.

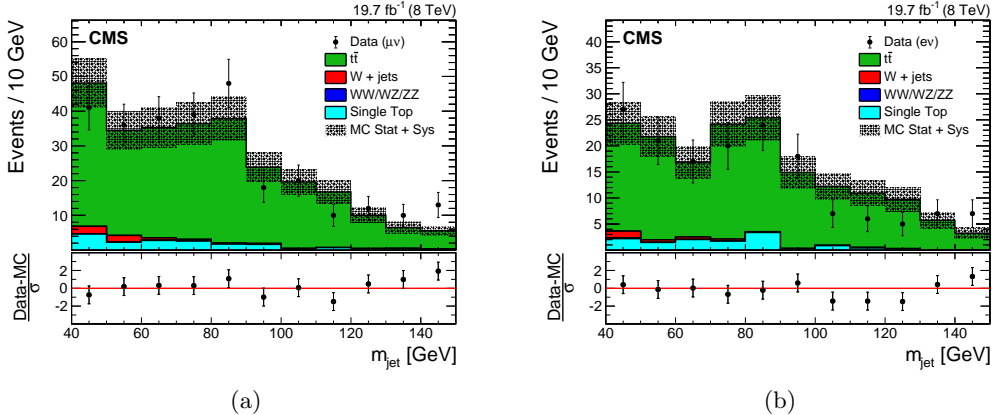


**Figure 8.13:** Distributions in pruned jet mass  $m_{\text{jet}}$  in the top quark enriched control sample in the electron (a) and muon (b) channels of the  $\ell\nu b\bar{b}$  analysis. The hatched region indicates the overall uncertainty in the background. In the lower panels, the bin-by-bin residuals,  $(\text{Data} - \text{MC})/\sigma$  are shown, where  $\sigma$  is the sum in quadrature of the statistical uncertainty of the 8 TeV data, the simulation, and the systematic uncertainty in the  $t\bar{t}$  background.

take into account differences between muon and electron momentum resolutions, the signal invariant mass distribution is parametrized separately in the two lepton flavor categories.

Figure 8.15 shows examples of the fitted signal distribution through a CB function, for several signal benchmarks and in different  $m_{\text{jet}}$  categories of the  $\ell\nu q\bar{q}$  analysis. Similar results are obtained for the  $W'$  signal used in the  $\ell\nu b\bar{b}$  analysis.

Because of the limited number of available simulated samples, a liner interpolation is performed for each parameter of the CB function between the shapes obtained for some reference mass points, in order to extrapolate the distribution for intermediate values of the resonance mass. The resolution of the reconstructed diboson invariant mass is given by the

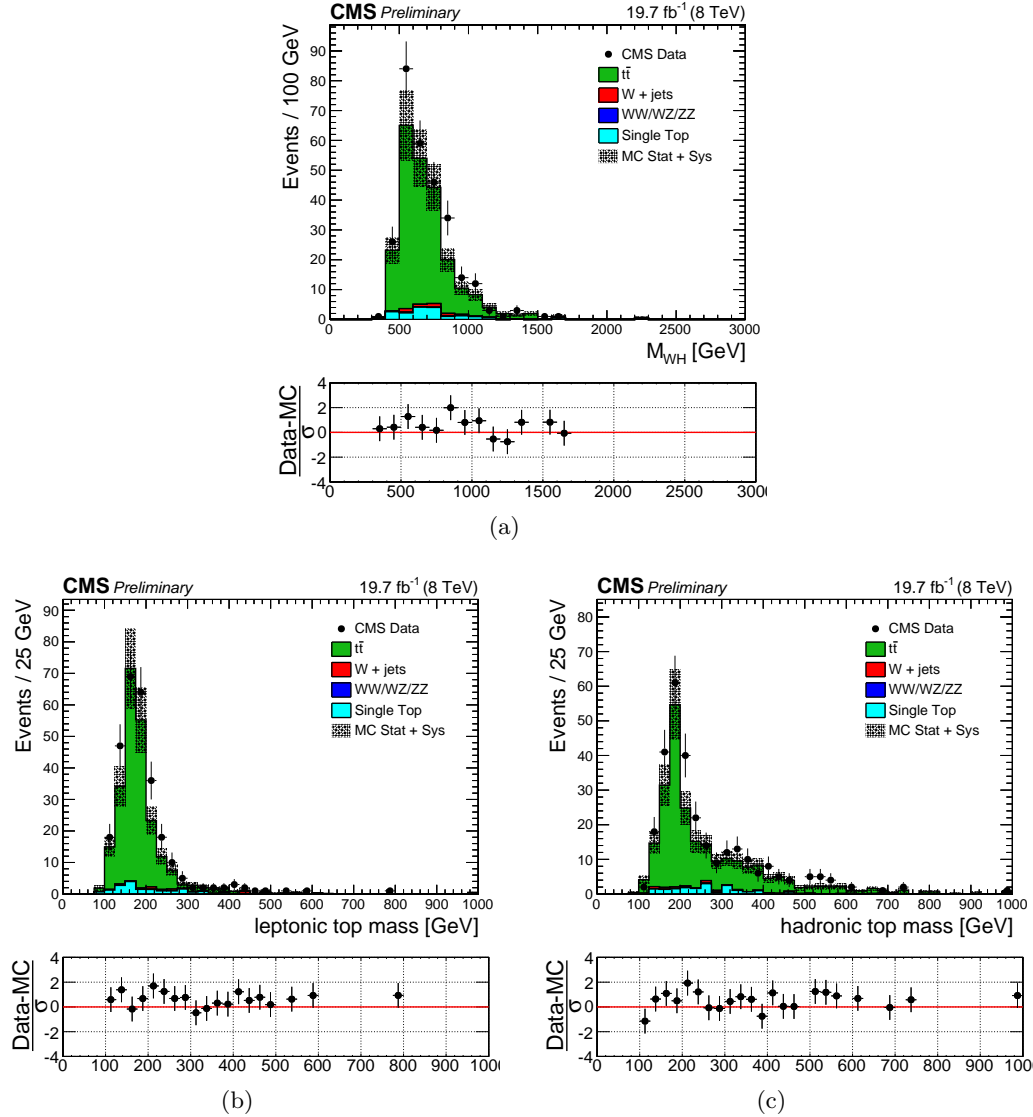


**Figure 8.14:** Distributions for 8 TeV data and for simulation in  $m_{\text{WH}}$  (a),  $m_{\text{top}}^l$  (b) and  $m_{\text{top}}^h$  (c) in the top quark enriched control sample for the muon channel of the  $\ell\nu b\bar{b}$  analysis.

width of the Gaussian core and it ranges between 7 and 4% depending on the resonance mass, as summarized in Fig. 8.16. The resolution is dominated by the jet and  $E_{\text{T}}^{\text{miss}}$  contributions.

The signal selection efficiency, evaluated for each category, is defined as the number of selected signal events over the number of generated ones, which include all the possible lepton flavours (e,  $\mu$  and  $\tau$ ). As shown in Fig. 8.17 the efficiency for a Z' or bulk graviton signal in the WW-enriched category is  $\approx 2$  times larger compared to a W' signal. On the other hand, the efficiency for a W' signal in the WZ-enriched category is  $\approx 4$  times larger compared to a Z' or bulk graviton signal. For both categories and for each signal hypothesis the efficiency is smaller compared to the large  $m_{\text{jet}}$  window used for V tagging. However, the resulting loss in sensitivity in each of the category is recovered with a combination of the two  $m_{\text{jet}}$  categories which allows the use of all the available data. With this solution the discrimination between the two type of signals is maximized together with a gain in sensitivity of 10–20% depending on the resonance mass.

A linear interpolation of the signal efficiency is performed between the values obtained for

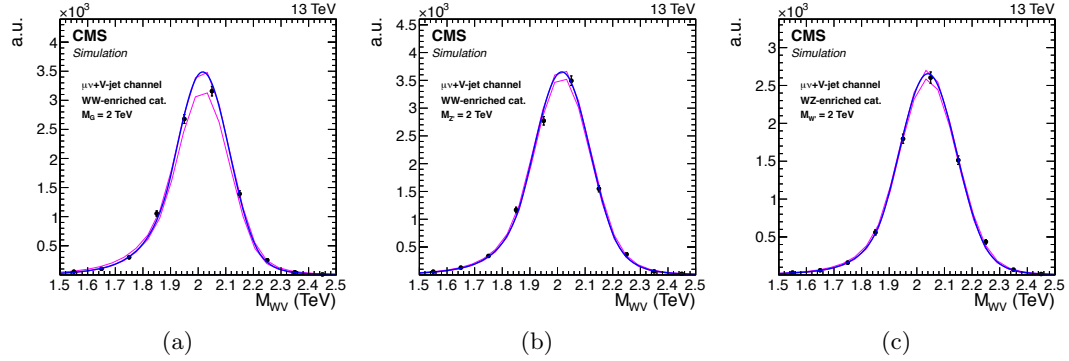


**Figure 8.15:** Modeling of the reconstructed signal distribution with a double-sided Crystal Ball function, for different signal benchmarks and in different  $m_{\text{jet}}$  categories of the  $\ell\nu q\bar{q}$  analysis: bulk graviton (a) and  $Z'$  (b) signals in the WW-enriched category; (c)  $W'$  signal in the WZ-enriched category. In all cases, a signal sample with a generated mass of 2 TeV is considered.

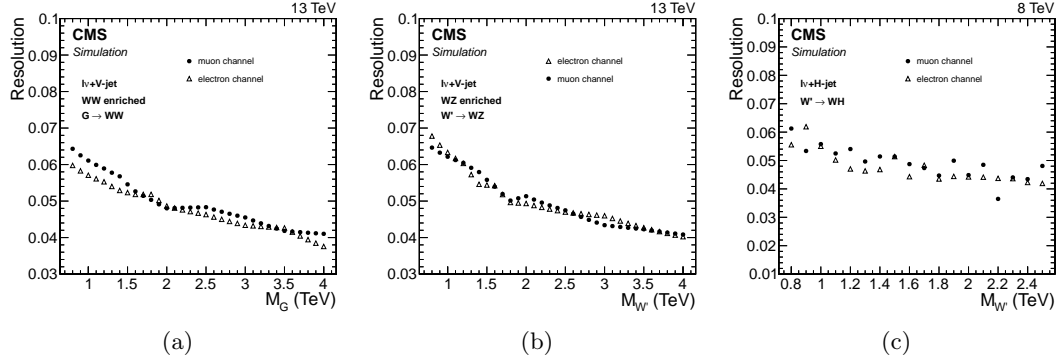


**Figure 8.16:** Relative resolution of the fitted signal distribution as given by the width of the Gaussian core, as a function of the generated resonance mass for different signal benchmarks and for the two analysis: bulk graviton (a) and  $W'$  (b) signals in the WW-enriched and WZ-enriched category, respectively, of the  $\ell\nu q\bar{q}$  analysis; (c)  $W'$  signal for the  $\ell\nu b\bar{b}$  analysis.

some reference mass points in order to extrapolate the efficiency for intermediate resonance masses for which a simulated sample is not available. The efficiency for the electron channel is lower compared to the muon channel over most of the phase space due to the tighter requirements on the electron  $p_T$  and  $E_T^{\text{miss}}$ . This effect is less visible in the  $\ell\nu b\bar{b}$  channel (Fig. 8.18) where the electron selections are less strict. For all cases, at low masses the efficiency increases with the resonance mass because of the increase in the acceptance of the lepton,  $E_T^{\text{miss}}$  and  $m_{WV}/WH$  selections together with the inefficiency of the jet algorithms in reconstructing the merged jet for a low boosted V boson (Fig. 6.13). At larger resonance masses the efficiency slightly decreases due to  $\tau_{21}$  selection inefficiency for very high  $p_T$  V jets, as described in Section 7.2. For the electron channel this effect is compensated by a larger increase in the lepton selection acceptance, resulting in a nearly flat efficiency at high resonance masses. Similar considerations hold for the efficiency in the  $\ell\nu b\bar{b}$  channel shown in Fig. 8.18.

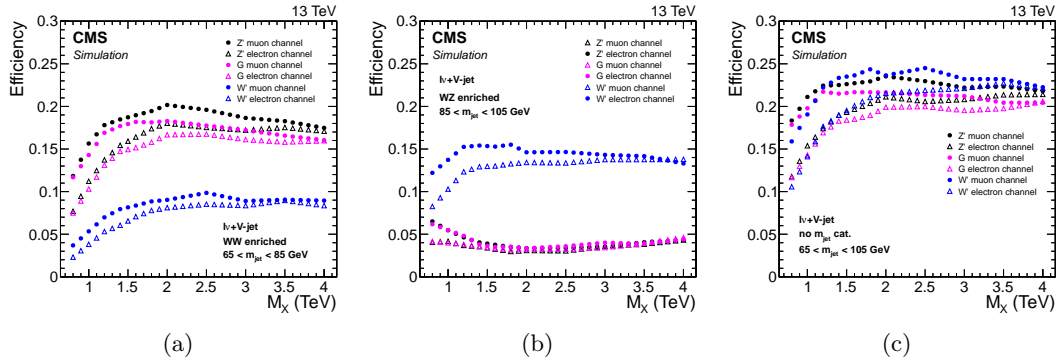


**Figure 8.17:** Signal efficiency in the  $\ell\nu\bar{q}\bar{q}$  analysis channel as a function of the generated resonance mass for all signal benchmarks and for different  $m_{\text{jet}}$  selection: (a) WW-enriched category; (b) WZ-enriched category; (c)  $65 < m_{\text{jet}} < 105 \text{ GeV}$ .

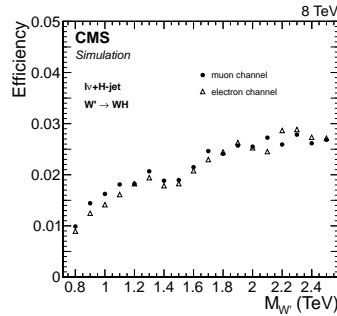


**Figure 8.18:** Signal efficiency in the  $\ell\nu\bar{b}\bar{b}$  analysis channel as a function of the generated  $W'$  mass.

## 8.5 Systematic uncertainties

This section describes the systematic uncertainties in the signal ad background predictions affecting both the normalizations and the  $m_{\ell\nu+\text{jet}}$  distributions. The uncertainties described below are include as nuisance parameters in the calculation of the limits on the cross section as well as of the p-values of potential excesses of events observed in the data.

### 8.5.1 Systematic uncertainties in the background estimation

The uncertainty in the  $W+\text{jets}$  background normalization is mainly due to the uncertainties in the parameters extracted from the fit of the data in the pruned jet mass sideband. This contribution is statistical in nature since it depends on the amount of data in the  $m_{\text{jet}}$  sideband regions, and it is evaluated varying the fit parameters from the final fit values by random amounts sampled from the covariance matrix. An additional effect due to the difference arising from alternative parametrization of the  $W+\text{jets}$   $m_{\text{jet}}$  distribution is taken into account and added in quadrature to the pure statistical contribution. This contribution is found to constitute up to 15% of the total uncertainty. The total uncertainty on the  $W+\text{jets}$  yields remains below 10% in the  $\ell\nu\bar{q}\bar{q}$  channel, while uncertainties above 40% are obtained for the  $\ell\nu\bar{b}\bar{b}$  channel where the amount of data in the sidebands is largely reduced by the tight b tagging requirements.

As described in Section 8.2.3 the extrapolated background shape in the signal region is computed from the product of  $F_{\text{data},\text{SB}}^{\text{W+jets}}$  and  $\alpha_{\text{MC}}$ . Thus, the shape uncertainty comes from both uncertainties in the  $W+\text{jets}$   $m_{\ell\nu+\text{jet}}$  shape obtained from the fit of the data in the lower

$m_{\text{jet}}$  sideband region and in the modelling of the transfer function  $\alpha_{\text{MC}}$ . Both contributions are mainly statistical in nature, as they are driven by the available amount of data in the sideband and by the number of simulated W+jets events passing the analysis requirements, respectively. These effects are estimated from the covariance matrix of the fit and included in the final limit and p-value calculations after a procedure which diagonalizes the matrix to decorrelate the fitted parameters. In this procedure, the new parameters are defined in such a way to be centered at zero and with error equal to unity. The background fit parameterization is then redefined as a function of these new, uncorrelated parameters. This new fit function together with the uncertainties in the fitted parameter is used to describe the background distribution in the limit and p-value calculations explained in Section 8.6.

Additionally, the  $\alpha_{\text{MC}}$  (Fig. 8.7) is affected by variations due to the choice of the parametrization used to model the W+jets distribution. Previous studies showed that additional variations of about the same size are due to the use of different parton showering algorithms [133]. This effect has been evaluated comparing the  $\alpha$  obtained with simulated samples with parton showering implemented through HERWIG++ and PYTHIA. All these variations are found to be equal or slightly smaller than the statistical uncertainties on the  $\alpha$ , and hence the associated systematic effect is taken into account by enlarging the errors on the decorrelated fit parameters by a factor  $\sqrt{2}$ . This is sufficiently conservative to cover all the shape variations. In a similar way, variations in the  $F_{\text{data},\text{SB}}^{\text{W+jets}}$  due to the same effects, are as well taken into account.

The uncertainties in the W+jets normalization are treated as uncorrelated among the different lepton flavor channels and  $m_{\text{jet}}$  categories, while the uncertainties in the W+jets distribution are partially correlated according to the following scheme:

- uncertainties in the  $F_{\text{data},\text{SB}}^{\text{W+jets}}$  parameters are correlated;
- uncertainties in the  $\alpha_{\text{MC}}$  parameters are uncorrelated.

This solution takes into account the fact that in the different  $m_{\text{jet}}$  categories the same data in the sideband are used to estimate the W+jets distribution, while the transfer function is used to predict the shape in the two orthogonal signal regions defined by the categories.

The systematic uncertainty in the normalization of the  $t\bar{t}$ /single top quark backgrounds is driven by the uncertainties in the data-to-simulation scale factors estimated in the top quark enriched control sample (Section 8.3). In the  $\ell\nu q\bar{q}$  channel these uncertainties are measured to be 4.6% and 8.4% in the muon and electron channel, respectively. For the  $\ell\nu b\bar{b}$  channel, this uncertainty amounts to 5.6%. For the single top quark background an additional systematic uncertainty related to the cross section calculations is assigned to be 15% and 5%, for the 8 and 13 TeV data analysis respectively [141, 142].

The  $t\bar{t}$  background distribution in  $m_{\ell\nu+\text{jet}}$  is taken from simulation and this choice is found to be reasonable given the agreement between data and simulation in the top quark enriched control sample (Fig. 8.14(a)). However, previous studies [133] showed that variations in the shape occur due to the choices of regularization or factorization scales (varied up and down by a factor of 2), to the matching scales in the MADGRAPH simulation, and to different generators (MADGRAPH or POWHEG). In order to cover all these effects, the errors on the decorrelated fit parameters for the  $t\bar{t}$  distribution is enlarged by a factor of 2.

The systematic uncertainties in the diboson background normalization is due to the uncertainty in the inclusive cross sections, which are assigned to be 10% [143] and 3% [144] for the 8 and 13 TeV data analysis, respectively. For the  $\ell\nu q\bar{q}$  channel, the uncertainty in the

diboson background normalization is as well due to the uncertainty of 3% in the measured data-to-simulation scale factors for the V tagging efficiency derived in the top quark enriched control sample (Section 7.2).

Additional sources of systematic uncertainties in the background normalization are due to the uncertainty in the integrated luminosity, and in the measured data-to-simulation scale factors for the efficiency of lepton trigger and identification, described in the following section.

A summary of the systematic uncertainties in the normalization of the predicted background is provided in Tables 8.5 and 8.6 for the  $\ell\nu q\bar{q}$  and  $\ell\nu b\bar{b}$  analysis channel, respectively.

Source	W+jets	t <bar>t</bar>	single top quark	diboson
Integrated luminosity	-	2.6%	2.6%	2.6%
Cross section	-	-	15%	10%
Data-driven prediction	42% ( $\mu$ ) / 59% (e)	5.6%	5.6%	-
Lepton trigger ( $\mu/e$ )	-	1% / 1%	1% / 1%	1% / 1%
Lepton identification ( $\mu/e$ )	-	1% / 3%	1% / 3%	1% / 3%

**Table 8.5:** Summary of the systematic uncertainties in the normalization of the predicted background in the  $\ell\nu bb$  analysis at 8 TeV.

Source	W+jets	t <bar>t</bar>	single top quark	diboson
Integrated luminosity	-	2.7%	2.7%	2.7%
Cross section	-	-	5%	3%
V-tagging efficiency	-	-	-	3%
Data-driven prediction	5–9%	5–8%	5–8%	-
Lepton trigger ( $\mu/e$ )	-	1% / 1%	1% / 1%	1% / 1%
Lepton identification ( $\mu/e$ )	-	1% / 3%	1% / 3%	1% / 3%

**Table 8.6:** Summary of the systematic uncertainties in the normalization of the predicted background in the  $\ell\nu q\bar{q}$  analysis at 13 TeV.

### 8.5.2 Systematic uncertainties in the signal prediction

Systematic uncertainties affecting the predicted signal efficiency (or normalization) and  $m_{\ell\nu+jet}$  distribution arise from several sources as described in the following and summarized in Tables 8.7 and 8.8. The effect of each source is evaluated for each considered simulated signal hypothesis as a function of the resonance mass.

One the primary sources affecting the signal normalization for the  $\ell\nu q\bar{q}$  channel is due to uncertainties in data-to-simulation scale factors for the V tagging efficiency, derived from top quark enriched control sample as described in Section 7.2. These uncertainties include separately the uncertainty of 3% on the scale factor measured in tt> events with an average  $p_T \approx 200$  GeV, and the uncertainty due to the extrapolation of the scale factor to higher momenta, which is assigned to be 6–10% depending on the signal mass. Additional uncertainties are assigned due to the pruned jet mass scale and resolution measured in tt> events (Table 7.2). These are computed by rescaling or smearing the  $m_{jet}$  value according to the uncertainties in the respective  $m_{jet}$  scale or resolution. The selection efficiencies are recalculated on these

modified events, with the resulting changes taken as systematic uncertainties that depend on the resonance mass.

In a similar way, systematic uncertainties are assigned in the  $\ell\nu b\bar{b}$  channel due to the uncertainty in the H tagging efficiency. This contribution arises from both uncertainties in the data-to-simulation scale factors for the pruned jet mass scale and resolution, derived from the top quark enriched control sample with 8 TeV data, and for b-tagged jet identification efficiencies (Section 6.4.3). These sources introduce a systematic uncertainty in the mass tagging and b tagging of the Higgs boson of 2–10% and 2–8%, respectively, depending on the signal mass.

The accuracy on energy and momentum measurements for leptons and jets represents an important source of systematic uncertainties in the signal efficiency. In particular, the muon momentum scale and resolution, the electron energy scale and resolution, and the jet energy scale and resolution are considered. The event selection is applied to the signal samples after varying the lepton four-momenta within one standard deviation of the corresponding uncertainty in the muon momentum scale [98] or electron energy scale [145], or applying an appropriate Gaussian momentum/energy smearing in case of resolution uncertainties. The same procedure is also applied for the jet four-momenta using the corresponding energy scale and resolution uncertainties. In this process, variations in the lepton and jet four-momenta are propagated consistently to the  $\vec{p}_T^{\text{miss}}$  vector. The signal efficiency is then recalculated using modified lepton and jet four-momenta separately for each source of systematic uncertainties. The largest relative change in the signal efficiency compared to the default value is taken as the systematic uncertainty for that specific source. The induced relative migration among V jet mass categories is evaluated for the  $\ell\nu q\bar{q}$  channel, but do not affect the overall signal efficiency. The muon, electron, and jet uncertainties are assumed to be uncorrelated. Finally, the resulting changes on the reconstructed resonances are propagated on the reconstructed  $m_{\ell\nu+\text{jet}}$  signal distribution, resulting in a small effect on both peak position and width of the Gaussian core.

The systematic uncertainties in the lepton trigger, identification, and isolation efficiencies are derived using a dedicated T&P analysis in  $Z \rightarrow \ell^+\ell^-$  events. For both analysis channels, an uncertainty of 1% is assigned to the trigger efficiency for both lepton flavors, while for lepton identification and isolation efficiency, the systematic uncertainty is estimated to be 1% for the muon and 3% for electron flavors.

The 2.7% and 2.6% uncertainty in the integrated luminosity affects to the normalization of both signal and backgrounds in the  $\ell\nu q\bar{q}$  and  $\ell\nu b\bar{b}$  channel, respectively, as obtained in measurements performed for the 2015 and 2012 data taking periods [146, 147].

For the  $\ell\nu q\bar{q}$  channel, uncertainties on the signal yield due to variations in the parton distribution function and the choice of factorization ( $\mu_f$ ) and renormalization ( $\mu_r$ ) scales are also taken into account. The PDF uncertainties are evaluated using the NNPDF 3.0 [65] PDF set. The uncertainty related to the choice of  $\mu_f$  and  $\mu_r$  scales is evaluated following the proposal in Refs. [148, 149] by varying the default choice of scales in the following 6 combinations of factors:  $(\mu_f, \mu_r) \times (1/2, 1/2), (1/2, 1), (1, 1/2), (2, 2), (2, 1)$ , and  $(1, 2)$ . The uncertainty in the signal cross section from the choice of PDFs and of factorization and renormalization scales ranges from 4 to 77%, and from 1 to 22%, respectively, depending on the resonance mass, particle type and its production mechanism. For the  $\ell\nu b\bar{b}$  channel, only the impact of the proton PDF uncertainties on the signal efficiency is evaluated with the PDF4LHC prescription [150, 151], using the MSTW2008 [152] and NNPDF 2.1 [153] PDF

sets. This effect is found to be  $< 0.5\%$ .

Finally, the systematic uncertainty due to the modelling of pileup is estimated by reweighting the signal simulation samples such that the distribution of the number of interactions per bunch crossing is shifted according to the uncertainty in the inelastic proton-proton cross section compared with that found in data. This contribution is found to be 0.5% in both channels.

**Table 8.7:** Summary of the systematic uncertainties in the signal prediction for the  $\ell\nu b\bar{b}$  analysis channel and their impact on the event yield in the signal region and on the reconstructed  $m_{WH}$  shape (mean and width) for both muon and electron channels.

Source	Relevant quantity	Uncertainty (%)
Lepton trigger ( $\mu/e$ )	Signal yield	1 / 1
Lepton identification ( $\mu/e$ )	Signal yield	1 / 3
Lepton $p_T$ scale ( $\mu/e$ )	Signal yield	1 / 0.5
Lepton $p_T$ resolution ( $\mu/e$ )	Signal yield	0.1 / 0.1
Jet energy scale	Signal yield	1–3
Jet energy resolution	Signal yield	0.5
Integrated luminosity	Signal yield	2.6
Pileup	Signal yield	0.5
PDFs	Signal yield	< 0.5
H jet mass tagging efficiency	Signal yield	2–10
H jet b tagging efficiency	Signal yield	2–8
Jet energy scale	Resonance shape (mean)	0.5
Jet energy scale	Resonance shape (width)	4
Jet energy resolution	Resonance shape (mean)	0.2
Jet energy resolution	Resonance shape (width)	4
Lepton $p_T$ resolution	Resonance shape (mean)	0.1
Lepton $p_T$ resolution	Resonance shape (width)	1.2
Lepton $p_T$ scale	Resonance shape (mean)	0.7
Lepton $p_T$ scale	Resonance shape (width)	2.5

## 8.6 Testing new resonance hypothesis

The purpose of this analysis is to infer a constraint on the existence of a new resonance decaying into diboson for a set of different signal mass hypotheses. The comparison between the diboson invariant mass distribution observed in data and the SM background prediction is used to check for the presence of the new resonance. A hypothesis test is built to decide between a null hypothesis given by the predicted SM background only, against an alternative hypothesis which includes both background as well as the sought after signal. In principle one can either test the background-only hypothesis and exclude it if there is a large deviation of the data from the SM background prediction, or test the signal hypothesis and exclude it if there is a large deviation of the data from the expected signal model. In particular, if no significant deviation from the SM background prediction is observed in data, compatible with the signal hypothesis, an upper limit on production cross section of such signal is usually set, up to a certain degree of belief. The CMS community has agreed upon a procedure for computing upper limits, which is based on the modified frequentist method, often referred to as  $CL_s$ . While a detailed description of such method can be found in Refs. [154, 155], the basic ingredients will be summarized Section 8.6.1. A description of the procedure followed

**Table 8.8:** Summary of the systematic uncertainties in the signal prediction for the  $\ell\nu q\bar{q}$  analysis and their impact on the event yield in the signal region and on the reconstructed  $m_{WV}$  shape (mean and width) for both muon and electron channels. The last uncertainty results in migrations between event categories, but does not affect the overall signal efficiency.

Source	Relevant quantity	Uncertainty (%)
Lepton trigger ( $\mu/e$ )	Signal yield	1 / 1
Lepton identification ( $\mu/e$ )	Signal yield	1 / 3
Lepton $p_T$ scale ( $\mu/e$ )	Signal yield	0.7 / 0.2
Lepton $p_T$ resolution ( $\mu/e$ )	Signal yield	0.1 / 0.1
Jet energy and $m_{jet}$ scale	Signal yield	0.2–4
Jet energy and $m_{jet}$ resolution	Signal yield	0.1–2
Integrated luminosity	Signal yield	2.7
Pileup	Signal yield	0.5
PDFs ( $W'$ )	Signal yield	4–19
PDFs ( $Z'$ )	Signal yield	4–13
PDFs ( $G_{bulk}$ )	Signal yield	9–77
Scales ( $W'$ )	Signal yield	1–14
Scales ( $Z'$ )	Signal yield	1–13
Scales ( $G_{bulk}$ )	Signal yield	8–22
V tagging efficiency	Signal yield	3
V tagging $p_T$ -dependence	Signal yield	6–10
Jet energy scale	Resonance shape (mean)	1.3
Jet energy scale	Resonance shape (width)	3
Jet energy resolution	Resonance shape (mean)	0.1
Jet energy resolution	Resonance shape (width)	3
Lepton $p_T$ resolution	Resonance shape (mean)	0.1
Lepton $p_T$ resolution	Resonance shape (width)	0.1
Lepton $p_T$ scale	Resonance shape (mean)	0.1
Lepton $p_T$ scale	Resonance shape (width)	0.5
Jet energy and $m_{jet}$ scale	Migration	2–24

to quantify an excess of events is provided in Section 8.6.3. A summary of the final results will be given in the next chapter.

### 8.6.1 Limit setting procedure

The procedure to establish the exclusion of a given signal hypothesis is based on a frequentist significance test which uses a log-likelihood ratio as a test statistic. In order to construct the test statistic a likelihood function is defined as

$$\mathcal{L}(data|\mu, \theta) = \text{Poisson}(data|\mu \cdot s(\theta) + b(\theta)) \cdot p(\tilde{\theta}|\theta). \quad (8.5)$$

In this definition,  $s$  and  $b$  denote the expected signal and background event yields, respectively, which, before the scrutiny of the observed data entering the statistical analysis, are subject to multiple uncertainties that are treated by introducing nuisance parameters  $\theta$ , so that signal and background expectations depend on these parameters as  $s(\theta)$  and  $b(\theta)$ . The exclusion of a signal hypothesis is generally expressed as an upper limit on the *signal strength modifier*  $\mu$  which scales the cross section used as input in the evaluation of the

expected signal yields. With this definition, the likelihood represents the Poisson probability of observing a certain amount of data when the expected yield is  $\mu \cdot s(\theta) + b(\theta)$  and given the probability  $p(\tilde{\theta}|\theta)$  of measuring a value  $\tilde{\theta}$  for the nominal nuisance parameter  $\theta$ . Note that, in this likelihood definition, “data” stands for a generic dataset, either experimental or a pseudo-data generated randomly.

The likelihood can be either binned or unbinned. In the first case the function  $\text{Poisson}(data|\mu \cdot s + b)$  in Eq. 8.5 is the product of Poisson probabilities for observing  $n_i$  events in each bin  $i$  of the signal+background model

$$\prod_i \frac{(\mu s_i + b_i)^{n_i}}{n_i!} e^{-(\mu s_i + b_i)}. \quad (8.6)$$

For the unbinned case each event enters the calculation as follows

$$k^{-1} \prod_i (\mu S f_s(x_i) + B f_b(x_i)) e^{-(\mu S + B)}, \quad (8.7)$$

where  $f_s(x)$  and  $f_b(x)$  are the probability density functions of signal and background of the observable  $x$ , while  $S$  and  $B$  are the total event rates expected for signal and background. In this analysis the unbinned form for the likelihood is used, where the observable  $x$  coincides with the reconstructed diboson invariant mass.

To compare the compatibility of the data with the background-only and signal+background hypotheses, where the prediction for the signal is allowed to be scaled by some factor  $\mu$ , the test statistic  $\tilde{q}_\mu$  is constructed based on the profile likelihood ratio as

$$\tilde{q}_\mu = -2 \ln \frac{\mathcal{L}(data|\mu, \hat{\theta}_\mu)}{\mathcal{L}(data|\hat{\mu}, \hat{\theta})}, \quad \text{with} \quad 0 \leq \hat{\mu} \leq \mu. \quad (8.8)$$

Here  $\hat{\theta}_\mu$  denotes the value of  $\theta$  that maximizes the likelihood for the hypothesized  $\mu$ , i.e. it is the conditional maximum-likelihood (ML) estimator of  $\theta$  (and thus is a function of  $\mu$ ). The procedure of refitting the nuisance parameters to maximize the likelihood for each possible value of the parameter of interest  $\mu$ , is usually referred to as “profiling”. The denominator is the maximized (unconditional) likelihood function, i.e.,  $\hat{\mu}$  and  $\hat{\theta}$  are the global maximum of the likelihood. The presence of the nuisance parameters broadens the profile likelihood as a function of  $\mu$  relative to what one would have if their values were fixed. This reflects the loss of information about  $\mu$  due to the systematic uncertainties. Higher values of  $\tilde{q}_\mu$  correspond to increasing incompatibility between the data and the hypothesized signal of strength  $\mu$ . The lower constraint for  $\hat{\mu}$  in the denominator excludes the possibility of negative signal yields. The upper constraint is introduced to avoid that data with  $\hat{\mu} > \mu$  (upward fluctuations) are considered as representing less compatibility with  $\mu$  than what obtained with data.

The observed value of the test statistic,  $\tilde{q}_\mu^{\text{obs}}$  for the given signal strength modifier  $\mu$  under test is computed, as well as the nuisance parameters  $\hat{\theta}_0^{\text{obs}}$  and  $\hat{\theta}_\mu^{\text{obs}}$  maximizing the likelihood under the background-only and signal+background hypothesis, respectively. Furthermore, the probability density functions of the chosen test statistic  $\tilde{q}_\mu$  under the signal+background hypothesis,  $f(\tilde{q}_\mu|\mu, \hat{\theta}_\mu^{\text{obs}})$ , and the background-only hypothesis, and  $f(\tilde{q}_\mu|0, \hat{\theta}_0^{\text{obs}})$ , are constructed by means of ensembles of toy MC pseudo-experiments generated according to the same Poisson probabilities used to build the likelihood. In this process the nuisance parameters are fixed to the values  $\hat{\theta}_0^{\text{obs}}$  and  $\hat{\theta}_\mu^{\text{obs}}$  obtained by fitting the observed data.

Using the  $f(\tilde{q}_\mu|0, \hat{\theta}_0^{\text{obs}})$  and  $f(\tilde{q}_\mu|\mu, \hat{\theta}_\mu^{\text{obs}})$  distributions, two p-values are computed

$$\begin{aligned} p_\mu \equiv \text{CL}_{s+b} &= P(\tilde{q}_\mu \geq \tilde{q}_\mu^{\text{obs}} | \mu s(\hat{\theta}_\mu^{\text{obs}}) + b(\hat{\theta}_\mu^{\text{obs}})) = \int_{\tilde{q}_\mu^{\text{obs}}}^{+\infty} f(\tilde{q}_\mu | \mu, \hat{\theta}_\mu^{\text{obs}}) d\tilde{q}_\mu \\ p_0 \equiv \text{CL}_b &= P(\tilde{q}_\mu \geq \tilde{q}_\mu^{\text{obs}} | b(\hat{\theta}_0^{\text{obs}})) = \int_{\tilde{q}_\mu^{\text{obs}}}^{+\infty} f(\tilde{q}_\mu | 0, \hat{\theta}_0^{\text{obs}}) d\tilde{q}_\mu. \end{aligned} \quad (8.9)$$

The two probabilities are shown in the example in Fig. 8.19(a). In the classical frequentist approach, the level of agreement between the data and hypothesized  $\mu$  is evaluated by using the  $\text{CL}_{s+b}$  probability only, and one says that the hypothesized signal  $\mu$  is excluded at 95% CL if  $\text{CL}_{s+b} \leq 0.05$ .

However, such a definition as a caveat. If the distributions of the test statistic for the signal+background and background-only hypotheses have a not negligible overlap as in the plot (c) of Fig. 8.19(b), the experiment would tend to exclude the hypothesized signal  $\mu$  even if the experiment in this case has little sensitivity to discriminate it against the background. In fact, in this case the experimental data are highly contaminated with background and a statement about the signal would be a mistake of interpretation. To prevent the inference of a signal in such cases, the so-called modified frequentist approach has been introduced at the time of LEP [154, 155]. In this approach, the level of agreement between the data and hypothesized  $\mu$  is evaluated by using instead the quantity

$$\text{CL}_s = \frac{\text{CL}_{s+b}}{\text{CL}_b}, \quad (8.10)$$

and the hypothesized signal  $\mu$  is excluded at 95% confidence level (CL) if  $\text{CL}_s \leq 0.05$ . It is straightforward to see from plot (a) of Fig. 8.19(b) that, if the distribution of the test statistic for the signal+background hypothesis is well separated from the background-only distribution, then  $\text{CL}_s \sim \text{CL}_{s+b}$  and there is no risk of misinterpretation.

In order to quote, as conventionally done, 95% CL observed upper limits, the full procedure is iterated for different values of  $\mu$ , until  $\text{CL}_s = 0.05$  is found. This value of  $\mu$  is denoted as  $\mu_{95\%}$ , and one can infer that the hypothesized resonance  $X \rightarrow WV/VH$  with a cross section  $\mu$ -times larger than the one predicted by some specific theoretical model  $\sigma_{th}$  used as input to the statistical analysis, is excluded at 95% CL. In this analysis, model-independent limits on the cross section are set by rescaling the  $\mu^{95\%} = \sigma_{95\%}/\sigma_{th}$  by the input cross section in order to obtain  $\sigma_{95\%}$ .

In addition to the observed upper limit derived from the actual data distribution, it is important to study also the expected limit given the observed data. In fact, the expected limit quantifies the sensitivity of the experiment independent from statistical fluctuations in the data. In order to compute the median-expected upper limit, and the associated  $\pm 1\sigma$  and  $\pm 2\sigma$  bands, a large set of background-only pseudo-experiments is generated and, for each of them, the  $\mu_{95\%}$  is calculated. From the cumulative distribution of  $\mu_{95\%}$ , the median value is taken as the expected limit, while the  $\pm 1(2)\sigma$  uncertainty bands on the expected limits are extracted from the values of the 16% (2.5%) and 84% (97.5%) quantiles.

### 8.6.2 The asymptotic approximation

In order to compute the  $\text{CL}_s$  the probability density functions of the test statistics are required. In particular, one needs the probability density functions  $f(\tilde{q}_\mu | \mu')$ , where  $\mu' = 0$  or  $\mu' = \mu$ , which are obtained from MC toys requiring very expensive computational resources. An approximation for the  $\text{CL}_s$  method, valid in the large sample limit, also referred to as “asymptotic approximation” has been proposed in Ref. [156] and it is briefly described in the following.

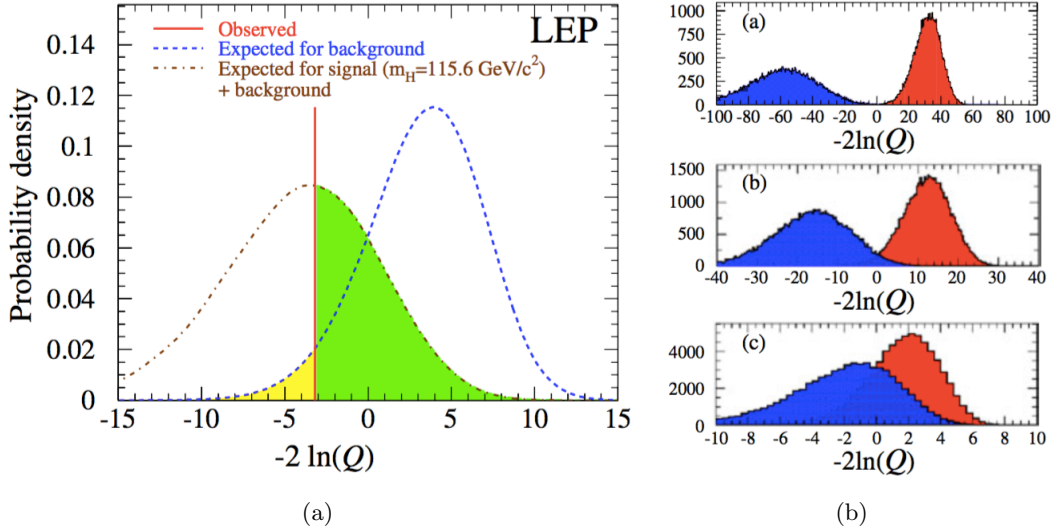


Figure 8.19: blabla

By using the Wald approximation [157] the desired distribution  $f(\tilde{q}_\mu | \mu')$  can be obtained by expressing the test statistic given by the log-likelihood ratio as

$$\tilde{q}_\mu = \frac{(\mu - \hat{\mu})^2}{\sigma^2} + \mathcal{O}(1/\sqrt{N}), \quad (8.11)$$

where  $\hat{\mu}$  follows a Gaussian distribution with a mean  $\mu'$  and standard deviation  $\sigma$ , and  $N$  represents the data sample size. For large data samples ( $N \rightarrow \infty$ ), the  $\mathcal{O}(1/\sqrt{N})$  can be neglected and it can be shown [158] that the distribution  $f(\tilde{q}_\mu | \mu')$  of the test statistic  $\tilde{q}_\mu$  follows a *noncentral chi-square* distribution for one degree of freedom with noncentrality parameter

$$\Lambda = \frac{(\mu - \mu')^2}{\sigma^2}. \quad (8.12)$$

For the special case  $\mu' = \mu$  one has  $\Lambda = 0$  and the test statistic is distributed as a chi-square for one degree of freedom. For the general case in which  $\mu' \neq \mu$ , the standard deviation  $\sigma$  of  $\hat{\mu}$  has to be evaluated, which depends on the MLE estimator of the nominal nuisance parameters. The evaluation of  $\sigma$  is greatly simplified considering a special, artificial data set, referred to as the “Asimov data set”, where all statistical fluctuations are suppressed and the estimators for all parameters are replaced by their expectation values as follows:

$$\hat{\mu} = \mu' \quad \text{and} \quad \hat{\theta} = \theta. \quad (8.13)$$

With these assumptions the test statistic  $\tilde{q}_{\mu,A}$  for the Asimov dataset is given by

$$\tilde{q}_{\mu,A} \approx \frac{(\mu - \mu')^2}{\sigma^2} = \Lambda. \quad (8.14)$$

From the Asimov data set one therefore obtains an estimate of the noncentrality parameter  $\Lambda$  that characterizes the distribution  $f(\tilde{q}_\mu | \mu')$ . Equivalently, the above equation can be used to obtain the variance  $\sigma^2$  which characterizes the distribution of  $\hat{\mu}$ , namely,

$$\sigma_A^2 = \frac{(\mu - \mu')^2}{\tilde{q}_{\mu,A}}, \quad (8.15)$$

so that the distribution obtained by using  $\sigma_A^2$  has a median given by the corresponding Asimov value  $\tilde{q}_{\mu,A}$ . Using these formulae, asymptotic relations are derived which are easily solved for the observed upper limits with the  $CL_s$  method, as well as for the expected median and error bands.

### 8.6.3 Quantifying an excess of events

The presence of the signal is quantified by the background-only p-value, i.e. the probability for the background to fluctuate and give an excess of events as large or larger than the observed one. As for the upper limits, this evaluation requires defining a test statistic and the construction of its probability density function. For a given resonance mass hypothesis  $M_X$ , the test statistic used in this case is  $\tilde{q}_0$ , defined as

$$\tilde{q}_0 = -2 \ln \frac{\mathcal{L}(\text{data}|0, \hat{\theta}_0)}{\mathcal{L}(\text{data}|\hat{\mu}, \hat{\theta})}, \quad \text{with } \hat{\mu} \geq 0. \quad (8.16)$$

The probability density function  $f(\tilde{q}_0|0, \hat{\theta}_0^{\text{obs}})$  is built by generating toy MC pseudo-data under the assumption of the background-only hypothesis. From this distribution, the p-value corresponding to a given experimental observation  $\tilde{q}_0^{\text{obs}}$  is evaluated:

$$p_0 = P(\tilde{q}_0 \geq \tilde{q}_0^{\text{obs}} | b(\hat{\theta}_0^{\text{obs}})) = \int_{\tilde{q}_0^{\text{obs}}}^{+\infty} f(\tilde{q}_0|0, \hat{\theta}_0^{\text{obs}}) d\tilde{q}_0. \quad (8.17)$$

This probability is converted into a *significance*, also referred to as *Z value*, as follows

$$Z = \Phi^{-1}(1 - p_0). \quad (8.18)$$

A significance of  $5\sigma$ , corresponding to a p-value of  $2.87 \times 10^{-7}$ , is conventionally used in high energy physics to claim a discovery, and  $3\sigma$  for an evidence.

It can be demonstrated that in the asymptotic approximation (Section 8.6.2), the likelihood ratio test statistic  $\tilde{q}_0$  follows a chi-square distribution for one degree of freedom, and a fair estimate of the p-value and of the significance can be obtained from the observed value  $\tilde{q}_0^{\text{obs}}$  itself, without the need for generating pseudo-data, as follows

$$\begin{aligned} p_0 &= \frac{1}{2} [1 - \text{erf}(\sqrt{\tilde{q}_0^{\text{obs}}}/2)] \\ Z &= \sqrt{\tilde{q}_0^{\text{obs}}}. \end{aligned} \quad (8.19)$$

The p-value discussed above is evaluated at a fixed resonance mass  $M_X$  and can be referred to as a *local p-value*. In this search, a scan is performed over a wide range of resonance mass hypotheses with the aim of finding the minimum local p-value, which describes the probability of a background fluctuation for that particular resonance mass hypothesis. However, it is important to distinguish the probability of finding a fluctuation in some particular location from the probability of finding such a fluctuation anywhere else. The former is associated to the so called *local significance*, whereas the latter is referred to as the *global significance*. The fact that the global significance is usually smaller than the largest local one is often referred to as the “look-elsewhere effect” (LEE). As demonstrated in Ref. [159], the global and local p-values are related to each other by a multiplicative factor, usually referred to as “trial factor”, proportional to the number of independent search regions. In the asymptotic approximation the trial factor grows linearly with the local significance, through a proportional

constant that is related to the ratio between the mass range under consideration divided by its resolution. In particular, it can be shown that

$$\text{trial\#} = \frac{p_{\text{global}}}{p_{\text{local}}} \approx \frac{1}{3} \frac{\text{mass range}}{\text{mass resolution}} Z_{\text{local}}. \quad (8.20)$$

The trial factor is best estimated through MC methods as it will be shown in Section 9.2. However, a good agreement with the equation above is obtained.

# Results with 8 TeV data

---

The final results of the analysis performed with 8 TeV data and focused on the search for a heavy charged resonance decaying into W and Higgs bosons in the  $\ell\nu b\bar{b}$  final state, are presented and discussed in this chapter. In particular, the final observed  $m_{\text{WH}}$  spectrum is used to check for the presence of a new resonance. Firstly, a search is conducted for local enhancement in the  $m_{\text{WH}}$  distribution, which might be due to a signal. As described in the following, since no significant excesses are found, upper limits are set on the production cross section of the new resonance.

## 9.1 Final $m_{\text{WH}}$ distribution

The predicted number of background events in the signal region after the inclusion of all backgrounds is summarized in Table 9.1 and compared with observations. The yields are quoted in the range  $0.7 < m_{\text{WH}} < 3 \text{ TeV}$ . The expected background is derived with the sideband procedure described in Section 8.2. The uncertainties in the background prediction from data are statistical in nature, as they depend on the number of events in the sideband region. The muon channel has more expected background events than the electron channel owing to the lower  $E_T^{\text{miss}}$  requirement and its worse mass resolution at high  $p_T$ .

**Table 9.1:** Observed and expected yields in the signal region together with statistical uncertainties.

	$e\nu + \text{H-jet}$	$\mu\nu + \text{H-jet}$
Observed yield	9	16
Expected total background	$11.3 \pm 3.1$	$14.9 \pm 3.1$
W+jets	$4.7 \pm 2.9$	$7.0 \pm 3.1$
Top	$6.3 \pm 1.1$	$7.3 \pm 0.4$
VV	$0.4 \pm 0.1$	$0.6 \pm 0.2$

Figure 9.1 shows the final observed  $m_{\text{WH}}$  spectra after all selection criteria have been applied. The highest mass event is in the electron category and has  $m_{\text{WH}} \approx 1.9 \text{ TeV}$ . The observed data and the predicted background in the muon channel agree. In the electron channel, an excess of three events is observed with  $m_{\text{WH}} > 1.8 \text{ TeV}$ , where about 0.3 events are expected, while in the muon channel no events with  $m_{\text{WH}} > 1.8 \text{ TeV}$  are observed, where about 0.3 events are expected.

## 9.2 Significance of the data

A comparison between the  $m_{\text{WH}}$  distribution observed in data and the largely data-driven background prediction is used to test for the presence of a resonance decaying into WH. As described in Section 8.6, the statistical test is performed based on a profile likelihood discriminant for an unbinned shape analysis. Systematic uncertainties in the signal and background yields are treated as nuisance parameters and profiled in the statistical interpretation

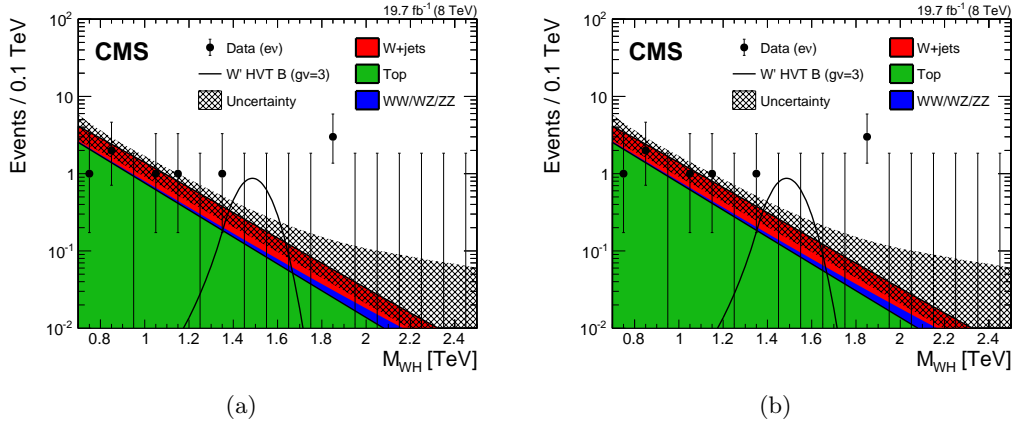


**Figure 9.1:** Final distributions in  $m_{\text{WH}}$  for data and expected backgrounds for electron (a) and muon (b) categories. The 68% error bars for Poisson event counts are obtained from the Neyman construction [160]. The hatched region indicates the statistical uncertainty of the fit combined with the systematical uncertainty in the shape. This figure also shows a hypothetical  $W'$  signal with mass of 1.5 TeV, normalized to the cross section predicted by the HVT model B with parameter  $g_V = 3$  as described in Section.

using log-normal priors, while Gaussian priors are used for shape parameters only. The local significance of the observations is evaluated in the context of the described statistical test, under the assumptions of a narrow resonance decaying into the WH final state and lepton universality for the W boson decay, by combining the two event categories. Correlations arising from the uncertainties common to both channels are taken into account. The result is shown in Fig. 9.2. The highest local significance of 2.2 standard deviations is found for a resonance mass of 1.8 TeV, driven by the excess in the electron channel described in the previous section. The corresponding local significance for a resonance of 1.8 TeV in the electron channel is 2.9 standard deviations, while in the muon channel there is no significance.

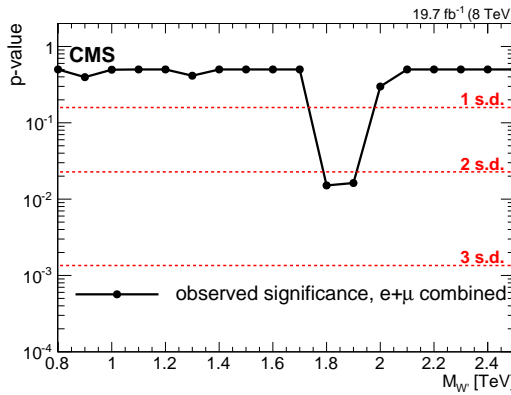


**Figure 9.2:** Local p-value of the combined electron and muon data as a function of the  $W'$  boson mass, probing a narrow WH resonance.

Taking into account the look-elsewhere effect (Section 8.6.3), the local significance of 2.9 standard deviations can be translated into a global significance value by computing the trial factor as given by Eq. 8.20. Considering the mass range 0.8–2.5 TeV and the step of 0.1 TeV used for the search, a trial factor of  $\approx 16.4$  is obtained. The factor, when multiplied by the local p-value, gives a global significance of 1.9 standard deviations when searching

for resonances over the full mass range and across two channels. In order to cross check this final value, the LEE is also estimated by means of background-only pseudo-experiments. The relation between the global and local significances obtained with this method is shown in Fig. 9.3, and it agrees with the calculation performed with the trial factor. It can be concluded that the results are thus statistically compatible with the SM expectation within 2 standard deviations.

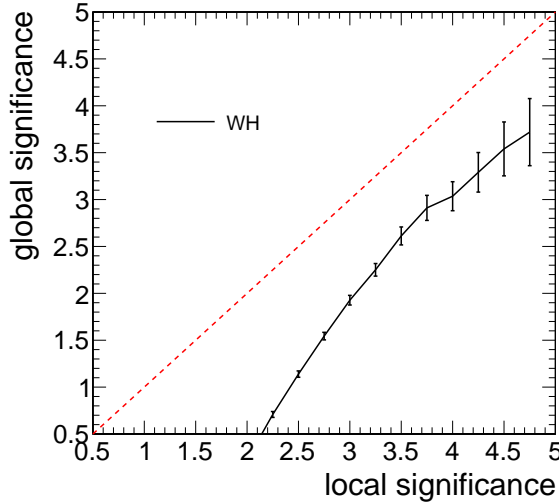


**Figure 9.3:** Global significance as a function of the local significance which corresponds to the maximal significance in the  $m_{\text{WH}}$  range 0.8–2.5 TeV in the two categories. The global significance is estimated with a frequentist approach using background-only pseudo-experiments and corresponds to the fraction of toys (translated from a p-value to significance) with at least a certain local significance in the  $m_{\text{WH}}$  range in the two categories.

### 9.3 Cross section limits

Since no excesses with significance larger than three standard deviations are observed, upper limits are set on the production cross section of the new resonance following the modified-frequentist  $\text{CL}_s$  method described in Section 8.6. Exclusion limits can be set as a function of the  $W'$  resonance mass, under the narrow-width approximation. The results are interpreted in the HVT model B and in the context of the little Higgs model.

Figure 9.4 shows the expected and observed exclusion limits at 95% CL on the product of the  $W'$  production cross section and the branching fraction of  $W' \rightarrow \text{WHWH}$  for the electron and muon channels separately, and for the combination of the two. The limits are compared with the prediction of the two theoretical models. For the combined channels, the observed and expected lower limits on the  $W'$  mass are 1.4 TeV in the LH model and 1.5 TeV in the HVT model B. For the electron (muon) channel, the observed and expected lower limits on the  $W'$  mass are 1.2 (1.3) TeV in the LH model and 1.3 (1.3) TeV in the HVT model B.

These results are finally combined with other searches for heavy resonances decaying into diboson performed with pp collisions at 8 and 13 TeV as described in Chapter 11.

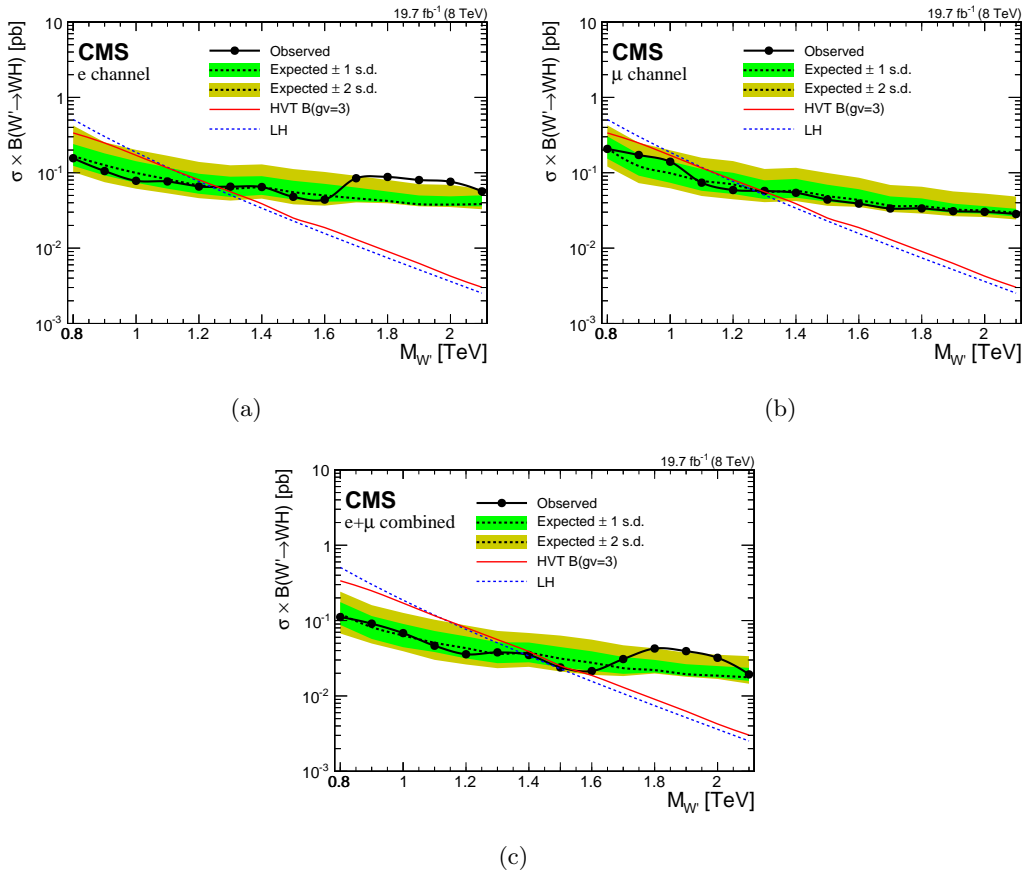


**Figure 9.4:** Observed (solid) and expected (dashed) upper limits at 95% CL on the product of the  $W'$  production cross section and the branching fraction of  $W' \rightarrow WH$  for electron (a) and muon (b) channels, and the combination of the two channels (c). The products of cross sections and branching fractions for  $W'$  production in the LH and HVT models are overlaid.

# Results with 13 TeV data

---

In this chapter, the final results of the analysis performed with 13 TeV data and focused on the search for a heavy resonances decaying into a pair of vector bosons (WW/WZ) in the  $\ell\nu q\bar{q}$  final state, are presented and discussed. As for the analysis conducted with 8 TeV data described in the previous chapter, the final  $m_{WV}$  spectrum observed in data is used to check for the presence of a new resonance. No bins with an excess with significance larger than three standard deviations are observed and upper limits are set on the production cross section of such resonances under a variety of signal benchmarks by combining all the event categories.

## 10.1 Final $m_{WV}$ distribution

The final  $m_{WV}$  spectra observed in data and for the background predicted with the  $\alpha$  ratio method (Section 8.2) for all event categories are shown in Fig. 10.1. The observed data and the predicted background are found to well agree. The highest mass events are at  $m_{WV} = 2.95$  and 3.15 TeV for the muon and electron category, respectively.

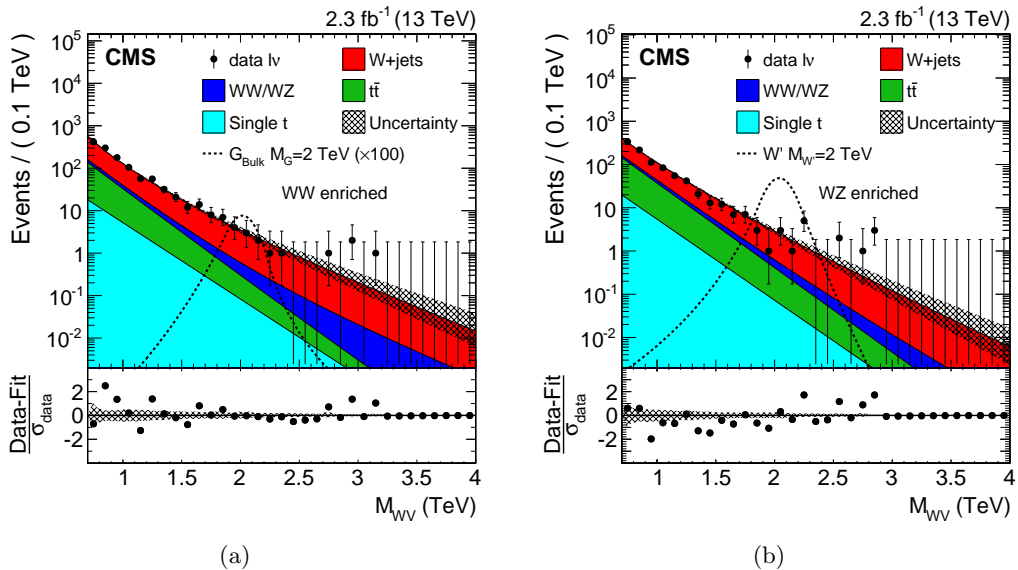


**Figure 10.1:** Final  $m_{WV}$  distributions for data and expected backgrounds obtained combining muon and electron channels in the WW-enriched (a) and WZ-enriched (b) signal regions. In each plot the solid curve represents the background estimation provided by the  $\alpha$  ratio method. The hatched band includes both statistical and systematic uncertainties. The data are shown as black points. At the bottom of each plot are the bin-by-bin fit residuals,  $(N_{\text{data}} - N_{\text{fit}})/\sigma_{\text{data}}$ , shown together with the uncertainty band of the fit normalized by the statistical uncertainty of data,  $\sigma_{\text{data}}$ . The distributions for a bulk graviton and for a  $W'$  signal are also shown with black dashed lines.

## 10.2 Cross section limits

Since no excesses with significance larger than three standard deviations are observed, upper limits are set on the production cross section of the new resonance by combining all event categories. The asymptotic approximation of the  $\text{CL}_s$  criterion described in Section 8.6 is followed. The exclusion limits computed with this approach are found to agree with the results obtained using the modified frequentist prescription. Systematic uncertainties are treated as nuisance parameters in the statistical interpretation using log-normal, and they are profiled following the frequentist convention as discussed in Section 8.6.

Exclusion limits are set in the context of the bulk graviton model and of the HVT Models A and B, under the assumption of a natural width negligible compared to the experimental resolution. Figure 10.2 shows the resulting 95% CL expected and observed exclusion limits on the signal cross section as a function of the resonance mass for all signal hypotheses. The limits are compared with the product of cross section and branching fraction ( $\sigma \times \mathcal{B}$ ) to WW for a bulk graviton with  $k/\bar{M}_{\text{Pl}} = 0.5$ , and with  $\sigma \times \mathcal{B}$  for WZ and WW for spin-1 particles predicted by the HVT Models A and B. In this context, a scenario is considered, where the  $W'$  and  $Z'$  bosons are expected to be degenerate in mass (triplet hypothesis). In addition, the statistical interpretation is provided in a scenario where only a charged ( $W'$ ) or a neutral ( $Z'$ ) resonance is expected at a given mass (singlet hypothesis).

In the narrow-width bulk graviton model, the sensitivity of the search is not large enough to set mass limits, however, cross sections are excluded in the range 0.007–0.4 pb. For HVT Model A (B), the data exclude singlet  $W'$  resonances with masses  $< 1.6$  (1.9) TeV and  $Z'$  resonances with masses below  $< 1.5$  (1.6) TeV. Under the triplet hypothesis, spin-1 resonances with masses  $< 1.9$  and  $< 2$  TeV are excluded for HVT Models A and B, respectively.

These results supersede the ones obtained analyzing 8 TeV data, where the lower mass limit of 1.5 TeV for a  $W'$  in the context of the HVT model B is reached (Fig. 9.4). However, the most stringent limits are obtained in the final combination of these results with other searches for heavy resonances decaying into diboson with 8 and 13 TeV data, as described in Chapter 11.

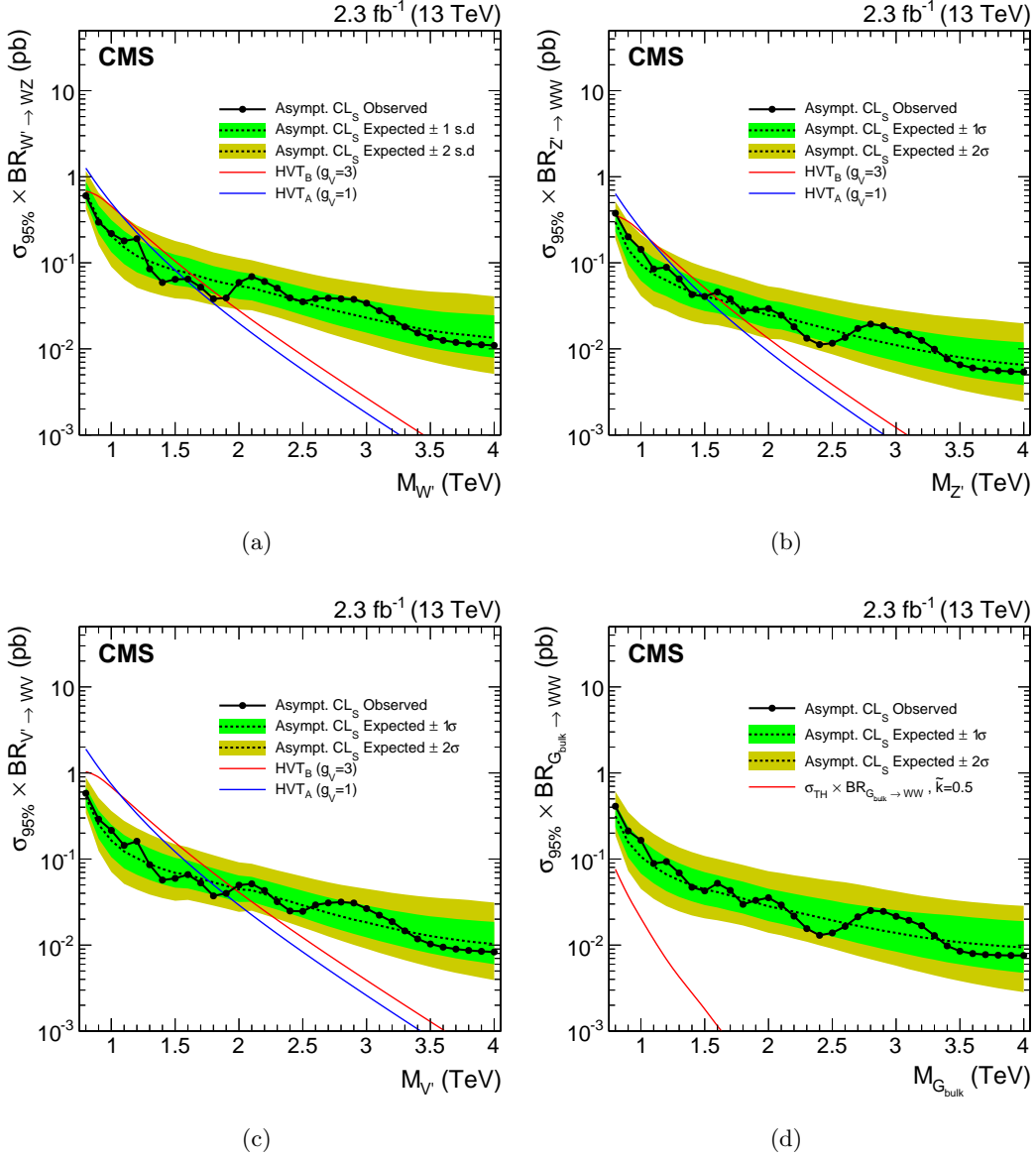


**Figure 10.2:** Observed (black solid) and expected (black dashed) 95% CL upper limits on the production of a narrow-width resonance decaying to a pair of vector bosons for different signal hypotheses. In the upper plots, limits are set in the context of a spin-1 charged  $W'$  (a) and neutral  $Z'$  (b) resonances, and compared with the prediction of the HVT Models A and B. (c) Limits are set in the same model under the triplet hypothesis ( $W'$  and  $Z'$ ). (d) Limits are set in the context of a bulk graviton with  $k/\bar{M}_{\text{Pl}} = 0.5$  and compared with the prediction.

# Combination of searches for diboson resonances at $\sqrt{s} = 8$ and 13 TeV

---

In addition to the analyses described in this work, several similar searches for narrow-width massive resonances decaying to pairs of W, Z, and Higgs bosons in various final states have been performed with the CMS experiments in both LHC Run 1 and Run 2 [133–135, 138, 161–164]. As these searches have individually very similar sensitivity to benchmark physics scenarios of interest, a statistical combination to maximize the overall sensitivity is performed and presented in this chapter. Furthermore, the combination of these analyses is fundamental to fully understand the compatibility of the excess observed in the  $\ell\nu b\bar{b}$  final state at  $m_{\text{WH}} = 1.8$  TeV as discussed in Chapter 9. The interest in this excess was further enhanced by the observation of an excess at the same diboson invariant mass values by the ATLAS experiment in the all-hadronic final state [165].

The analyses taken into account in the statistical combination are based on pp collision data collected by the CMS experiment during 2012 and 2015 at  $\sqrt{s} = 8$  TeV and 13 TeV, corresponding to an integrated luminosity of  $19.7 \text{ fb}^{-1}$  and  $2.3\text{--}2.7 \text{ fb}^{-1}$ , respectively. Analyses with all-leptonic, semi-leptonic, and all-jets final states are considered. This includes the decay into charged leptons ( $\ell$ ) and neutrinos ( $\nu$ ) of W and Z bosons, as well as reconstructed jets containing the decay products of hadronically decaying W or Z bosons. The latter are labeled as q $\bar{q}$  final states that include  $W \rightarrow q\bar{q}' \rightarrow \text{jet}$  and  $Z \rightarrow q\bar{q} \rightarrow \text{jet}$ . For Higgs bosons, hadronic decays labeled as b $\bar{b}$  or q $\bar{q}q\bar{q}$  final states referring to  $H \rightarrow b\bar{b}$  or  $H \rightarrow q\bar{q}'q\bar{q}'$  are considered.

Altogether, results are combined corresponding to the following final states:  $\ell\nu q\bar{q}$  (13 TeV, this work) [135], q $\bar{q}q\bar{q}$  (13 TeV) [135],  $\ell\ell b\bar{b}/\ell\nu b\bar{b}/\nu\nu b\bar{b}$  (13 TeV) [138],  $3\ell\nu$  (8 TeV) [162],  $\ell\nu q\bar{q}$  (8 TeV) [133],  $\ell\ell q\bar{q}$  (8 TeV) [133], q $\bar{q}q\bar{q}$  (8 TeV) [134],  $\ell\nu b\bar{b}$  (8 TeV, this work) [163], q $\bar{q}b\bar{b}/6q$  (8 TeV) [161], q $\bar{q}\tau\tau$  (8 TeV) [164]. As for the analyses described in this thesis, also the other searches feature a similar experimental signature given by highly boosted bosons in the final state. Therefore, all these analyses exploit same V tagging and H tagging algorithms to help resolve jet decays of massive bosons and achieve large suppression of SM backgrounds.

The results are interpreted in the context of the BSM models described in Section 2.3 and summarized in Table 4.1, namely, heavy vector triplet and singlet models predicting W' and Z' bosons, and the bulk graviton model. Combined cross section limits as a function of resonance mass are obtained. This work represents the first combined search for high mass resonances with both WW/WZ and WH/ZH signatures.

This chapter is organized as follows. A summary of the analyses entering the combination is given in Section 11.1. The combination procedure is described in Section 11.2, and finally the results are presented and discussed in Section 11.3.

## 11.1 Inputs to the combination

A statistical combination is carried out of searches for new heavy resonances that are performed on top of the steeply falling invariant mass distribution of two reconstructed W, Z or Higgs bosons. Various decay modes of these bosons are considered. The  $Z \rightarrow \ell\ell$  candidates are reconstructed from electron and muon candidates, while  $W \rightarrow \ell\nu$  candidates are reconstructed from identified muons or electrons with the method described in Section 6.6, which makes use of the missing transverse momentum under the constraint that the  $\ell\nu$  invariant mass is equal to the known W-boson mass. The  $H \rightarrow \tau\tau$  candidates are reconstructed from electron, muon and hadronically-decaying  $\tau$  candidates in combination with missing transverse momentum. The  $W \rightarrow q\bar{q}'$ ,  $Z \rightarrow q\bar{q}$ ,  $H \rightarrow b\bar{b}$  and  $H \rightarrow q\bar{q}'\bar{q}\bar{q}'$  candidates are reconstructed with jet algorithms with a distance parameter of 0.8 (CA for the 8 TeV data analyses, AK for the 13 TeV analyses).

All analyses are focused on high mass resonances which decay in highly boosted W/Z/H bosons. Hence, their decay products are reconstructed close-by in angle, requiring the special reconstruction techniques already described previously in this thesis. For highly boosted W/Z/H bosons decaying to electron, muon and  $\tau$  candidates, identification and isolation requirements are adapted such that the nearby reconstructed leptons do not reduce the identification efficiency.

For highly boosted V bosons decaying to quark anti-quark pairs, the V algorithm described in Section 7.2 is applied. In the 8 TeV data analyses, a V jet candidate is identified if its pruned mass,  $m_{\text{jet}}$ , falls in a range around the W or Z mass. In the 13 TeV data analyses, two distinct categories enriched in W or Z bosons are defined by two exclusive ranges in  $m_{\text{jet}}$  as described in Section 8.1. In the 8 TeV data analyses the sensitivity is further enhanced by distinguishing two categories, a low purity (LP) and a high purity (HP) one based on the  $\tau_{21}$  variable. This same strategy is followed in the dijet 13 TeV analysis. Although the HP category dominates the total sensitivity of the analyses, the LP category is retained, since for large masses of a new resonance it provides improved signal efficiency with only moderate background contamination.

Higgs-boson identification is similarly performed using a pruned jet mass window around the Higgs mass together with b-tagging algorithms applied to the H jet or to its subjets as described in Section 7.3. To distinguish  $H \rightarrow WW \rightarrow q\bar{q}'q\bar{q}'$  jets from background, a similar technique as V tagging is applied using the  $\tau_{42}$  ratio. The selection efficiencies for each signal and channel are summarized in Table 11.1.

In all-jets final states, the background dominated by QCD multijets production is estimated with a fit of signal+background to the data, where the background is described by a smooth functional form. In semi-leptonic final states, the dominant backgrounds from V+jets production are estimated using data in  $m_{\text{jet}}$  sidebands with the method described in Section 8.2. In all-leptonic final states, the dominant background from standard model diboson production is estimated using simulated events.

More details are given in the following for the analyses where not all signal models presented in the combination were originally considered.

### 11.1.1 Reinterpretations

In the searches for new heavy resonances decaying into a pair of vector bosons (WW, ZZ or WZ) in the semi-leptonic ( $\ell\nu q\bar{q}$  and  $\ell\ell q\bar{q}$ ) final states [133] with pp collision data collected at  $\sqrt{s} = 8$  TeV, exclusion limits at 95% CL have been set on the production cross section of a bulk graviton. The results were published with a parametrization for the reconstruction efficiency as a function of W and Z boson kinematics, enabling a reinterpretation in the

**Table 11.1:** Summary of the signal efficiencies of all analysis channels for all signal models for a 2 TeV resonance. For analyses with categorization in high-purity (HP) and low-purity (LP) categories, both efficiencies are quoted in the form HP/LP. The signal efficiencies are in percent and include the SM branching ratios of the bosons to the final state of the analysis channel, effects from detector acceptance, as well as reconstruction and selection efficiencies.

Channel	HVT				RS bulk	
	$W'$		$Z'$		$G_{\text{bulk}}$	
	WZ	WH	WW	ZH	WW	ZZ
$3\ell\nu$ (8 TeV)	0.6	-	-	-	-	-
$\ell\ell q\bar{q}$ (8 TeV)	1.1/-	-	-	0.2/-	-	3.0/1.0
$\ell\nu q\bar{q}$ (8 TeV)	4.8/-	-	9.4/-	-	10.6/7.1	-
$q\bar{q}q\bar{q}$ (8 TeV)	5.9/5.5	0.8/0.7	5.7/5.3	0.8/0.7	3.8/3.1	5.7/4.2
$\ell\nu bb$ (8 TeV)	-	0.9	-	-	-	-
$q\bar{q}\tau\tau$ (8 TeV)	-	1.2	-	1.3	-	-
$q\bar{q}bb/6q$ (8 TeV)	-	3.0/1.8	-	1.7/1.1	-	-
$\ell\nu q\bar{q}$ (13 TeV)	10.2/-	1.7/-	19.4/-	-	18.1/-	-
$q\bar{q}q\bar{q}$ (13 TeV)	9.7/12.3	1.8/2.5	8.2/10.6	1.9/2.6	8.7/12.4	11.0/13.5
$\ell\ell bb$ (13 TeV)	-	-	-	1.5	-	-
$\ell\nu bb$ (13 TeV)	-	4.0	-	-	-	-
$\nu\nu bb$ (13 TeV)	-	-	-	4.2	-	-

context of neutral and charged the spin-1 resonances as predicted by HVT models. The reinterpretation in the context of this model is obtained by rescaling the bulk graviton signal efficiencies by scale factors taking into account the different kinematics of W and the Z bosons from  $W'$  and  $Z'$  production compared to the graviton production. The scale factors have been derived for each mass point by means of the tables published in Ref. [133]. Since the efficiency parametrization is restricted to the HP category of the analyses, the LP category is not used for the  $W'$  and  $Z'$  interpretations of these channels. The  $m_{\text{jet}}$  window that defines the signal regions of the analysis channels is such that the  $\ell\nu q\bar{q}$  channel is sensitive to both the charged and neutral resonance predicted by HVT models. This is taken into account in the statistical combination.

The searches for new heavy resonances decaying into a pair of vector bosons (WW, ZZ or WZ) in the semi-leptonic ( $\ell\nu q\bar{q}$  and  $\ell\ell q\bar{q}$ ) [133, 133, 135], and all-hadronic ( $q\bar{q}q\bar{q}$ ) final states [134, 135] at 8 and 13 TeV, are also sensitive to WH and ZH signatures, since a small fraction of jets initiated by Higgs bosons have a pruned jet mass in the range considered to identify W or Z bosons. These searches were therefore re-interpreted with WH and ZH signals to profit from this additional signal sensitivity. The additional signal efficiencies for those signals are indicated in Table 11.1.

The search for resonances in the  $q\bar{q}\tau\tau$  final state [161] was optimized for a resonance  $Z'$  decaying into Z and a Higgs boson. However, given the large  $m_{\text{jet}}$  window ( $65 < m_{\text{jet}} < 105$  GeV) used to identify the hadronically decaying Z boson, this analysis channel is also sensitive to the production of the charged spin-1  $W'$  resonance decaying into W and Higgs bosons as predicted in HVT models. This overlap is also taken into account in the statistical combination.

## 11.2 Combination procedure

In all the analysis channels a search is performed for a peak on top of the falling background distribution in the diboson invariant mass by means of a maximum likelihood fit to the data. As done for the main analyses described in this work (Section 8.6), the likelihood function is maximized to obtain the best fit of the signal strength modified  $\mu$  for each signal and resonance mass hypothesis. The function is constructed from the reconstructed diboson invariant mass distribution observed in data, the background prediction, and the signal resonance shape to test for the presence of a new resonance decaying to two bosons. For the  $3\ell\nu$ ,  $q\bar{q}q\bar{q}$ ,  $q\bar{q}b\bar{b}/6q$ , and  $q\bar{q}\tau\tau$  analyses, the likelihood function is computed using events binned as a function of reconstructed diboson invariant mass as in Equation 8.6. For the remaining analyses ( $\ell\nu q\bar{q}$ ,  $\ell\ell q\bar{q}$ ,  $\ell\nu b\bar{b}$ ), the functional form for an unbinned likelihood is similarly defined using functional forms that describe the shape of the reconstructed diboson invariant mass for background and signal resonance as given by Equation 8.7.

The treatment of the background in the maximum likelihood fit depends on the analysis channel. In the  $q\bar{q}q\bar{q}$  and  $q\bar{q}b\bar{b}/6q$  analyses, the background fit function parameters are left floating in the maximum likelihood fit, such that the background prediction is simultaneously obtained with the signal  $\mu$  for every hypothesis. The remaining analyses ( $\ell\nu q\bar{q}$ ,  $\ell\ell q\bar{q}$ ,  $\ell\ell b\bar{b}$ ,  $\ell\nu b\bar{b}$ ,  $\nu\nu b\bar{b}$ ) follow the same procedure as for the analyses described in this work: the background is estimated using data sidebands and uncertainties related to its parametrized shape are treated as nuisance parameters constrained with Gaussian probability density functions in the maximum likelihood fit. Except for the cases described in Section 11.1, which have been found to be negligible, selection are exclusive. The combined likelihood is then obtained from the product of the likelihoods of each individual analysis channel.

The asymptotic approximation of the  $CL_s$  criterion (Section 8.6.2) is used with the test statistic given by Eq. 8.8 to set upper limits on the cross section for resonance production. When combining 8 and 13 TeV analyses, limits are set on the signal scale factor  $\mu$  taking into account the production cross section ratio evaluated from theory between 8 TeV and 13 TeV.

The dominant sources of systematic uncertainties are treated as nuisance parameters constrained with a log-normal probability density function. All nuisance parameters are profiled following the frequentist convention discussed in Section 8.6. When the likelihoods of multiple analyses channels are combined, the correlation of systematic effects across analysis channels is taken into account by categorizing the uncertainties into fully correlated (associate to same nuisance parameter) and fully uncorrelated (associate to different nuisance parameters). Table 11.2 summarizes which uncertainties are treated as correlated among 8 and 13 TeV analyses, electron and muon channels, HP and LP categories and W, Z and Higgs enriched categories in the combination. Further categorisation within individual analyses are described therein.

The most important and only nuisance parameters treated as correlated between 8 and 13 TeV analyses are those related to the PDFs and the choice of factorization ( $\mu_f$ ) and renormalization ( $\mu_r$ ) scales used to estimate the signal cross sections. They have been re-evaluated for this combination for both 8 and 13 TeV analyses, estimating the full impact on the expected signal yield rather than the impact on only the signal acceptance. The PDF uncertainties are evaluated using the NNPDF 3.0 [65] PDFs. The uncertainty related to the choice of  $\mu_f$  and  $\mu_r$  scales is evaluated following the proposal in Refs. [148, 149] by varying the default choice of scales in the following 6 combinations of factors:  $(\mu_f, \mu_r) \times (1/2, 1/2)$ ,  $(1/2, 1)$ ,  $(1, 1/2)$ ,  $(2, 2)$ ,  $(2, 1)$ , and  $(1, 2)$ . The experimental uncertainties are all treated as uncorrelated between 8 and 13 TeV. At 13 TeV the systematic uncertainties are dominated by the statistical uncertainty of the datasets used to evaluate scale factors applied to the signal

**Table 11.2:** Correlation of systematic uncertainties.

Systematic uncertainty	Type	8+13 TeV	e+μ	HP+LP	W+Z+Higgs
Lepton trigger	yield	no	no	yes	yes
Lepton identification	yield	no	no	yes	yes
Lepton momentum scale	yield, shape	no	no	yes	yes
Jet energy scale	yield, shape	no	yes	yes	yes
Jet energy resolution	yield, shape	no	yes	yes	yes
Jet mass scale	yield	no	yes	yes	yes
Jet mass resolution	yield	no	yes	yes	yes
b tagging	yield	no	yes	yes	yes
W tagging $\tau_{21}$ (HP/LP)	yield	no	yes	yes	yes
Integrated luminosity	yield	no	yes	yes	yes
Pileup	yield	no	yes	yes	yes
PDF	yield	yes	yes	yes	yes
$\mu_f, \mu_r$ scales	yield	yes	yes	yes	yes

simulation to reproduce data.

## 11.3 Results

In this section the combination of the individual analysis channels described in Section 11.1 is presented, for each of the signal hypothesis described in Section 2.3. For each channel the 95% CL exclusion limits on the signal strength modifier  $\mu = \sigma_{95\%}/\sigma_{\text{theory}}$  are presented.

### 11.3.1 Limits on W' and Z' singlets

Figures 11.1(a) and 11.1(b) show the comparison and combination of the results obtained in the 8 and 13 TeV searches for a W' singlet resonance for model A and model B, respectively. The 95% CL exclusion limits on the signal strength in the resonance mass range  $0.6 < m_{W'} < 4$  TeV for model A and  $0.8 < m_{W'} < 4$  TeV for model B are shown. Table 11.3 summarizes the resulting resonance mass exclusion limits. Below resonance mass values of about 1.4 TeV, the  $3\ell\nu$  channel at 8 TeV is most sensitive. At higher masses, the qqqq̄ search at 13 TeV dominates the sensitivity. The overall sensitivity benefits from the combination up to resonance masses of about 2 TeV, lowering the cross section exclusion limit by up to a factor 1/3 when comparing to the most sensitive single channel. Above masses of 2 TeV the 8 TeV channels do not add any significant contribution compared to the qqqq̄ search at 13 TeV. The observed mass limit is not affected by the combination compared to that obtained from the 13 TeV searches. However, the expected mass limit is slightly improved from 2.3 to 2.4 TeV.

**Table 11.3:** Resonance mass 95% CL exclusion limits in HVT model scenarios.

Model	Observed limit (TeV)	Expected limit (TeV)
W' (model A)	2.3	2.1
Z' (model A)	2.2	2.0
HVT (W' +Z') (model A)	2.4	2.4
W' (model B)	2.3	2.4
Z' (model B)	2.3	2.1
HVT (W' +Z') (model B)	2.4	2.6

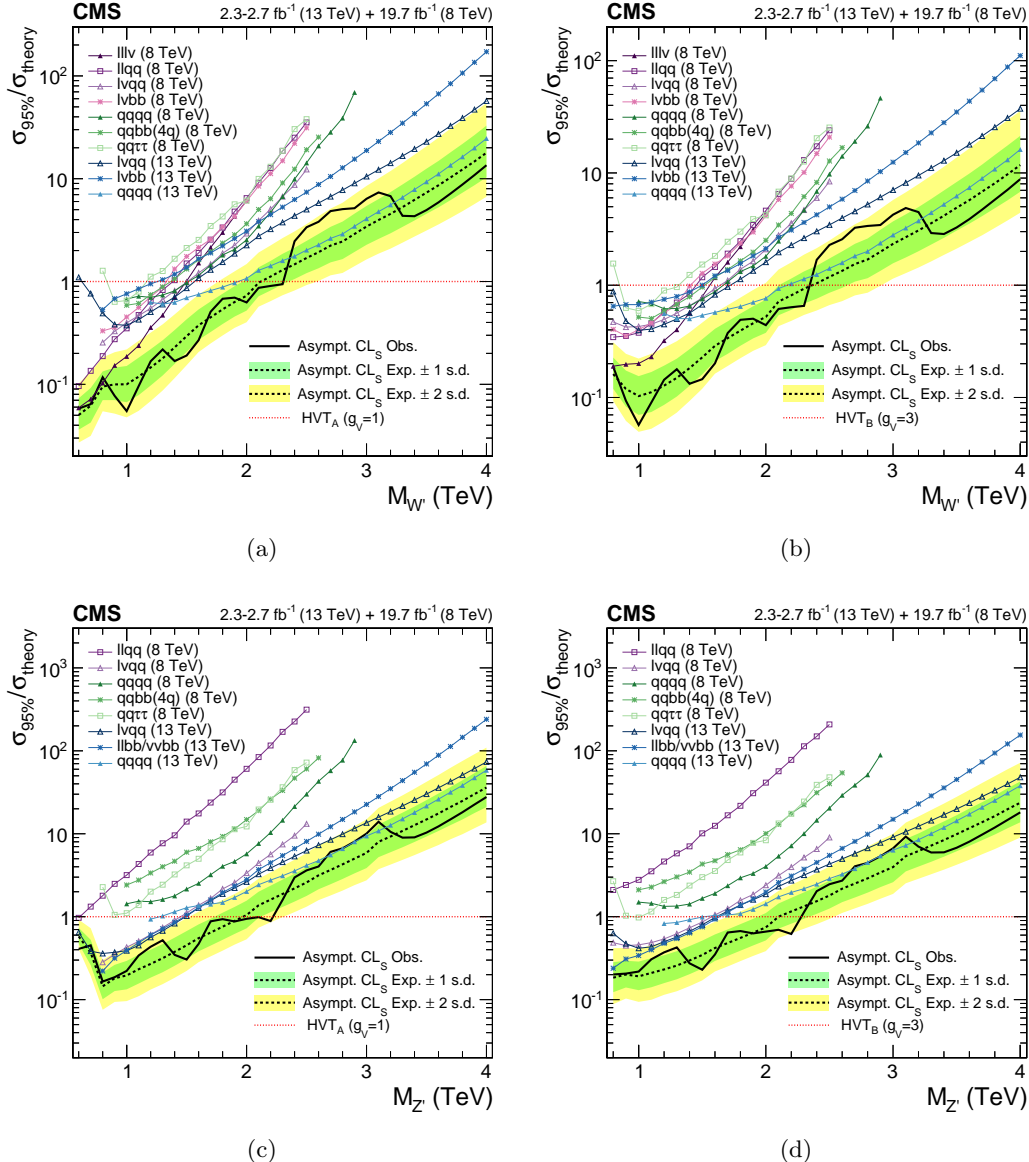


**Figure 11.1:** Exclusion limits at 95% CL on the signal strength for (top)  $W' \rightarrow WZ/WH$  and (bottom)  $Z' \rightarrow WW/ZH$  in (left) HVT model A and (right) HVT model B as a function of the resonance mass obtained by combining the 8 and 13 TeV diboson searches. In each of the plots the different colored lines correspond to the searches entering the combination.

Figures 11.1(c) and 11.1(d) show the comparison and combination of the results obtained in the 8 and 13 TeV searches for a  $Z'$  singlet resonance for model A and model B, respectively. The  $\ell\nu q\bar{q}$  channel at 8 TeV and the  $q\bar{q}q\bar{q}$ ,  $\ell\nu q\bar{q}$ ,  $\ell\ell b\bar{b}/\nu\nu b\bar{b}$  channels at 13 TeV dominate the sensitivity over the whole range, with 8 and 13 TeV analyses giving almost equal contributions for masses below 2 TeV. Above this value, the sensitivity is mainly driven by the 13 TeV analyses. Under this signal hypothesis the sensitivities reached by the 8 and 13 TeV channels are similar at low resonance masses. As for the  $W'$  case, the mass limit is not affected by the combination compared to what is obtained from the 13 TeV searches.

### 11.3.2 Limits on heavy vector triplet ( $W' + Z'$ )

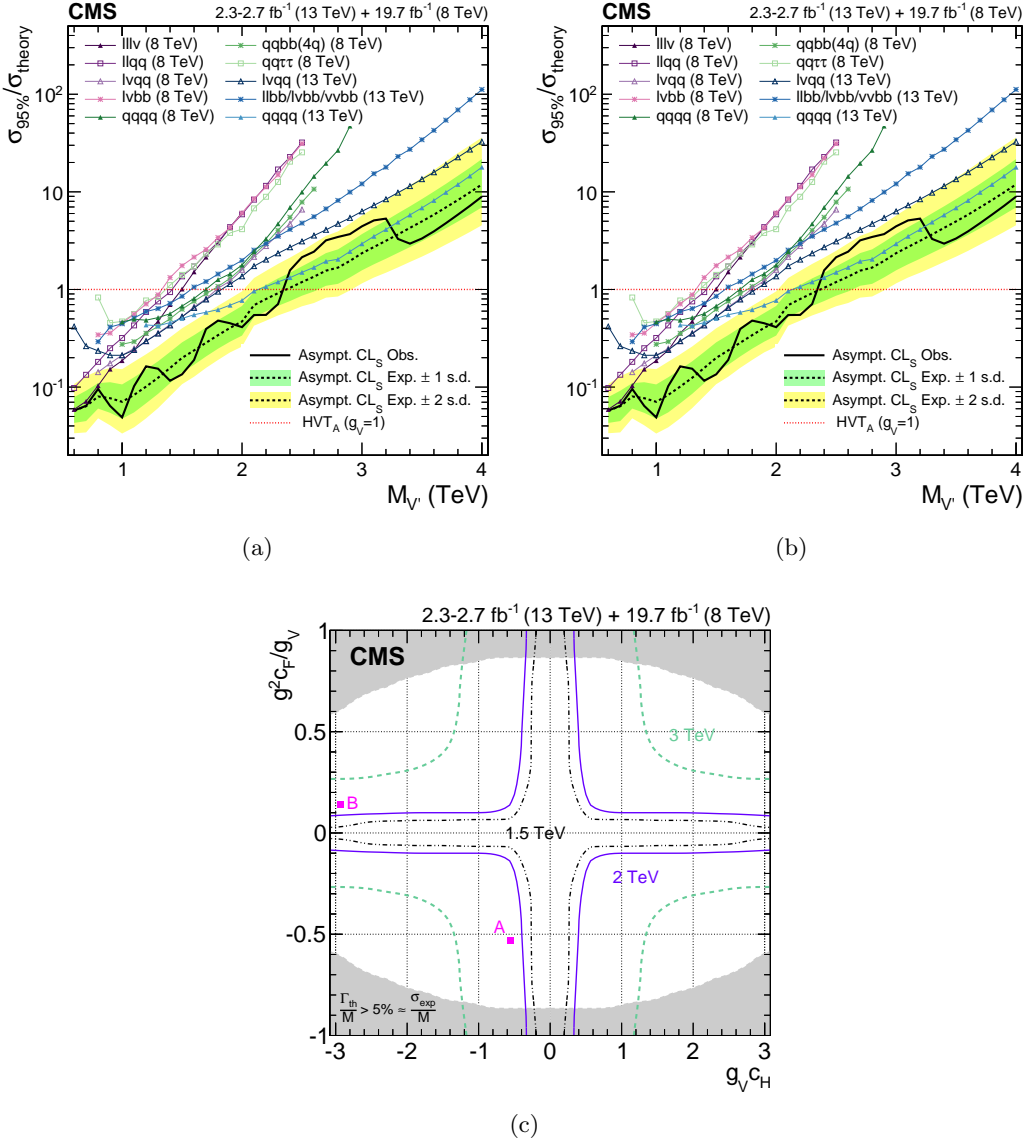


**Figure 11.2:** Exclusion limits at 95% CL on the signal strength in (a) HVT model A and (b) HVT model B as a function of the resonance mass obtained by combining the 8 and 13 TeV diboson searches. In both plots the different colored lines correspond to the searches entering the combination. (c) Exclusion regions in the plane of the HVT-model couplings ( $g_V c_H$ ,  $g^2 c_F/g_V$ ) for three resonance masses, 1.5, 2, and 3 TeV, where  $g$  denotes the weak gauge coupling. The points A and B of the benchmark models used in the analysis are also shown. The boundaries of the regions outside these lines that are excluded by this search are indicated by the solid and dashed lines. The areas indicated by the solid shading correspond to regions where the resonance width is predicted to be more than 7% of the resonance mass and the narrow-resonance assumption is not satisfied.

Figures 11.2(a) and 11.2(b) shows the comparison and combination of the results obtained in the 8 and 13 TeV searches for a heavy vector triplet scenario. As for the  $W'$  and  $Z'$  cases, the observed mass limit of 2.4 TeV obtained combining 8 and 13 TeV searches is determined by the 13 TeV channels.

In Fig. 11.2(c), a scan of the coupling parameters and the corresponding observed 95% CL

exclusion contours in the HVT model from the combination of the 8 and 13 TeV analyses are shown. The parameters are defined as  $g_{VH}$  and  $g^2 c_F/g_V$ , in terms of the coupling strengths (Section 2.3.3) of the new resonance to the Higgs boson and to fermions. The range of the scan is limited by the assumption that the new resonance is narrow. A contour is overlaid, representing the region where the theoretical width is larger than the experimental resolution of the searches, and hence where the narrow-resonance assumption is not satisfied. This contour is defined by a predicted resonance width of 5%, corresponding to the narrowest resonance mass resolution of the considered searches.

### 11.3.3 Limits on bulk graviton

Figure 11.3 shows the comparison and combination of the results obtained in the 8 and 13 TeV VV searches in the bulk graviton scenario with  $k/\bar{M}_{Pl} = 0.5$ . The sensitivity is mainly driven by the 13 TeV  $q\bar{q}q\bar{q}$  and  $\ell\nu q\bar{q}$  channels. Under this signal hypothesis, the sensitivity reached by the 13 TeV searches supersedes the 8 TeV combination down to very low resonance masses (0.7 TeV), since this signal is produced via gluon-fusion in contrast to the HVT resonances produced via  $q\bar{q}$  annihilation. Hence, the contribution given by 8 TeV channels is less significant with respect to the spin-1 resonance hypotheses. The combination yields the most stringent signal strength limits on narrow bulk graviton resonances ( $k/\bar{M}_{Pl} = 0.5$ ) to date in the mass range from 0.6 to 4 TeV.

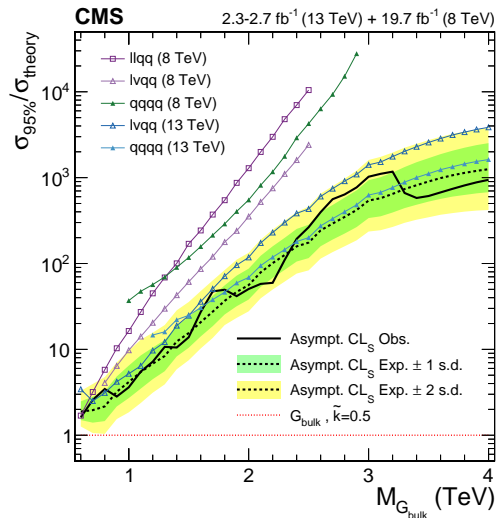


**Figure 11.3:** Exclusion limits at 95% CL on the signal strength as a function of the resonance mass obtained by combining the 8 and 13 TeV diboson searches in the bulk graviton scenario with  $k/\bar{M}_{Pl} = 0.5$ . The different colored lines correspond to the searches entering the combination.

### 11.3.4 Significance at 2 TeV

ATLAS reported an excess in the all-hadronic  $VV \rightarrow q\bar{q}q\bar{q}$  search corresponding to a local significance of  $3.4\sigma$  for a  $W'$  resonance with a mass of 2 TeV [165]. For CMS, the largest deviation of  $2.2\sigma$  has been observed in the semi-leptonic  $WH \rightarrow \ell\nu b\bar{b}$  search described in this work (Chapter 9). The combined significance of the 8 and 13 TeV CMS searches in the range 1.8–2.0 TeV is here evaluated and showed in Figure 11.4 for a  $W'$  hypothesis.

Combining all 8 TeV VH searches in the  $W'$  hypothesis, the local significance of the excess at 1.8 TeV is slightly reduced to  $2.1\sigma$ . Combining all 8 TeV VV and VH searches,

it is increased back to  $2.2\sigma$ , since the VV searches observed a small deviation in the same resonance mass range. However, in combination with the 13 TeV VV and VH searches, the overall significance at 1.8 TeV is reduced to  $0.8\sigma$ . This remains the largest significance for the overall combination of 8+13 TeV searches considering all signal hypothesis over the mass range 1.8–2.0 TeV, thus not supporting the excesses observed in the two individual channels in 8 TeV data.

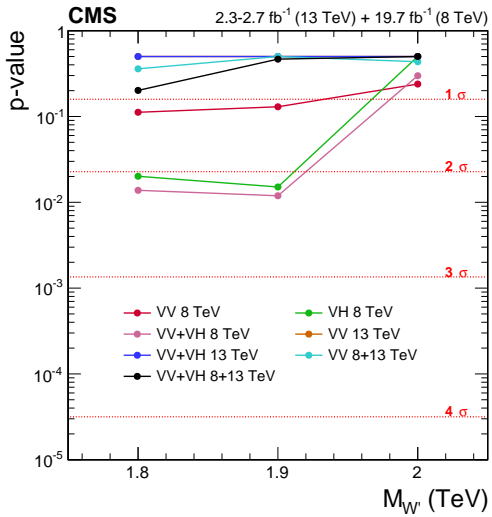


**Figure 11.4:** Local p-values of the excesses observed in the resonance mass range 1.8–2 TeV in the various combinations of searches for a  $W'$  hypothesis.

## CHAPTER 12

# Conclusions

---

A search for new massive resonances decaying into a pair of vector bosons (WW/WZ) or into a W boson and a Higgs boson (WH) in semi-leptonic final states has been presented. In particular two analyses have been described featuring a similar search strategy.

The first analysis is performed with pp collision data at  $\sqrt{s} = 8$  TeV collected in 2012, and is focused on the final state given by the W boson decay to  $\ell\nu$ , with  $\ell = \mu$  or e, and the Higgs boson decay to a pair of bottom quarks. The second analysis is performed with pp collision data at  $\sqrt{s} = 13$  TeV collected in 2015, and also in this case a final state is considered given by the  $W \rightarrow \ell\nu$  decay together with the decay of the second boson into quarks, where the second boson (V) can be either a W or a Z.

In both analyses, each event is reconstructed as a leptonic W boson candidate recoiling against a jet with mass compatible with the Higgs or V boson mass for the  $\ell\nu b\bar{b}$  or  $\ell\nu q\bar{q}$  analysis channel, respectively. Specialized methods, referred to as V tagging and H tagging, are exploited to help resolve jet decays of massive bosons and achieve large suppression of background from multijet processes. In particular, the H tagging algorithm combines jet substructure information with identification techniques based on the peculiarities of b jets.

In the  $\ell\nu b\bar{b}$  analysis channel, no excess of events above the standard model prediction is observed in the muon channel, while an excess with a local significance of 2.9 standard deviations is observed in the electron channel at  $m_{WH} \approx 1.8$  TeV. Taking into account the look-elsewhere effect, the results are statistically compatible with the standard model within 2 standard deviations. In the context of the little Higgs and the heavy vector triplet models, upper limits at 95% CL are set on the  $W'$  production cross section in a range from 100 to 10 fb for masses between 0.8 and 2.5 TeV, respectively. Within the little Higgs model, a lower limit on the  $W'$  mass of 1.4 TeV has been set. A heavy vector triplet model that mimics the properties of composite Higgs models has been excluded up to a  $W'$  mass of 1.5 TeV.

These results are superseded by the limits set by the analysis in the  $\ell\nu q\bar{q}$  final state. No evidence for a signal is found in this search with new 2015 data, and the result is interpreted as an upper limit on the production cross section of a narrow-width resonance as a function of its mass, in the context of several benchmark models for spin-1 and spin-2 resonances. In particular, for the same heavy vector triplet model as mentioned above the data exclude a  $W'$  resonance with masses  $< 1.9$  TeV.

However, the best results are provided by a statistical combination of all searches performed in CMS with 8 and 13 TeV data for massive resonances decaying to pairs of W, Z, and Higgs bosons in various final states. The results are interpreted in the context of heavy vector singlet and triplet models predicting a  $W'$  and a  $Z'$  decaying to WZ, WH, WW, and ZH and a model with a bulk graviton that decays into WW and ZZ. The combined significance of a potential resonance at 1.8–2.0 TeV has been evaluated and has been found to be 0.8 standard deviations for the hypothesis of a  $W'$ , thus the excesses observed in the  $\ell\nu b\bar{b}$  channel in 8 TeV data is not supported. The combination yields mass limits at the 95% CL on spin-1 resonance in the range 2.2–2.4 TeV, depending on the specific benchmark. The most stringent cross section limits on a narrow-width bulk graviton resonance with  $\tilde{k} = 0.5$  to date are set in the mass range from 0.6 to 4 TeV.

## **Part II**

# **Calibration and upgrade of the CMS pixel barrel detector**

# CHAPTER 13

# Introduction

---

The extremely high particle fluxes at small distances from the interaction point require the innermost tracking layers to be composed of pixel devices delivering spatial information with high resolution. Over the full acceptance of the CMS detector, the silicon pixel system provides two or more hits per track, which allow secondary vertices to be reconstructed for tagging long-lived objects, like b or c quarks and  $\tau$ -leptons, and to distinguish them from a large background of light quark and gluon jets. It is also an important detector for identifying the primary vertex, and separating it from dozens of additional pileup vertices. Hence, this detector plays a special role in the physics analyses described in this thesis. In fact, its performance has a large impact on the identification of b-quark jets as well as on jet substructure observables, being the latter highly dependent on pileup. The pixel detector consists of central barrel layers (BPix) and forward disks (FPix). This part of the thesis is dedicated to different aspects of the BPix system, including its calibration and upgrade.

The pixel detector was installed in 2008 and showed an excellent performance during the first period of data taking at the LHC (2010–2012). During the first long shut-down of the machine (2012–2015), that allowed to increase the center-of-mass energy of the collisions to 13 TeV, the detector was extracted for repair and re-installed into CMS, and successfully continued taking data throughout the first two years of LHC Run 2 (2015–2016). The excellent performance of the BPix at the re-start of collisions have been made possible by the efforts spent during LS1 in recovering the broken channels as well as in re-calibrating the detector after the radiation damage suffered during Run 1.

The current planning for the LHC and injector chain foresees other two long shut-downs, LS2 and LS3 (Fig. 13.1). In the period through LS2 (2019–2020), the injector chain will be improved, and during LS3 (2024–2026) the LHC itself will be upgraded with new components to optimize the bunch overlap at the interaction region. Further upgrades are foreseen beyond 2030.

The present pixel detector was originally designed for a luminosity of  $1 \times 10^{34} \text{ cm}^{-2} \text{ s}^{-1}$  and a pileup of 25 in LHC collisions with 25 ns bunch spacing. These parameters have already been exceeded in 2016, when collisions at 13 TeV happened at instantaneous luminosities up to  $1.5 \times 10^{34} \text{ cm}^{-2} \text{ s}^{-1}$  with an average pileup of 25 [51]. Based on the excellent LHC performances to date, it can be anticipated that the peak luminosity will keep increasing until 2018 reaching values up to  $1.7\text{--}1.8 \times 10^{34} \text{ cm}^{-2} \text{ s}^{-1}$ , and beyond these after LS2. Thus, starting from 2017 the CMS experiment must be prepared to operate with an average pileup of 50 as a baseline, with the possibility that it may be significantly higher (up to 100) if collisions will happen at 50 ns bunch spacing after LS2. In order to maintain efficient and robust tracking at CMS, the pixel detector will be replaced with an upgraded pixel system, referred to as *Phase 1 pixel upgrade*, in the LHC winter shutdown 2016/2017. The design of the upgraded detector allows to cope with the aforementioned harsh conditions expected at the LHC in the upcoming years. A more complex upgrade step is planned for the LS3 and referred to as *Phase 2 upgrade*. It will include deeper changes in the whole CMS, among which a complete substitution of the entire tracker detector system.

The Phase 1 pixel detector is expected to be operative up to the Phase 2 upgrade, around

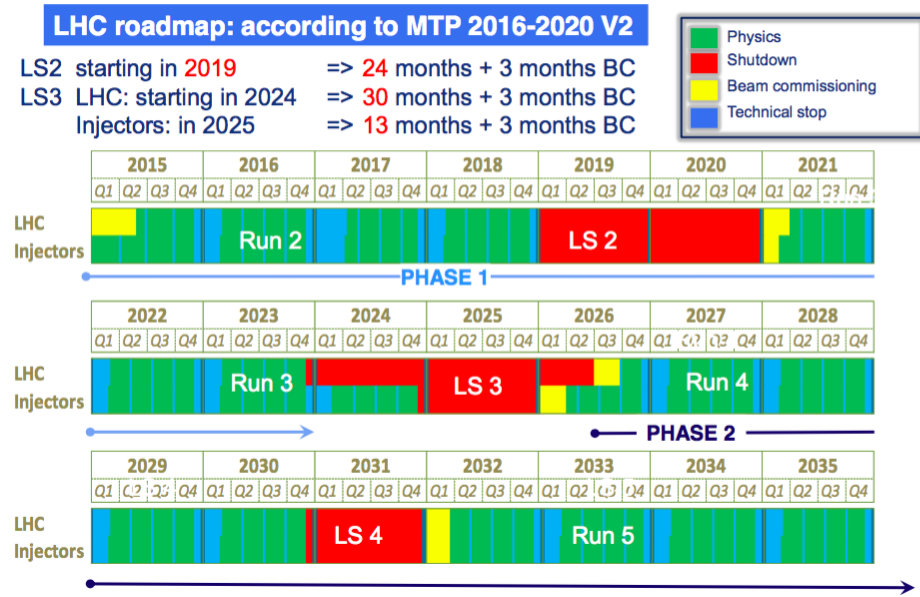


**Figure 13.1:** The outline LHC schedule up to 2035 as officially approved in June 2015 [166].

2023. During the planned 5 years of operation before LS3, the LHC is expected to deliver about  $500 \text{ fb}^{-1}$ . The proposed Phase 1 upgrade system has been designed and tested to be operative up to this target, with the only exception of the innermost layer. In fact, the estimated hadron fluence that will be accumulated in the innermost pixel layer is too high for the pixel sensor, thus a replacement of the innermost barrel layer is planned after  $250 \text{ fb}^{-1}$ .

The Phase 1 pixel upgrade project is now at its last stage of assembly and testing of the entire system. A test stand has been setup at the University of Zurich (UZH) in 2014 and was operated until the end of 2016. It has been fundamental to test the performance of the complete upgraded BPix system and gain experience in its operation. This activity is crucial in view of the success of the installation and commissioning of the new detector planned for the beginning of March 2017, as well as for excellent and stable performance during its first year of data-taking.

This part of the thesis is organized as follows. First, a description of the design and functionality of the present BPix detector is given in Chapter 14. The work carried out during LS1 aimed at optimizing the detector for LHC Run 2 is discussed in Chapter 15. The same chapter also includes details on the operations conducted during its re-installation into CMS and commissioning. Chapter 16 provides an overview of the design and features of the upgraded BPix system. In this chapter, a section is dedicated to the description of the test stand at UZH which I contributed to setup. The last section focuses on the development of new tests and procedures to be used during the upgraded detector assembly and commissioning.

# The CMS pixel barrel detector

---

This chapter provides an introduction to the design and functionality of the present CMS pixel barrel detector. It was developed, designed and built at the Paul Scherrer Institute (PSI) in cooperation with the Eidgenössische Technische Hochschule Zurich (ETH) and the University of Zurich (UZH). Section 14.1 gives an overview of the detector design and mechanical structure, followed by a description of the detector module and its main building blocks (Section 14.2). In Section 14.3, the detector readout and control system are described. The last section provides an introduction to the structure and functionality of the pixel online software (POS) used for controlling and calibrating the detector. The detector calibration and its performance at the re-start of collisions in 2015 are discussed in the next chapter.

## 14.1 Design

The CMS BPix detector [167] consists of three cylindrical layers at mean radii of 4.4, 7.3 and 10.2 cm from the center of the detector and with a length of 53 cm. A three dimensional representation of the detector can be seen in Fig. 14.1(a). The layers are composed of 768 modular detector units that consist of thin segmented silicon sensors, with a pixel size of  $100 \times 150 \mu\text{m}^2$  providing about 48 million readout channels. The pixels are almost square shaped in order to achieve a similar track resolution in both the  $r\phi$  and  $z$  direction.

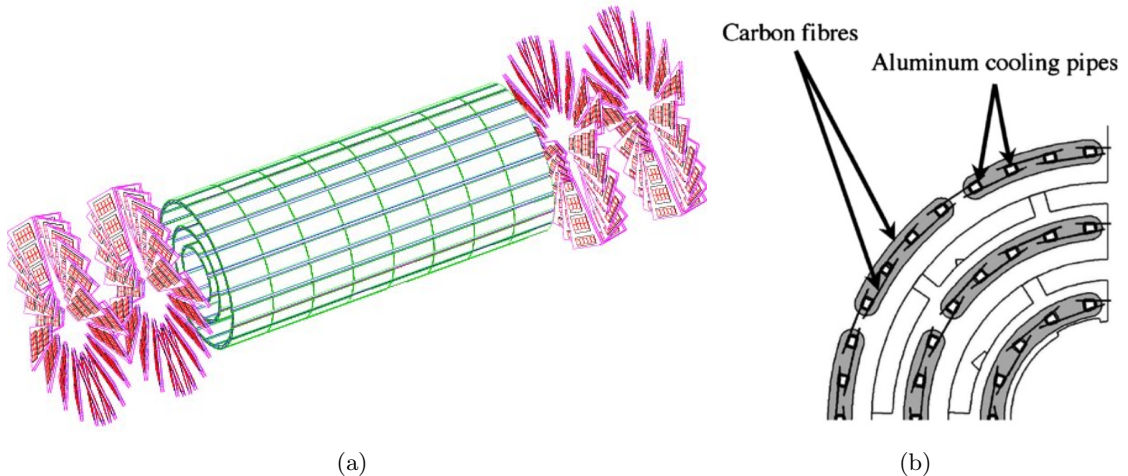


**Figure 14.1:** (a) Layout of the CMS pixel detector with three barrel layers (green) and two forward disks at each endcap (red). (b) Detailed view in  $r\phi$  of the geometric layout.

Sets of 8 modules are screwed on 0.25 mm thin carbon fibre ladders that are glued to aluminum cooling pipes with 0.3 mm wall thickness. The cylindrical shape of the barrel is achieved by assembling several ladders on each layer half shell. The three half shells are then mounted together at the end flange building up half of the BPix detector. The total number of ladders per half shell is 10 for layer 1, 16 for layer 2 and 22 for layer 3. To guarantee full

spatial coverage ladders are mounted with overlap on alternating sides of the cooling tubes. This is shown in Fig. 14.1(b). The resulting two detector parts are mechanically separated and the half shells are joined together with special ladders equipped with half modules. The overall layout results in 96 half modules and 672 full modules.

The BPix detector is connected to four 2.2 m-long half cylinders (supply tubes) that carry the services along the beam pipe, accommodate the cooling lines and house the electronics for detector readout and control. The supply tubes are a complex system in design as well as in production due to the thin radial shell thickness (1–2 cm), the large number of circuits, plugs and sensors, the fine wires and thin printed circuit boards that are assembled. The detector and the supply tubes are connected via a six layer printed circuit board (PCB) which is mounted on the detector end flange and distributes the power and the control signals to the individual modules. The final BPix system consists of two independent half cylinders placed at  $+x$  (inner) and  $-x$  (outer) coordinates, with each half shell connected to two supply tubes placed at  $+z$  and  $-z$  coordinates.

A liquid cooling system based on  $C_6F_{14}$  is used to cool down the sensors and the electronics. The cooling plant is located outside the CMS detector and the fluid is guided along the ladders inside the aluminum pipes (Fig. 14.1(b)).

## 14.2 Detector modules

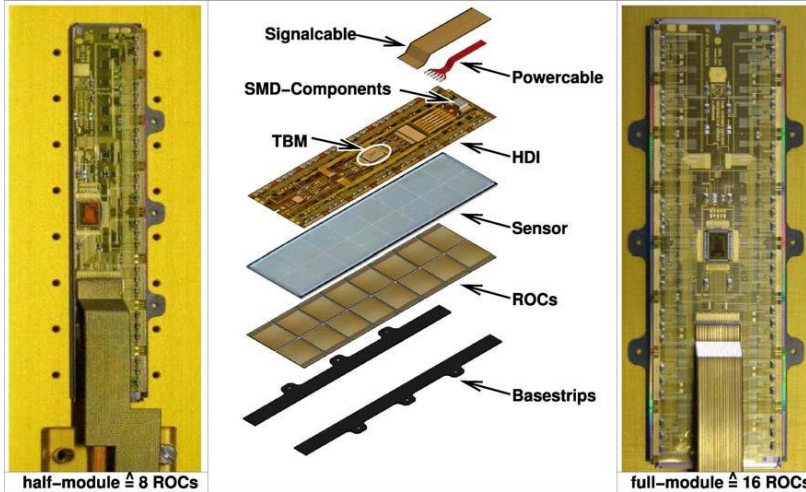
The BPix modules are made of a thin, segmented silicon sensor [168] with a dimension of  $66.6 \times 18.6 \text{ mm}^2$  that enables the detection of particles that pass through it by measuring the ionization charge that they produce. The charge measurement is performed by readout chips (ROCs) [169] that are connected to the sensor using the bump-bonding technique with Indium solder. Full modules consist of two rows of 8 ROCs, while half modules use a smaller sensor with  $1 \times 8$  ROCs. Each ROC has a size of  $7.9 \times 9.8 \text{ mm}^2$  and reads a matrix of 4160 pixel readout channels. Table 14.1 summarizes the configuration of full and half modules on the three different BPix detector layers. The ROCs are wire-bonded to a three-layer high-density interconnect (HDI) flex printed circuit glued onto the backside of the sensor. A token bit manager (TBM) chip [170], mounted on the top of the HDI, controls the readout of the ROCs, receives all external control signals, and distributes them to the ROCs. Base-strips made of  $250 \mu\text{m}$  thick silicon nitride ( $Si_3N_4$ ) are glued underneath the ROCs allowing the module to be mounted on the mechanical support structure. A power cable consisting of 6 copper coated aluminum wires is soldered to the HDI and brings analog, digital and high voltage to the module. The control and readout signals are sent through a two layer Kapton signal cable which is wire-bonded to the HDI. Additionally, the HDI distributes the signals and the voltages to the ROCs. The signal cables from the modules are plugged into the end flange that exists on both sides of the barrel and connects the three layers to the detector supply tubes. The modules are attached to cooling frames, with the cooling tubes being an integral part of the mechanical structure. The size of a full module is  $66.6 \times 26 \text{ mm}^2$  and the weight is up to 3.5 g depending on the length of the signal and power cables. The average power consumption of a full module is 2 W. A view of each component of the BPix module is shown in Fig. 14.2.

### 14.2.1 Sensor

The sensor is made from a *n*-type silicon wafer with a thickness of  $285 \mu\text{m}$ . Charged particles that travel through the sensor material leave electron-hole pairs as the result of multiple interactions with the atoms in the material. For charged particles at intermediate energies

**Table 14.1:** Number of modules, readout chips and pixel channels for the three detector layers.

radius (cm)	full modules #	half modules #	ROCs #	pixels ( $10^6$ )
4.4	128	32	2304	9.6
7.3	224	32	3840	16.0
10.2	320	32	5376	22.4
Total	672	96	11520	48

**Figure 14.2:** Picture of a BPix half module (left) and full module (right). In the center, the components of the module are shown. From top to bottom: the Kapton signal cable, the power cable, the HDI with the TBM, the silicon sensor, the 16 ROCs and the base strips [171].

( $0.1 \leq \beta\gamma \leq 1000$ ), the average energy loss  $dE$  in a thickness  $dx$  of material is described by the *Bethe-Bloch formula*

$$-\left\langle \frac{dE}{dx} \right\rangle = 4\pi N_A r_e^2 m_e c^2 z^2 \frac{Z}{A} \frac{1}{\beta^2} \left[ \frac{1}{2} \ln \frac{2m_e c^2 \beta^2 \gamma^2 W_{\max}}{I^2} - \beta^2 - \frac{\delta(\beta\gamma)}{2} \right]. \quad (14.1)$$

In the above equation,  $N_A$  is the Avogadro's number,  $r_e$  the classical electron radius,  $m_e$  the electron mass,  $z$  the charge of the particle,  $Z$  ( $A$ ) the atomic number (mass) of the material ( $Z = 14$  and  $A = 28.1$  u for silicon),  $W_{\max}$  the maximum energy transfer to an electron in a single collision,  $I$  the mean excitation energy, and  $\delta$  a density effect correction. At a particle velocity  $\beta \approx 0.96$  ( $\beta\gamma \approx 3$ ) a broad minimum is reached. At higher energies the logarithmic term leads to a slow rise again, which is eventually canceled by the density correction. A particle with an energy loss in the minimum is called a minimum ionizing particle (MIP).

The energy loss in a finite medium is subject to statistical fluctuations well described by a *Landau distribution* (Fig. 14.3). If a particle is not stopped in the medium, the energy loss (and therefore the number of charge carriers) varies around the peak of the distribution (most probable value or MPV). In rare but measurable cases ( $\delta$ -rays or  $\delta$ -electrons), the transferred energy is large, so that these cases are responsible for the asymmetric long tail towards high charge deposits. Due to this tail the most probable value of energy transfer is about 30% lower than the average value. For a MIP crossing the sensor at an angle of  $90^\circ$  the most

probable number of electron-hole pairs generated in  $1\text{ }\mu\text{m}$  of silicon is 76. Therefore, a MIP generates a signal of about 22,500 electron-hole pairs (MPV).

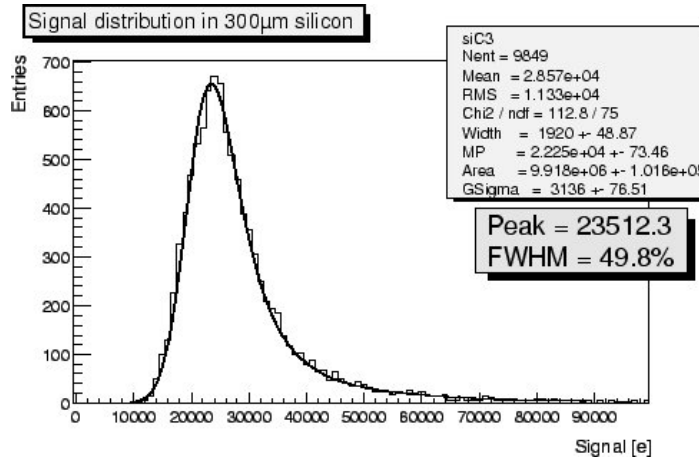


**Figure 14.3:** Measured MIP signal distribution in a Silicon detector of  $300\text{ }\mu\text{m}$  thickness.

The silicon sensor used for the CMS pixel detector adopts a double sided  $n^+$ -in- $n$  design: pixels consist of high dose  $n^+$  implants on a high resistance  $n$  substrate. The backside of the substrate is p-doped, therefore the p-n junction is placed on this side of the sensor. A cross-section of the sensor is shown in Fig. 14.4. If the junction is reverse biased, a depletion zone forms that extends towards the pixel implants. In this zone, an electric field is established that allows ionization charge to drift. Electrons drift toward  $n^+$  implants while holes drift toward the back of the sensor. In Fig. 14.4, the bulk of the silicon is p-type because of the type inversion occurring in the bulk after prolonged exposure to high fluences of radiation. In fact, the effective concentration of impurities gradually decreases with exposure, until a transition to the other type material behavior occurs. At this stage, the depletion zone grows from the pixel implants toward the back of the sensor, enabling the collection of electrons even when the sensor is only partially depleted. Extremely high operating voltages can therefore be avoided, reducing the problems of leakage currents and high-voltage breakdowns. Furthermore, the double-sided processing of  $n^+$ -in- $n$  detectors allows a guard ring concept which keeps all sensor edges at ground potential and avoids the risk of disruptive discharges to the very closely spaced ROCs.

Additional processing is needed on the readout side to electrically isolate the  $n^+$  implants from each other. The electron accumulation layer induced by ionizing radiation otherwise tends to short-circuit the pixel implants. A moderated p-spray technique is used, which consists of a medium dose p-type Boron implants.

The position resolution of single-pixel hits is given by the pixel pitch divided by the  $\sqrt{12}$ . However, the spatial resolution can be improved exploiting charge sharing among adjacent pixels. A group of pixels collecting a signal from the same particle is usually called “cluster”. Significant charge sharing is a consequence of the Lorentz drift in the strong magnetic field of  $3.8\text{ T}$  inside CMS. In fact, charge carriers released by the ionizing particle in the silicon sensor do not follow the electric field lines to the collection electrodes, but are deflected by the Lorentz force (Fig. 14.4). Furthermore, the readout of the pulse height allows for an interpolation of the amounts of collected charge for each of the pixels in the cluster. This effect influenced the choice of the barrel pixel size which have been optimized to achieve

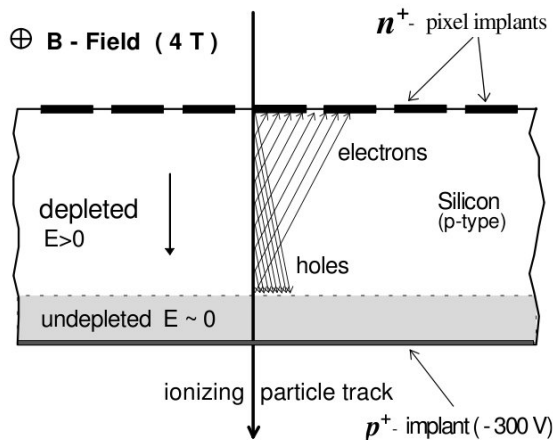


**Figure 14.4:** Illustration of a charged particle crossing a sensor of the CMS pixel detector. The charge carriers produced by the passage of the ionizing particle are collected at the high dose  $n^+$  implants.

optimal spatial resolution. Two-pixel clusters and the interpolation allow a much better resolution, limited only by fluctuations of the charge deposition. Since division of the signal charge among more than two pixels increases the data rate and reduces the signal charge per pixel without an improvement of the resolution, an ideal choice of the pixel size in the direction perpendicular to the magnetic field ( $r\phi$ ) is therefore given by the length over which charges are spread when they reach the surface of the sensor. For a  $\sim 300 \mu\text{m}$  sensor thickness and a Lorentz angle of  $28^\circ$  this amounts to  $\sim 150 \mu\text{m}$ . A slightly smaller size of  $100 \mu\text{m}$  was chosen to maintain charge sharing, and hence resolution, after irradiation. The area of a pixel must also be large enough to accommodate the readout electronics. With one dimension fixed by the Lorentz drift, this leads to a more or less quadratic shape of  $100 \mu\text{m}(r\phi) \times 150 \mu\text{m}(z)$ , resulting in comparable resolution in both directions. The typical pixel resolutions are  $9 \mu\text{m}$  in  $r\phi$  and  $24 \mu\text{m}$  in  $z$  (Section 15.5).

### 14.2.2 Readout chip

The readout chip is responsible for measuring the charge deposited by a particle in the sensor's pixel. It amplifies and samples the signal with a time resolution of 25 ns, which is the time between two LHC bunch crossings. The pixel hit information has to be stored on-chip during the CMS Level-1 trigger latency of  $3.2 \mu\text{s}$  after which they are either read out or discarded. Each pixel sensor is connected via a bump bond to its own readout circuit on the ROC, referred to as *Pixel Unit Cell* (PUC). The PUCs are arranged in  $26 \times 80$  double columns. Each double column represents an independent readout unit controlled by a circuit sitting in the column periphery. The ROC periphery controls the PUC, buffers data and houses global functions common to all pixels.

To control and optimize the readout, 26 digital-to-analog converters (DAC) can be programmed using a serial protocol similar to I<sup>2</sup>C modified to operate at 40 MHz.

The PUC can receive a signal either through a charge deposition in the sensor or by injecting a calibration signal. Within the PUC, the signal is first passed through a two stage pre-amplifier/shaper system to a comparator where zero-suppression is performed. It compares the shaper output to a threshold value which is programmed by a DAC distributed globally to all pixels. Since variations of the threshold of the individual pixels caused by

transistor mismatch, voltage drops or preamplifier gain variations can lead to an increased noise rate, each pixel has a 4-bit DAC to trim the threshold. Furthermore, a mask bit allows to disable noisy pixels. When the rising edge of the signal has passed the threshold, the signal height is sampled after some delay and stored in the sample-and-hold capacitance until the readout mechanism is started from the periphery. During this time the pixel becomes insensitive.

Since the L1 trigger latency time in CMS is  $3.2\ \mu\text{s}$  (128 bunch crossings), the information of a hit pixel, including the associated bunch crossing number and the analog pulse height signal, can not be kept on the pixel itself during this time without introducing a significant inefficiency. In the *Column Drain Architecture* chosen for the CMS pixel readout, all pixel hits occurring in a pixel double column are immediately and quickly copied into the column periphery in order to free the pixels for the next hit. In this case the probability of having a second hit in the pixel during the latency is significantly reduced. Each double column informs the column periphery immediately of any hits that have been occurred by sending to the periphery a current with adjustable intensity. The column periphery writes the value of the bunch crossing counter into a time stamp buffer and initiates a token scan of the double column passing a readout token from cell to cell. Once the hit pixel is found, in the readout block of the PUC the token signal initiates the transfer of pixel address and analog pulse-height information, which are stored in a data buffer located in the periphery waiting for the L1 trigger. The hit pixels remain inactive until their hit information has been transferred. The double column periphery verifies the trigger by comparing the time stamp with a counter running behind the bunch crossing counter by the trigger delay. In case of agreement the column is set into readout mode and the data acquisition is stopped, otherwise the data are discarded. When the readout token arrives at the double column periphery the validated data are sent to the chip periphery and the double column is reset. The ROCs are read out serially via a 40 MHz analog link.

A picture of the BPix readout chip is shown in Fig. 14.5.

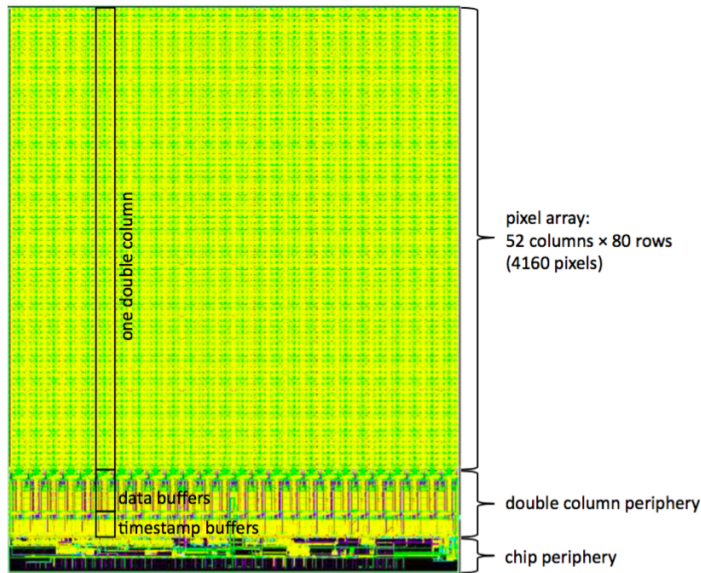


**Figure 14.5:** Picture of the CMS pixel readout chip showing the three main building blocks: double column, double column periphery and chip periphery [47].

### 14.2.3 Token bit manager

A token bit manager chip is wire-bonded to the HDI and controls the readout of the ROCs. It serves as an interface for data acquisition and programming and is responsible to synchronize the readout of the ROCs on the module. For each incoming L1 trigger, the TBM sends a token in a fixed order from chip to chip, and waits until the token returns from the last chip in the chain. The chip that has the token transmits all hits for a given trigger and then passes the token to the next chip. Upon the arrival of the token, each ROC sends a three clock cycle header. While the header is transmitted, the token is passed through the chip looking for a double column with validated hits belonging to that token. The length of the header is sufficient for the token to skip all 26 double columns if no triggered hits were present and to be passed on to the next chip with the right timing. Triggers and readout tokens are both counted and hits are only readout when the token number matches the readout number. It must be ensured that exactly one token for every trigger is issued and that there is never more than one. The ROCs in the module are either serviced by a single token that sequentially passes through all the 16 chips, or a second channel in a dual TBM chip is used such that the ROCs are divided into two groups of eight. This method is employed for the two innermost layers of the detector which experiences higher hit rates per module than the others. It requires two separate buses for the readout of the two groups of ROCs, and the data streams are also individually transmitted through two separate readout links for the data acquisition. The TBM multiplexes the signal from the ROCs, adds a header and a trailer to the data stream and drives the signal through the readout link. In addition, the TBM distributes the L1 trigger and the clock to the ROCs. The header contains an event number and the trailer a status information, such as the stack overflow warning.

The TBM keeps track of triggers arriving while the token is still under way with a trigger stack of 32 entries that is filled each time a trigger arrives and reduced every time a token returns. In case of a stack overflow, the TBM withholds the incoming triggers from the ROCs until the stack is reduced. It notifies the data acquisition that events have become lost in this case. The TBM chip also includes a communication component called the HUB which serves as a port for programming commands sent from the DAQ.

## 14.3 Detector readout and control

A schematic drawing of the pixel readout and control systems is shown in Fig. 14.6. The path on the right shows the readout part of the system. Signals from a group of ROCs are amplified and converted into a 40 MHz analog optical signal in the analog opto-hybrid circuits mounted on the supply tube. Optical fibers allow the data to be transferred over approximately 60 m distance to the underground counting room, where a VME front-end driver unit (FED) [172] digitizes the signal, builds event fragments and sends them to the DAQ. The signal path in the middle shows the fast detector control link. In the counting room, the control signals are driven by front-end control (FEC) units [173] which are used to program the detector modules. The signals enter the supply tubes through optical fibers to be converted in digital opto-hybrid circuits. Several other electronic devices are needed by the system and are placed on the supply tubes. Some of these components need to be programmed. This happens through a dedicated slow control link corresponding to the signal path on the left. Also shown in Fig. 14.6 is the Timing Trigger and Control (TTC) [174] system which distributes the clock and trigger signals to all detector components. The individual electronic devices of the detector readout and control system are described in more detail in the following.

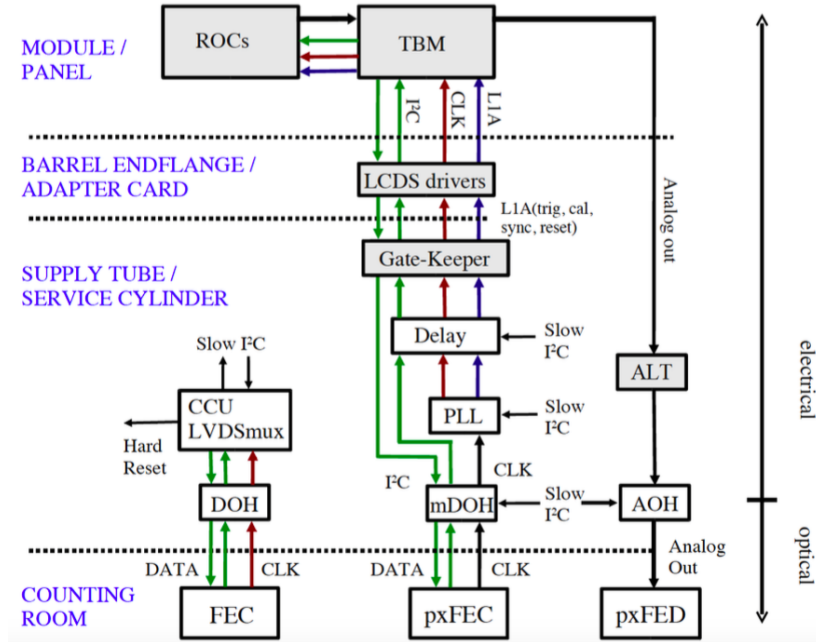


Figure 14.6: Overview of the BPix readout and control system [175].

### 14.3.1 Readout of the analog signal

An example of an analog readout signal from a module with a single pixel hit is shown in Fig. 14.7. The TBM header uses eight clock cycles and starts with three ultra black levels (UBL). An UBL is simply a large negative signal level well outside of the range of pixel data. The three UBLs are followed by a black level (BL), which defines the zero level of the differential analog signal. The four remaining clock cycles encode an 8-bit event number. The minimal readout of each ROC starts with an UBL, a BL and a level called last DAC which represents the value of the most recently programmed DAC. A pixel hit adds a block of six clock cycles to the ROC minimal readout: two for the double-column address, three for the row address, and one for the pulse height. In order to speed up the transmission of digital pixel hit information while maintaining the global 40 MHz clock, the pixel addresses are not sent in a common binary fashion, but the available signal amplitude is divided into six possible analog levels (2.5 bits/clock). The readout is terminated by the TBM trailer, containing two UBLs, two BLs, and four clock cycles with the TBM status information.

The data stream which contains all hit information belonging to a single trigger is sent out by the TBM through the module Kapton cable. The Kapton cable consists of differential analog lines separated by quiet lines from the lines for the fast digital signals. The analog signals are split from the digital signals on the end flange boards that drive the signals to the PCB on which the analog optical hybrids (AOHs) [176] are plugged. The electric analog signals are amplified in an Analog Level Translator (ALT) chip and converted into 40 MHz analog optical signals in the AOHs. Each AOH is equipped with 6 lasers with adjustable gain and threshold, which drive the signal through optical fibers to the front-end drivers.

A total of 32 FED modules, located in the underground counting room, receive the data packets. They convert the signals from optical to electrical, perform the digitization at the LHC frequency, and decode the pixel hit information. The pixel FED also builds event fragments and sends them to the CMS central DAQ system. It is a 9 U VME module designed at HEPHY Vienna that includes optical receivers, ADCs and several FPGAs for

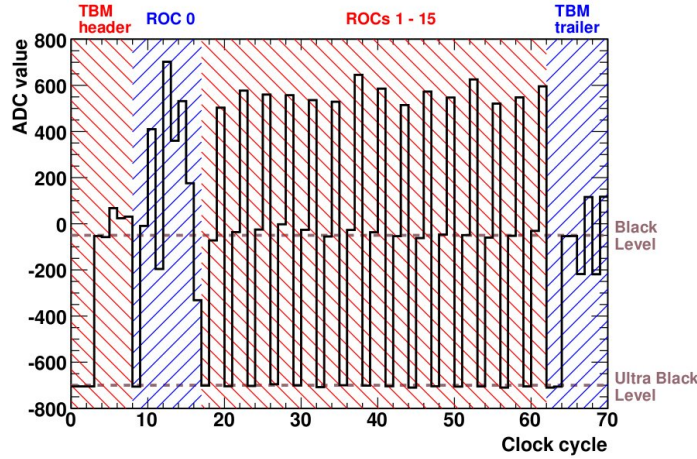


**Figure 14.7:** Analogue readout of a pixel module with one hit in ROC 0.

signal processing.

A FED has three opto-receiver devices each of which has twelve input channels where the fibers terminate. Each input channel is equipped with a 10-bit ADC. The ADC has a clock with adjustable phase w.r.t. the global clock in steps of 1.6 ns to select the optimum digitization sampling point for each input. A programmable offset voltage can be set for each optical input in order to compensate for bias shifts in the analog signal. An additional, single optical input receives TTC signals such as clock, trigger and reset. Each channel has a 1k words 32-bit data buffer (FIFO1) which stores the digitized module signal (Fig. 14.7). The data package from four or five (depending on the location) FIFO1 channels are collected in a FIFO2 with a size of 8k words and a width of 64 bits plus 4 control bits. During the data transfer to FIFO2 the input event number is compared with that of the CMS TTC system. The data of all FIFO2 memories are collected by two final memories (FIFO3) of 8k words each over two buses of 64+4 bits at 40 MHz. Four front FPGAs, each handling 9 inputs, house FIFO1 and FIFO2 buffers, while a center FPGA houses the FIFO3 where the whole event fragment is built, together with the S-link connection to the central DAQ. The FED can also be operated in a transparent mode making unprocessed ADC output data available for calibration and testing purpose.

### 14.3.2 Detector control and programming

The detector control and programming is performed through front-end control modules (pixel FECs or pxFECs) located in the underground counting room. The function of the pixel control system is to send the 40 MHz clock, the trigger and control signals (e.g. resets) to the front-end electronics, and to program all front-end devices (TBMs and ROCs). All the signals are sent through optical fibers and converted to electrical signals by digital optical hybrids (DOHs) [176] mounted on the supply tube before forwarding them to the pixel modules. A DOH is connected to four optical fibers, two for receiving and two for sending signals. The LHC 40 MHz clock and trigger information is encoded in one signal which is sent over a single fiber to the DOH. A modified version of the common I<sup>2</sup>C protocol has been developed to cope with the required volume of the data that have to be downloaded to configure the detector modules. The main modifications include the increase of the clock speed to 40 MHz and dropping the requirement of an acknowledge signal. Each DOH contains two laser drivers and two PIN diodes. The DOH is mounted on the digital opto-board together with other

electronic devices needed by the system. In particular, a phase-locked loop (PLL) chip [177] is used to split the clock from the trigger, and the Delay25 chips [178] adjust the relative phases of all control signals. The Gate-Keeper chip converts the LVDS signals used by PLLs and Delay25s to low current differential signals (LCDS) used by the pixel front-end chips. Finally, the LCDS-driver chips mounted on the end flange PCB are used to drive the signals on the Kapton cables to each detector module. In addition, these chips are used to compensate the signal phases for the different Kapton cable lengths.

The electronics on the supply tubes (DOHs, PLLs, Delay25s, AOHs, and so on) have to be controlled and programmed. This is achieved through a system of four CCU (Communication and Control Unit) boards equipped with 9 CCU chips each [179]. This is indicated in Fig. 14.6 as “slow I<sup>2</sup>C”, since the standard I<sup>2</sup>C protocol is implemented for this task. The boards are mounted on the supply tubes and each of them supervises one quarter of the detector.

The slow control links are implemented as a ring architecture. A ring consists of 9 CCUs, two optical drivers and receivers that bring clock, trigger and control data to the CCUs, and a front-end controller (tracker FEC or tkFEC) which provides the communication with the CCUs and the programming signals. Each CCU distributes the digital control and programming signals to a set of individual boards forming one readout sector of the detector. A CCU chip supports two I<sup>2</sup>C channels to communicate with the front-end electronics, and three PIA channels to generate the necessary signals to reset the circuits and the ROCs of one sector. Eight CCUs are used for the control of the eight sectors in which each supply tube is divided, the ninth CCU is a dummy chip used for redundancy. Since a large number of front-end channels depend on the same control link, a very high reliability of the system is of utmost importance. A CCU failure leads to a loss of communication to all electronics attached to it. A redundancy scheme based on doubling signal paths and bypassing of interconnection lines, between the CCUs and between the CCUs and the FEC, is supported. The dummy CCU allows to mitigate a single DOH failure. The CCU is equipped with two DOHs which form separated control rings and thus ensure a high operational reliability. The DOHs on the CCU board are programmed by the first two CCU chips.

### 14.3.3 Supply tubes

As mentioned previously in this chapter, the readout and control circuits of the pixel detector are integrated on four supply tube half cylinders. In addition, the supply tubes bring the power and cooling lines to the detector. A schematic view of a supply tube is shown in Fig. 14.8. A supply tube is divided into 8 sectors which contain the power lines and electronics of two readout groups, one serving the modules of the first two layers, the other serving the modules of the third layer. One sector includes an analog opto-board with six AOHs, a digital opto-board with two DOHs, two PLL chips, two Delay25 chips and two Gate-Keeper chips. A total of 192 AOHs and 72 DOHs are used for the pixel barrel detector. For each sector, 44 optical fibers drive the communication with the front-end modules, 36 for the analog readout and 8 for the digital control. The CCU board is placed in the central sector of the supply tube.

The stability of the analog signal is strongly affected by the temperature dependence of the AOHs. A shift of 50 ADC counts is observed in the level of the analog signal for a temperature variation of the AOH of 1° C. The FED is able to internally correct for a drift within a temperature range of ±2° C. Consequently, the temperature of the AOHs has to be controlled within a very narrow range in order to assure a stable operation of the detector. The barrel pixel supply tubes are equipped with a total of 124 temperature sensors and 8 humidity sensors. The temperature sensors are placed on the CCU boards, the analog

opto-board and on the supply tube cooling lines.

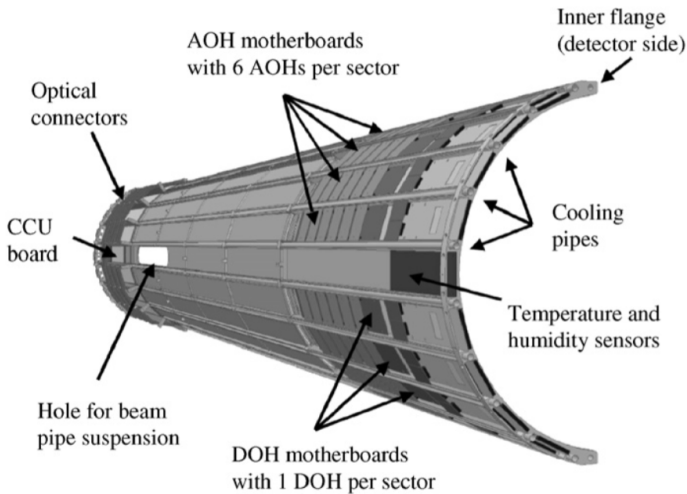


**Figure 14.8:** Layout of a BPix supply tube [167].

## 14.4 Pixel online software

The pixel online software [180] is the framework used for controlling and calibrating the CMS pixel detector and that runs on the PCs of the CMS control room at LHC-P5. Its main functionalities are to configure the detector, perform calibrations, analyze calibration data and monitor the detector during data taking. The pixel online software is based on the XDAQ toolkit [181] and is written in C++. It has a very complex structure built from a large number of different applications and packages. The dependencies among the main applications and packages is presented in Fig. 14.9. The top level application is represented by the **PixelSupervisor** which is responsible for the overall coordination of the pixel DAQ. Its main function is to coordinate the activities of the other supervisors, particularly during configuration and calibration. It is also responsible for updating the configuration database with new settings obtained by calibrations. Among the other supervisors there is the **PixelFECSupervisor** that controls the pxFECs and is responsible for loading the configuration parameters for the ROCs and TBMs from the configuration database and programming those parameters into the detector. Similarly, the **PixelTKFECSupervisor** controls the tkFECs and the initialization of all the electronics placed on the supply tubes. The **PixelFEDSupervisor** controls the FEDs. An additional supervisor is included in the software to control the pixel TTC module used for trigger and timing. Among other things the TTC module is used during calibrations to generate triggers. The various supervisors run as independent processes, or even on different computers. Therefore, in order to communicate with each other they must exchange messages on the network. This is done using the XML-based SOAP (Simple Object Access Protocol) protocol. A set of classes such as **PixelFEDIInterface**, **PixelFECInterface**, and **FECSoftware**, provides the direct communication between the supervisors and the VME hardware via Hardware Access Library (HAL) [182].

A function manager acts as an interface between the global run control (Run Control and Monitoring System or RCMS) and POS. It is a JAVA application that basically passes the state machine of CMS (Halted, Running, Configured, and so on) to the **PixelSupervisor**.

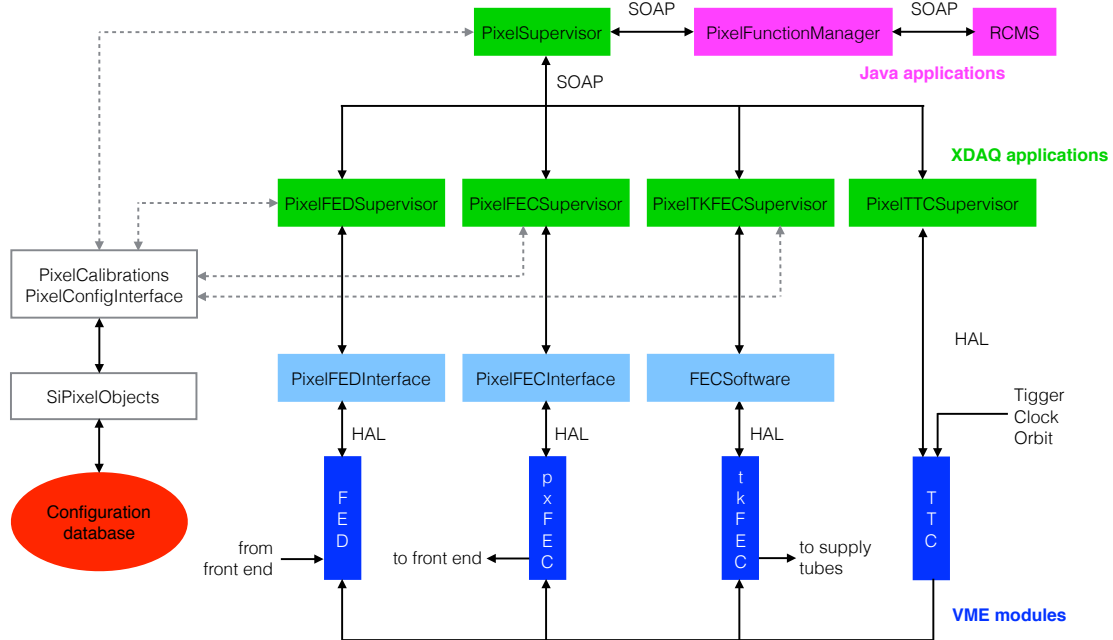


**Figure 14.9:** Illustration of the dependencies among the main applications and packages implemented in the pixel online software.

which then forwards state requests to the underlying supervisors to carry out the different tasks needed in state transitions of the run control.

Another key element of the software is represented by the **PixelConfigInterface** package which provides access methods for retrieving and storing configuration data. Several different classes are available in the **SiPixelObjects** package, each responsible for storing a specific set of detector settings as well as the configuration needed by the calibration code (e.g., which detector parameter to scan and its range). For instance, the **PixelNameTranslation** class translates from the naming scheme used to label each individual ROC to the hardware addresses used by both the FEC and the FED to identify a specific ROC. Similarly, the **PixelDACSettings** and **PixelTBMSettings** classes store, respectively, the DAC settings for all ROCs on one module and the settings for one TBM. The **PixelSupervisor** features a web GUI that can be accessed as an html page. It displays information about the current configuration, or if it is not configured it allows the user to select a possible configuration from a list and configure the detector using that choice. The GUI is also used to run and monitor the detector calibrations. The calibration routines are implemented in independent and separate classes contained in the **PixelCalibrations** package. The description of the detector calibration procedures is presented in the following chapter.

# Optimization and commissioning for LHC Run 2

---

The CMS pixel detector was designed to cope with the high radiation environment of LHC and to operate with the highest performance even after the accumulation of significant radiation doses. Nevertheless, radiation damage affects hit efficiency and resolution and hence, it is necessary to monitor its effects during operation. As described in this chapter, throughout Run 1, re-calibrations of the detector have been performed to compensate for these effects and recover full performance.

During LS1, both BPix and FPix were extracted from CMS for maintenance with the purpose to recover broken channels. In this period, the calibration procedure has been exercised and improved in view of commissioning and operation for Run 2.

The pixel detector has been operated with a coolant temperature of 7.4 °C in 2008–2011 and 0 °C in 2012, which for the pixel sensors translates to values of about 10 °C higher. In order to limit the impact of radiation damage, during Run 2 the detector has been operated at much lower temperature, down to -10 °C. This has been made possible thanks to a major effort during the long shut-down to implement a tracker wide sealing that ensures minimal humidity levels. The flow of dry gas into the tracker volume was increased and a new safety system was developed that shuts down the detector safely in case a sudden increase of temperature, electric current or humidity is detected. During LS1, the pixel detector functionalities at very low temperature have been checked and its (temperature dependent) settings re-calibrated to allow for optimal operations under such conditions. This activity, described in the following, have been crucial to achieve a quick and reliable re-installation and commissioning for Run 2, as well as for stable and excellent operations during 2015 and 2016.

## 15.1 Effects of radiation damage in LHC Run 1

One of the first visible effect of radiation is the increase of the sensor leakage current with integrated luminosity, due to damages in the silicon bulk. The most fundamental type of bulk radiation damage is a defect, produced by the displacement of an atom of the semiconductor material from its normal lattice site. The vacancy left behind, together with the original atom now at an interstitial position, constitutes a trapping site for normal charge carriers. The formation of mid-gap states facilitates the transition of electrons from the valence to the conduction band leading to an increase of the leakage current in the depletion region. The primary defects caused by irradiation are not stable but able to move through the crystal. As result of this diffusion process, there is the possibility of combination of more complex defects. This process is called *annealing*, with a beneficial part reducing the damage and a reverse one degrading macroscopic sensor properties, called *reverse annealing*. During beneficial annealing, with a time constant of a few days at room temperature, the leakage current decreases, while later it rises due to reverse annealing process until it finally saturates at a value which is significantly above the initial level. At temperatures below 0 °C however, both

effects can be frozen and the detector current remains constant. Thus, irradiated detectors should be operated and stored at low temperature, while it is favorable to shortly expose them to room temperature to take advantage of the beneficial annealing.

Figure 15.1 shows the increase of the leakage current for the pixel barrel layers measured from readings of the high voltage power supplies as a function of the integrated luminosity and of time in 2011-2012. The damage was only partially recovered by beneficial annealing that took place during a longer shut-down after about  $6 \text{ fb}^{-1}$  and a shorter technical stop after about  $13 \text{ fb}^{-1}$  delivered integrated luminosity. Between the end of 2011 and the beginning of 2012 the operating temperature was decreased from  $7.4^\circ\text{C}$  to  $0^\circ\text{C}$  achieving a reduction in leakage current by a factor two and preventing reverse annealing which would eventually require too high depletion voltages. The data are compared to a parametrization that accounts for accumulated damage and for annealing, whose input is the fluence as predicted by a model of the CMS detector. The overall trend of the measurements is in agreement with this model except for the normalization. The reasons for this discrepancy in scale remain under investigation, with possibilities including uncertainties in the operational temperature and incorrect inputs to the model of the CMS detector.

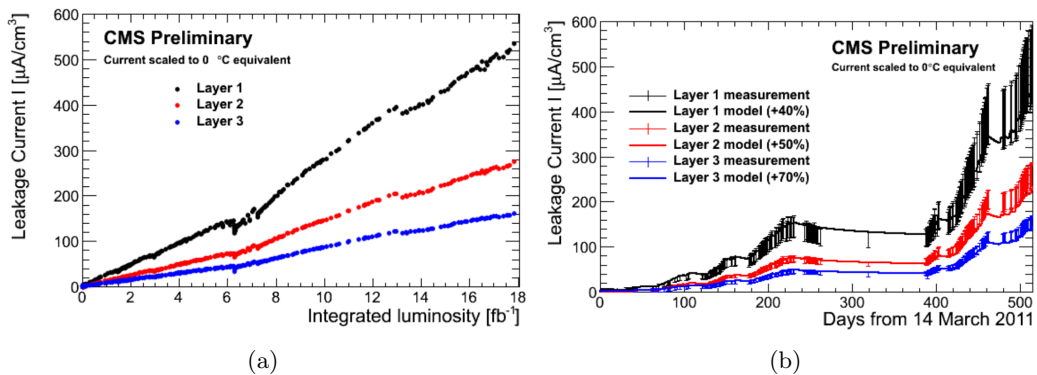


**Figure 15.1:** Leakage current scaled to  $0^\circ\text{C}$  operational temperature for the barrel layers as a function of the integrated luminosity (a) and time (b) in 2011-2012 [183].

The depletion voltage was also monitored during operations. With irradiation, defects with a negative space charge are generated throughout the bulk leading to variations in the effective doping concentration. When starting with n-type bulk, the effective doping concentration decreases because of the negatively charged defects until the bulk is transformed into an effective p-type. This process, called *type inversion*, happens at a relatively low dose of several  $10^{12} n_{eq}/\text{cm}^2$  (neutron equivalent fluence) [184]. As a consequence of this space charge sign inversion, the depletion zone now expands from the  $n^+$  pixel implants towards the p-type back. The depletion voltage scales with the bulk doping concentration: it initially decreases reaching a minimum at the inversion point, and then rises with the effective bulk doping concentration.

A dedicated scan of the bias voltage was performed several times per year, by varying the detector bias voltage from 0 V to the normal operating value of 150 V, and measuring the single hit efficiency. The results of the hit efficiency measurements for the innermost barrel layer between 2011 and the beginning of 2013 are shown in Fig. 15.2(a). The bias voltage that is needed to reach a depletion depth corresponding to full hit efficiency decreases with irradiation at first, then increases as expected due to the aforementioned changes in the effective doping. The dependence of the voltage needed to achieve full hit efficiency on the integrated luminosity is shown in Fig. 15.2(b) for the barrel layers and endcap disks.

The presence of a minimum for the layer 1 and layer 2 is evidence for type inversion occurrence.

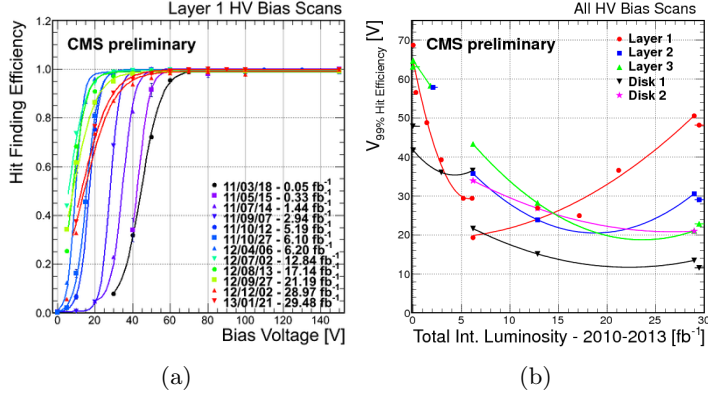


**Figure 15.2:** (a) Scans of the bias voltage performed on the innermost barrel layer. (b) Bias voltage corresponding to full single hit efficiency for all barrel layers and forward disks as a function of the integrated luminosity delivered in Run 1 [54].

The evolution of the pixel threshold (Fig. 15.3(a)) and the analog current (Fig. 15.3(b)) was also frequently monitored in Run 1, and an increase of both parameters with integrated luminosity was observed. The possible explanation for these changes is the radiation damage in the bad-gap reference voltage circuit, which would shift all voltage settings inside the ROC. Because of the described effect, a re-calibration of the analog voltage and the pixel threshold during technical stops was necessary to recover the optimal ROC performance.

The pixel hit resolution also exhibits a slow degradation with integrated luminosity as shown in Fig. 15.4. The two points of improvement correspond to re-calibrations of the pixel threshold.

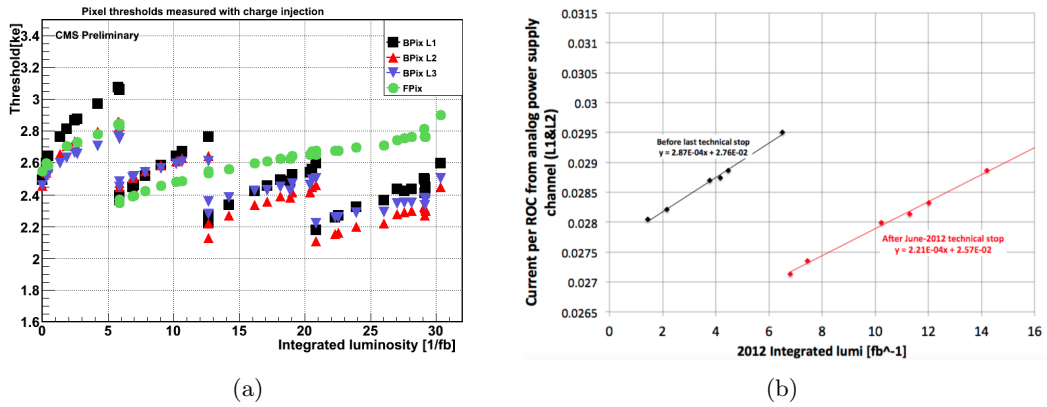


**Figure 15.3:** (a) Average pixel threshold in units of 1 ke for the barrel layers and forward disks, and (b) average analog current per ROC drawn by the power supply for BPix layers 1 and 2, as a function of the integrated luminosity delivered in Run 1 [54].

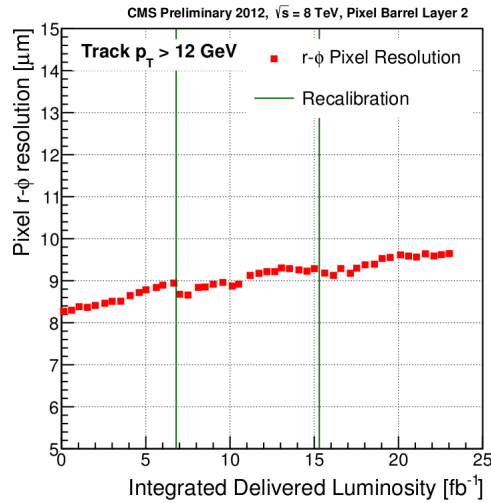


**Figure 15.4:** Single hit resolution for barrel layer 2 in the  $r\phi$  plane as a function of the integrated luminosity delivered in Run 1 [54].

## 15.2 Optimization for LHC Run 2

In Summer 2013, after the first LHC run, the BPix and FPix detectors were extracted from CMS, and throughout LS1 they were kept in a refrigerated, climate-controlled room environment (Fig. 15.5) located at the CMS experimental site, LHC-P5. The BPix was maintained in two cold boxes in a laboratory with repair workbenches, and all the electronics and computers necessary to control and readout the detector for maintenance and tests.



**Figure 15.5:** Barrel pixel detector temporarily installed in the clean room at LHC P5.

At the end of Run 1, the fraction of operational channels in the barrel pixel detector was 97.7% and the long shut-down was used to recover the faulty channels. The main reasons

were broken wire-bond connections between the ROC and the HDI as well as issues with the lasers on few AOHs. Furthermore, some modules had an old ROC design, which caused operational problems, and were therefore disabled. Replacements were attempted only for the barrel layer 3 outer shell, since the other layers and the inner shell of layer 3 were considered too risky to touch without breaking further parts. The defects in layer 3 made up 52% of the faulty channels. Two AOHs were found with disconnected wire bonds between the laser and the AOH PCB, and they were also replaced. Figure 15.6 shows pictures from the laboratory in LHC-P5 during this operation. In order to proceed with the replacement one of the two cold boxes was opened and the half shell of interest extracted using a support equipped with rails. The shields covering the AOHs were unscrewed and all the AOHs of the sector in the outside direction had to be unplugged in order to replace the two malfunctioning ones. Before restoring the detector in its original position inside the box, the two new AOHs were tested by checking with the oscilloscope the variations in the optical output when changing the laser bias settings with commands sent through the tkFEC. The same tests were performed for the other functioning AOHs that had to be unplugged to perform the replacement. It was found that during the operation, two additional AOHs were damaged and they had to be replaced as well.

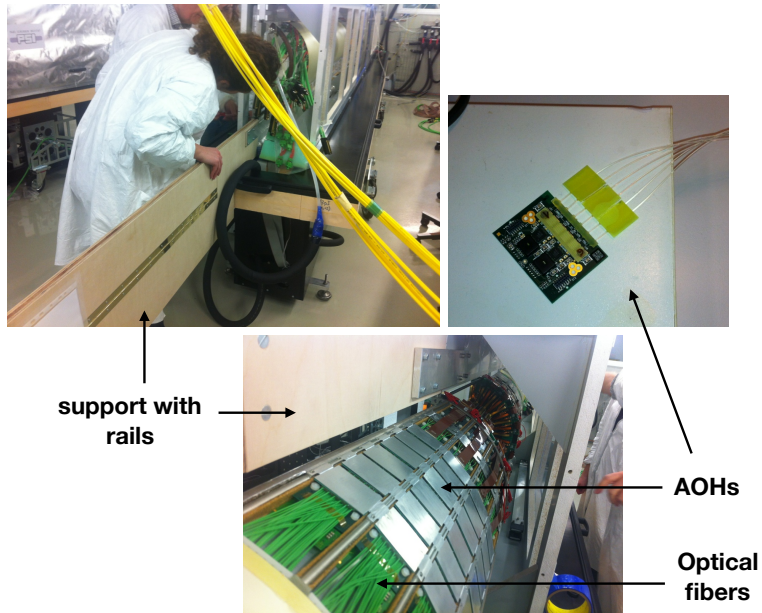


**Figure 15.6:** Pictures of the operations conducted in the clean room at LHC-P5 to replace the broken AOHs. The support with rails used to extract one half shell from the box is visible. The AOHs are mounted on the supply tube and covered by metal shields. A picture of an AOH is shown on the top right.

There was, however, a serious incident in mid-August 2014. After having replaced a BPix module, tests of the corresponding quadrant showed severe damage: 55 new unresponsive modules were found. It was decided to take that part of the detector to PSI for further tests and repairs. Shorts were discovered at the ROCs and in several modules between the TBM and cable pads. Eventually, the detector was repaired within three months using 40 new modules and 19 repaired ones. The shorts were suspected to be caused by humidity due to unobserved condensation in the cold box. After being repaired, the functionalities of the new modules were successfully confirmed and at the end of LS1 the good detector fraction was 99%.

Part of the time available during LS1 have been employed to exercise and improve calibration procedures in view of commissioning and operations for Run 2. An overview of the calibration procedure is given in the following.

## 15.3 Overview of pixel calibrations

Detector functionality and performance depend on proper calibrations of readout chain parameters. Most of these parameters are quite stable unless major changes occur, such as the detector operating temperature. Other parameters are more sensitive to environmental variations. For these parameters a re-calibration on a regular basis was necessary during Run 1 operations.

Further expertise in the calibration procedure was achieved during LS1 and it has been fundamental for the re-commissioning of the detector to prepare it for a successful data-taking in 2015–2016. In addition, the detector was fully re-calibrated at low temperature after re-installation. As for Run 1, in these two years, re-calibrations have been performed during technical stops, and in particular in mid-2016 when the analog current drawn by the ROCs of the innermost layer reached critical values ( $\approx 6\text{ A}$ ) that led to the trip of the power supplies in several occasions.

The calibrations are performed with POS which was installed and run on the computers available in the clean room. There are a large number of different calibration tasks that need to be executed sequentially and sometimes iterated. While a detailed description of each calibration as well as the implementation in POS can be found in Ref. [180], an overview of the most important steps is given in the following. The calibration process consists first of a part where the readout chain settings are adjusted. It is meant to put the detector in a state in which it can correctly reconstruct hits and involves tuning of the settings of the FED, of the electronic components placed on the supply tubes, as well as the threshold and timing settings of the ROCs, which are controlled by programmable DACs (Section 14.2.2). In the second part of the process the pulse height information is optimized. The steps involved here are lengthy and require several iterations to reach the target signal rise speed as well as the lowest practical value for the threshold of each ROC. In the final step, an optimization of the analog signal response is performed. Most of the calibrations produce directly new optimal settings which can then be used in subsequent runs. Other calibrations write binary data files which have to be analyzed offline, these include the pixel alive test, the threshold and noise measurement and the gain calibration.

### 15.3.1 Adjustment of readout chain settings

#### 1) Delay25 chip

As described in Section 14.3 (Fig. 14.6), the LHC clock, L1 trigger and programming signals are transmitted from the pxFEC placed in the underground counting room to the detector through fibers. The optical signals are first converted into digital signals by the DOH to be then sent to the detector through the Delay25, PLL and Gate-Keeper chips integrated in the same digital circuit. The clock and trigger are encoded as a single signal transmitted using one single fiber. As schematically illustrated in Fig. 15.7, this signal is decoded by the PLL chip and sent via two separate lines, LHC clock (CLK) and Calibrate/Trigger/Reset (CTR), through the Delay25 chip to the BPix modules. In addition, the CLK signal is split in the Gate-Keeper chip and one line (RCK) is returned and sent back to the pxFEC through the Delay25 chip. The digital programming and control data (SDA) also goes through the Delay25 and Gate-Keeper chips. If the gate is open the SDA is transmitted to the BPix modules

which sends the acknowledge signal (RDA) back, otherwise the data packet is returned in the Gate-Keeper.

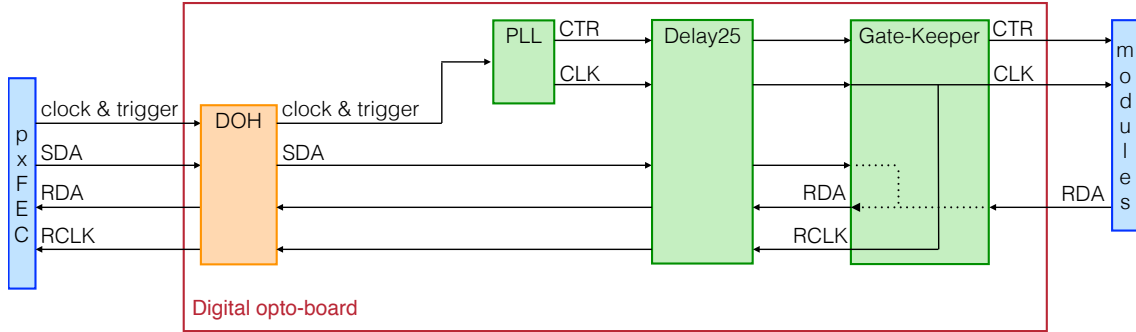


**Figure 15.7:** Diagram illustrating the functionality of the BPix digital circuit.

The SDA signal can only be decoded by the TBM if it is in phase with the CLK signal. The purpose of the Delay25 chip is to adjust the timing between the two lines to make this communication work. Hence, a calibration is performed where the delays for the SDA and RDA lines are scanned and for each set of values commands are sent to the TBM and the return status in the pxFEC is checked. The main output from this calibration is new SDA and RDA delay settings. If the calibration converges the old settings stored in the configuration database are updated with the new ones. An example of the scan is shown in Fig. 15.8 for one module. The set of values chosen by the algorithm is indicated with a red point and corresponds to a region where the communication between the TBM and the pxFEC has been established for each trial.

This calibration is fundamental to ensure correct communication with the pxFEC, but once the settings are found they do not need to be readjusted often.

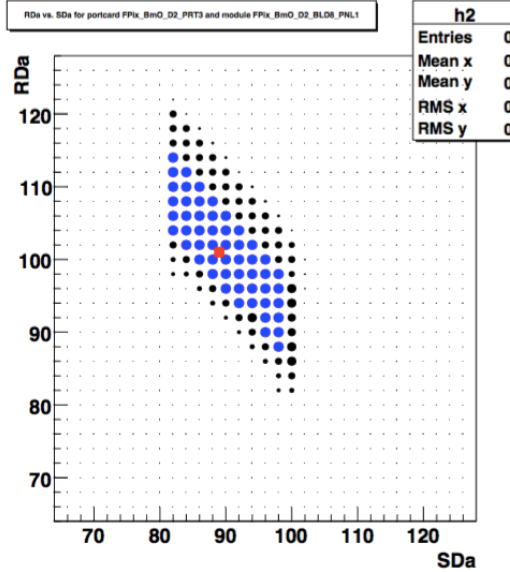


**Figure 15.8:** Example of output of the Delay25 calibration for one module. For each set of SDA and RDA delay settings the communication with the TBM is checked. The blue dots indicates areas with 100% communication efficiency. The black dots indicated partial efficiency where larger dots have higher efficiency. The red square indicates the point chosen by the algorithm.

## 2) FED receiver offset

This calibration adjusts the individual offsets included in each input channel of the FED such that the baseline of the analog signal (black level) is tuned to be near a given target value, normally 450 ADC counts, which is near the midpoint of the dynamic range of the ADC. The main output consists of new FED parameters that, if satisfactory, are used to update the previous settings. This calibration is performed often because the AOH is very temperature sensitive. Already 1 °C temperature change shifts the signal by 50 ADC counts (out of 1024). The pixel FED automatically corrects for baseline shifts during a run but it is important to start with a uniform baseline distribution. The baseline calibration adjusts each optical input to be  $\pm 5$  ADC counts from the target value. During normal LHC operations it is performed at least once a day during the LHC fills.

The calibration also produces an output file with the analog signal for each module where its several components are visible, namely the TBM header and trailer, and each ROC header (Fig. 15.9). It runs quickly and provides an information on the data buffer for each FED channel. It is therefore very useful as a debugging tool since it provides a feedback on the basic functionalities of optical links, AOHs, TBMs and ROCs, needed to assess the status of the detector.

If this step fails to converge, for instance when part of the analog signal is not visible, a calibration can be run that adjusts the timing of the signal digitization in the FED by changing the phase of the ADC clock. This calibration is usually very stable, and needs to be repeated only when the FEDs, fibers, or other parts of the detector are touched, or if modifications of the fine phase of the global clock occur.

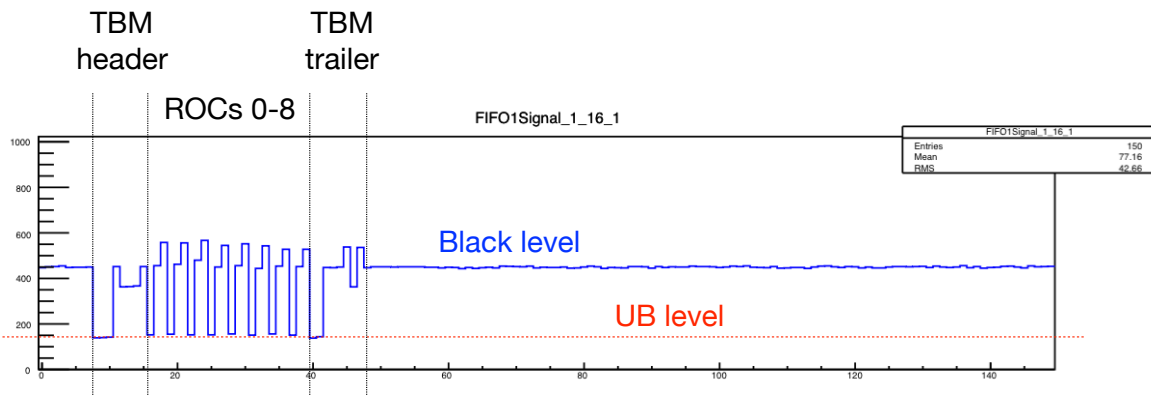


**Figure 15.9:** Example of analog signal from the TBM displayed at the end of the FED baseline calibration. The FED parameters are adjusted to center the baseline (or black level) in the middle of the FED ADC range.

## 3) AOH bias and gain

Each AOH is equipped with 6 lasers for which the bias and the gain can be adjusted individually. The optical fibers connected to the lasers are combined in groups of 12 and each of them is connect to one FED channel. The AOH bias is a setting that controls the laser bias current and hence, the amount of light (optical power) sent to the FED. The optical power, and hence the ADC counts in the FED, increases with the laser bias setting. As

shown in Fig. 15.10, at low values of the bias, the black (BL) and ultra black (UBL) levels are unaffected, so that there is no separation between the two. At some threshold, the BL begins to increase approximately linearly, followed by the UBL at a higher laser bias value and with about the same slope.

The maximum BL-UBL separation depends on the TBM settings discussed in the next section, and it is low if these parameters are configured to low values. In fact, the BL is independent on these settings, whereas the linear rise of the UBL begins at a later point if the configured values in the TBM are higher. As a consequence, the BL-UBL difference saturates at a higher laser bias value. The goal of the AOH bias calibration is to determine a laser bias setting for each FED channel that is just high enough to saturate the BL-UBL difference. The calibration measures this difference, using the levels from the TBM header and trailer, as a function of the laser bias. It is important, though, that during this scan the TBM settings are set to reasonable values, at least as high as they will be set in later calibrations and physics runs. Otherwise, the laser bias value determined from the saturation point will be too low.

Temperature variations alter the response of the AOH, essentially shifting the curves in Fig. 15.10 to the left or right by 4 bias counts for 5 °C variation. In order to provide a margin of error for these variations, the optimal laser bias setting is chosen by the calibration to be 4 counts higher than the saturation value. This offset can be externally configured before running the calibration.

It is also important that the laser bias is not too high to avoid that the signal moves out of the dynamic range of the FED. In the last part of the AOH bias calibration a coarse baseline adjustment is performed to bring the black level into the target range by re-adjusting the FED optical receiver offsets and laser bias settings. In this step the AOH bias is not decreased below the saturation value unless it is absolutely necessary. The main output of the calibration is a new configuration for the AOH bias and FED offset values that puts all FED baselines near the center of the dynamic range, with laser bias values that allow for a large BL-UBL separation. After the AOH bias calibration, the FED baseline calibration should be run to obtain a finer adjustment of the baseline (using the freedom to move each channel offset).

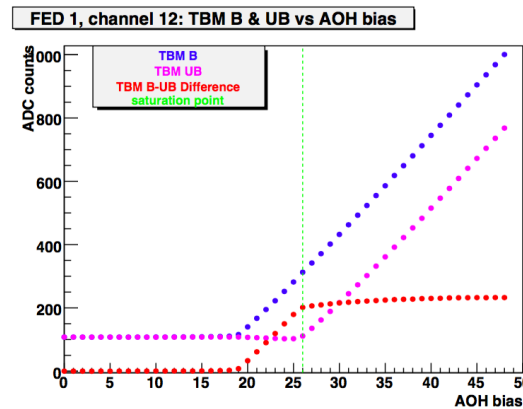


**Figure 15.10:** Black and ultra black levels as a function of the AOH laser bias. An optimal value for this parameter is found at the saturation value of the BL-UBL separation.

The gain is a setting for each AOH laser that can accept just 4 possible values (0, 1, 2, 3). This setting does not affect the black level, whereas it scales the size of deviations from the BL expanding or shrinking the signal. Larger settings correspond to larger deviations

and hence, to a larger BL-UBL separation. Although the adjustment of TBM and ROC parameters will be the primary method for tuning the UBL to the optimal value, the aim of this calibration is to set the laser gain at the lowest level that will allow the TBM UBL to be sufficiently low for an optimal readout of the signal. In fact, too high laser gain values will increase the power drawn and they are intended to be used to compensate for radiation damage over time. The optimal laser gain setting is chosen as the lowest value that provides an UBL below a user-defined threshold.

#### 4) TBM and ROC ultra black levels

With the black level set at about 450 ADC counts by the FED baseline calibration and automatic correction, the next step consists in a fine adjustment of the TBM and ROC ultra black levels. First, the TBM settings are calibrated to set the TBM header and trailer UBL to a value of about 250 ADC counts. There are three registers on the TBM affecting the UBL, where higher configured values correspond to lower UBL and hence, larger BL-UBL separation. Furthermore, two of them affect also the signal from the ROCs. A simultaneous scan of all three registers is usually performed. Although higher settings generally provide lower ultra black levels, at very high values the UBL may actually increase. Thus, if the calibration finds multiple settings that give the target UBL, it will choose the lower ones.

Dual TBMs represent a special case. The two channels on a dual TBM share the same registers, so that they cannot be adjusted independently to tune both ultra black levels at the target value. In this case, the settings are optimized such that one channel is at the target UBL, and the other is below.

A second calibration is run that sets the ultra black level for each ROC equal to the corresponding TBM's UBL. There are two DAC settings on the ROC which affect the UBL, and higher configured values correspond to lower UBL (and larger BL-UBL separation).

These calibrations have to be repeated every time the previous steps 2 and 3 are run and modify the correlated parameters.

#### 5) Threshold and charge injection delay

The rest of the calibrations require the use of the charge injection feature of the ROC. For the injected charge to be readout as a hit, it has to cross the comparator threshold and be validated by the trigger (which involves the timing of the injection). Thus, a calibration is first run that aims at finding the settings for each ROC for the comparator threshold and for the delay at which the charge is injected into the pixels. It is meant at quickly finding a working point in which the injected test charge can be read out. The amplitude of the injected signal is set by programming the corresponding DAC register ( $V_{cal}$ ). Since these settings are common to all pixels in a ROC, only few cells can be enabled for this calibration. A 2D scan of the threshold and delay settings is performed: for each pair of values, a defined number of triggers are sent and for each of them the event is readout from FIFO1 or FIFO3 to verify that the hits have been collected for each ROC. The settings are changed by programming the corresponding DAC registers,  $VcThr$  and  $CalDel$ .

It has to be mentioned that the  $CalDel$  setting is only relevant for calibration data taken with charge injection. For real data, only the trigger delay has to be known and programmed into the so called  $WBC$  register of each ROC. The trigger delay basically sets the bunch crossing in which data is read out and is estimated from the known cable/fiber lengths and delays introduced by the electronics.

An example of  $VcThr$  versus  $CalDel$  scan is shown in Fig. 15.11(a). For large  $VcThr$  values, which correspond to low thresholds, a large number of pixel fire due to noise such that to block a double column. For lower values, hits are collected in the  $CalDel$  range that corresponds to the  $WBC$  used. The curve bends to smaller delay values as the  $VcThr$  decreases. The explanation for this behavior is illustrated in Fig. 15.11(b). Since a low  $VcThr$  value corresponds to a higher threshold, the signal reaches the threshold later and hence a smaller delay is needed for the signal, i.e. the signal is injected earlier.

At the end of the calibration an optimal set of values is chosen in the region where the efficiency for detecting a pixel hit is 100%. The optimal working point is also chosen such that it is sufficiently far away from the noise level.

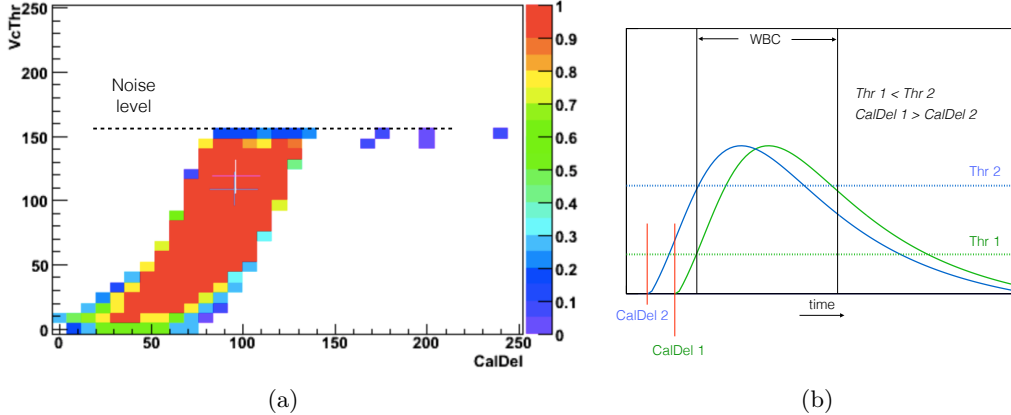


**Figure 15.11:** (a) Efficiency for detecting a hit as a function of the comparator threshold ( $VcThr$ ) and delay ( $CalDel$ ) settings for one ROC. Large values of  $VcThr$ , corresponding to a low threshold, generate much noise that saturates the digital circuit and no hits are detected. The optimal point is indicated in black while the blue point indicates the old settings. For small values of  $VcThr$  the signal reaches the threshold later and hence a smaller delay is needed for the signal. This behavior is illustrated in (b).

## 6) Address levels

The row and column address of the hit pixel is encoded in 6 discrete analog levels (Section 14.3.1) which have to be well separated for being correctly decoded by the FED. The position of the address levels is determined by measuring the levels of all pixels in a ROC and overlaying them in a histogram. Pixels are scanned to make sure that combinations of address levels that could potentially cause problems are probed, such as transitions from high to low levels and vice versa. An example of the results is shown in Fig. 15.12, where the six peaks corresponding to the six address levels can be seen. The separation between the levels is good and the decoding limits are chosen in the center between to neighboring peaks to be then downloaded to the FED. The separation can mainly be affected by dirty optical connectors and poor light transmission, or by large temperature changes not compensated by the automatic baseline correction. Hence, during stable running conditions this calibration is run once every few days.

## 7) Pixel alive test

In this test, the functionality of each pixel in a ROC is checked by verifying that it responds to an injected calibration signal above threshold. Charge is injected in each pixel several

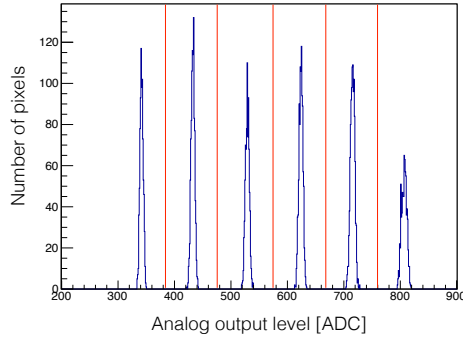


**Figure 15.12:** Address levels of all pixels in a ROC as received by the FED. The red lines are the separation limits used for the decoding of the pixel addresses in the FED.

times and the number of output signals is recorded. The pixel is fully working if all signals are registered; the pixel is defective, if no output signal is registered at all. The data are then analyzed offline to produce an efficiency map that displays the efficiency for each pixel. Examples of the results for two ROCs are shown in Fig. 15.13. For the case on the left all cells are functioning, whereas on the right an example is shown of a ROC with a large number faulty pixels.

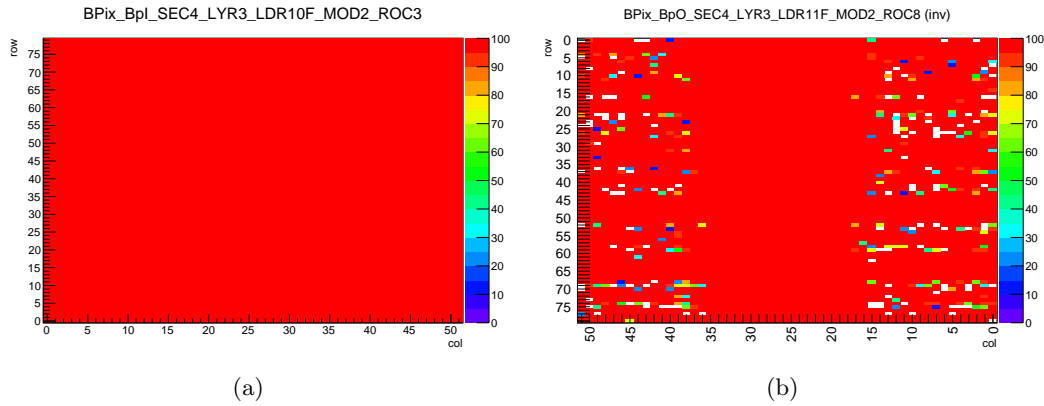


**Figure 15.13:** Examples of pixel alive test results for two ROCs: (a) all cells are functioning and (b) a large number of pixels are broken.

## 8) Measurement of threshold and noise

This is the last step of the calibration chain aimed at verifying and adjusting the basic functionality of the detector. At this stage it is important to perform a measurement of the threshold and noise of each pixel, which will be afterwards optimized in the second part of the procedure as described in the next section. In fact, the detection thresholds are an important parameter of the pixel detector since they influence the hit position resolution (Fig. 15.4).

The thresholds are measured through the so called “S-curve” scan, which provides the pixel response efficiency as a function of the amplitude of the injected test charge ( $V_{cal}$ ), varied from 0 to its maximum. The  $V_{cal}$  value where the signal shows 50% efficiency is

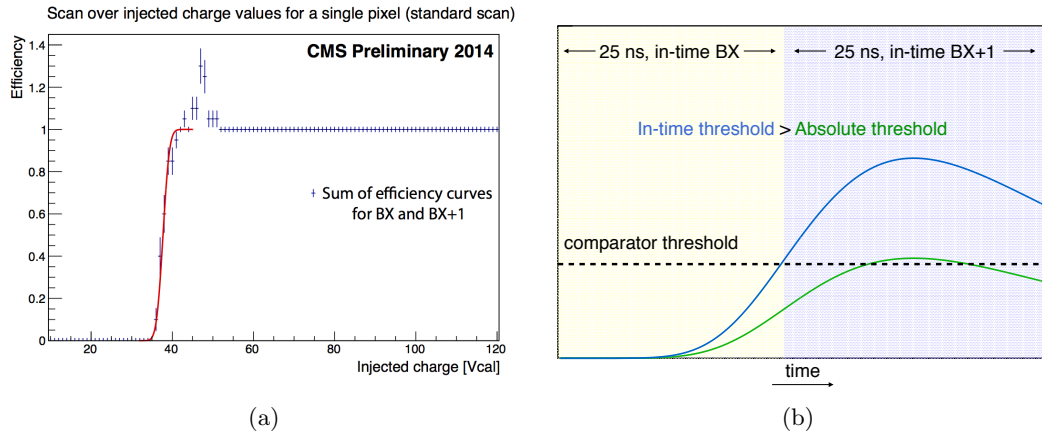


**Figure 15.14:** (a) Single pixel efficiency curve determined performing a scan over injected signal amplitudes ( $V_{cal}$ ). The curve is the result of the sum of efficiency curves for the in-time bunch crossing (BX) and the following one (BX+1). Points exceeding the 100% efficiency are due to statistical fluctuations of the two curves in the turn-on region. The effect on the fit is negligible. (b) Diagram illustrating the difference between in-time and absolute thresholds due to the finite rise-time of the signals.

defined as the threshold. As for the pixel alive test, the data are analyzed offline to produce the final results. An example of such scan is shown in Fig. 15.14(a) for a test conducted in the clean room at a temperature of -15 °C.

The finite rise-time of the signal complicates the threshold measurement. One should distinguish the *absolute threshold* defined as the comparator level above which the signal is accepted and the pixel hit is available for readout, and the *in-time threshold* where the signal is fast enough to be correctly labeled by the right bunch crossing. The difference between the two is due to *time-walk* and is related to the speed of the pixel amplifier. The absolute threshold is relevant when discussing noise and cross-talk, that is the optimum conditions under which the ROC still works. It also determines the pixel detector hit occupancy. The in-time threshold determines the lowest amplitude signals useful for hit reconstruction and affects the position resolution. Both thresholds can be measured using the S-curve method: for the in-time measurement the *WBC* (or trigger delay) is set to the nominal value; for the absolute threshold measurement the *WBC* is shifted down by one unit making the readout of the lowest amplitude (i.e. slowest) signal possible. By definition the in-time threshold is higher than the absolute. This behavior is illustrated in Fig. 15.14(b).

The noise can also be measured with the S-curve method since it is proportional to the width of the region where the signal efficiency rises from 0 to 100%. Both noise and threshold are measured in  $V_{cal}$  units, representing the parameter which determines the magnitude of the injected charge. The calibration of the  $V_{cal}$  unit itself was done during module testing using data from X-ray sources of known energies, and it varies from pixel to pixel and from ROC to ROC. On the average, one  $V_{cal}$  unit corresponds to 65.5 electrons, representing the slope of the calibration curve, whereas the average offset is -414 electrons. However, the spreads of the two distributions are rather large, the slope parameter has an RMS of 9 and the RMS of the offset is about 570 [185].

Running this method for the whole detector is very time consuming. Instead, for each ROC

the thresholds and noise are measured using only 81 pixels, which was found to be sufficient to determine the average values. The results of the noise and threshold measurements performed in 2015 during commissioning for Run 2 will be discussed in Section 15.4.

### 15.3.2 Optimization of the pulse height information

#### 1) Signal rise speed

The in-time threshold depends on the amount of time-walk introduced in the amplification and shaping that occur before the signal reaches the comparator. The speed of the pixel amplifier is controlled by *Vana*, a 8-bit DAC that regulates the voltage applied to the analog part of the ROC, which can be varied in the range from 800 to 1,300 mV. The *Vana* has to be optimized such that a compromise is obtained between the desire to minimize the time-walk and the need to keep the current drawn by the analog part of the ROC, or analog current, at a reasonable level. During module testing the optimal *Vana* setting was determined for each BPix ROC by measuring directly the analog current drawn by the ROC, and then choosing the value that corresponds to 26–28 mA. In fact, this value for the current has been found optimal to avoid exceeding the limit of the power supply. Nevertheless, the radiation damage affects the ROC analog current and a re-calibration is necessary during operations (Fig. 15.3(b)).

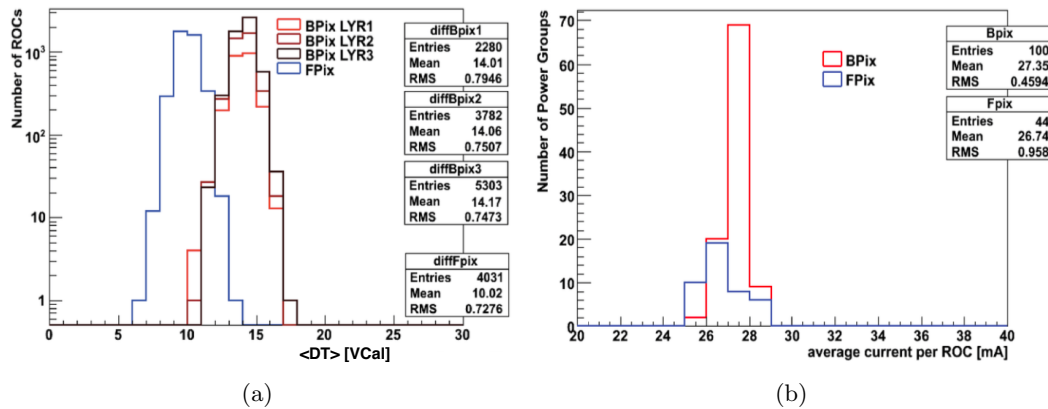


**Figure 15.15:** (a) Final distributions in DT obtained at the end of the optimization of the signal rise speed in 2012 for each barrel pixel layer and for FPix . The target DT value is chosen to reach an average analog current per ROC of 26–28 mA (b).

Once the detector is fully assembled, it is no longer possible to access the value of the analog current for each ROC, since at this stage the only available information is the total current drawn from a single power supply, which services more than one-hundred ROCs. Thus, a procedure has been developed in the past to optimize *Vana* that does not make use of this information. The analog current can indeed be directly related to the time-walk, whose value DT can be obtained by the difference between the in-time and absolute thresholds. The higher *Vana*, the faster is the detector (smaller DT), but also the higher the current drawn by the ROC. The target value of DT is then chosen such that the average analog current per ROC in each power group is near the optimal value of 26–28 mA. However, the correct target for DT depends on radiation damage and temperature, so that a fixed number to target cannot be given. Instead, one should tune the target based on the average analog current per ROC as read from the power supply. Figure 15.15 shows the DT distributions for both

BPix and FPix measured in 2012, as well as the corresponding average analog current per ROC. For BPix, a target DT value of 14  $V_{cal}$  was found to be sufficient to reach the optimal current.

In order to optimize the DT, the calibration is implemented as an iterative procedure, which makes use of the in-time and absolute threshold measurements given by the S-curve method. It has been found from calibrations performed during Run 1 that the relation  $\Delta(DT) = DT - DT_{target} \simeq \Delta V_{ana}$  holds [186]. Using this relation, the new  $V_{ana}$  settings are computed for each iteration and then downloaded to the ROCs for the next iteration. In each iteration, the absolute threshold and charge injection timing has to be re-calibrated (step 5 in Section 15.3.1) because of their dependence on  $V_{ana}$ . Figure 15.16 illustrates the evolution of the  $V_{ana}$  settings with the iterations showing how these converge to the value corresponding to the target DT.

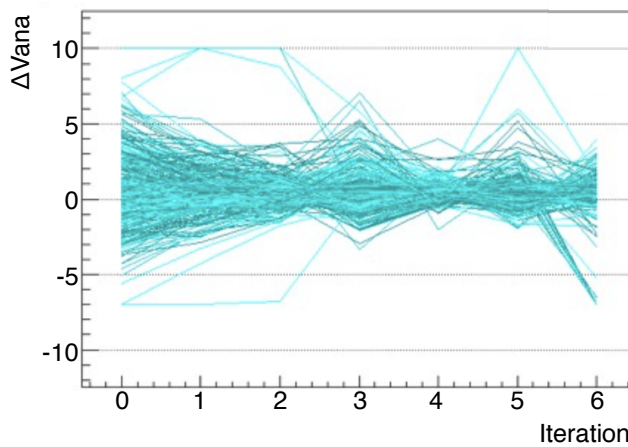


**Figure 15.16:** Example of optimization of the signal rise speed obtained from tests conducted in the clean room during LS1. The evolution of the  $V_{ana}$  settings for some ROCs with the iterations is shown and illustrates how these converge to the values corresponding to the target DT.

## 2) Threshold minimization

This step is meant to set the threshold of each ROC at the lowest practical value, so that the threshold is low enough to detect low amplitude signals and ensure high hit resolution, but above the noise level. The procedure for minimizing the threshold starts setting a large value of the comparator threshold (for instance 50  $V_{cal}$ ) in each ROC such that it is above the level of noise. The threshold is then lowered by 2 units and a pixel alive test or S-curve is run to check whether a ROC is failing because the threshold is too low and noise occurs. The procedure is iterated until all ROCs reach the minimum achievable value. For each iteration the charge injection timing has to be re-optimized as well. Several scripts have been implemented during LS1 to automatize this time consuming procedure. An example of the results from tests conducted in the clean room during LS1 is shown in Fig. 15.17. The final threshold and noise distributions for the whole detector obtained with this method before the start of data-taking in 2015 are discussed in Section 15.4.

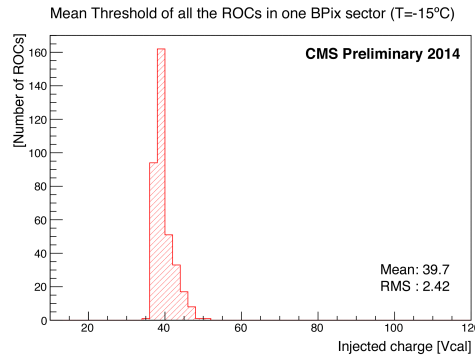


**Figure 15.17:** Distribution of the minimized thresholds for all the ROCs in one BPix sector. The measurement was performed at  $-15^{\circ}\text{C}$  coolant temperature in the clean room during LS1.

### 3) Analog signal response calibration

The final part of the calibration procedure is aimed at maximizing the range and linearity of the detector. In fact, the hit position is interpolated from the charge information of all pixels in a cluster. For a precise position resolution it is therefore crucial to know for each pixel the exact response curve (or pixel gain) that converts the analog pulse height (in ADC counts) into the corresponding charge. The response curve is measured by injecting signals with increasing amplitudes to each pixel and measuring the analog pulse height. Before this calibration, the linearity of the response curve is optimized by adjusting few DAC registers in the ROC. The linearity is required for two reasons. On one hand the non-linear behavior in the low range does not allow to reconstruct the charge of the signal, on the other hand fewer parameters have to be stored in the data base. The  $VhldDel$  register controls the delay that is applied to each pulse before its height is sampled and stored in the sample and hold capacitance until the readout mechanism is started from the periphery. The supply voltage of the sample and hold circuit is regulated by the  $Vsf$  register.

Figure 15.18 shows the pulse height as a function of  $VhldDel$  settings at low, medium, and high values of  $Vsf$ , for a fixed injected signal amplitude. A good  $Vsf$  value is one for which this curve rises and then falls so that the pulse heights at the two endpoints (lowest and highest  $VhldDel$ ) are equal. The figure also includes a plot of these endpoints as a function of  $Vsf$ ; the rightmost intersection point is the  $Vsf$  value chosen. Low values of  $Vsf$ , below  $\sim 90$  are discarded because they are found to be not optimal for a correct readout. After choosing the  $Vsf$  value,  $VhldDel$  is set to the value that maximizes the pulse height.

Several ROC DAC settings also affect the scaling of the pulse height signal that is sent out to the FED. The difference in recorded pulse height between a small and large amount of collected charge should be preferably large. However, the pulse height signal should not go too low to be confused with the UB level, nor too high to exceed the FED's dynamic range. Hence, a calibration is run to optimize these settings as well.

After these fine adjustments, the measurement of the response curve for each pixel is performed. For each pixel about 30 charge values are injected. During the scan, the acquired data is stored in binary files and is later analyzed offline. All pixels have to be calibrated, therefore, the procedure is time consuming and takes about 8 hours for the whole detector. An example of such measurement for one pixel is shown in Fig. 15.19. For comparison, an example exhibiting a non-linear behavior for a non optimal  $Vsf$  setting is also shown. The saturation in the high range is less important since it occurs for charges of more than 30-40 ke.

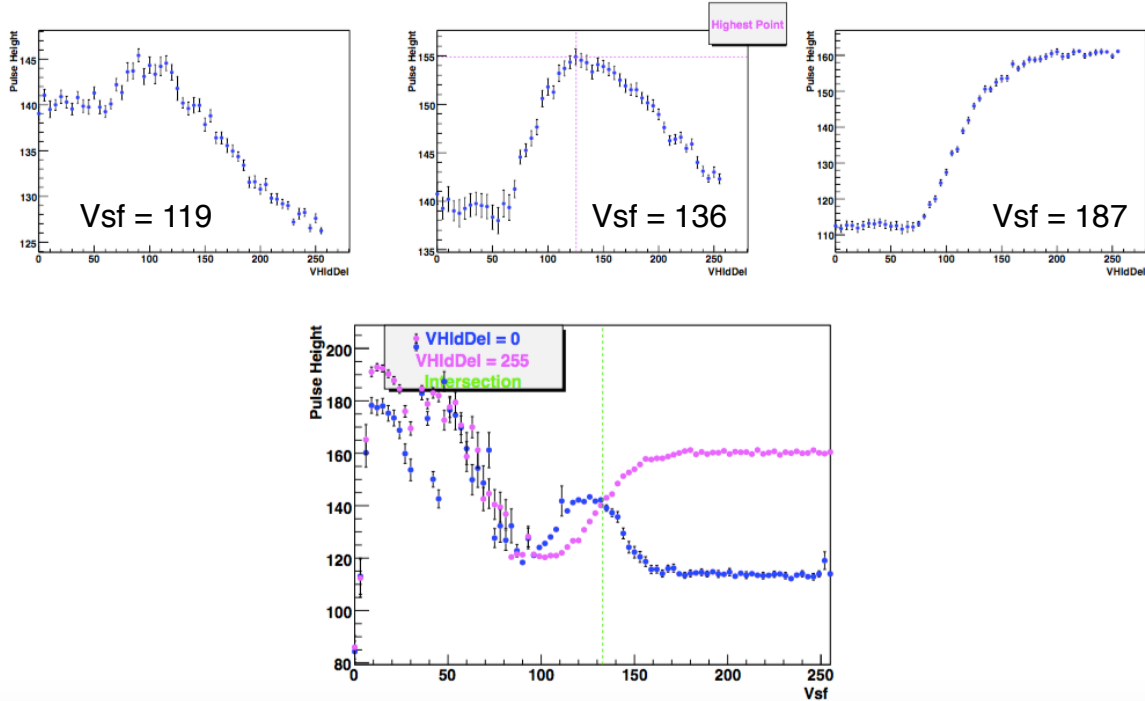


**Figure 15.18:** Top row: pulse height as a function of  $VhldDel$  for low, medium, and high values of  $Vsf$ . As  $Vsf$  increases, the right endpoint shifts to the right. The best  $Vsf$  value is the one for which the pulse heights measured at the extremes of the  $VhldDel$  range are equal. Bottom plot: pulse height at the extremes, as a function of  $Vsf$ . Low values of  $Vsf$  are discarded because not optimal.

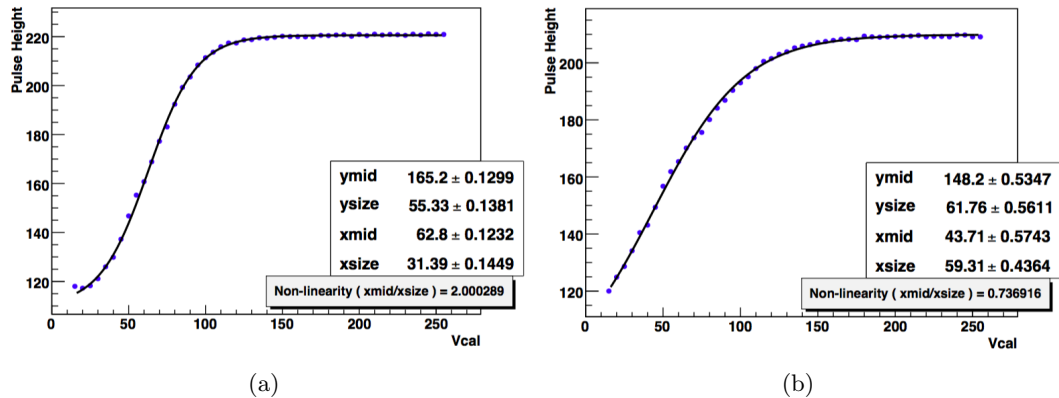


**Figure 15.19:** Examples of pixel response curve (gain calibration) representing the scan of the pulse height as a function of  $Vcal$ . The scan on the left presents poor linearity as performed for a not optimal value of  $Vsf$ .

The pixel response curves are parametrized with the following function:

$$PH = f(Vcal) = y_{mid} + y_{size} \cdot \tanh\left(\frac{Vcal - x_{mid}}{x_{size}}\right), \quad (15.1)$$

where  $PH$  is the recorded pulse height,  $(x_{mid}, y_{mid})$  is the point at the center of the quasi-linear rise region of the hyperbolic tangent,  $x_{size}$  and  $y_{size}$  are the horizontal and vertical

scales of the quasi-linear region, respectively. If  $x_{mid}/x_{size} \approx 1$ , the response curve is linear in the whole region of interest. Thus, the linear region below the saturation is parametrized by only the slope (gain) and offset (pedestal) of a linear fit. These parameters are then used in the data reconstruction. The results of the gain calibration performed for the whole detector before the start of data-taking in 2015 are discussed in Section 15.4.

## 15.4 Re-commissioning for LHC Run 2

The barrel pixel detector was installed back into CMS on 8th December 2014. The operations, described in Section 15.4.1, were coordinated by the PSI and UZH teams (Fig. 15.20), and were completed in only 5 days. After that, the FPix detector was also installed following a similar check out procedure as for BPix so that most work was already completed before Christmas. The full pixel detector was re-commissioned in January 2015 within about a fortnight using the procedure described in the previous section. Section 15.4.2 presents the results of the detector calibrations performed for the whole detector at low temperature after the installation. Finally, in Section 15.5, the detector performance at the beginning of the LHC Run 2 are discussed.

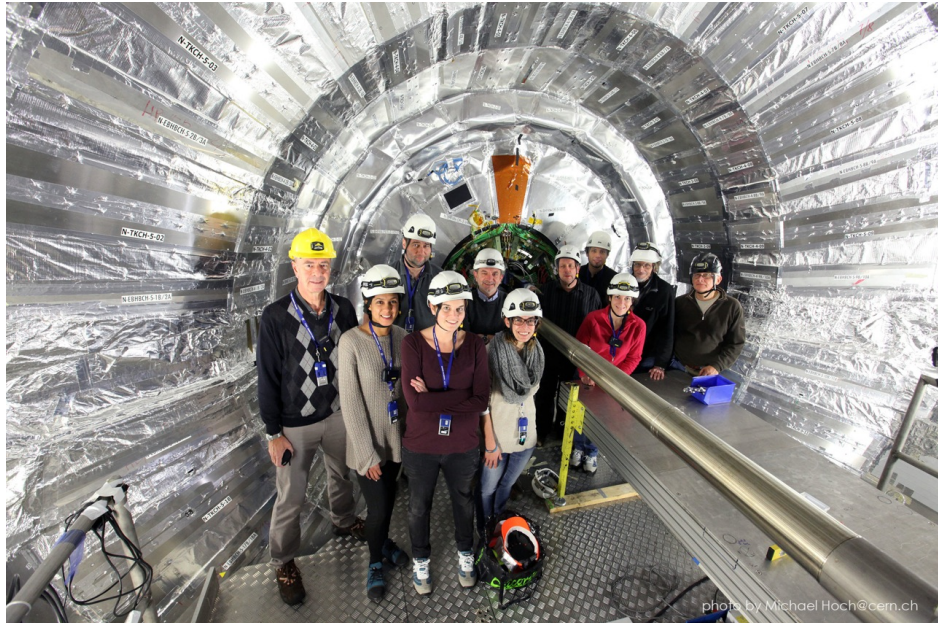


**Figure 15.20:** Pictures taken on the CMS underground platform after the re-installation of the barrel pixel detector in December 2014. The operations were coordinated by the PSI and UZH teams.

### 15.4.1 Installation into CMS

The barrel pixel detector re-installation into CMS took place only three months later than originally planned due to the incident mentioned in the previous section. Particular care was given to the centering of the detector with respect to the new beam pipe, required for the upgraded pixel detector planned for Spring 2017 (Chapter 16), since before it had been slightly shifted irradiating one side stronger than the other. Figure 15.21 shows pictures taken on the CMS underground platform illustrating the operations conducted in the first two days. The first day, each half of the detector was moved inside a transport box from the

clean room and lowered down to the cavern through the main shaft. A system with rails on top and bottom inside CMS had been designed to insert the pixel detector and the supply tubes along the beam pipe. The transport box with the detector was lifted to the insertion table and the rail system inside the box was joint with the rail system inside CMS using temporary extension rails. In this way, the detector could slide out of the transport box into its final position. The following day, all cooling loops, power cables and fibers were connected, and first attempts to power the detector and to test a sector were made. A picture of the detector in the final position with all power and control cables and optical fibers connected is shown in Fig. 15.22.

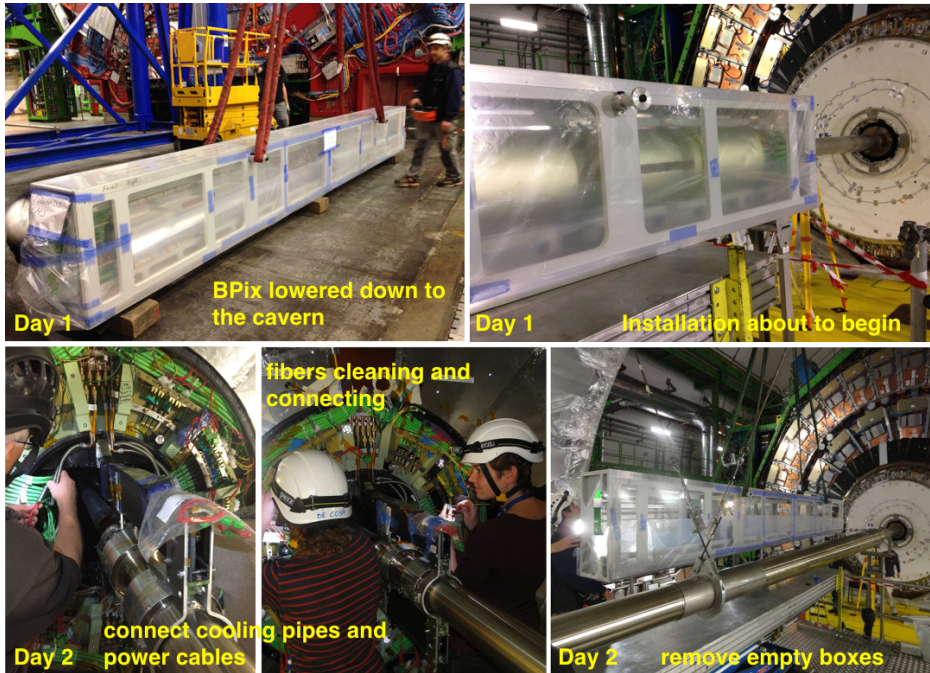


**Figure 15.21:** Pictures illustrating the steps of the BPix re-installation in December 2014. The operation has been completed in 2 days.

After the installation, the detector was then checked out at room temperature of about  $16^{\circ}\text{C}$ . The basic set of calibrations was run from the CMS control room aimed at assessing the detector status and setting the basic operating parameters. These include calibrations of the Delay25 chip, FED baseline, AOH bias and gain, TBM and ROC UB, and address levels. The absence of a good quality TBM signal in the FED (Fig. 15.9) or bad address levels indicate poor optical connections. This kind of problems were immediately established and solved underground on the platform by re-cleaning the optical connectors with special tools. Few iterations were needed. These operations were completed in about 3 days establishing the functionality of the whole BPix detector. Only 1% dead or disabled channels were found and most of them were acknowledged during LS1. The check out procedure was repeated after the insertion of the FPix.

### 15.4.2 Calibrations at $-10^{\circ}\text{C}$

As discussed at the beginning of this chapter, it was planned to operate the detector at  $-10^{\circ}\text{C}$  since low temperatures are favorable to mitigate the effects of radiation damage and guarantee excellent performance. Since the detector settings largely depend on the temperature, a full

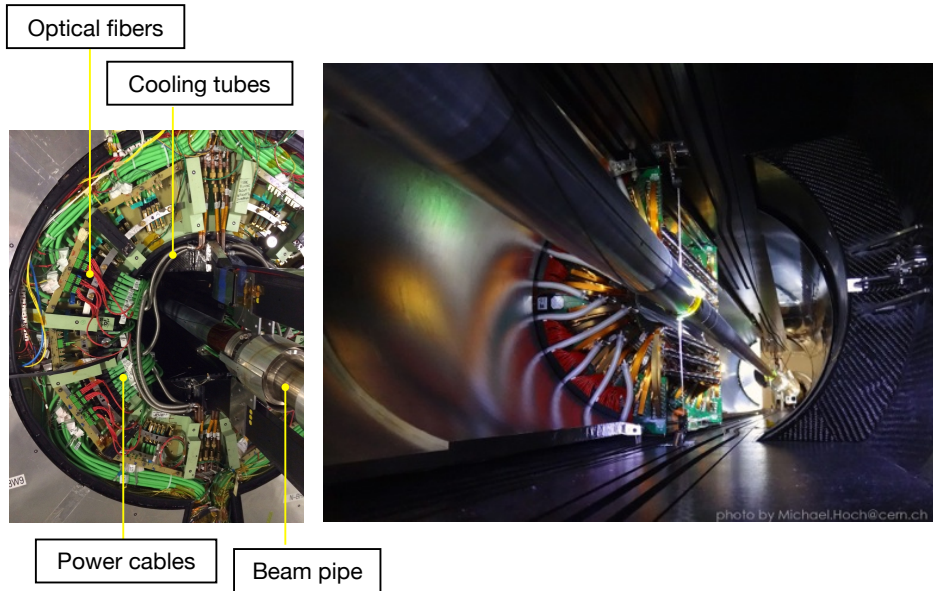


**Figure 15.22:** View of half of the barrel pixel detector in its final position inside CMS. The central beam pipe and the detector end-flanges with cooling lines and power and signal cables can be seen.

calibration of the detector under the new conditions has to be performed. Because of the limited amount of time, it was not possible to achieve this before the re-installation, and tests were conducted for only few sectors aimed at verifying some basic functionalities at such low temperatures. The full calibration procedure was instead run in January 2015 and completed in only 8 days, including the final optimization of the signal performance (Section 15.3.2). The improvements added to the procedure during LS1 as well as the time spent in practicing it were crucial to make these time consuming operations much faster and smoother with respect to 2011 and 2012.

The results of the optimization of the signal rise speed are presented in Fig. 15.23, which shows the distributions in DT for all the ROCs at the beginning and at the end of the procedure. A value for the DT of 12  $V_{cal}$  was chosen as a target. The corresponding average current per ROC measured from the power supplies for each power group are also shown separately for layers 1 and 2 (Fig. 15.23(b)), and layer 3 ((Fig. 15.23(c))).

Figure 15.24 shows the final threshold and noise distributions for all pixels obtained after the procedure of minimization described in Section 15.3.2. The spread of the thresholds in each ROC is also shown, quantified by the RMS of the individual ROC distributions. A final average threshold of  $\approx 40$   $V_{cal}$  (2,200 electrons) was obtained showing agreement with the results of the tests performed in the clean room (Fig. 15.17) and with the Run 1 values (Fig. 15.3). Finally, the measured distributions of the gain and pedestal for each pixel used for the offline reconstruction of clusters are presented in Fig. 15.25. The distribution of the linearity parameter of the response curve as extracted from the fits is also shown.

## 15.5 Performance at the start of Run 2

The detector re-calibration discussed in the previous section has been crucial to ensure excellent performance during the start-up of data-taking in 2015. Figure 15.26 shows the average threshold, RMS and noise in units of 1 ke for each barrel pixel layer as a function

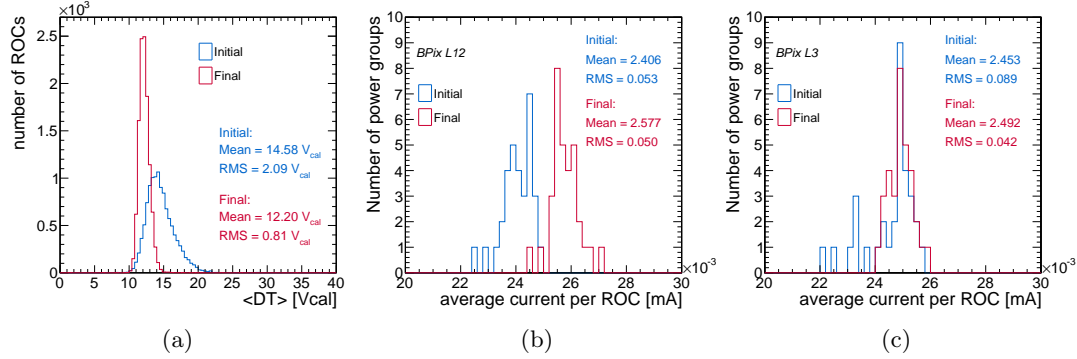


**Figure 15.23:** (a) Distributions in DT at the beginning and end of the optimization of the signal rise speed performed in 2015 for BPix Run 2 commissioning. (b-c) Corresponding average analog current after reaching the target DT value of 12 Vcal.

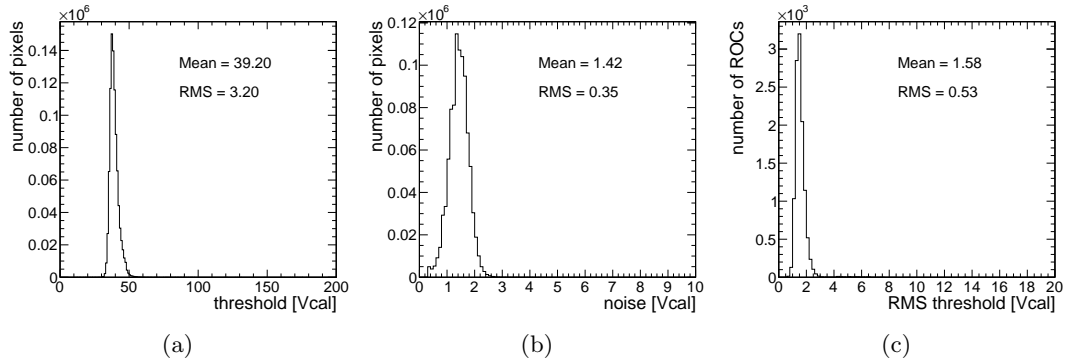


**Figure 15.24:** (a) Threshold and (b) noise distribution for pixels after the calibrations performed in 2015 for Run 2 commissioning. (c) The RMS of the threshold distributions within single ROCs quantifying its spread among cells. All distributions are in units of Vcal (1 Vcal = 65.5 electrons).

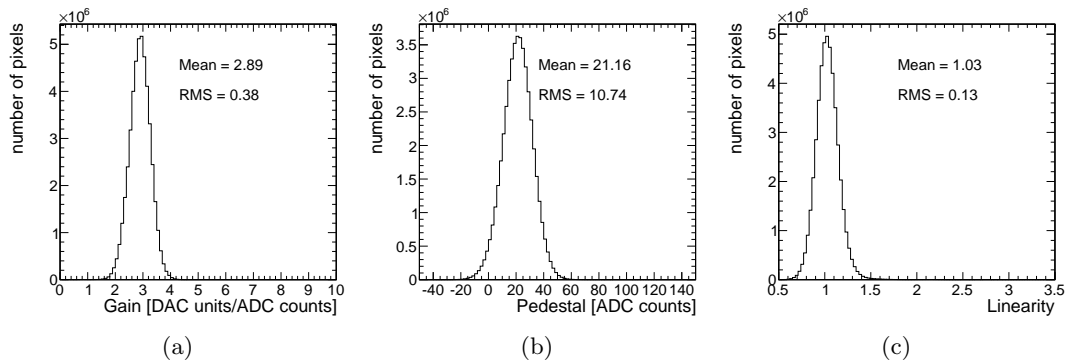


**Figure 15.25:** Gain (a) and pedestal (b) distributions extracted from the linear fits to the gain response curves of all pixels. These parameters are used for the offline reconstruction of clusters. (c) Distribution of the linearity parameter of the response curve as extracted from the fit.

of the integrated luminosity delivered in 2015. Due to the different levels of irradiation, the old and new modules have been monitored separately. The threshold of the new modules rapidly increased with irradiation as was observed also in Run 1 (Fig. 15.3). The noise quickly reached similar values as that of the old modules, which no longer experience such large changes due to irradiation.

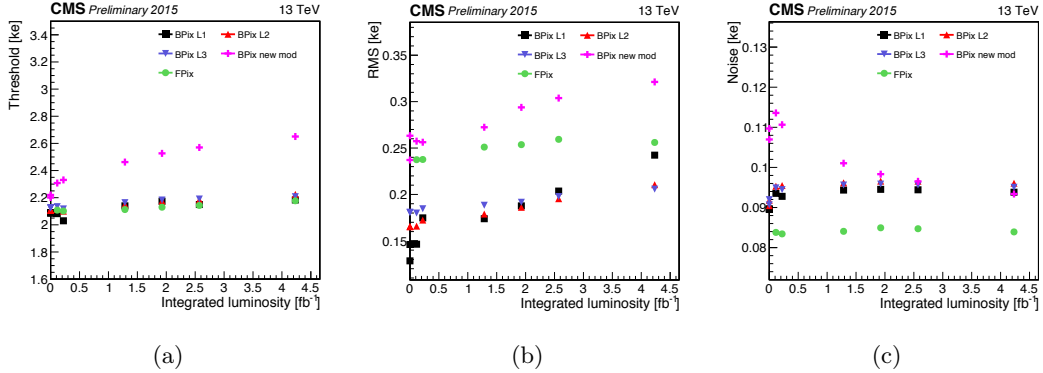


**Figure 15.26:** Average pixel thresholds (a), RMS (b), and noise (c) measured with charge injection, using the S-curve method. The BPix modules substituted during LS1 are considered separately [54].

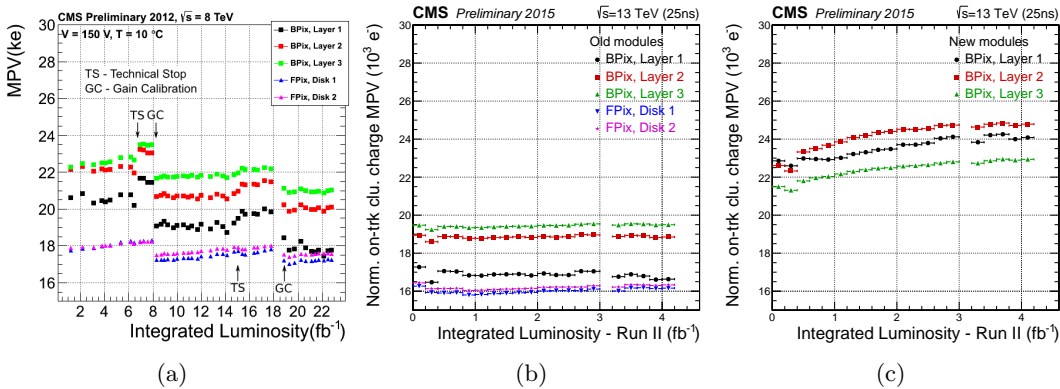


**Figure 15.27:** The MPV of the on-track cluster charge as a function of integrated luminosity (a) in 2012, and in 2015 separately for (b) old and (c) new modules [54].

Cluster properties like charge and size are important indicators of detector conditions and they have been monitored throughout the year by the pixel group. The cluster charge is determined by fitting the Landau distribution (Fig. 14.3) arising from the hits of tracks with  $p_T > 1 \text{ GeV}$  and extracting the MPV parameter. In the Run 1 measurements, the MPV changed significantly throughout the year and also after calibrations during technical stop periods (Fig. 15.27(a)). While the MPV of old modules did not change much in 2015 (Fig. 15.27(b)), the new modules showed a rapid increase (Fig. 15.27(c)). This behavior was also observed for old modules in Run 1 in the beginning of their lifetime. No significant change in the cluster size (Fig. 15.28) was observed.

Finally, the hit resolution has also been measured by the pixel group for layer 2 with tracks that have hits on layer 1 and layer 3. The tracks are re-fitted without the hit in the middle, and the residual between the original and the interpolated hit positions are measured.

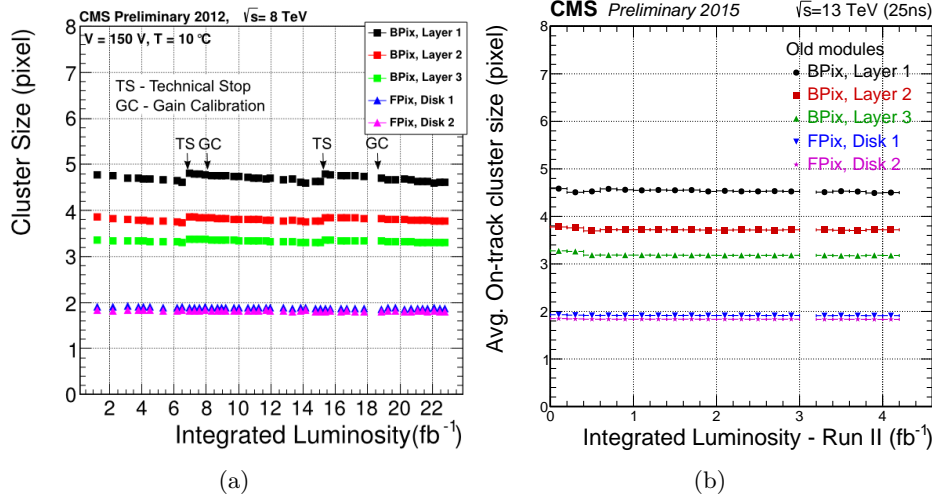


**Figure 15.28:** Average on-track cluster size as a function of integrated luminosity in (a) Run 1 and (b) Run 2. Both old and new modules showed very similar behavior [54].

The residual distribution is then fitted with a student-t function. Figure 15.29 shows the hit resolution as a function of the delivered luminosity in 2015. A large improvement was observed with respect to the measurements performed at the end of Run 1 (Fig. 15.4).

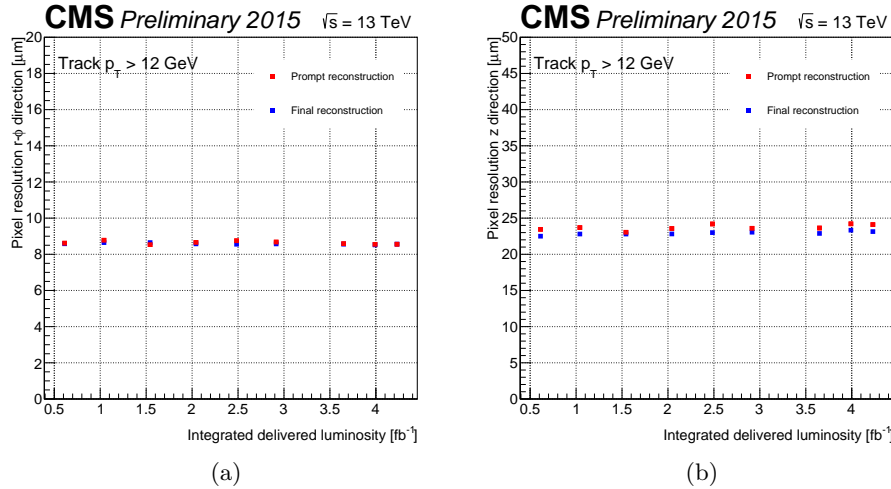


**Figure 15.29:** Hit resolution of barrel pixel modules in (a) the  $r\phi$  and (b) the beam direction as a function of integrated luminosity in 2015 [54].

# Phase I upgrade of the CMS pixel barrel detector

---

The present pixel detector will be replaced with a new pixel system in order to maintain the excellent tracking performance of CMS with the upcoming higher luminosity conditions at the LHC. This project is referred to as *Phase I pixel upgrade* [187]. The new upgrade detector comprises four barrel layers and three forward disks at each endcap to provide on average one more spatial point measurement per track compared to the present system, in the whole detector acceptance. It also provides improved track impact parameter resolution reducing the radius of the innermost layer and increasing radial acceptance. Further improvement is obtained thanks to optimized engineering of the mechanical design and services of the detector, that provide a substantial reduction of the passive material in the tracking volume despite the addition of one barrel layer. Since the innermost sensitive layer is closer to the interaction point compared to the present detector, faster front-end electronics have been developed to operate with high hit efficiency and low dead-time. In this chapter, the main features of the new barrel pixel system are introduced.

At the end of LS1 eight prototype Phase-1 pixel modules were installed in the CMS detector, on the third unpopulated forward disk. This so-called pilot system was commissioned and integrated into the central DAQ and control system with the aim of gaining operation experience under realistic conditions [188].

As for the present barrel pixel detector, the supply tubes have been assembled and tested at the University of Zurich, while the modules have been mounted on the detector mechanical structure at PSI. The integration of the supply tubes with the detector is currently ongoing and the installation into CMS and commissioning of the complete system is planned for March 2017.

Several procedures for testing the new system have been developed over the last three years, thanks to a test stand assembled at the University of Zurich. The test stand, described in this chapter, includes a slice of the CMS pixel data-acquisition system and all components of the upgrade readout chain, together with a number of detector modules. It allowed for detailed evaluation and verification of the components placed on the supply tubes before their integration. I have contributed to the assembly of the test system and I implemented some of its functionalities. Furthermore, I employed the system to test new calibration procedures that I developed to be included in the main pixel online software. The aim of the procedure is to guarantee a quick verification of the detector functionality during assembly and commissioning. This work, detailed in the following, has been crucial to gain experience with the new barrel pixel system and to acknowledge and implement several modifications to the pixel software to be able to operate with the detector.

## 16.1 Motivations

The proposed upgrade of the CMS pixel detector aims at maintaining the excellent performance of the present detector up to and beyond an instantaneous luminosity of  $2 \times 10^{34} \text{ cm}^{-2} \text{ s}^{-1}$  and a pileup of 50. The limitations of the present detector for increased luminosity and pileup can be seen in Fig. 16.1, which shows the hit efficiency for the various layers of the present pixel detector in collisions during 2016. The leading effect is a dynamic data loss in the readout chip which increases with instantaneous luminosity and trigger rate. This loss of data depends on both the occupancy and trigger rates and comes primarily from two sources, buffer size and readout speed. Between L1 triggers, pixel hits are stored in a finite sized buffer before being readout at the next L1 trigger. Therefore, if this buffer is full the ROC cannot record any more hits and subsequent hits are lost. Furthermore, when a L1 trigger initiates the readout, the involved double columns are blocked from having hits recorded and the buffer is cleared only after data have been sent. Thus, data can be lost if the readout is slow or the L1 trigger rate is very high. Simulation studies showed that for an instantaneous luminosity of  $2 \times 10^{34} \text{ cm}^{-2} \text{ s}^{-1}$  and a bunch crossing time of 25 ns (50 ns), the expected dynamic inefficiency for the present pixel detector increases up to 15% (50%) for ROCs in the first barrel layer. As a consequence, the track reconstruction efficiency is affected. This can be seen in Fig. 16.2, which shows the track reconstruction efficiency for muons coming from the Z boson decay as a function of the number of primary vertices, as measured in 2016 data with a T&P method. The efficiency is high and well described in the simulation, but slowly degrades as the number of pileup events increases. A new ROC for the upgrade pixel detector will largely reduce these effects.

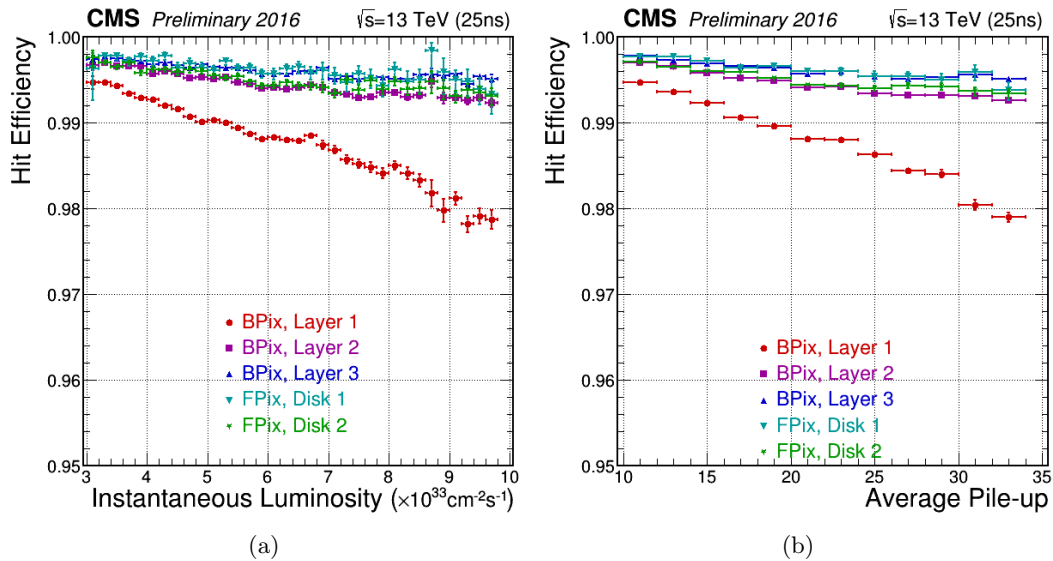


**Figure 16.1:** Hit efficiency for the various layers of the present pixel detector for 2016 collisions as a function of (a) the instantaneous luminosity and (b) the average number of inelastic pp collisions [54].

Further effects contributing to inefficiencies in the track reconstruction arise from failures in the tracking algorithms for events with a large number of hits. In fact, with more interactions per crossing giving rise to additional hits in the tracking detectors, the pattern recognition becomes more challenging. Under these conditions, the CPU time required for tracking largely

increases in both the HLT and offline processing. In addition, keeping the same level of tracking efficiency results in a higher level of fake tracks; alternatively, the tracking can be tuned for lower fake rate at the expense of reduced efficiency. In order to keep both the CPU time and fake rate under control for luminosities of  $2 \times 10^{34} \text{ cm}^{-2} \text{ s}^{-1}$ , the tracking has to be tuned to have generally lower efficiency than at lower luminosities. This is obtained requiring hits in 3 pixel barrel layers. With an extra pixel layer negative effects of pileup can be partly mitigated.

Degradation in the performance of the present detector are further due to radiation damage resulting in reduced charge collection and hence, in degradation of hit detection efficiency and resolution. Although the degradation can initially be mitigated mostly by increasing the voltage, and modification of the pixel cluster hit templates, eventually the reduced collected charge cannot be compensated. The hit efficiency is expected to be less affected but the reduced charge sharing and eventual breaking up of clusters will degrade the hit resolution. The upgrade pixel sensor would suffer similar radiation damage, however, such effects can be compensated by a much lower comparator threshold for the new readout chip. This improvement largely mitigates the effects of reduced collected charge, so degradation in hit resolution should be much reduced comparing to the same radiation fluence.

The passive material in the tracking volume is known to lead to tracking inefficiencies. In particular, a significant portion of material is present in the region near  $|\eta| = 1.5$  where the end flange with services from BPix meets the FPix. This material also contributes to additional challenges for track pattern recognition in a high-pileup environment. The upgrade pixel detector, even with an extra layer features less passive material in the tracking volume, due to a new lightweight construction, cooling, and relocation of passive material out of the tracking region.

Details on the new detector layout and front-end electronics are given in the next chapter.

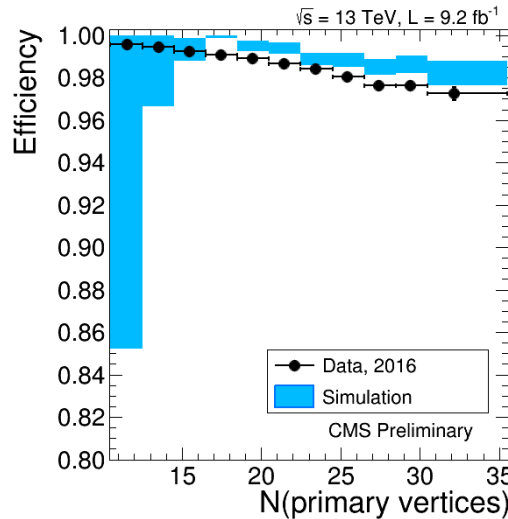


**Figure 16.2:** Track reconstruction efficiency for 2016 data and simulation for muons coming from the Z decay as a function of the number of primary vertices [89].

## 16.2 Detector layout

The proposed upgrade pixel detector consists of four barrel layers and three disks on either side of the interaction point. The layouts of the present and upgrade pixel systems are compared in Fig. 16.3. The barrel layers have a length of 548.8 mm and are placed at radii of 30, 68, 109, and 160 mm. Compared to the present BPix, there is one new layer at high radius. The radius of the innermost layer is reduced by 10 mm while layers 2 and 3 are almost unchanged.

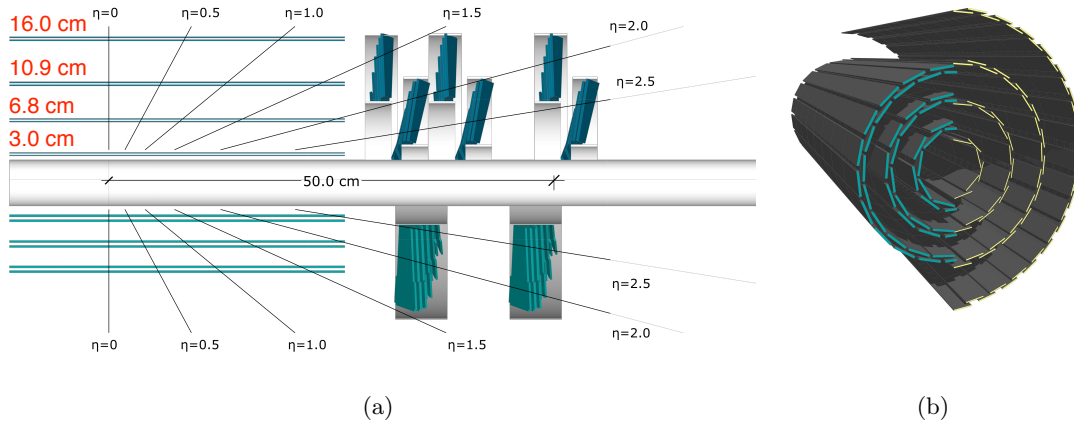


**Figure 16.3:** (a) Layout of the proposed upgrade pixel detector compared to the present detector in longitudinal view. (b) Three-dimensional view of the upgrade and present BPix detectors.

The total number of BPix modules will increase to 1,184 compared to 768 modules in the present detector, with an increase in the number of pixel channels from 48 million to 79 million. The modules are mounted on lightweight mechanical structures built from carbon fiber. The design and composition of the modules are similar in the whole pixel detector, except for the innermost layer where a considerable higher data rate is expected. Furthermore, half modules are no longer used to join the two halves, whereas a slightly more complex design of the mechanical support structure enables the use of full modules throughout. The pixel detector modules will be described in more details in the next section.

The cooling pipe diameter is significantly reduced with respect to the present detector thanks to the usage of a two-phase CO<sub>2</sub> cooling system, which requires a much smaller mass flow than C<sub>6</sub>F<sub>14</sub>. This reduces substantially the amount of material in the tracking region. A further, significant reduction is achieved by moving the module connector area from the detector end flange to higher  $z$ , outside of the tracker acceptance, by using longer and more flexible module cables. As a replacement, micro twisted pair cables made of copper and with a diameter of only 127  $\mu\text{m}$  are used. Multiple twisted pairs are used to transmit the different signals, including clock and trigger, I<sup>2</sup>C and data signals. Power is transmitted in parallel through multiple copper cladded aluminium wires with a diameter of 90  $\mu\text{m}$ . Signal and power cables are braided into a single strand. Module cables have lengths between 95 and 110 cm depending on the position. Each wire of the strand is soldered onto a custom made board that fits into a commercial connector. The connector on the module side is soldered to the HDI. The obtained reduction in the material budget can be seen in Fig. 16.4, which shows a comparison of the radiation length and nuclear interaction length of the present and upgrade pixel detectors as a function of  $\eta$ .

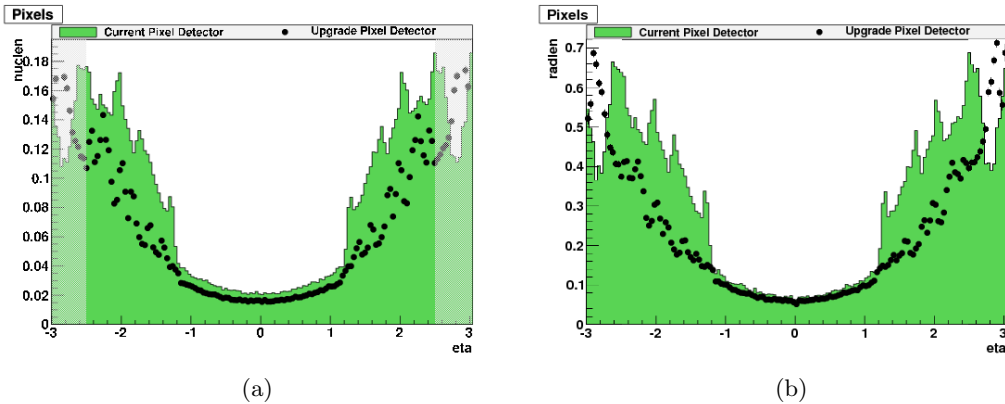


**Figure 16.4:** Material budget in the pixel detector shown in units of radiation length (a), and in units of nuclear interaction length (b) as a function of  $\eta$ ; this is given for the present (green histogram) and upgrade (black points) pixel detector. The shaded region at high  $\eta$  is outside the region for track reconstruction [187].

The overall layout of the system is unchanged. The detector barrel is complemented with four supply tubes on the  $+z$  and  $-z$  sides. The supply tubes carry electrical connections and cooling lines from the patch panels to the barrel detector, and house auxiliary front-end electronics. The upgrade system has to fit in the same mechanical envelope as the present system and reuse existing services, power cables and optical fibers. This puts strong constraints on the design of the new system. In particular, higher bandwidth electronics is need. Since the upgrade detector has 1.9 times more channels than the present detector, the power consumption increases accordingly. The upgrade system uses DC-DC power converters [189] to supply the necessary current to the modules while reusing the existing infrastructure.

### 16.3 Pixel modules

The pixel modules for the upgrade are of similar design compared to the ones employed in the present detector. The main changes concern the design of the ROCs and the TBMs, as described in the following. Figure 16.5 shows a drawing of the pixel module employed for the outer barrel layers. The innermost barrel layer features a different ROC that allows to cope with even more extreme conditions at such small radii, while its modules differ mostly by the way they are mounted and by the cables used. Furthermore, they feature two TBMs mounted on the HDI. From top to bottom, the figure shows the cables with a connector print, the HDI with the TBM mounted in the center, the silicon pixel sensor,  $2 \times 8$  ROCs and base strips for mounting.

The sensor used in the upgrade is built with the same technology as the one used in the present detector. For the innermost layer, where the close proximity to the interaction point leads to the highest radiation damage, the sensor is expected to operate up to an integrated luminosity of  $250 \text{ fb}^{-1}$ . For this reason it is planned to exchange this layer once during the detector's expected lifetime of  $500 \text{ fb}^{-1}$ . The sensors in the rest of the detector can sustain the entire duration because of the greater distance from the interaction point.

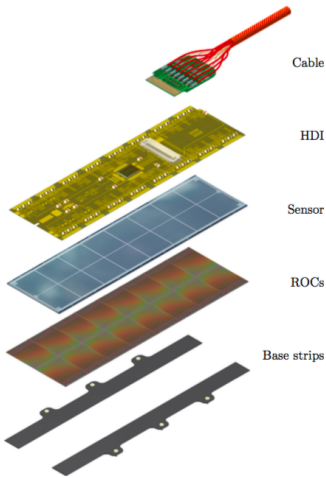


**Figure 16.5:** Exploded view of the new pixel module employed for the outer barrel layers of the upgrade BPix detector.

### 16.3.1 The digital ROC

The ROC for the upgrade detector [190] is not a completely new development but rather an evolution of the well-proven ROC operating in CMS since its commissioning. It is designed in the same 250 nm CMOS technology and the well-understood core of its double-column architecture is mostly unaltered. However, to cope with the higher data bandwidth the readout protocol has been changed from a 40 MHz analog to a 160 MBit/s digital readout. An ADC digitizes the analog pulse height information in the ROC periphery. The key additional elements are an 8-bit successive approximation current ADC running at 80 MHz with a programmable range, and a PLL which generates the 160 and 80 MHz clocks for the serial readout links and the ADC, respectively, from the 40 MHz LHC master clock. To reduce data losses, the number of hit buffer cells in each double column has been increased from 32 to 80 and the time stamp buffers have been increased from 12 to 24. To limit the increase of the area used by the buffers the layout has been entirely redesigned. An additional readout buffer stage has been introduced in the ROC periphery to reduce dead time during the column readout: the data is transferred (after being digitized) into the new readout buffer immediately after the trigger arrives so that the double columns are again operative. Improved performance of the analog amplifier and the discriminator in the pixel unit cell allow for operations at lower threshold, which is reduced from about 3,500 electrons in the present detector to under 2,000 electrons after the upgrade. This guarantees higher radiation tolerance and therefore, a longer lifetime of the detector.

The chip just described is suitable for the whole upgrade pixel detector except for the innermost barrel layer, where the data rates up to  $600 \text{ MHz/cm}^2$  are expected, four times higher compared to the second layer. In order to cope with such extreme conditions the newly developed PROC600 [191] readout chip is used in the innermost layer. The new chip features a new 40 MHz dynamic cluster column drain mechanism based on dynamic cluster ( $2 \times 2$  pixels) finding in the double column.

### 16.3.2 The TBM and readout

In contrast to the present detector, for the upgrade all barrel modules use at least two data channels in order to improve the bandwidth of the readout. Because of the limited number of

fibers available for this purpose, two channels are always multiplexed into one data stream through a Data-Keeper multiplexer and encoder. For this purpose few modifications have been applied to the TBM. In particular, it now combines the digital 160 Mbit/s readout from the ROCs from two buses into a 320 Mbit/s signal to which it then applies 4-to-5 bit encoding. This results in a 400 Mbit/s data stream. The readout scheme is adapted to the different barrel layers (Fig. 16.6). Layers 3 and 4 employ a dual core TBM, referred to as TBM08, that passes two tokens simultaneously to achieve the parallel readout of two groups of 8 ROCs, called Port 0 (or Channel  $\alpha$ ) and Port 1 (or Channel  $\beta$ ). The data are then combined into one data stream as described above, readout over a single optical fiber. Except for the multiplexing step, this is very similar to the method used for the first two layers of the present detector (Section 14.2.3). Layer 2 employs a different TBM, called TBM09. For the readout this TBM behaves as two TBM08s (TBM A and TBM B in Fig. 16.6), each equipped with its own Data-Keeper. This TBM is capable of issuing four tokens simultaneously, so that the 16 ROCs are therefore divided into four groups that are readout in parallel. The two Data-Keepers then produce one 400 Mbit/s data stream each and two fibers are required for the readout. For the modules of the innermost layer, the TBM10 is used, which consists of two identical TBM09 chips identified by two different HUB addresses. In this case eight tokens are passed in parallel on these modules, resulting in four 400 Mbit/s data streams and hence, four fibers for transmission.

An extensive set of control registers have been built into the TBM, which allow various functions and operating modes of the TBM to be controlled by issuing commands to the TBM through the communication control HUB. For the TBM09 the commands have to be issued to both TBM08s controlled by one unique HUB.

As for the present detector, the module output signal is characterized by TBM header and trailer, ROC headers and pixel hit information, which are now encoded in binary data as shown in Fig. 16.7. A TBM readout begins by transmitting a twelve clock cycle (160 MHz) header sequence. The next sixteen clock cycles of the header are used to transmit the 8-bit event counter, 2 bits of error information, and 8 bits encoding the data contained in the last 8-bit TBM register accessed. Coincident with the next to last clock cycle, the token is transmitted to the ROCs. The TBM now goes into standby mode, waiting for the last ROC in the chain to return the token to the TBM. At this stage, the TBM transmits a twelve clock cycle trailer sequence. The next sixteen clock cycles of the trailer include 10 bits with the values programmed in the TBM registers that control its mode of operations, and a 6-bit stack count value. The counting is used to monitor the timeout on the token returning. If the token fails to return, before the timer expires, the TBM will automatically issue a ROC reset, ending the token pass. The data contained in the ROCs are deleted, and error bits are returned in the TBM trailer 8 clock cycles later. The ROC data consist of 12 bits for the header, 16 bits used for the pixel hit address and the final 8 bits for the pulse height.

In order to readout the new fully digital pixel system a VME-digital FED has been firstly designed. It is a hybrid solution featuring new daughter boards on the existing FED, and it has been used at the beginning of the operations with the pilot system and with test stands. This solution will be replaced by a  $\mu$ TCA system with high-speed signal links providing data rates up to 10 Gbits/sec. Since the results presented in this work are based on the VME system, only this is described in the following.

The ADC daughter boards of the analog FED are not needed anymore for digital transmission. For the purpose of system developments, a special add-on board was produced, which is mounted on the current VME module for data readout, receives the 400 Mbit/s digitized data, and passes the data to the FPGAs in the same format as the present system.

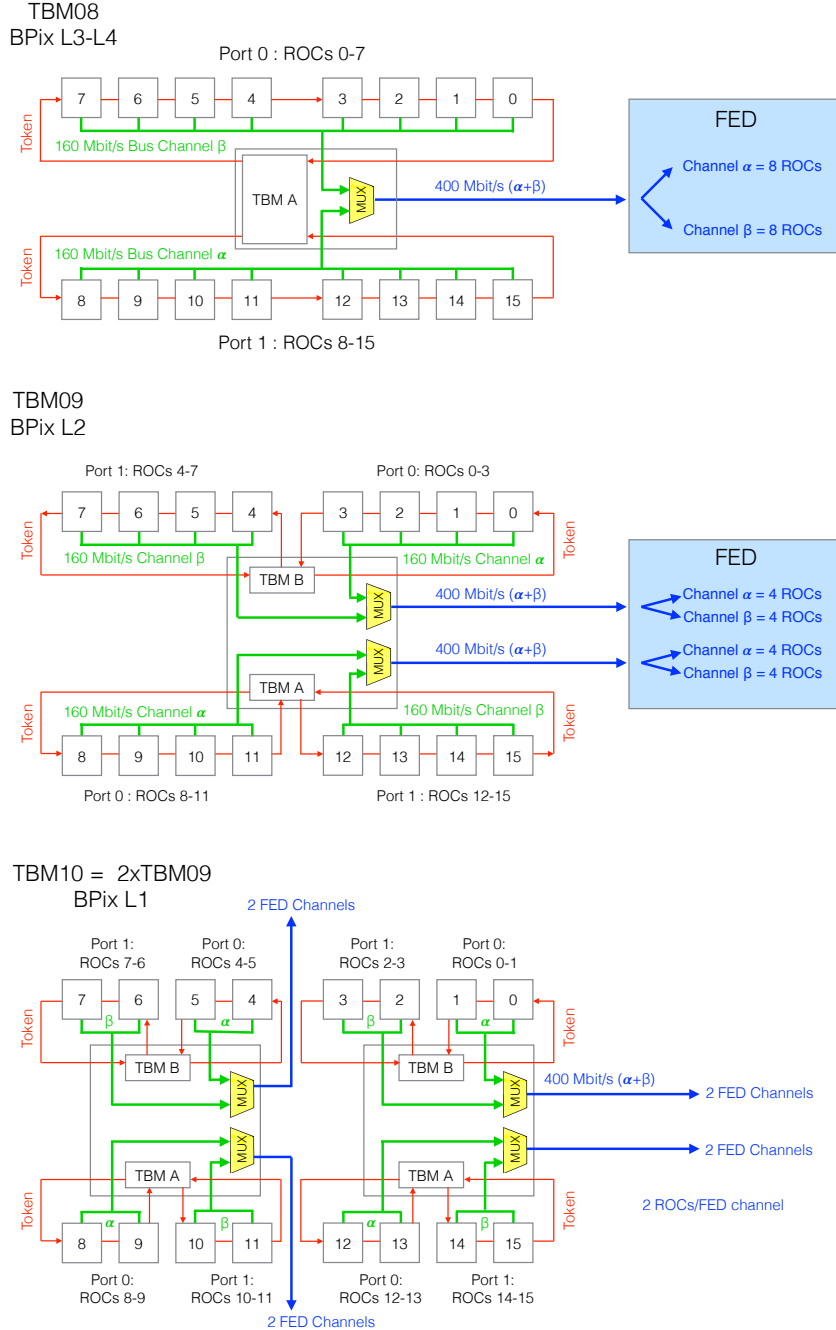


**Figure 16.6:** Readout scheme of the different TBMs used in the BPix layers.

Thanks to this modular approach, the other parts of the FED did not require any hardware modification, allowing for a quick start of the tests with the new upgrade pixel system.

As shown in Fig. 16.6, the signal from each fiber is split at the FED into two channels, whose content is buffered and processed in the FIFOs. Each channel will then correspond to the data from half of the initial number of ROCs originally present in one fiber.

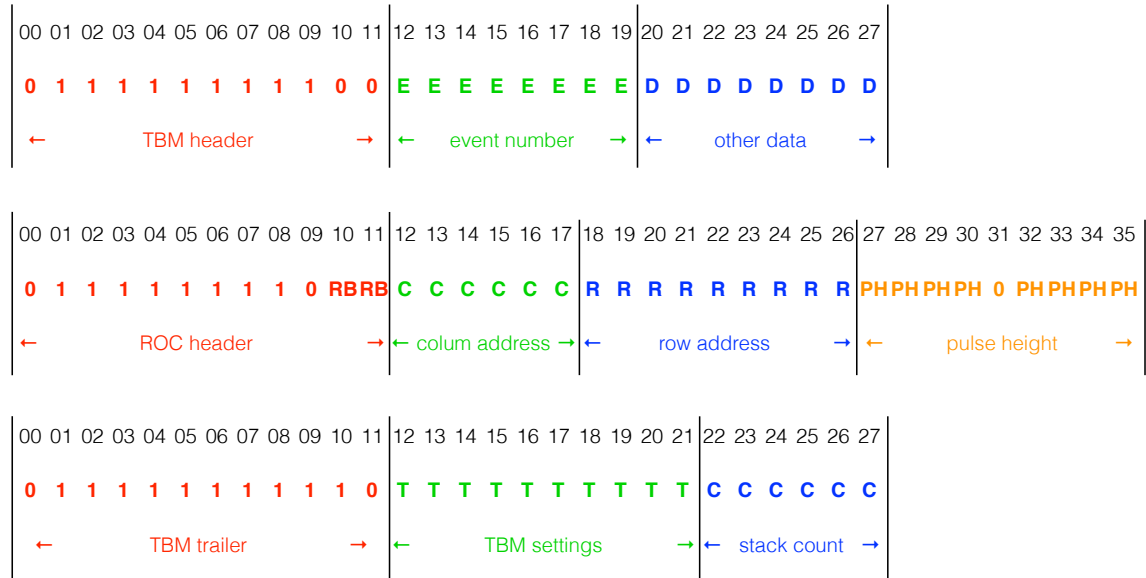


**Figure 16.7:** Decoding of the module digital output data.

## 16.4 Supply tubes

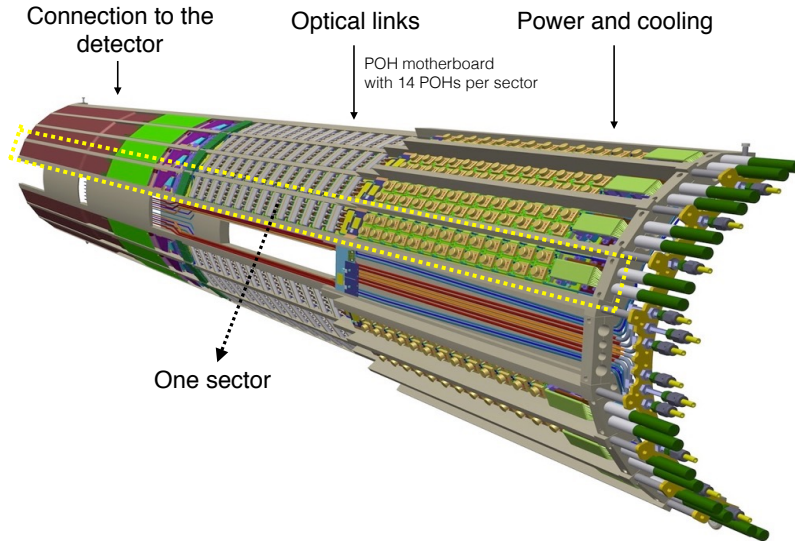


**Figure 16.8:** Layout of one of the four supply tubes for BPix equipped with the new electronic components. Each supply tube is divided into 8 sectors.

As for the present detector, the power, readout and control circuits, as well as the cooling lines are housed by four half-cylinder supply tubes. Figure 16.8 shows the layout of one supply tube together with some of the new electronic components. The mechanical structure of the supply tubes is made from layers of carbon fiber foam. Each supply tube is divided

into 8 sectors, which hold the electronics for one readout group of detector modules.

Each sector includes DOHs as well as the auxiliary chips (PLL, Delay25, Gate-Keeper) for the transmission of control, clock and trigger signals. The change from analog to digital module readout in the upgrade system also requires the adoption of new optical links. So-called pixel opto-hybrids (POHs) [192] are used for the transmission of the module readout data as a replacement of the AOHs used for the present detector. The POHs are built from four transmitter optical subassemblies (TOSA), linear laser-driver and level-translator chips and have been designed specifically for their use in the pixel upgrade system. All other components used in the control and readout chain are identical to the ones used in the present system. CCU chips are used for slow control, monitoring and timing distribution. Furthermore, pairs of DC-DC converters are mounted on the service cylinders. Each sector consists of a stack of boards, DC-DC converters, optical links and cooling loops, resulting in tight space constraints and a non-trivial assembly procedure.

The complete supply tube system has been integrated and tested sector by sector at the University of Zurich. A picture of one supply tube after integrating all its components are shown in Fig. 16.9.

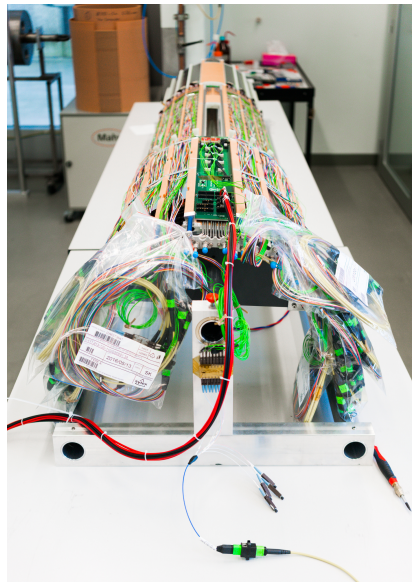
## 16.5 The test stand

In order to test the performance of the complete upgrade pixel system and gain experience in its operations, a test stand for BPix has been set up at the University of Zurich in 2014. The setup includes a slice of the full CMS pixel DAQ system together with prototypes of all components of the upgrade power system, control and readout chain as well as a number of detector modules. The system test was operated at UZH until November 2016 when the integration of the supply tubes started. Its main goals include:

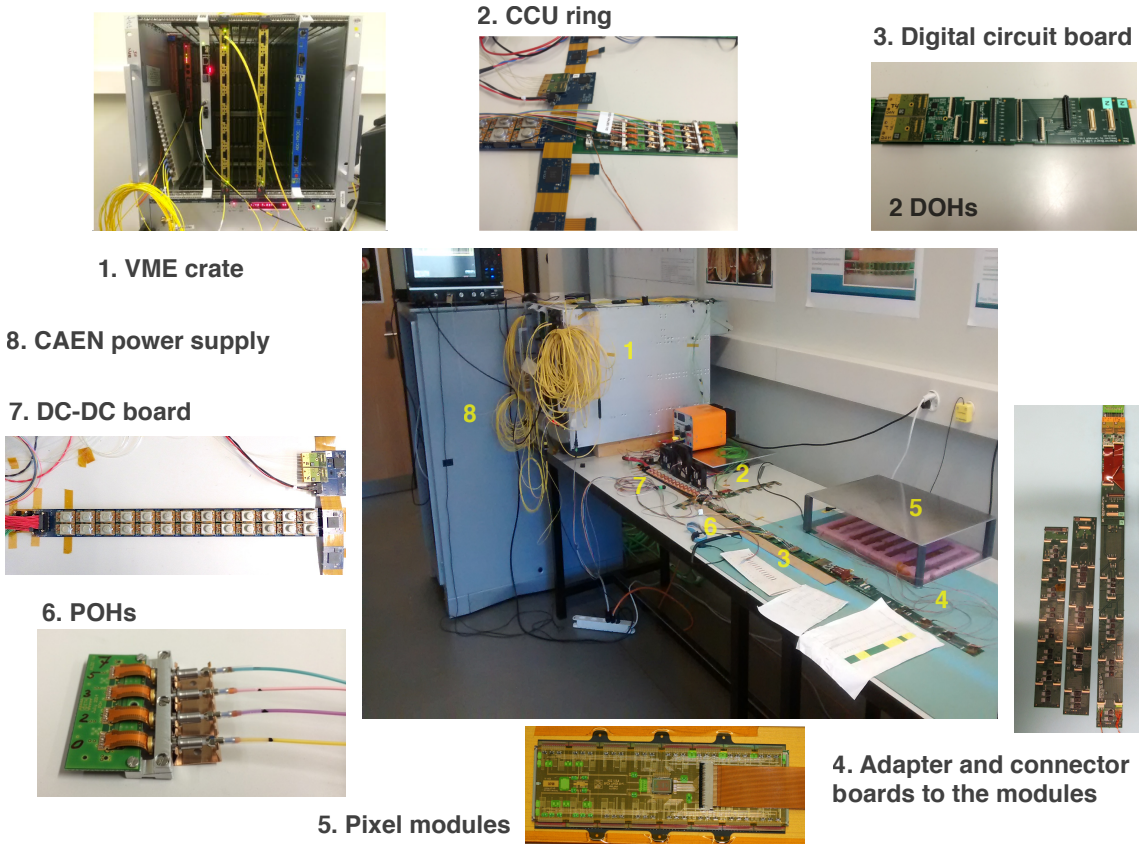
- evaluate all components of the detector system prior to full production;
- establish test and calibration procedures for the assembly and commissioning (Section 16.6);
- exercise the transition from the VME- to the  $\mu$ TCA-based DAQ system.

Figure 16.10 shows a picture of the test stand, which consists of several sensor modules, electronics for their operation, a CAEN power supply and a VME back-end system to control and readout the modules. The test stand is also equipped with a linux PC connected to the VME and used to run and control the system through the installed XDAQ applications.

Most of the tests that have been conducted with this system make use of a standalone software based on the socket technology provided by the PYTHON framework, which allows for a direct communication with the hardware. These tools have been firstly developed for the testing of the present pixel detector prior to assembly [193], and necessitated many fundamental changes to be able to operate with the upgrade system. I implemented part



**Figure 16.9:** Picture of one of the four supply tubes with all its components assembled at the University of Zurich.



**Figure 16.10:** Test stand setup at UZH including all components of one BPix sector together with a few pixel modules. The CAEN power supply and the VME back-end system are also indicated.

of this transition and I was able to perform the first tests with the POHs. In the example shown in Fig. 16.11, the POH laser bias setting is varied from 0 to 40 and for each value the ADC counts (or optical power) at the VME-analog FED are checked. This scan is performed for different values of POH laser gain setting. The optical power sharply increases until the saturation of the receiver at the FED is reached. This test ensures the slow I<sup>2</sup>C communication with the auxiliary electronic components of the system. Other tests have been performed after pixel modules have been added to the system and aimed at establishing the functionality of the fast I<sup>2</sup>C communication to/from the TBM. This was checked by verifying for instance the presence of the TBM signal at the corresponding POH output through an optical probe plugged into the oscilloscope. If the fast I<sup>2</sup>C communication through the digital circuit is functional, the TBM sends the 400 Mbit/s data stream upon the arrival of a trigger as shown in Fig. 16.12.

This kind of tests is not suitable when dealing with a large number of channels. For detector assembly and commissioning the full functionality of each module has to be checked and calibrations have to be performed over the whole detector. In order to achieve this in a reasonable amount of time, the full pixel online software (Section 14.4) has to be used and upgraded to be able to operate with the new system. Many fundamental changes to the software have been firstly applied for the pilot system, as well as for operations with the FPix test stand at CERN. These changes mainly concerned the `FEDIInterface` class, where the new features of the digital VME-FED had to be implemented. In order to test and

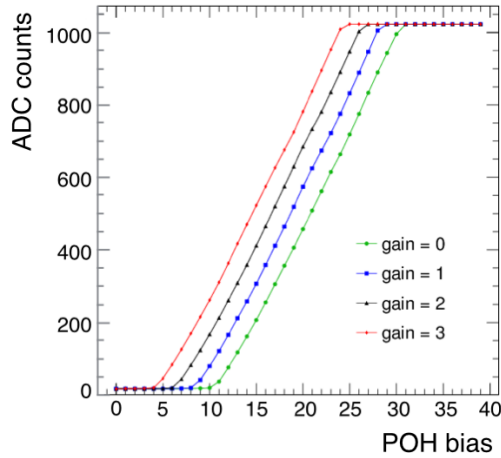


**Figure 16.11:** Typical result of the scan of a POH laser bias and gain. For each value of the laser settings, the optical power is readout at the VME-analog FED.

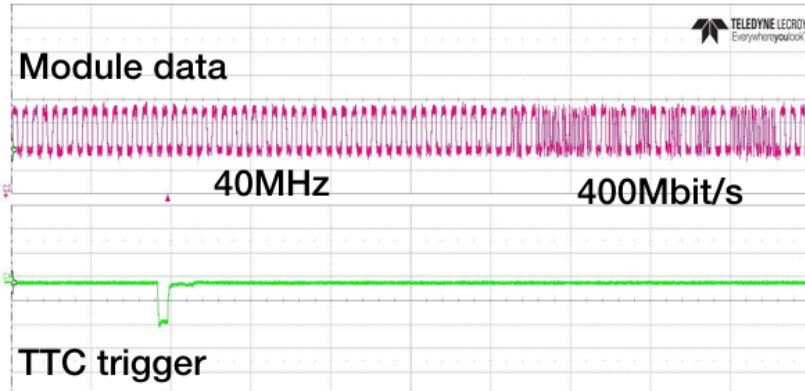


**Figure 16.12:** Module output signal initialized by a trigger sent by the TTC. The signal is acquired at the oscilloscope with an optical probe connected to the POH laser output. The 400 Mbit/s signal contains TBM trailer and header, and the headers from 8 ROCs.

debug the new developments I installed POS and applied the modifications required to run it with the system test at UZH. After establishing the basic functionalities, I developed new calibrations for the upgrade detector as described in the next section. This work represents the first attempt to operate the upgrade BPix system with POS and hence, has been crucial to understand, implement and test new BPix specific developments.

In mid-2016 a separate table has been setup in the same laboratory to operate the upgrade electronics with the  $\mu$ TCA DAQ system as this became available only at a later time. A new  $\mu$ TCA version of POS was developed in the meantime by the FPix group, and the second test stand has been very useful to gain expertise with the new developments. Several of the new features for the upgrade system that I included in the VME-POS have been easily exported to the  $\mu$ TCA-POS. The transition has been straightforward since I developed the new code such that it is transparent with respect to the parts of the software handling the  $\mu$ TCA or VME communication.

## 16.6 Testing and calibration

Since the upgrade system features a new digital readout, some of the steps in the calibration procedures developed for the present detector become obsolete, whereas new kind of tests are needed. In particular, the adjustment of the FED receiver offset, of the UB and address levels are dropped for obvious reasons. In this section, a calibration procedure for the Phase-1 detector is described with main focus on the new developments. This procedure is suitable for testing each sector of the detector after assembly at PSI as well as for the commissioning of the whole detector at CERN. It is implemented in several steps, each aimed at testing one particular functionality. Each step produces new detector settings, such as POH bias and gain or TBM and ROC DACs, after a dedicated scan of a set of parameters. The procedure has been fully tested with the table top system at UZH and few pixel modules, and results will be presented and discussed in the following. Only modules equipped with TBM08 and TBM09 have been used for these tests, since the TBM10 was not available at the time of this work. The TBM10 features slightly different readout and programming mechanisms, and additional modifications to the software are required. Further improvements to this preliminary version of the procedure have been implemented later on by the BPix group in order to have a finalized version for detector commissioning that also includes specific developments to operate with the TBM10.

### 16.6.1 Delay adjustments

The synchronization between the 160 Mbit/s ROC data and the 400 Mbit/s final output data stream has to be adjusted in order to be able to correctly readout the module output signal. The data alignment can be adjusted by programming two 8-bit registers internal to the TBM. The first register controls the phases of the 160 MHz and 400 MHz PLLs integrated in the TBM. For the TBM09 only one of the two cores (TBM A and TBM B in Fig. 16.6) has to be programmed since the PLLs are common to both. The second register controls the delay in the data stream of the two readout groups of ROCs (Port 0 and Port 1 in Fig. 16.6), and for TBM09 it has to be programmed for each core. All the above timing settings can be varied in the range 0–7 ns in steps of 1 ns so that 3 bits are sufficient for each of them.

After configuring the settings of the Delay25 chip to ensure communication between the pxFEC and the modules, the first step is to perform a scan of the TBM PLL phases. For each set of values the digital data are readout at the FED, and it is checked that the TBM had sent header and trailer. This is done for a number of triggers defined by the user and for each FED channel corresponding to the same module (Fig. 16.6). The TBM header and trailer are only available in the FIFO1, which can be accessed only if the normal data flow to the other FIFOs is interrupted. This is achieved by programming a FED register. An example of such scan for one module is shown in Fig. 16.13(a), where the efficiency for TBM header and trailer to be recorded is measured as a function of the two phases. The efficiency is averaged over all the FED channels. At the end of the test new settings for the TBM are produced, corresponding to a pair of phase values corresponding to 100% efficiency. Since there might be more than one bin corresponding to 100% efficiency only the first one is chosen. However, this algorithm can be improved by picking a bin from a region that presents small variations. If no 100% efficiency bins are found, the bin corresponding to the maximum is picked and a error flag is saved in the output file. The histogram with the resulting scan is also saved for each module. This test ensures that the TBM settings are correct to be able to read out the signal. It is also very useful to have a feedback on the status of the detector, for instance after installation, similarly to the FED baseline calibration for the present detector (Fig. 15.9). In fact, with this test it is verified that clock, trigger

and programming signals are correctly arriving at the pixel modules and that the TBM can be programmed. In addition, low efficiency might indicate poor optical connections and the problem can be immediately solved by cleaning the fibers. Issues in the mapping between modules and FED channels, as well as possible broken channels, can also be identified at this stage.

The second step consists of scanning the ROC delays, and for each set of values it is checked that each ROC had sent the header. As for the scan of the TBM PLL phases, this is done for a number of triggers defined by the user, and the efficiency is measured for each ROC. For the TBM09 the same value is programmed for the two cores. A histogram is produced with the efficiency averaged over all ROCs and FED channels for each pair of delay values, as shown in Fig. 16.13(b). New settings for the TBM are also produced, corresponding to the delay values giving 16 ROC headers recorded at the FED. The choice of the best settings follows the same strategy described above for the TBM PLL phases. This test ensures that the TBM settings are correct to be able to read out the signal and it also verifies the functionality of the token passage.

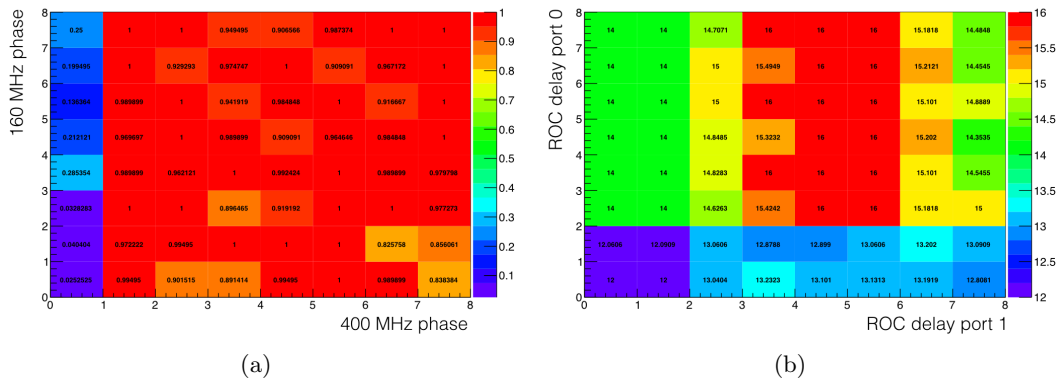


**Figure 16.13:** (a) Example of scan of the TBM PLL phases for one module. For each pair of values the module signal is read out several times at the digital FED, and the presence of TBM header and trailer is verified. An efficiency is obtained by dividing by the number of times the signal has been read out. (b) Example of scan of the delays in the data from the two ROC readout groups. For each pair of values the presence of each ROC header in the readout data at the digital FED is verified. The average number of ROCs that sent the header is obtained by dividing by the number of times the signal has been read out.

### 16.6.2 POH bias and gain

The tests described in the previous section assume that the POH laser settings are good enough to allow for a correct readout of the signal. In fact, a too low laser bias and gain result in a small difference between the 0 and 1 levels of the digital signal and consequently to a large error bit rate. It has been found with the test stand that a bias of 40 and a gain of 3 are sufficient to be able to correctly read out the signal so that the tests of the previous section can be safely run with such values. However, once the functionality of the TBM has been verified a scan of the POH setting should be run to obtain a finer adjustment aimed at minimizing the power consumption. An approximate indication of the error bit rate can be obtained by measuring the known TBM signal. In this calibration, a scan of the POH bias and gain is performed, and for each value it is checked that the TBM had sent header and

trailer. An example of such scan is shown in Fig. 16.14. At the end of the calibration new settings are produced corresponding to a safe area, i.e. 5 units above the beginning of the saturation.

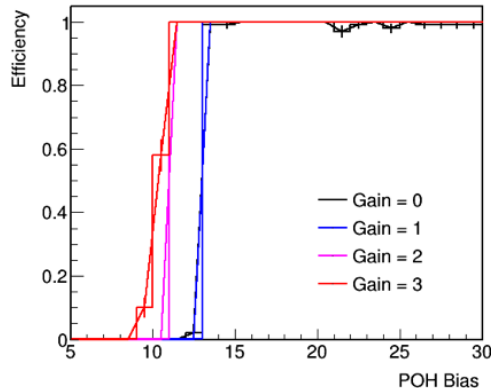


**Figure 16.14:** Example of scan of a POH laser bias and gain. For each value of the laser settings the module signal is read out several times at the digital FED and the presence of TBM header and trailer is verified.

### 16.6.3 Read back test

As discussed in Section 16.3.2, the ROC header is followed by 3 bits where the first one is always a 0, and the other two contain one bit for a start signal and one bit for the so called read back data as explained in the following. The read back data contain different information depending on the value programmed in the ROC read back register. For instance, for a value of 12 the ROC analog current is returned. It has been found after several tests that not all delay settings allow for a correct read out of the information contained in the ROC read back data. Hence, another scan of the TBM PLL phases and ROC delays is performed and for each value the information in the read back data is verified as explained in the following.

The read back word is encoded in sixteen bits (Table 16.1), which cannot be sent at once given the limited size of the ROC data stream. As mentioned above, every time the readout is initialized by a trigger, one bit is sent for the message data and another one is sent to indicate the start of the word. Thus, sixteen triggers have to be sent before the entire word can be decoded. Of the sixteen bits collected, the first eight bits are used for the required information (for instance the analog current), four bits contain the value written to the read back register (for instance 12 for the analog current), and the last four bits encode the ROC I<sup>2</sup>C address (from 0 to 15).

In order to ensure that the TBM settings chosen by the previous algorithms allow for a correct read back, a scan is performed over the TBM PLL phases and ROC delays, and for each value it is checked that the ROC address in the read back word is the expected one. This is indeed known from the mapping of FED channels and ROCs specified in the detector configuration database. At the end of the scan, it is verified that the current settings from previous calibrations give a correct read back of the ROC address for each ROC, otherwise new settings are produced. Examples of such scans are shown in Fig. 16.15. In order to acquire statistics the 16-bit word is read several times. The algorithm to chose the optimal phases or delays is the same as for the tests described in Section 16.6.1.

**Table 16.1:** Mechanism used by the ROC to send read back data. Sixteen triggers are needed to read out the full 16-bit word. One bit is used to indicate the start of the message. In this example, the ROC 2 is read out, and the value written in the read back register is 12, which allows for the readout of the analog current. The latter is equal to 88 ADC counts.

Trigger #	1	2	3	4	5	6	7	8	9	10	11	12	13	14	15	16
Message start	0	0	0	0	0	0	0	0	0	0	0	0	0	0	0	1
Message data	0	0	1	0	1	1	0	0	0	1	0	1	1	0	0	0
Comment	ROC I <sup>2</sup> C address				last value written to the read back register				Analog current							

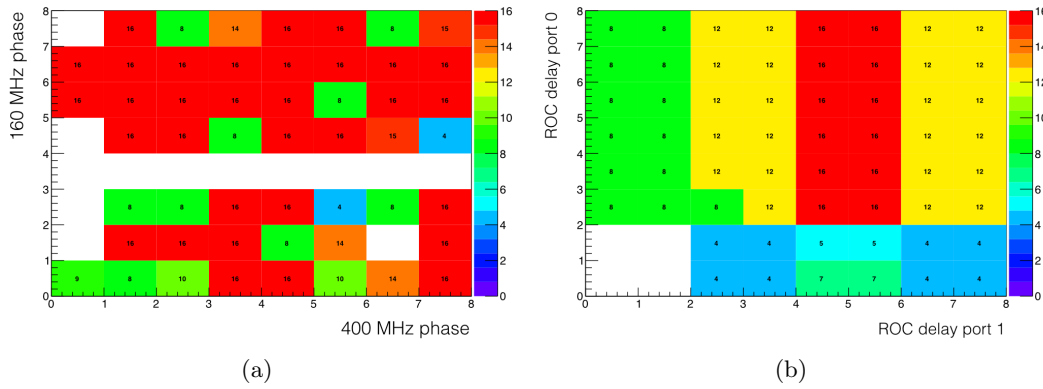


**Figure 16.15:** (a) Example of scan of the TBM PLL phases (a) and ROC delays (b) for one module. For each pair of values it is verified that the message data obtained with the read back mechanism contain the expected ROC I<sup>2</sup>C address. If the timing is correct, 16 ROCs per module have to be correctly identified.

#### 16.6.4 ROC analog current and digital voltage

The read back mechanism described in the previous section allows to access the ROC analog current information ( $I_{ana}$ ). For the present detector it is possible to access only the total current of a large number of ROCs provided by a reading of the power supply, so that only an average value per ROC can be obtained. As discussed in Chapter 15, the analog current increases with irradiation and a re-calibration of the ROC analog voltage setting  $V_{ana}$  is necessary to bring back the current in the safe range and recover the optimal ROC performance (Fig. 15.3(b)). The  $V_{ana}$  calibration for each ROC is a time consuming procedure that converges after a large number of iterations of the S-curve test, which provides measurements of the threshold every time the settings are changed (Section 15.3.2). A much more simple procedure has been developed for the upgrade ROCs, since the measurement of the analog current is directly provided in the read back data. The value is returned in ADC units and a conversion curve measured for each ROC during module testing is applied to obtain the corresponding value in mA. The curve is of the form

$$I_{ana}(\text{ADC}) = a + b \times I_{ana}(\text{mA}) + c \times I_{ana}^2(\text{mA}), \quad (16.1)$$

and its parameters are saved for each ROC in the detector configuration database. As shown in Fig. 16.16, for each value of the  $V_{ana}$  setting the analog current is read out from the ROC read back bits, and the conversion curve above applied to the original value in ADC.

At the end of the scan, a  $V_{ana}$  setting corresponding to the target  $I_{ana}$  value of 25 mA is chosen.

The same calibration code can be also configured to perform a measurement of the digital voltage  $V_d$  for each ROC. This parameter is controlled by a corresponding DAC and it is useful to monitor it as well during operations. Its value can be returned by using the same read back mechanism but by changing the value written in the read back register. As for the analog current, a ADC/mV conversion curve has been measured for each ROC during module testing and it is applied in the final result of this measurement.

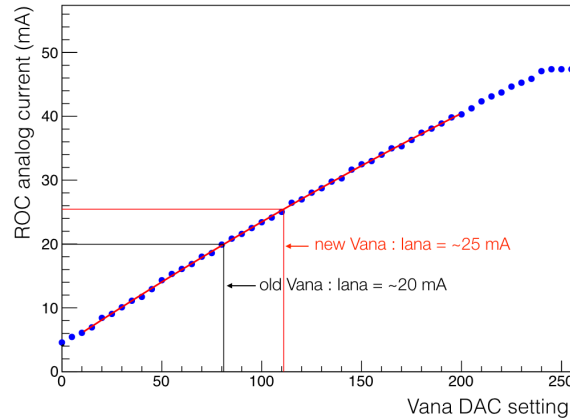


**Figure 16.16:** ROC analog current as readout with the ROC read back mechanism as a function of the analog voltage regulator setting.

# CHAPTER 17

# Conclusions

---

The contributions to the calibration and upgrade of the CMS pixel barrel detector have been presented in this part of thesis. First, a major effort was made during the first long shut-down to recover the full detector performance after the first LHC physics run. This effort included the replacement of broken components and the re-calibration of detector parameters at low temperature needed to compensate for the effects of radiation damage. The detector was re-installed into CMS in December 2014 and commissioned in January 2015 for the second LHC physics run at the highest center-of-mass energy of 13 TeV. The entire operation was completed in only a few days thanks to the expertise gained during the long shut-down. The first pp collision at 13 TeV occurred on March, 21st 2015 and since then the detector was running stable with a high data-taking efficiency.

Furthermore, I contributed to the Phase 1 upgrade pixel project. The upgrade detector will allow to maintain the excellent tracking performance of CMS at the upcoming higher luminosity conditions at the LHC. A test stand at the University of Zurich has been set up and run with the aim of testing the performance of the complete upgrade pixel system and gain experience in its operations. The setup includes a slice of the full CMS pixel DAQ together with all the upgrade electronics for the power, readout and control systems as well as newly developed pixel modules. The test system has been employed to implement and test new developments in the pixel online software used to operate with the detector. Although the software architecture remains unchanged, several calibration procedures for the present detector become obsolete with the new digital readout of the upgrade system, whereas novel tests have been developed. Additional fundamental modifications had to be understood and implemented to be able to operate the software with the upgrade detector. The Phase 1 pixel upgrade project is now at its last stage of assembly and testing of the entire system. The novel calibration procedures are aimed at guaranteeing the success of these operations, as well as of the installation and commissioning of the new system planned for March 2017.

# **Part III**

# **Summary**

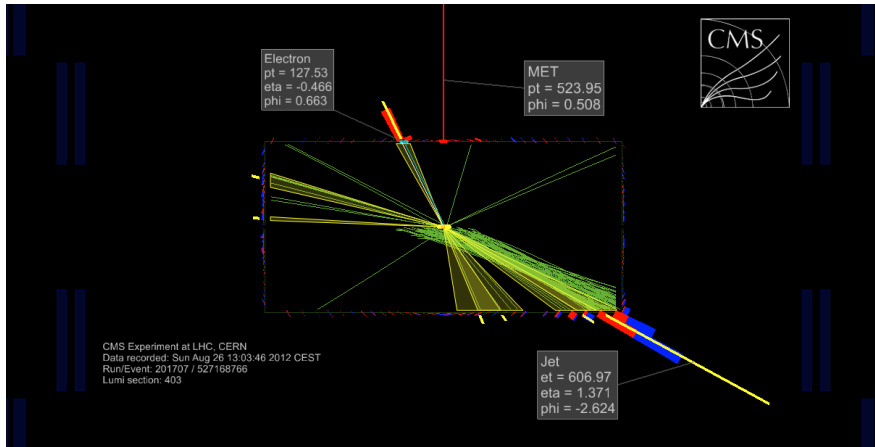
# APPENDIX A

## Studies on track reconstruction problems

---

A scan of the displays of all the events in 8 TeV data with  $m_{\text{WH}} > 1.6 \text{ TeV}$  passing all the selection criteria for the  $\ell\nu b\bar{b}$  final state (Table 8.1), reported that presence of two events characterized by a rare specific kind of noise. This noise arises from an anomalous behaviour of the tracking algorithm in the transition region between the barrel (TOB) and endcap (TEC) regions of the silicon tracker, namely, in the pseudorapidity range  $1 < |\eta| < 1.5$  (Fig. 3.5). As a consequence, many fake (displaced) tracks are associated to the selected H jet candidate. Figure A.1 shows the event display of one of the two events affected by this problem, while Figure A.2 shows the same feature in simulation.

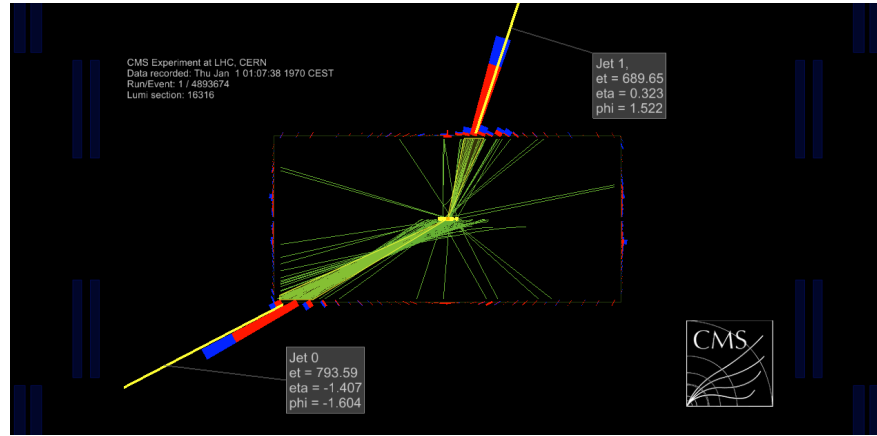
In order to reject this type of noise, it is common in CMS analyses to apply a standard filtering algorithm that discards the event if there is an anomalous amount of tracks that have been seeded in the TOB-TEC transition region. The efficiency of this filter on signal events is about 97% independently on the H jet  $p_T$ .



**Figure A.1:** Display of one typical anomalous event found in data recorded by the CMS experiment. Many fake and displaced tracks are reconstructed creating a bias in the jet reconstruction. Only tracks with  $p_T$  larger than 2 GeV are shown.

However, further checks performed on the anomalous events showed that after applying the standard filter residual noise can still be identified in the problematic  $\eta$  region. Therefore, it has been decided for the analysis described in this work to apply an additional requirement on the  $\eta$  of the selected H jet candidate (Section 6.4.2). In particular, CA8 jets are rejected if their pseudorapidity falls in the problematic region  $1 < |\eta| < 1.8$ . As described in the following, the choice for this fiducial cut is motivated by the disagreement between data and simulation in the rate at which the noise occur.

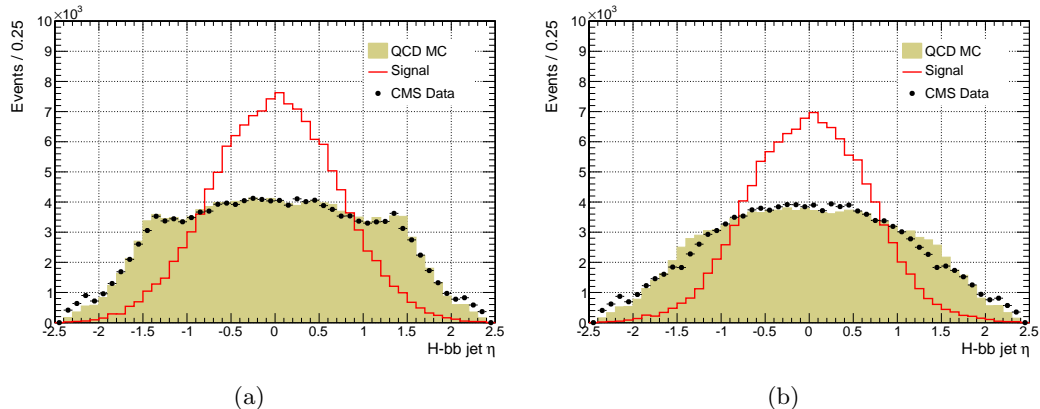
The efficiency of the standard filter is studied as a function of the H jet  $p_T$  and  $\eta$  in a dijet sample with high statistics in both data and simulation. The sample is selected requiring at least two jets, with  $p_T > 400 \text{ GeV}$  for the leading jet and  $p_T > 80 \text{ GeV}$  for the sub-leading



**Figure A.2:** Display of one typical anomalous event in simulation. Only tracks with  $p_T$  larger than 2 GeV are shown.

one. At least one of the jet has to be b-tagged using the same combined b tagging algorithm as for the main analysis selection, representing thus the H jet candidate. The jet that fails the b tagging is required to have low pruned mass ( $m_{jet} < 40$  GeV).

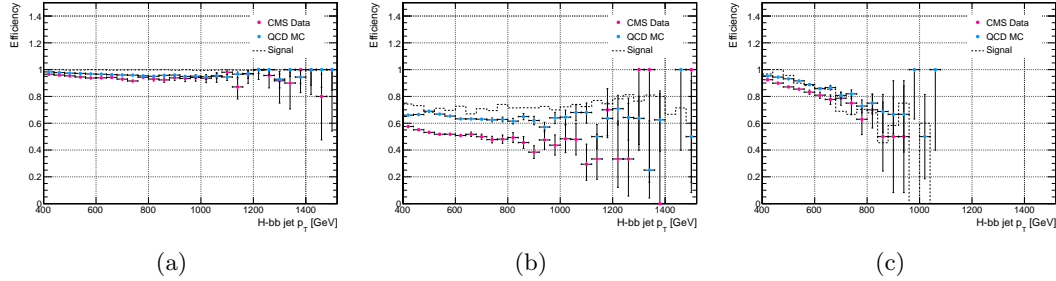
Figure A.3 shows the effect of the filter on the jet  $\eta$  distribution comparing data, simulated signal and QCD background: the signal distribution is rather unaffected while data and QCD background distributions show a reduction of events in the problematic  $\eta$  region after applying the filter, as expected.



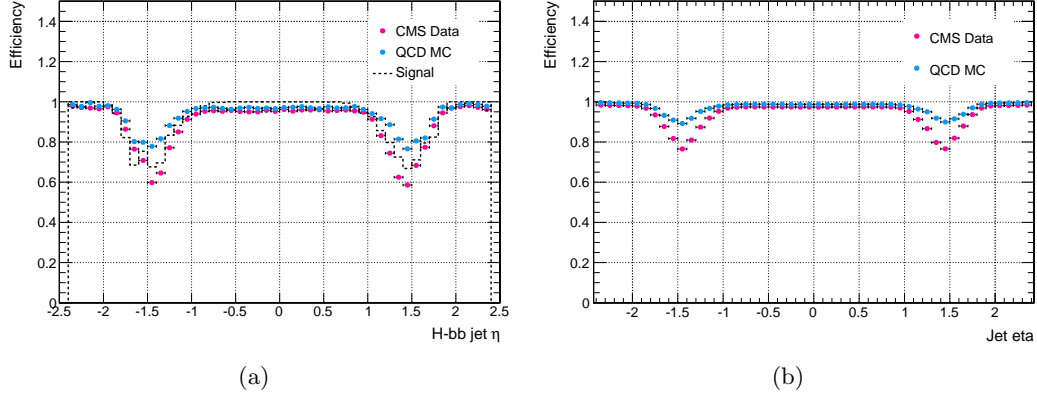
**Figure A.3:** Comparison of the H jet  $\eta$  distributions for data, and simulated signal and QCD background before (a) and after (b) applying the tracking noise filter. Signal jets are mostly central in the detector.

Figure A.4 shows the filter efficiency on data and simulated signal and QCD background as a function of the H jet candidate  $p_T$  for different jet  $\eta$  regions. A little dependence of the filter efficiency with the jet  $p_T$  is observed in the regions  $0 < |\eta| < 1$  and  $1.0 < |\eta| < 1.5$ , while in the forward region  $1.5 < |\eta| < 2.4$  the efficiency decreases with the jet  $p_T$ . The performance of the filter in the different  $\eta$  regions is summarized in Figure A.5(a). A large discrepancy between data and simulation is found in the pseudorapidity region  $1.0 < |\eta| < 1.8$ , where the simulation does not sufficiently well describe the full material budget of the tracking detector. The same studies are also performed removing the b-tagging requirement. The filter efficiency as a function of the leading jet  $\eta$  for this case is shown in Fig. A.5(b), for both data and

simulation. The increase in efficiency compared to what obtained in b-tagging shows that the b-tagging requirement enriches the samples with events characterized by this noise up to 30%, making this analysis systematically prone to it.



**Figure A.4:** Efficiency of the tracking noise filter as a function of the H jet  $p_T$  for data, and simulated signal and QCD background for jets reconstructed in the pseudorapidity regions  $0 < |\eta| < 1$  (a),  $1.0 < |\eta| < 1.5$  (b), and  $1.5 < |\eta| < 2.4$  (c).



**Figure A.5:** Efficiency of the tracking noise filter as a function of the leading jet  $p_T$  for data, and simulated signal and QCD background. (a) The leading jet is required to be b-tagged with the combined b tagging algorithm used in the main analysis. (b) The b tagging requirements for the leading jet are removed.



# Bibliography

- [1] F. Mandl and G. Shaw, “Quantum Field Theory”. Wiley, 1984.
- [2] Tevatron Electroweak Working Group, CDF, DELPHI, SLD Electroweak and Heavy Flavour Groups, ALEPH, LEP Electroweak Working Group, SLD, OPAL, D0, L3 Collaboration, “Precision Electroweak Measurements and Constraints on the Standard Model”, [arXiv:1012.2367](https://arxiv.org/abs/1012.2367).
- [3] Particle Data Group Collaboration, “Review of Particle Physics”, *Chin. Phys. C* **40** (2016) 100001, doi:[10.1088/1674-1137/40/10/100001](https://doi.org/10.1088/1674-1137/40/10/100001).
- [4] S. L. Glashow, “Partial-symmetries of weak interactions”, *Nucl. Phys.* **22** (1961) 579, doi:[10.1016/0029-5582\(61\)90469-2](https://doi.org/10.1016/0029-5582(61)90469-2).
- [5] S. Weinberg, “A Model of Leptons”, *Phys. Rev. Lett.* **19** (1967) 1264, doi:[10.1103/PhysRevLett.19.1264](https://doi.org/10.1103/PhysRevLett.19.1264).
- [6] A. Salam, “Gauge unification of fundamental forces”, *Rev. Mod. Phys.* **52** (1980) 525, doi:[10.1103/RevModPhys.52.525](https://doi.org/10.1103/RevModPhys.52.525).
- [7] F. Englert and R. Brout, “Broken Symmetry and the Mass of Gauge Vector Mesons”, *Phys. Rev. Lett.* **13** (1964) 321, doi:[10.1103/PhysRevLett.13.321](https://doi.org/10.1103/PhysRevLett.13.321).
- [8] P. Higgs, “Broken symmetries, massless particles and gauge fields”, *Physics Letters* **12** (1964) 132, doi:[10.1016/0031-9163\(64\)91136-9](https://doi.org/10.1016/0031-9163(64)91136-9).
- [9] P. W. Higgs, “Broken Symmetries and the Masses of Gauge Bosons”, *Phys. Rev. Lett.* **13** (1964) 508, doi:[10.1103/PhysRevLett.13.508](https://doi.org/10.1103/PhysRevLett.13.508).
- [10] P. W. Higgs, “Spontaneous Symmetry Breakdown without Massless Bosons”, *Phys. Rev.* **145** (1966) 1156, doi:[10.1103/PhysRev.145.1156](https://doi.org/10.1103/PhysRev.145.1156).
- [11] G. S. Guralnik, C. R. Hagen, and T. W. B. Kibble, “Global Conservation Laws and Massless Particles”, *Phys. Rev. Lett.* **13** (1964) 585, doi:[10.1103/PhysRevLett.13.585](https://doi.org/10.1103/PhysRevLett.13.585).
- [12] UA1 Collaboration, “Recent Results on Intermediate Vector Boson Properties at the CERN Super Proton Synchrotron Collider”, *Phys. Lett. B* **166** (1986) 484, doi:[10.1016/0370-2693\(86\)91603-5](https://doi.org/10.1016/0370-2693(86)91603-5).
- [13] UA2 Collaboration, “Measurement of the Standard Model Parameters from a Study of W and Z Bosons”, *Phys. Lett. B* **186** (1987) 440, doi:[10.1016/0370-2693\(87\)90324-8](https://doi.org/10.1016/0370-2693(87)90324-8).
- [14] DELPHI, OPAL, LEP Electroweak, ALEPH, L3 Collaboration, “Electroweak Measurements in Electron-Positron Collisions at W-Boson-Pair Energies at LEP”, *Phys. Rept.* **532** (2013) 119, doi:[10.1016/j.physrep.2013.07.004](https://doi.org/10.1016/j.physrep.2013.07.004), [arXiv:1302.3415](https://arxiv.org/abs/1302.3415).
- [15] CDF, D0 Collaboration, “Combination of CDF and D0 W-Boson Mass Measurements”, *Phys. Rev. D* **88** (2013) 052018, doi:[10.1103/PhysRevD.88.052018](https://doi.org/10.1103/PhysRevD.88.052018), [arXiv:1307.7627](https://arxiv.org/abs/1307.7627).

- [16] LHC Higgs Cross Section Working Group Collaboration, “Handbook of LHC Higgs Cross Sections: 1. Inclusive Observables”, doi:10.5170/CERN-2011-002, arXiv:1101.0593.
- [17] CMS Collaboration, “Observation of a new boson with mass near 125 GeV in pp collisions at  $\sqrt{s} = 7$  and 8 TeV”, *JHEP* **06** (2013) 081, doi:10.1007/JHEP06(2013)081, arXiv:1303.4571.
- [18] ATLAS Collaboration, “Observation of a new particle in the search for the Standard Model Higgs boson with the ATLAS detector at the LHC”, *Phys. Lett. B* **716** (2012) 1, doi:10.1016/j.physletb.2012.08.020, arXiv:1207.7214.
- [19] ATLAS, CMS Collaboration, “Combined Measurement of the Higgs Boson Mass in pp Collisions at  $\sqrt{s} = 7$  and 8 TeV with the ATLAS and CMS Experiments”, *Phys. Rev. Lett.* **114** (2015) 191803, doi:10.1103/PhysRevLett.114.191803, arXiv:1503.07589.
- [20] ATLAS, CMS Collaboration, “Measurements of the Higgs boson production and decay rates and constraints on its couplings from a combined ATLAS and CMS analysis of the LHC pp collision data at  $\sqrt{s} = 7$  and 8 TeV”, *JHEP* **08** (2016) 045, doi:10.1007/JHEP08(2016)045, arXiv:1606.02266.
- [21] ATLAS Collaboration, “Study of the spin and parity of the Higgs boson in diboson decays with the ATLAS detector”, *Eur. Phys. J.* **C75** (2015), no. 10, 476, doi:10.1140/epjc/s10052-015-3685-1, 10.1140/epjc/s10052-016-3934-y, arXiv:1506.05669. [Erratum: Eur. Phys. J.C76,no.3,152(2016)].
- [22] CMS Collaboration, “Study of the Mass and Spin-Parity of the Higgs Boson Candidate Via Its Decays to Z Boson Pairs”, *Phys. Rev. Lett.* **110** (2013), no. 8, 081803, doi:10.1103/PhysRevLett.110.081803, arXiv:1212.6639.
- [23] CMS Collaboration, “Constraints on the spin-parity and anomalous HVV couplings of the Higgs boson in proton collisions at 7 and 8 TeV”, *Phys. Rev. D* **92** (2015) 012004, doi:10.1103/PhysRevD.92.012004, arXiv:1411.3441.
- [24] S. Dimopoulos, S. Raby, and F. Wilczek, “Supersymmetry and the scale of unification”, *Phys. Rev. D* **24** (1981) 1681, doi:10.1103/PhysRevD.24.1681.
- [25] J. A. Casas, J. R. Espinosa, and M. Quiros, “Improved Higgs mass stability bound in the standard model and implications for supersymmetry”, *Phys. Lett. B* **342** (1995) 171, doi:10.1016/0370-2693(94)01404-Z, arXiv:hep-ph/9409458.
- [26] Planck Collaboration, “Planck 2015 results. XIII. Cosmological parameters”, *Astron. Astrophys.* **594** (2016) A13, doi:10.1051/0004-6361/201525830, arXiv:1502.01589.
- [27] K. Becker, M. Becker, and J. H. Schwarz, “String Theory and M-Theory: A Modern Introduction”. Wiley, 2006.
- [28] N. Arkani-Hamed, S. Dimopoulos, and G. R. Dvali, “The Hierarchy problem and new dimensions at a millimeter”, *Phys. Lett. B* **429** (1998) 263, doi:10.1016/S0370-2693(98)00466-3, arXiv:hep-ph/9803315.

- [29] C. D. Hoyle et al., “Sub-millimeter tests of the gravitational inverse-square law”, *Phys. Rev. D* **70** (2004) 042004, doi:10.1103/PhysRevD.70.042004, arXiv:hep-ph/0405262.
- [30] L. Randall and R. Sundrum, “A Large mass hierarchy from a small extra dimension”, *Phys. Rev. Lett.* **83** (1999) 3370, doi:10.1103/PhysRevLett.83.3370, arXiv:hep-ph/9905221.
- [31] K. Agashe, H. Davoudiasl, G. Perez, and A. Soni, “Warped gravitons at the LHC and beyond”, *Phys. Rev. D* **76** (2007) 036006, doi:10.1103/PhysRevD.76.036006, arXiv:hep-ph/0701186.
- [32] A. L. Fitzpatrick, J. Kaplan, L. Randall, and L.-T. Wang, “Searching for the Kaluza-Klein graviton in bulk RS models”, *JHEP* **09** (2007) 013, doi:10.1088/1126-6708/2007/09/013, arXiv:hep-ph/0701150.
- [33] B. Bellazzini, C. Csaki, and J. Serra, “Composite Higgses”, *Eur. Phys. J. C* **74** (2014) 2766, doi:10.1140/epjc/s10052-014-2766-x, arXiv:1401.2457.
- [34] R. Contino, D. Marzocca, D. Pappadopulo, and R. Rattazzi, “On the effect of resonances in composite Higgs phenomenology”, *JHEP* **10** (2011) 081, doi:10.1007/JHEP10(2011)081, arXiv:1109.1570.
- [35] D. Marzocca, M. Serone, and J. Shu, “General composite Higgs models”, *JHEP* **08** (2012) 013, doi:10.1007/JHEP08(2012)013, arXiv:1205.0770.
- [36] T. Han, H. E. Logan, B. McElrath, and L.-T. Wang, “Phenomenology of the little Higgs model”, *Phys. Rev. D* **67** (2003) 095004, doi:10.1103/PhysRevD.67.095004, arXiv:hep-ph/0301040.
- [37] M. Perelstein, “Little Higgs models and their phenomenology”, *Prog. Part. Nucl. Phys.* **58** (2005) 247, doi:10.1016/j.ppnp.2006.04.001, arXiv:hep-ph/0512128.
- [38] M. Schmaltz and D. Tucker-Smith, “Little Higgs review”, *Ann. Rev. Nucl. Part. Sci.* **55** (2005) 229, doi:10.1146/annurev.nucl.55.090704.151502, arXiv:hep-ph/0502182.
- [39] N. Arkani-Hamed, A. G. Cohen, E. Katz, and A. E. Nelson, “The Littlest Higgs”, *JHEP* **07** (2002) 034, doi:10.1088/1126-6708/2002/07/034, arXiv:hep-ph/0206021.
- [40] G. Burdman, M. Perelstein, and A. Pierce, “Large Hadron Collider tests of a little Higgs model”, *Phys. Rev. Lett.* **90** (2003) 241802, doi:10.1103/PhysRevLett.90.241802, arXiv:hep-ph/0212228. [Erratum: *Phys. Rev. Lett.* 92, 049903 (2004)].
- [41] D. Pappadopulo, A. Thamm, R. Torre, and A. Wulzer, “Heavy Vector Triplets: Bridging Theory and Data”, *JHEP* **09** (2014) 060, doi:10.1007/JHEP09(2014)060, arXiv:1402.4431.
- [42] V. Barger, W. Y. Keung, and E. Ma, “Gauge model with light  $W$  and  $Z$  bosons”, *Phys. Rev. D* **22** (1980) 727, doi:10.1103/PhysRevD.22.727.
- [43] G. Altarelli, B. Mele, and M. Ruiz-Altaba, “Searching for new heavy vector bosons in  $p\bar{p}$  colliders”, *Z. Phys. C* **45** (1989) 109, doi:10.1007/BF01556677.

- [44] L. Evans and P. Bryant, “LHC Machine”, *JINST* **3** (2008) S08001.
- [45] W.J. Stirling, “Parton luminosity and cross section plots”.  
<http://www.hep.ph.ic.ac.uk/~wstirlin/plots/plots.html>. *Private communication*.
- [46] ATLAS Collaboration, “The ATLAS Experiment at the CERN Large Hadron Collider”, *JINST* **3** (2008) S08003, doi:10.1088/1748-0221/3/08/S08003.
- [47] CMS Collaboration, “The CMS experiment at the CERN LHC”, *JINST* **3** (2008) S08004, doi:10.1088/1748-0221/3/08/S08004.
- [48] LHCb Collaboration, “The LHCb Detector at the LHC”, *JINST* **3** (2008) S08005, doi:10.1088/1748-0221/3/08/S08005.
- [49] ALICE Collaboration, “The ALICE experiment at the CERN LHC”, *JINST* **3** (2008) S08002, doi:10.1088/1748-0221/3/08/S08002.
- [50] F. Marcastel, “CERN’s Accelerator Complex”.  
<https://cds.cern.ch/record/1621583>. General Photo, 2013.
- [51] CMS Collaboration, “CMS Public Luminosity Results”.  
<https://twiki.cern.ch/twiki/bin/view/CMS/CMSPublic/LumiPublicResults>.
- [52] N. Cartiglia, “Measurement of the proton-proton total, elastic, inelastic and diffractive cross sections at 2, 7, 8 and 57 TeV”, arXiv:1305.6131.
- [53] CMS Collaboration, “The CMS tracker system project”, CMS Technical Design Report CERN-LHCC-98-006, CERN, 1997.
- [54] CMS Collaboration, “Pixel Performance Results”.  
<https://twiki.cern.ch/twiki/bin/view/CMS/PixelOfflinePlots>.
- [55] CMS Collaboration, “The CMS electromagnetic calorimeter project”, CMS Technical Design Report CERN-LHCC-97-033, CERN, 1997.
- [56] CMS Collaboration, “The CMS hadron calorimeter project”, CMS Technical Design Report CERN-LHCC-97-031, CERN, 1997.
- [57] P. Adzic et al., “Energy resolution of the barrel of the CMS electromagnetic calorimeter”, *JINST* **2** (2007) P04004, doi:10.1088/1748-0221/2/04/P04004.
- [58] M. A. Dobbs et al., “Les Houches guidebook to Monte Carlo generators for hadron collider physics”, in *Proceedings of the Workshop on Physics at TeV Colliders, Les Houches, France, May 26-June 3, 2003*, p. 411. 2004. arXiv:hep-ph/0403045.
- [59] J. C. Collins and D. E. Soper, “The Theorems of Perturbative QCD”, *Ann. Rev. Nucl. Part. Sci.* **37** (1987) 383, doi:10.1146/annurev.ns.37.120187.002123.
- [60] ZEUS Collaboration, “The ZEUS detector: Status report 1993”,.
- [61] H1 Collaboration, “The H1 detector at HERA”, *Nucl. Instrum. Meth. A* **386** (1997), no. 2, 310, doi:10.1016/S0168-9002(96)00893-5.
- [62] G. Altarelli and G. Parisi, “Asymptotic freedom in parton language”, *Nucl. Phys. B* **126** (1977), no. 2, 298, doi:10.1016/0550-3213(77)90384-4.

- [63] J. Pumplin et al., “New generation of parton distributions with uncertainties from global QCD analysis”, *JHEP* **07** (2002) 012, doi:10.1088/1126-6708/2002/07/012, arXiv:hep-ph/0201195.
- [64] H.-L. Lai et al., “New parton distributions for collider physics”, *Phys. Rev. D* **82** (2010) 074024, doi:10.1103/PhysRevD.82.074024, arXiv:1007.2241.
- [65] R. D. Ball et al., “Impact of Heavy Quark Masses on Parton Distributions and LHC Phenomenology”, *Nucl. Phys. B* **849** (2011) 296, doi:10.1016/j.nuclphysb.2011.03.021, arXiv:1101.1300.
- [66] T. Sjöstrand, S. Mrenna, and P. Z. Skands, “A Brief Introduction to PYTHIA 8.1”, *Comput. Phys. Commun.* **178** (2008) 852, doi:10.1016/j.cpc.2008.01.036, arXiv:0710.3820.
- [67] T. Sjöstrand, S. Mrenna, and P. Z. Skands, “PYTHIA 6.4 Physics and Manual”, *JHEP* **05** (2006) 026, doi:10.1088/1126-6708/2006/05/026, arXiv:hep-ph/0603175.
- [68] J. Alwall et al., “MadGraph 5 : Going Beyond”, *JHEP* **06** (2011) 128, doi:10.1007/JHEP06(2011)128, arXiv:1106.0522.
- [69] S. Frixione, P. Nason, and C. Oleari, “Matching NLO QCD computations with Parton Shower simulations: the POWHEG method”, *JHEP* **11** (2007) 070, doi:10.1088/1126-6708/2007/11/070, arXiv:0709.2092.
- [70] S. Frixione, P. Nason, and B. R. Webber, “Matching NLO QCD and parton showers in heavy flavor production”, *JHEP* **08** (2003) 007, doi:10.1088/1126-6708/2003/08/007, arXiv:hep-ph/0305252.
- [71] GEANT4 Collaboration, “GEANT4 — a simulation toolkit”, *Nucl. Instrum. Meth. A* **506** (2003) 250, doi:10.1016/S0168-9002(03)01368-8.
- [72] CMS Collaboration, “Measurement of the Underlying Event Activity at the LHC with  $\sqrt{s} = 7$  TeV and Comparison with  $\sqrt{s} = 0.9$  TeV”, *JHEP* **09** (2011) 109, doi:10.1007/JHEP09(2011)109, arXiv:1107.0330.
- [73] CMS Collaboration, “Study of the underlying event at forward rapidity in pp collisions at  $\sqrt{s} = 0.9$ , 2.76, and 7 TeV”, *JHEP* **04** (2013) 072, doi:10.1007/JHEP04(2013)072, arXiv:1302.2394.
- [74] J. M. Campbell, R. K. Ellis, and D. L. Rainwater, “Next-to-leading order QCD predictions for W + 2 jet and Z + 2 jet production at the CERN LHC”, *Phys. Rev. D* **68** (2003) 094021, doi:10.1103/PhysRevD.68.094021, arXiv:hep-ph/0308195.
- [75] J. M. Campbell, R. K. Ellis, and C. Williams, “Vector boson pair production at the LHC”, *JHEP* **07** (2011) 018, doi:10.1007/JHEP07(2011)018, arXiv:1105.0020.
- [76] J. M. Campbell and R. K. Ellis, “Top-quark processes at NLO in production and decay”, *J. Phys. G* **42** (2015) 015005, doi:10.1088/0954-3899/42/1/015005, arXiv:1204.1513.
- [77] J. M. Campbell, R. K. Ellis, and F. Tramontano, “Single top production and decay at next-to-leading order”, *Phys. Rev. D* **70** (2004) 094012, doi:10.1103/PhysRevD.70.094012, arXiv:hep-ph/0408158.

- [78] Y. Li and F. Petriello, “Combining QCD and electroweak corrections to dilepton production in FEWZ”, *Phys. Rev. D* **86** (2012) 094034, doi:10.1103/PhysRevD.86.094034, arXiv:1208.5967.
- [79] M. Czakon and A. Mitov, “Top++: A Program for the Calculation of the Top-Pair Cross-Section at Hadron Colliders”, *Comput. Phys. Commun.* **185** (2014) 2930, doi:10.1016/j.cpc.2014.06.021, arXiv:1112.5675.
- [80] P. Skands, S. Carrazza, and J. Rojo, “Tuning PYTHIA 8.1: the Monash 2013 Tune”, *Eur. Phys. J. C* **74** (2014) 3024, doi:10.1140/epjc/s10052-014-3024-y, arXiv:1404.5630.
- [81] CMS Collaboration, “Event generator tunes obtained from underlying event and multiparton scattering measurements”, *Eur. Phys. J. C* **76** (2016) 155, doi:10.1140/epjc/s10052-016-3988-x, arXiv:1512.00815.
- [82] CMS Collaboration, “Description and performance of track and primary-vertex reconstruction with the CMS tracker”, *JINST* **9** (2014) P10009, doi:10.1088/1748-0221/9/10/P10009, arXiv:1405.6569.
- [83] W. Adam, B. Mangano, T. Speer, and T. Todorov, “Track Reconstruction in the CMS tracker”, Technical Report CMS-NOTE-2006-041, CERN, 2006.
- [84] P. Billoir, “Progressive track recognition with a Kalman like fitting procedure”, *Comput. Phys. Commun.* **57** (1989) 390, doi:10.1016/0010-4655(89)90249-X.
- [85] R. Frhwirth, “Application of Kalman filtering to track and vertex fitting”, *Nucl. Instrum. Meth. A* **262** (1987) 444, doi:10.1016/0168-9002(87)90887-4.
- [86] T. Speer et al., “Vertex Fitting in the CMS Tracker”, Technical Report CMS-NOTE-2006-032, CERN, 2006.
- [87] K. Rose, “Deterministic annealing for clustering, compression, classification, regression, and related optimization problems”, *Proceedings of the IEEE* **86** (Nov, 1998) 2210, doi:10.1109/5.726788.
- [88] W. Waltenberger, R. Frhwirth, and P. Vanlaer, “Adaptive vertex fitting”, *J. Phys. G* **34** (2007), no. 12, N343.
- [89] CMS Collaboration, “Tracking Performance Results”.  
<https://twiki.cern.ch/twiki/bin/view/CMSPublic/PhysicsResultsTRK>.
- [90] S. Baffioni et al., “Electron reconstruction in CMS”, *Eur. Phys. J. C* **49** (2007) 1099, doi:10.1140/epjc/s10052-006-0175-5.
- [91] CMS Collaboration, “Commissioning of the Particle-flow Event Reconstruction with the first LHC collisions recorded in the CMS detector”, CMS Physics Analysis Summary CMS-PAS-PFT-10-001, CERN, 2010.
- [92] CMS Collaboration, “Particle-Flow Event Reconstruction in CMS and Performance for Jets, Taus, and MET”, CMS Physics Analysis Summary CMS-PAS-PFT-09-001, CERN, 2009.
- [93] W. Adam, R. Fröhwirth, A. Strandlie, and T. Todorov, “Reconstruction of electrons with the Gaussian-sum filter in the CMS tracker at the LHC”, *J. Phys. G* **31** (2005) N9.

- [94] CMS Collaboration, “Measurements of Inclusive W and Z Cross Sections in pp Collisions at  $\sqrt{s} = 7$  TeV”, *JHEP* **01** (2011) 080, doi:10.1007/JHEP01(2011)080, arXiv:1012.2466.
- [95] CMS Collaboration, “Performance of Electron Reconstruction and Selection with the CMS Detector in Proton-Proton Collisions at  $\sqrt{s} = 8$  TeV”, *JINST* **10** (2015) P06005, doi:10.1088/1748-0221/10/06/P06005, arXiv:1502.02701.
- [96] CMS Collaboration, “ECAL Performance Results”.  
<https://twiki.cern.ch/twiki/bin/view/CMSPublic/EcalDPGResults>.
- [97] CMS Collaboration, “Search for physics beyond the standard model in dilepton mass spectra in proton-proton collisions at  $\sqrt{s} = 8$  TeV”, *JHEP* **04** (2015) 025, doi:10.1007/JHEP04(2015)025, arXiv:1412.6302.
- [98] CMS Collaboration, “Performance of CMS muon reconstruction in pp collision events at  $\sqrt{s} = 7$  TeV”, *JINST* **7** (2012) P10002, doi:10.1088/1748-0221/7/10/P10002, arXiv:1206.4071.
- [99] CMS Collaboration, “CMS Physics: Technical Design Report Volume 1: Detector Performance and Software”, CMS Technical Design Report CERN-LHCC-2006-001, CERN, 2006.
- [100] CMS Collaboration, “CMS Performance Results for EPS 2015”, CMS Detector Performance Note CMS-DP-2015-016, CERN, 2015.
- [101] R. Radogna, “Search for high-mass resonances decaying into muon pairs with the CMS experiment at LHC”. PhD thesis, Università degli Studi di Bari Aldo Moro, 2016.
- [102] CMS Collaboration, J. Brooke, “Performance of the CMS Level-1 Trigger”, in *Proceedings of the 36th International Conference on High Energy Physics, Melbourne, Australia, July 4-11, 2012*, p. 508. 2013. arXiv:1302.2469.
- [103] G. P. Salam and G. Soyez, “A Practical Seedless Infrared-Safe Cone jet algorithm”, *JHEP* **05** (2007) 086, doi:10.1088/1126-6708/2007/05/086, arXiv:0704.0292.
- [104] S. Catani, Y. L. Dokshitzer, M. H. Seymour, and B. R. Webber, “Longitudinally invariant  $k_t$  clustering algorithms for hadron hadron collisions”, *Nucl. Phys. B* **406** (1993) 187, doi:10.1016/0550-3213(93)90166-M.
- [105] S. D. Ellis and D. E. Soper, “Successive combination jet algorithm for hadron collisions”, *Phys. Rev. D* **48** (1993) 3160, doi:10.1103/PhysRevD.48.3160, arXiv:hep-ph/9305266.
- [106] Y. L. Dokshitzer, G. D. Leder, S. Moretti, and B. R. Webber, “Better jet clustering algorithms”, *JHEP* **08** (1997) 001, doi:10.1088/1126-6708/1997/08/001, arXiv:hep-ph/9707323.
- [107] M. Wobisch and T. Wengler, “Hadronization corrections to jet cross-sections in deep inelastic scattering”, in *Proceedings of the Workshop on Monte Carlo generators for HERA physics, Hamburg, Germany, April 27-30, 1998*, p. 270. 1998.  
arXiv:hep-ph/9907280.
- [108] M. Cacciari, G. P. Salam, and G. Soyez, “The anti- $k_t$  jet clustering algorithm”, *JHEP* **04** (2008) 063, doi:10.1088/1126-6708/2008/04/063, arXiv:0802.1189.

- [109] CMS Collaboration, “Identification techniques for highly boosted W bosons that decay into hadrons”, *JHEP* **12** (2014) 017, doi:10.1007/JHEP12(2014)017, arXiv:1410.4227.
- [110] CMS Collaboration, “Jet energy scale and resolution in the CMS experiment in pp collisions at 8 TeV”, arXiv:1607.03663. Submitted to *JINST*.
- [111] CMS Collaboration, “Determination of Jet Energy Calibration and Transverse Momentum Resolution in CMS”, *JINST* **6** (2011) P11002, doi:10.1088/1748-0221/6/11/P11002, arXiv:1107.4277.
- [112] CMS Collaboration, “Pileup Jet Identification”, CMS Physics Analysis Summary CMS-PAS-JME-13-005, CERN, 2013.
- [113] CMS Collaboration, “Pileup Removal Algorithms”, CMS Physics Analysis Summary CMS-PAS-JME-14-001, CERN, 2014.
- [114] CMS Collaboration, “Jet algorithms performance in 13 TeV data”, CMS Physics Analysis Summary CMS-PAS-JME-16-003, CERN, 2014.
- [115] M. Cacciari, G. P. Salam, and G. Soyez, “FastJet User Manual”, *Eur. Phys. J. C* **72** (2012) 1896, doi:10.1140/epjc/s10052-012-1896-2, arXiv:1111.6097.
- [116] M. Cacciari and G. P. Salam, “Dispelling the  $N^3$  myth for the  $k_t$  jet-finder”, *Phys. Lett. B* **641** (2006) 57, doi:10.1016/j.physletb.2006.08.037, arXiv:hep-ph/0512210.
- [117] M. Cacciari and G. P. Salam, “Pileup subtraction using jet areas”, *Phys. Lett. B* **659** (2008) 119, doi:10.1016/j.physletb.2007.09.077, arXiv:0707.1378.
- [118] CMS Collaboration, “Jet energy scale and resolution performances with 13 TeV data”, CMS Detector Performance Note CMS-DP-2016-020, CERN, 2016.
- [119] CMS Collaboration, “Search for resonant pair production of Higgs bosons decaying to  $b\bar{b}$  and  $\tau^+\tau^-$  in proton-proton collisions at  $\sqrt{s} = 8$  TeV”, CMS Physics Analysis Summary CMS-PAS-EXO-15-008, CERN, 2015.
- [120] CMS Collaboration, “Identification of b-quark jets with the CMS experiment”, *JINST* **8** (2013) P04013, doi:10.1088/1748-0221/8/04/P04013, arXiv:1211.4462.
- [121] W. Waltenberger, “Adaptive Vertex Reconstruction”, Technical Report CMS-NOTE-2008-033, CERN, 2008.
- [122] CMS Collaboration, “Measurement of  $B\bar{B}$  Angular Correlations based on Secondary Vertex Reconstruction at  $\sqrt{s} = 7$  TeV”, *JHEP* **03** (2011) 136, doi:10.1007/JHEP03(2011)136, arXiv:1102.3194.
- [123] CMS Collaboration, “Performance of b tagging at  $\sqrt{s} = 8$  TeV in multijet,  $t\bar{t}$  and boosted topology events”, CMS Physics Analysis Summary CMS-PAS-BTV-13-001, CERN, 2013.
- [124] CMS Collaboration, “Identification of b quark jets at the CMS Experiment in the LHC Run 2”, CMS Physics Analysis Summary CMS-PAS-BTV-15-001, CERN, 2016.
- [125] CMS Collaboration, “Missing transverse energy performance of the CMS detector”, *JINST* **6** (2011) P09001, doi:10.1088/1748-0221/6/09/P09001, arXiv:1106.5048.

- [126] CMS Collaboration, “Performance of the CMS missing transverse momentum reconstruction in pp data at  $\sqrt{s} = 8$  TeV”, *JINST* **10** (2015) P02006, doi:10.1088/1748-0221/10/02/P02006, arXiv:1411.0511.
- [127] CMS Collaboration, “Performance of missing energy reconstruction in 13 TeV pp collision data using the CMS detector”, CMS Physics Analysis Summary CMS-PAS-JME-16-004, CERN, 2016.
- [128] J. Bauer, “Prospects for the Observation of Electroweak Top-Quark Production with the CMS Experiment”. PhD thesis, Karlsruher Institut für Technologie, 2010.
- [129] CMS Collaboration, “Studies of jet mass in dijet and W/Z + jet events”, *JHEP* **05** (2013) 090, doi:10.1007/JHEP05(2013)090, arXiv:1303.4811.
- [130] S. D. Ellis, C. K. Vermilion, and J. R. Walsh, “Techniques for improved heavy particle searches with jet substructure”, *Phys. Rev. D* **80** (2009) 051501, doi:10.1103/PhysRevD.80.051501, arXiv:0903.5081.
- [131] S. D. Ellis, C. K. Vermilion, and J. R. Walsh, “Recombination Algorithms and Jet Substructure: Pruning as a Tool for Heavy Particle Searches”, *Phys. Rev. D* **81** (2010) 094023, doi:10.1103/PhysRevD.81.094023, arXiv:0912.0033.
- [132] J. Thaler and K. Van Tilburg, “Identifying Boosted Objects with N-subjettiness”, *JHEP* **03** (2011) 015, doi:10.1007/JHEP03(2011)015, arXiv:1011.2268.
- [133] CMS Collaboration, “Search for massive resonances decaying into pairs of boosted bosons in semi-leptonic final states at  $\sqrt{s} = 8$  TeV”, *JHEP* **08** (2014) 174, doi:10.1007/JHEP08(2014)174, arXiv:1405.3447.
- [134] CMS Collaboration, “Search for massive resonances in dijet systems containing jets tagged as W or Z boson decays in pp collisions at  $\sqrt{s} = 8$  TeV”, *JHEP* **08** (2014) 173, doi:10.1007/JHEP08(2014)173, arXiv:1405.1994.
- [135] CMS Collaboration, “Search for massive resonances decaying into WW, WZ or ZZ bosons in proton-proton collisions at  $\sqrt{s} = 13$  TeV”, arXiv:1612.09159. Submitted to *JHEP*.
- [136] CMS Collaboration, “V Tagging Observables and Correlations”, CMS Physics Analysis Summary CMS-PAS-JME-14-002, CERN, 2014.
- [137] M. Bahr et al., “Herwig++ Physics and Manual”, *Eur. Phys. J. C* **58** (2008) 639, doi:10.1140/epjc/s10052-008-0798-9, arXiv:0803.0883.
- [138] CMS Collaboration, “Search for heavy resonances decaying into a vector boson and a Higgs boson in final states with charged leptons, neutrinos, and b quarks”, arXiv:1610.08066. Submitted to *Phys. Lett. B*.
- [139] M. Czakon, D. Heymes, and A. Mitov, “High-precision differential predictions for top-quark pairs at the LHC”, *Phys. Rev. Lett.* **116** (2016) 082003, doi:10.1103/PhysRevLett.116.082003, arXiv:1511.00549.
- [140] M. J. Oreglia, “A study of the reactions  $\psi' \rightarrow \gamma\gamma\psi'$ ”. PhD thesis, Stanford University, 1980. SLAC Report SLAC-R-236.

- [141] CMS Collaboration, “Measurement of the single-top-quark  $t$ -channel cross section in pp collisions at  $\sqrt{s} = 7$  TeV”, *JHEP* **12** (2012) 035, doi:10.1007/JHEP12(2012)035, arXiv:1209.4533.
- [142] P. Kant et al., “HatHor for single top-quark production: Updated predictions and uncertainty estimates for single top-quark production in hadronic collisions”, *Comput. Phys. Commun.* **191** (2015) 74, doi:10.1016/j.cpc.2015.02.001, arXiv:1406.4403.
- [143] CMS Collaboration, “Measurement of  $W^+W^-$  and ZZ production cross sections in pp collisions at  $\sqrt{s} = 8$  TeV”, *Phys. Lett. B* **721** (2013) 190, doi:10.1016/j.physletb.2013.03.027, arXiv:1301.4698.
- [144] T. Gehrmann et al., “ $W^+W^-$  Production at Hadron Colliders in Next to Next to Leading Order QCD”, *Phys. Rev. Lett.* **113** (2014) 212001, doi:10.1103/PhysRevLett.113.212001, arXiv:1408.5243.
- [145] CMS Collaboration, “Energy Calibration and Resolution of the CMS Electromagnetic Calorimeter in pp Collisions at  $\sqrt{s} = 7$  TeV”, *JINST* **8** (2013) P09009, doi:10.1088/1748-0221/8/09/P09009, arXiv:1306.2016.
- [146] CMS Collaboration, “CMS Luminosity Measurement for the 2015 Data Taking Period”, CMS Physics Analysis Summary CMS-PAS-LUM-15-001, CERN, 2015.
- [147] CMS Collaboration, “CMS Luminosity Based on Pixel Cluster Counting - Summer 2013 Update”, CMS Physics Analysis Summary CMS-PAS-LUM-13-001, CERN, 2013.
- [148] M. Cacciari et al., “The  $t\bar{t}$  cross-section at 1.8 and 1.96 TeV: A Study of the systematics due to parton densities and scale dependence”, *JHEP* **04** (2004) 068, doi:10.1088/1126-6708/2004/04/068, arXiv:hep-ph/0303085.
- [149] S. Catani, D. de Florian, M. Grazzini, and P. Nason, “Soft gluon resummation for Higgs boson production at hadron colliders”, *JHEP* **07** (2003) 028, doi:10.1088/1126-6708/2003/07/028, arXiv:hep-ph/0306211.
- [150] M. Botje et al., “The PDF4LHC Working Group Interim Recommendations”, arXiv:1101.0538.
- [151] S. Alekhin et al., “The PDF4LHC Working Group Interim Report”, arXiv:1101.0536.
- [152] A. D. Martin, W. J. Stirling, R. S. Thorne, and G. Watt, “Parton distributions for the LHC”, *Eur. Phys. J. C* **63** (2009) 189, doi:10.1140/epjc/s10052-009-1072-5, arXiv:0901.0002.
- [153] R. D. Ball et al., “Impact of heavy quark masses on parton distributions and LHC phenomenology”, *Nucl. Phys. B* **849** (2011) 296, doi:10.1016/j.nuclphysb.2011.03.021, arXiv:1101.1300.
- [154] A. L. Read, “Presentation of search results: The CL<sub>S</sub> technique”, *J. Phys. G* **28** (2002) 2693, doi:10.1088/0954-3899/28/10/313.
- [155] T. Junk, “Confidence level computation for combining searches with small statistics”, *Nucl. Instrum. Meth. A* **434** (1999) 435, doi:10.1016/S0168-9002(99)00498-2, arXiv:hep-ex/9902006.

- [156] G. Cowan, K. Cranmer, E. Gross, and O. Vitells, “Asymptotic formulae for likelihood-based tests of new physics”, *Eur. Phys. J. C* **71** (2011) 1554, doi:10.1140/epjc/s10052-011-1554-0, 10.1140/epjc/s10052-013-2501-z, arXiv:1007.1727. [Erratum: *Eur. Phys. J. C* **73** (2013) 2501].
- [157] A. Wald, “Tests of Statistical Hypotheses Concerning Several Parameters When the Number of Observations is Large”, *Transactions of the American Mathematical Society* **54** (1943) 426.
- [158] S. S. Wilks, “The Large-Sample Distribution of the Likelihood Ratio for Testing Composite Hypotheses”, *Ann. Math. Statist.* **9** (03, 1938) 60, doi:10.1214/aoms/1177732360.
- [159] E. Gross and O. Vitells, “Trial factors or the look elsewhere effect in high energy physics”, *Eur. Phys. J. C* **70** (2010) 525, doi:10.1140/epjc/s10052-010-1470-8, arXiv:1005.1891.
- [160] F. Garwood, “Fiducial Limits for the Poisson Distribution”, *Biometrika* **28** (1936) 437, doi:10.1093/biomet/28.3-4.437.
- [161] CMS Collaboration, “Search for a massive resonance decaying into a Higgs boson and a W or Z boson in hadronic final states in proton-proton collisions at  $\sqrt{s} = 8$  TeV”, *JHEP* **02** (2016) 145, doi:10.1007/JHEP02(2016)145, arXiv:1506.01443.
- [162] CMS Collaboration, “Search for new resonances decaying via WZ to leptons in proton-proton collisions at  $\sqrt{s} = 8$  TeV”, *Phys. Lett. B* **740** (2015) 83, doi:10.1016/j.physletb.2014.11.026, arXiv:1407.3476.
- [163] CMS Collaboration, “Search for massive WH resonances decaying into the  $\ell\nu b\bar{b}$  final state at  $\sqrt{s} = 8$  TeV”, *Eur. Phys. J. C* **76** (2016) 237, doi:10.1140/epjc/s10052-016-4067-z, arXiv:1601.06431.
- [164] CMS Collaboration, “Search for Narrow High-Mass Resonances in Proton-Proton Collisions at  $\sqrt{s} = 8$  TeV Decaying to a Z and a Higgs Boson”, *Phys. Lett. B* **748** (2015) 255, doi:10.1016/j.physletb.2015.07.011, arXiv:1502.04994.
- [165] ATLAS Collaboration, “Search for high-mass diboson resonances with boson-tagged jets in proton-proton collisions at  $\sqrt{s} = 8$  TeV with the ATLAS detector”, *JHEP* **12** (2015) 055, doi:10.1007/JHEP12(2015)055, arXiv:1506.00962.
- [166] CERN, “LHC commissioning schedule”. <https://lhcb-commissioning.web.cern.ch/lhc-commissioning/schedule/LHC-long-term.htm>.
- [167] H. C. Kästli et al., “CMS barrel pixel detector overview”, *Nucl. Instrum. Meth. A* **582** (2007) 724, doi:10.1016/j.nima.2007.07.058, arXiv:physics/0702182.
- [168] Y. Allkofer et al., “Design and performance of the silicon sensors for the CMS barrel pixel detector”, *Nucl. Instrum. Meth. A* **584** (2008) 25, doi:10.1016/j.nima.2007.08.151, arXiv:physics/0702092.
- [169] H. C. Kästli et al., “Design and performance of the CMS pixel detector readout chip”, *Nucl. Instrum. Meth. A* **565** (2006) 188, doi:10.1016/j.nima.2006.05.038, arXiv:physics/0511166.

- [170] E. Bartz, “The 0.25 $\mu$ m Token Bit Manager Chip for the CMS Pixel Readout”, in *Proceedings of the 11th Workshop on Electronics for LHC and Future Experiments, Heidelberg, Germany, 12–16 September, 2005*, p. 153. 2005.  
doi:10.5170/CERN-2005-011.153.
- [171] S. König et al., “Assembly of the CMS pixel barrel modules”, *Nucl. Instrum. Meth. A* **565** (2006) 62, doi:10.1016/j.nima.2006.04.081.
- [172] M. Pernicka et al., “The CMS Pixel FED”, in *Proceedings of the Topical Workshop on Electronics for Particle Physics, Prague, Czech Republic, 3–7 September, 2007*, p. 487. 2007. doi:10.5170/CERN-2007-007.487.
- [173] K. A. Gill et al., “Progress on the CMS Tracker control system”, in *Proceedings of the 11th Workshop on Electronics for LHC and Future Experiments, Heidelberg, Germany, 12–16 September, 2005*, p. 353. 2005. doi:10.5170/CERN-2005-011.353.
- [174] B. G. Taylor, “Timing distribution at the LHC”, in *Proceedings of the 8th Workshop on Electronics for LHC Experiments, Colmar, France, 9–13 September, 2002*, p. 63. 2002. doi:10.5170/CERN-2002-003.63.
- [175] D. Kotliński et al., “The control and readout systems of the CMS pixel barrel detector”, *Nucl. Instrum. Meth. A* **565** (2006) 73,  
doi:<http://dx.doi.org/10.1016/j.nima.2006.04.065>.
- [176] J. Troska et al., “Optical readout and control systems for the CMS tracker”, *IEEE Trans. Nucl. Sci.* **50** (2003) 1067, doi:10.1109/TNS.2003.815124.
- [177] P. Placidi, A. Marchioro, and P. Moreira, “CMS Tracker PLL Reference Manual”, Manual, CERN EP Microelectronics Group, 2000.
- [178] P. M. H. Correia, A. Marchioro and J. Schrader, “Delay25 - A 4 channel 1/2 ns programmable delay line”, Manual, CERN EP Microelectronics Group, 2005.
- [179] C. Paillard, C. Ljuslin, and A. Marchioro, “The CCU25: a network oriented communication and control unit integrated circuit in a 0.25  $\mu$ m CMOS technology”, in *Proceedings of the 8th Workshop on Electronics for LHC Experiments, Colmar, France, 9–13 September, 2002*, p. 174. 2002. doi:10.5170/CERN-2002-003.174.
- [180] Ryd, Anders and Stroiney, Steve and Das, Souvik and Ecklund, Karl, “CMS Pixel Online Software and Calibrations”, Manual, Cornell University, CERN, 2012.
- [181] V. Brigljevic et al., “Using XDAQ in application scenarios of the CMS experiment”, *eConf C* **0303241** (2003) MOGT008, arXiv:hep-ex/0305076.
- [182] CMS Collaboration, “A library developed for the CMS data acquisition system at CERN”, Manual, CERN, 2012.
- [183] CMS Collaboration, “Operational Issues of the Present CMS Pixel Detector”, *PoS Vertex2012* (2013) 051.
- [184] N. Wermes, L. Rossi, P. Fischer, and T. Rohe, “Pixel Detectors, From Fundamentals to Applications”. Springer-Verlag, 2006.
- [185] CMS Pixel Collaboration, “Status of the CMS Pixel detector”, *JINST* **4** (2009) P03019, doi:10.1088/1748-0221/4/03/P03019.

- [186] CMS Collaboration, “CMS Pixel status”, *Nucl. Instrum. Meth. A* **731** (2013) 13, doi:10.1016/j.nima.2013.04.001.
- [187] A. Dominguez et al., “The Pixel Detector Upgrade”, CMS Technical Design Report CERN-LHCC-2012-016. CMS-TDR-11, CERN, 2012.
- [188] CMS Collaboration, “Pilot system for the Phase 1 pixel upgrade of CMS”, *PoS VERTEX2015* (2015) 018.
- [189] L. Feld et al., “The DC-DC conversion power system of the CMS Phase-1 pixel upgrade”, *JINST* **10** (2015) C01052, doi:10.1088/1748-0221/10/01/C01052.
- [190] H. Kästli, “Frontend electronics development for the CMS pixel detector upgrade”, *Nucl. Instrum. Meth. A* **731** (2013) 88, doi:10.1016/j.nima.2013.05.056.
- [191] A. Starodumov, P. Berger, and M. Meinhard, “High rate capability and radiation tolerance of the PROC600 readout chip for the CMS pixel detector”, *JINST* **12** (2017) C01078.
- [192] J. Troska et al., “Prototype pixel optohybrid for the CMS phase 1 upgraded pixel detector”, *JINST* **7** (2012) C01113, doi:10.1088/1748-0221/7/01/C01113.
- [193] L. M. Caminada, “Study of the Inclusive Beauty Production at CMS and Construction and Commissioning of the CMS Pixel Barrel Detector”. PhD thesis, Zurich, ETH, 2010.